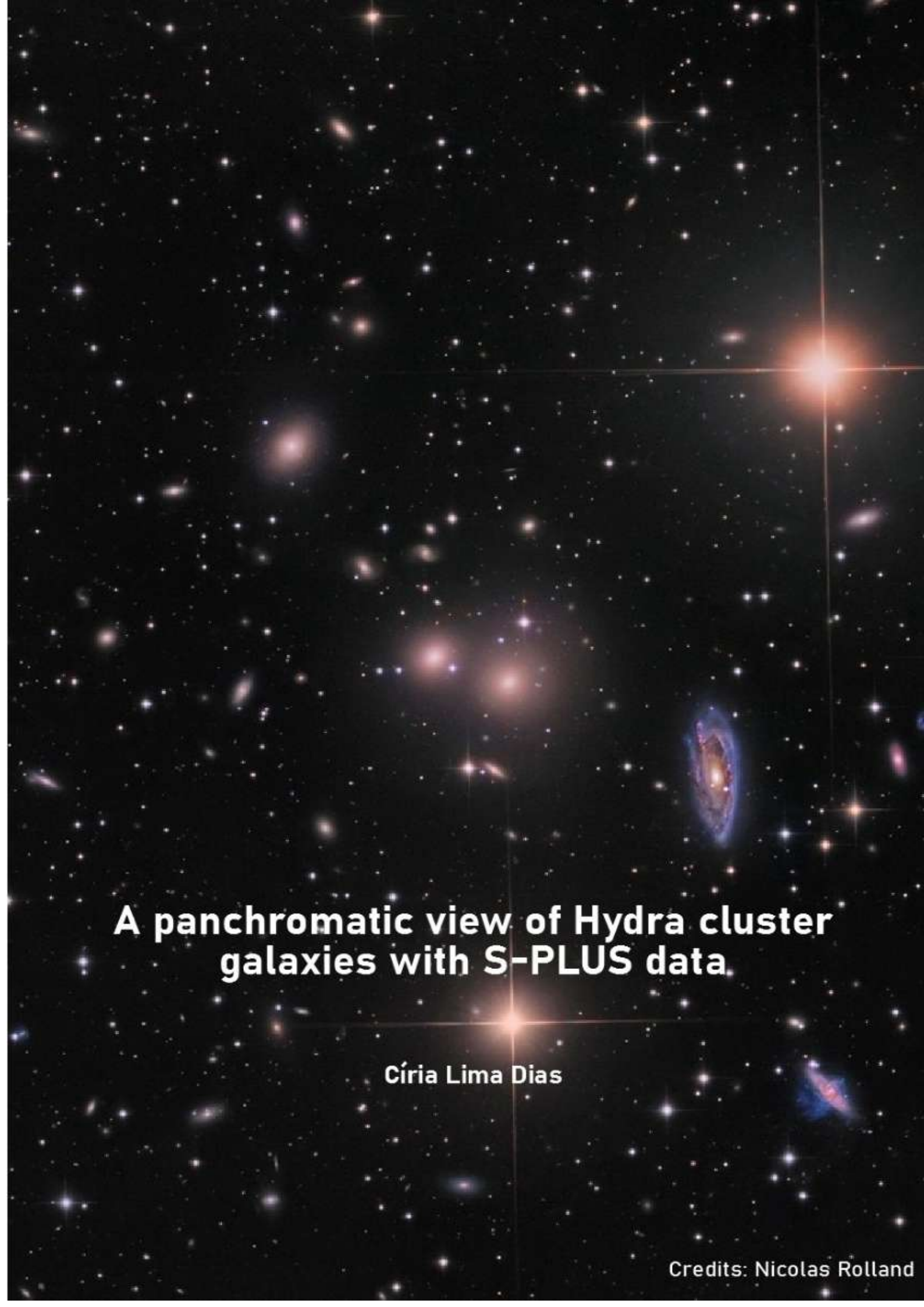

A panchromatic view of Hydra cluster galaxies with S-PLUS data

Círia Lima Dias

Credits: Nicolas Rolland

UNIVERSIDAD
DE LA SERENA
CHILE

DEPARTAMENTO
ASTRONOMÍA

A panchromatic view of Hydra cluster galaxies with S-PLUS data

Círia Lima Dias

UNIVERSIDAD
DE LA SERENA
CHILE

Doctoral Thesis

To fulfill the requirements for the degree of
Doctor of Philosophy in Astronomy
at Universidad de La Serena under the supervision of
Prof. dr. Antonela Monachesi (Astronomy, Universidad de La Serena)
Prof. dr. Sergio Torres Flores (Astronomy, Universidad de La Serena)

Círia Lima Dias

March 14, 2022

Contents

Acknowledgments

I have many people to thank for making this work a possibility. I have the hard task of trying to summarise my acknowledgements here.

First, I would like to thank my advisors Dr. Antonela Monachesi and Dr. Sergio Torres Flores, for their guidance and support.

I would like to express my sincere gratitude to my partner Dr. Paulo Lago for his encouragement and support during this journey.

My sincere thanks to Dr. Bruno Quint for welcoming me at the time that more needed, and for becoming the voice of my conscience.

I would like to thank my family Venina Miranda, Juarez Dias, and Emilia for raising me and educating me with their love.

I would like to thank all friends I made during my doctorate: Alex, Camila, Catalina Urrejola (for the best moments), Catalina Labayru, Dania, Daniel (always scaring me), Diego, Nahir (for your calm), Piera (always willing to help).

I acknowledge the University staff for their support.

I would like to thank the S-PLUS project and all collaborators especially Dr. Arianna Cortesi, Dr. Carlos Barbosa, Dr. Fábio R. Herpich, Dr. Claudia Mendes de Oliveira, Dr. Paola Dimauro, and Dr. Daniela Olave Rojas.

I would like to thank Dr. Rodrigo Carrasco and Dr. Facundo Gómez for accompanying and advising me during my thesis progress.

Finally, I acknowledge the financial support provided by ANID (CONICYT-PFCHA/Doctorado Nacional/2019-21191938), by the 'Vicerrectoría de Investigacion de la Universidad de La Serena' program 'Apoyo al fortalecimiento de grupos de investigacion', and by FONDECYT Regular grant 1181797.

1 Introduction

The evolution of scientific knowledge has naturally allowed us to ponder the existence of cloud-like objects in the night sky. In 1755, Immanuel Kant (1724-1804) suggested that these cloud-like objects or nebulae could be stellar systems such as the Milky Way. The astronomer Charles Messier during the period of 1771 to 1784 catalogued more than 100 cloud-like objects in the sky. Latter, William Parsons (1800-1867), known as Lord Rosse, recognised the spiral structure of several nebulae, and in 1864 John Herschel published a larger catalogue of such objects, containing around 5000 nebulae. Since Kant's hypothesis was confirmed by Edwin Hubble in 1925, we now know that many of these nebulae are galaxies, and to date we still continue on our quest for a better understanding of these objects, going further than catalogues, seeking for the understanding of the origin of their physical and structural properties. In particular, one of the many remarkable and still open questions in extragalactic astronomy is: How do galaxies evolve with/within environment? In this thesis, we will present our contribution to increase our knowledge about galaxies in a dense environment and their properties.

1.1 Galaxy formation

Galaxies are dynamically bound systems composed of hundreds of thousands to billions of stars, dark matter, gas, and dust, which can be found in different shapes, sizes, and colours. Their formation and evolution history determine their characteristics that we observe. Therefore, studying the properties of galaxies gives us clues about the different physical processes that they went through.

To explain how galaxies are formed we have to take into account the phenomena that occurred at the beginning of the Universe. At early times, quantum fluctuations amplified by cosmic inflation allowed some regions in the Universe to be denser than others, creating substructures due to gravitational instability (Jeans, 1902). These denser regions accumulate matter and give rise to the large-scale structures we now know. In the current cosmological model, so-called Λ Cold Dark Matter (ΛCDM) model (Spergel et al., 2007), these dense regions contain both baryonic and dark matter. When these regions reach an over-density threshold they collapse producing a single dark matter halo and their subsequent growth and evolution are driven in a hierarchical manner via the accretion and merger of smaller dark matter haloes (Peebles, 1965), allowing them to attract more massive objects, creating larger structures(Lacey & Cole, 1993). Galaxies later form at the centre of these dark matter haloes. An important phenomenon for the formation of galaxies is the gas cooling, which is responsible for the separation between baryonic matter and dark matter, causing the baryonic matter to fall into the potential well of a dark matter halo forming a protogalaxy in its centre (White & Rees, 1978, Kaiser, 1984).

The properties of the dark matter halo will influence the morphological structure of the formed galaxy. Disc galaxies are believed to form when the angular momentum, of the dark matter halo and baryonic matter, is conserved during the gas cooling. Then, the gas will fall rotating into the dark matter halo potential well, and settling into circular orbits before the stars in the disc are born, forming a disc that is supported by rotation (Larson, 1976). Elliptical galaxies are thought to be created by the merger between galaxies of equivalent mass (Toomre & Toomre, 1972, Gott & Thuan, 1976). Indeed, galaxies, in general, are not isolated in the Universe, they can accrete and/or lose material due to different kind of interactions. In addition, the merger of galaxies can generate new galaxies with different properties from the parent galaxies (Duc & Mirabel, 1999). As mentioned earlier, the features of a galaxy are a

consequence of its initial properties and the environment where it formed, as they largely determine the fate of its evolution. In addition, galaxies can be part of larger structures, like groups, clusters, and super-clusters, where the environment plays a role in its evolution and transformation. In the next section, we provide a brief description of the characteristics of different types of galaxies, and how these change with different environments, which is the objective of study of this thesis.

1.2 Galaxy morphological types

One of the first steps to understanding nature is to classify what we observe. In general, we like to classify in colours, shapes, sizes and other characteristics, regardless of the area of science we are studying. In the case of galaxies it is not different; in 1926 Edwin Hubble classified galaxies as: elliptical and lenticular (so-called 'early-types'), spiral and irregular galaxies (so-called 'late-types') based on their morphology in photographic plates (Hubble, 1926), as shown in Figure 1.1 by Kormendy & Bender (1996). The late-type galaxies are divided into two brands: ordinary and barred. The irregular galaxies are those that do not fit into any of the other classifications. Additionally, the light profiles of early-type and late-type galaxies are different, which, nevertheless, can be described by a Sérsic profile (Sérsic, 1963), defined in Equation 1.1.

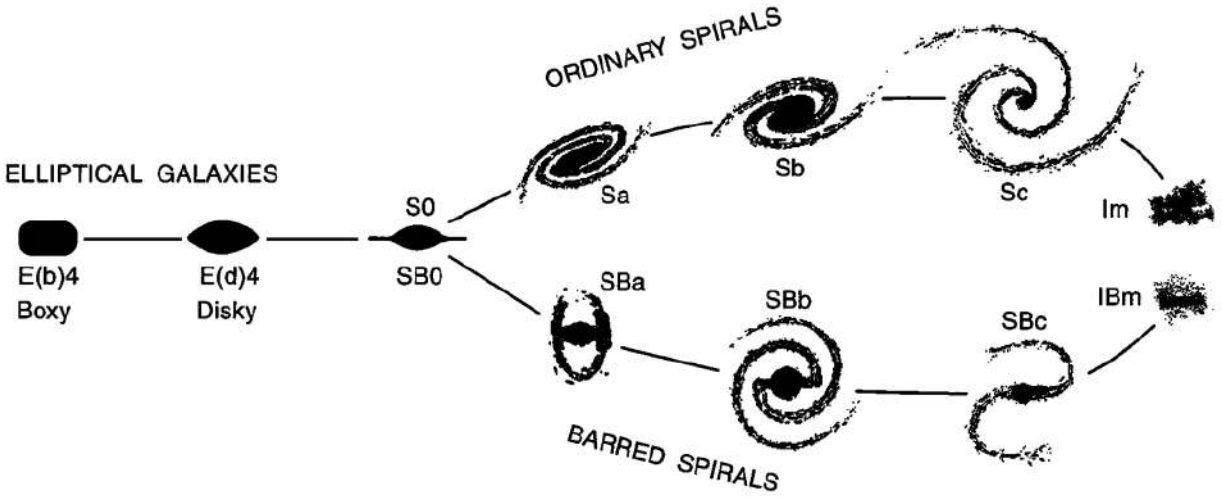

Figure 1.1: Hubble's morphological classification scheme (Hubble, 1936) modified by Kormendy & Bender (1996). In this illustration it is possible to see the different characteristics of different morphological types of galaxies including the irregular galaxies.

$$I(r) = I_e exp\left\{-b_n\left[\left(\frac{r}{R_e}\right)^{\frac{1}{n}} - 1\right]\right\} \tag{1.1}$$

where $I(r)$ is the intensity, R_e and I_e are the effective radius and the intensity at an R_e, respectively. n is the Sérsic index, also known as the concentration parameter, and b_n is a function of n that satisfies $\Gamma(2n) = 2\gamma(2n, b_n)$. In cases where the galaxy profile is more concentrated, n presents higher values. For instance, with n = 4 we obtain the well known de Vaucouleurs profile and it corresponds to the

typical profile of an elliptical galaxy. For n=1, we have a typical profile of an exponential disc. Figure 1.2 shows the Sérsic profile, note that the larger the Sérsic index the steeper is the central core, and the profile has an extended wing. The next section summarises the main properties of each type of galaxies, where we describe its typical light distribution, based on the Sérsic profile.

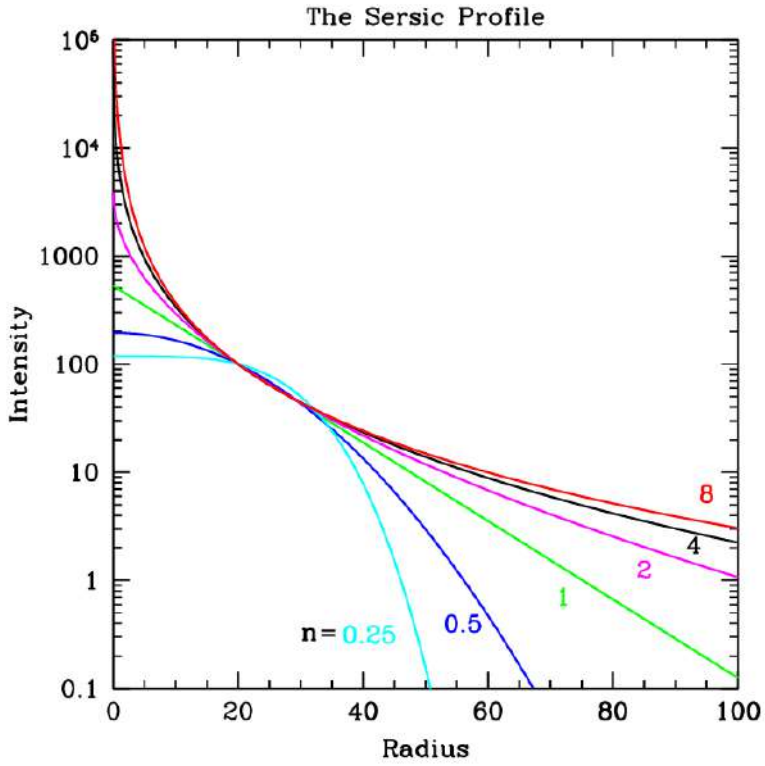

Figure 1.2: Sérsic profile for different n values. The profiles are coloured for different values of n. The x-axis shows the distance to the centre of the galaxy. The y-axis shows the profile intensity. Figure extracted from Peng et al. (2010a).

1.2.1 Elliptical Galaxies

Elliptical galaxies (EGs) are composed, in general, of an old and low mass population of stars, which results in their red colours. These galaxies have a low content of gas, possessing none or very low star formation. There is a wide range of luminosities within the EGs: from the very low luminous galaxies in the universe: Dwarf ellipticals, Dwarf spheroidals, to the brightest galaxies in the universe: central Dominant (cD) galaxies.

The elliptical galaxies, as the name already suggests, have isophotes with an ellipsoidal shape, varying its ellipticity from 0 to 7. In EGs, the light profile is smooth being in general well described by the de Vaucouleurs profile ($n = 4$). Less massive EGs tend to have lower Sérsic index values, whereas massive EGs tend to have higher Sérsic index values (Graham, 2013). The kinematics of these types of galaxies is mainly dominated by the stellar random motions. Indeed, the velocity dispersion of an EG (σ) is very well correlated with its luminosity (L), known as the Faber–Jackson relation ($L \propto \sigma^4$; Faber & Jackson, 1976).

1.2.2 Spiral Galaxies

The spiral galaxies (SGs) have a disc, halo, bulge, spiral arms, and they are separated into two groups: barred spirals (SB) and barless spirals (S). If the galaxy has tighter spiral arms and a larger bulge (compared to the galaxy's extent) it will be classified as Sa or SBa. If the spiral arms are more open and the bulge smaller, they will be classified as Sc or SBc. Spiral galaxies have an inhomogeneous brightness distribution, due to spiral arms concentrate star-forming regions, where massive, blue and bright stars can be found.

Another component that can be present in spiral galaxies is a bar. Aguerri et al. (2009) studying spiral galaxies, from the local Universe in the *r*-band, found that ~ 55 percent of their galaxy's sample contains a bar. This percentage can change with different filters and redshifts. The bar can carry gas to the central region of the galaxy, which can lead to star formation in the bulge or feed an active galactic nucleus (AGN).

In the case of a spiral galaxy the light profile is not well described by only one component. The discs can be well described by an exponential profile. The bulges, which represent an important component of spiral galaxies and are typically associated with an old stellar population, can be described by a Sérsic profile with a varying *n*. The bulges that are supported by rotation are known as pseudo-bulges, and generally have a lower Sérsic index, and a younger stellar population than the so-called classic bulges (Gadotti, 2009), which are those with properties similar to those of elliptical galaxies. In the case of barred galaxies it is necessary to add a third profile to describe the light distribution. In general a bar is well modeled by a Sérsic profile with the *n* lower than 1 (Peng et al., 2010a).

The spiral galaxies are supported by an ordered rotation, meaning that the stars and gas in the disc rotate orderly in the same direction. A well known empirical relation found in spiral galaxies is the Tully–Fisher scaling relation (Tully & Fisher, 1977), which describes the relation between the galaxy luminosity and the maximum rotation velocity of spirals ($L \propto V_{max}^{\alpha}$; with $2.5 < \alpha < 4$).

1.2.3 Lenticular Galaxies

Lenticular galaxies (S0s) are composed by the bulge and a second component, often with disc-like shape, however without the spiral arms. S0 galaxies have very little gas content, and as a result, they have no or very low star formation displaying a red-like colour. Like in a spiral, the S0 galaxy light profile can be described by a Sérsic profile for the bulge, and an exponential profile for the disc.

1.2.4 Irregular and Peculiar Galaxies

These types of galaxies have no definite shape and their brightness are not homogeneous, which makes it difficult to model it with a Sérsic profile. They display blue colours, which are associated with recent episodes of star formation in these systems. The irregular galaxies can be: Irr I which show some organised structure like arms, and Irr II for more disorganised objects.

1.3 Morphology, colour, and environmental relation

We saw in the previous section that distinct morphological types of galaxies have also different physical properties, such as colours. In this section, we review different studies that show how the colour of a galaxy has a relation to its morphology, and also the connection between morphology and environment. The colour of a galaxy provides information about its stellar content (age and metallicity), and the galaxy's luminosity gives information related to the galaxy mass (Faber & Gallagher, 1979). In this context, and in order to characterise galaxies, the colour magnitude diagram (CMD) appears as an excellent tool, since luminosity is related to the absolute magnitude of the galaxy.

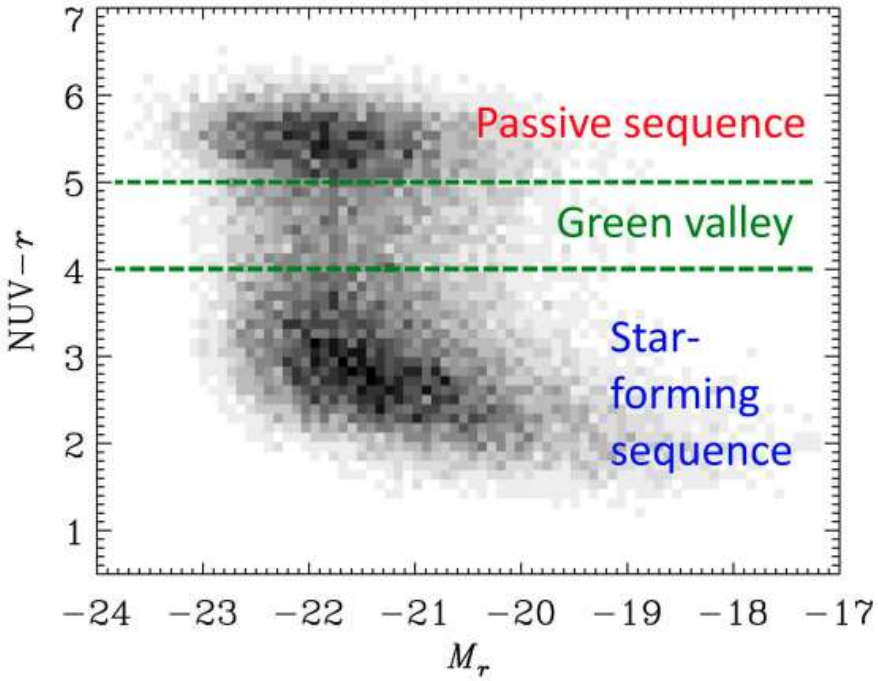

Figure 1.3: Colour-magnitude diagram of galaxies (Salim, 2014). The horizontal axis represents the SDSS *r*-band absolute magnitude and the vertical axis represents the (NUV - *r*) colour, where NUV is near-ultraviolet. This image shows clearly that galaxies populate this diagram in a blue cloud (star-forming sequence), green valley, and a red sequence (passive galaxies). This shows that galaxies are either forming stars or are quenched and that the transition period in the green valley is very short.

Strateva et al. (2001) using data from the Sloan Digital Sky Survey (SDSS, York et al., 2000) analysed 147,920 galaxies brighter than 21 (*g*-band), and observed that the galaxies show a bimodal distribution in colour in the local Universe: the majority of the galaxies are either red ($u-r > 2.2$) or blue ($u-r <$ 2.2). They found that this bimodal behaviour is only weakly dependent on the sample magnitude cut. Later, other works confirmed this behaviour at higher redshifts (Bell et al., 2004, Brammer et al., 2009). Figure 1.3 shows an illustrative CMD, where the bimodal colour behaviour can be seen in the red sequence and the blue cloud. The red sequence (passive sequence in Figure 1.3) is composed of elliptical and lenticular galaxies characterised by little or no ongoing star formation, also the dusty star-forming spiral galaxies are in this CMD region. The blue cloud (star-forming sequence in Figure 1.3) is composed of spirals and irregular galaxies distinguishable by ongoing star formation.

In addition, Figure 1.3 shows a transition zone, sparsely populated, between the red sequence and blue cloud; this region is known as the green valley. The redder spirals galaxies are usually found in this region. Galaxies migrate from the blue cloud to the red sequence through the green valley. This process is known as quenching, where the galaxy's star formation rate is very low, or zero, and leads to the bi-modality in the galaxy population (Peng et al., 2010b).

In addition to studying the galaxy population as a whole, we can also investigate if the environment has any effect on its formation and evolution. Dressler (1980) studying galaxies in the field and in clusters of galaxies found that the fraction of early-type galaxies increases as a function of the local density, whereas the fraction of late-type galaxies decreases in the same direction, as shown in Figure 1.4. Apparently, the environment is playing a role in the evolution of galaxies influencing their morphology. In the hierarchical galaxy formation scenario, elliptical galaxies are formed via the merger of galaxies (Kormendy et al., 2009), then it is expected to find more elliptical galaxies in dense environments, where mergers among galaxies are more common. Many studies emphasize the importance of the environment in the evolution of galaxies (Oemler, 1974, Davis & Geller, 1976, Butcher & Oemler, 1978, Gunn & Gott, 1972, Whitmore & Gilmore, 1991, Fasano et al., 2015). We present in the next section, some of the main physical processes, both internal and related to the environment, that can influence the shape and evolution of galaxies.

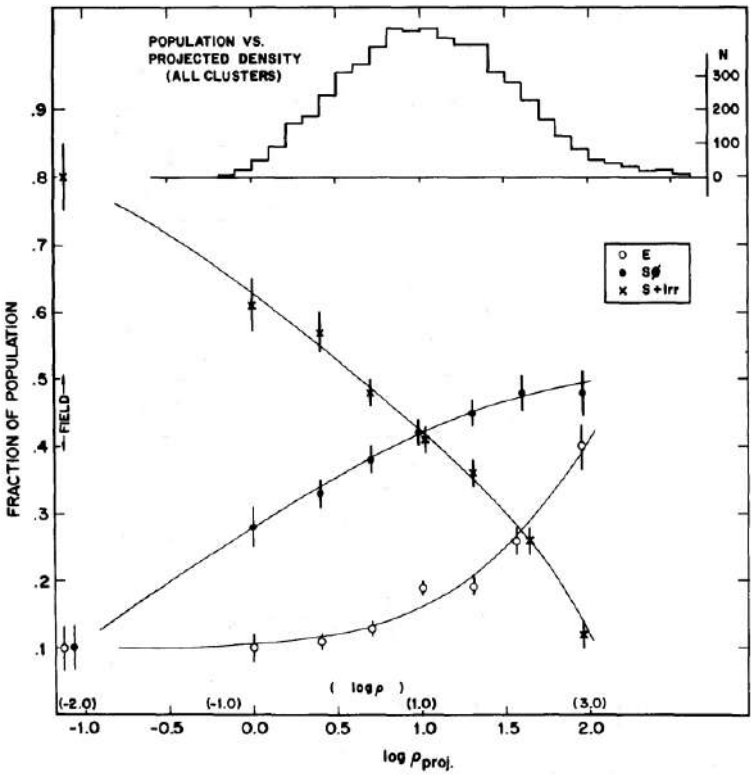

Figure 1.4: Fraction of Elliptical, Lenticular, and Spiral + Irregular galaxies as a function of the log of the projected density. The histogram shows the number of galaxies within a density bin. Figure extracted from Dressler (1980).

1.4 Galaxies: internal and environmental processes

Galaxies can experience several processes throughout their lifetimes which will mold their individual features and properties. For example, when a galaxy stops its star formation from the outside to the inside, known as outside-in quenching, the galaxy's central part is bluer than its outskirts. We seek to understand what mechanisms and processes may be influencing the evolution of galaxies and causing, for instance, the type of observed phenomenon just mentioned. These processes, in addition, can be regarded as environmental: those that are related to the galaxy living in a given neighbourhood and its contents, and internal: those that act internally to a galaxy regardless of its environment.

1.4.1 Internal processes

Star-formation feedback: Supernova explosions (Types Ia & II), stellar winds, radiation pressure, and photoionization leave an imprint on the evolution of a galaxy. These processes heat their surroundings preventing the gas from collapsing, thus impacting the formation of new stars in galaxies (Dekel & Silk, 1986, Ceverino & Klypin, 2009). Additionally, the supernovae can spread heavy elements throughout the galaxy, enriching the interstellar medium, which has an impact on the abundances of the future generations of stars and on the galaxy overall. Also, supernovae winds can eject gas outside galaxies (especially for low-mass galaxies), leading to gas depletion and, consequently, star formation quenching.

AGN feedback: The Active Galactic Nucleus of a galaxy can expel and heat the gas from the galaxy which prevents its cooling. This phenomenon affects the star formation of a galaxy decreasing its efficiency and, as a consequence, the galaxy becomes quenched (Nyland et al., 2018).

Secular bulge growth: The bulge growth can be caused by kinematic disturbances produced by the bar, which drives material into the centre of the galaxy. This phenomenon causes the formation of pseudo-bulges, which have flatter shapes and high rotation velocity than those of classical bulges (Kormendy & Kennicutt, 2004).

Inside-out disc growth: In the hierarchical model for disc formation, the discs must grow from the infall of gas from the extended dark matter halo (Fall & Efstathiou, 1980). There is some observational evidence of the inside-out disc growth, where the light profile of the old stellar population is more concentrated than the light profile of the young stellar population (Wang et al., 2011).

1.4.2 Environmental processes

Ram pressure stripping: When a galaxy falls into a cluster it starts to suffer ram pressure stripping (Gunn & Gott, 1972), which is the pressure that a fluid (the intracluster gas, in this case) exerts on another fluid (the galactic gas, in this case) that is moving through it. The galaxy gas will be stripped if the outside pressure exceed the galaxy' restoring pressure produced by the surface mass density of the galaxy. Due to ram pressure stripping the galaxy loses its gas (decreasing its gas reservoir), and as a consequence it lowers and even stops its star formation.

Galaxy harassment: This phenomenon occurs in clusters due to the tidal interactions between galaxies when a high-speed fly-by galaxy passes through or nearby other galaxy without merging. These

types of interactions can induce star formation as well as create tidal tails, warps, bars, and asymmetry in the galaxy (Moore et al., 1996). Additionally, this process is capable of destroying the discs of satellites galaxies, becoming specially relevant in the inner parts of clusters (Moore et al., 1996, 1998, 1999, Duc & Bournaud, 2008, Smith et al., 2015).

Galaxy mergers: Two or more galaxies can merge together. When the merger is produced by galaxies with a large relative luminosity ratio (1:4) it is known as a minor merger (Lotz et al., 2011), whilst mergers among galaxies of comparable masses are categorised as major mergers. When the galaxies that merge are gas-rich this process is known as a wet merger, if the galaxies are gas-poor it is known as a dry merger. Wet mergers can induce star formation and the accretion of gas into the central black hole of the galaxy (Hopkins et al., 2008).

Galaxy strangulation: When a galaxy falls into a cluster the gas supply is shut off. However, the galaxy can continue to form stars for several gigayears increasing its stellar mass and metallicity (Larson et al., 1980). The star formation of the galaxy eventually stops due to lack of gas.

Gas accretion: Galaxies are surrounded by HI clouds, tails, filaments, and other galaxies. Gas can be accreted through gas infall from the intergalactic medium and by interactions among galaxies. The cold gas that is accreted can feed the galaxy star formation (Stewart et al., 2011). A possible evidence of this phenomenon is that the rate of star formation in the solar neighbourhood is constant, thus suggesting that gas used by the star formation has been replaced by accretion (Fraternali & Binney, 2008).

1.5 Environmental and mass quenching

We mentioned in the previous section some examples of how the environment could shape the evolution of galaxies. Some of these phenomena cause the galaxy to stop forming new stars, and with time it becomes red and quenched. This process is known as environmental quenching and it is the main responsible for the quenching of star-forming galaxies at low masses ($M_\star < 10^{10} M_\odot$) and at low redshifts. At higher redshifts, the low mass galaxies are mostly quenched via mergers (Peng et al., 2010b). Additionally, there is another internal quenching mechanism, called mass-quenching, that dominates the quenching of massive galaxies ($M_\star > 10^{10.2} M_\odot$, Peng et al., 2010b). This quenching process is caused by hot gas ($> 10^{5.4} K$) that can drive both mass quenching and environment quenching (Gabor & Davé, 2015). The hot gas fails to cool, thus starving the galaxies of fuel to form new stars. This happens with haloes of masses greater than $10^{12} M_\odot$.

An illustration of what we just mentioned is shown in Figure 1.5, where the dominant mechanism for the quenching of galaxies as a function of mass and redshift is displayed. We can see in Figure 1.5 that for high mass galaxies the mass-quenching dominates regardless of redshift. Meanwhile, for low mass galaxies, the merging and environmental quenching are the dominant mechanisms for high and low redshift, respectively (Peng et al., 2010b). However, it is noteworthy that recent work found that at high redshift ($1.0 < z < 1.4$) the quenched fraction excess strongly increases with increasing stellar mass, which contrast with many studies of the local Universe (van der Burg et al., 2020a). Additionally, at high redshift, most of the massive galaxies ($M > 10^{10.5} M_\odot$) are quenched via pre-processing in group or protocluster environments (McNab et al., 2021).

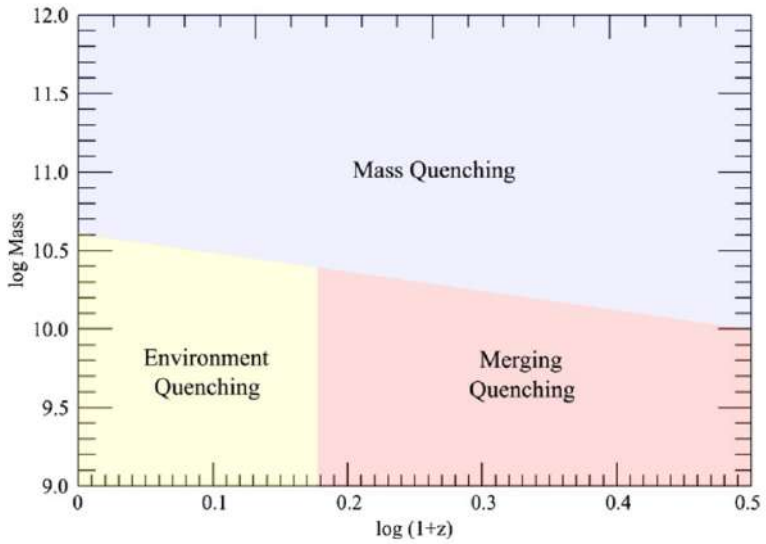

Figure 1.5: Diagram showing the dominant mechanisms for the quenching of galaxies as a function of mass and redshift. Figure extracted from Peng et al. (2010b).

1.6 The place where the environment plays a role: Galaxy clusters

This thesis aims to investigate the evolution of galaxies in dense environments, and clusters of galaxies are the densest environments, at large scale, we know in the Universe, making it the ideal laboratory for our investigation. A cluster can be found using a Colour-Magnitude Diagram of galaxies. In a Cluster, the majority of galaxies are early-type galaxies that are characterised by a red colour. Then, a cluster CMD should be dominated by red galaxies, that is called the red cluster sequence. In general, the closer to the virialization state a cluster is, then more early-type galaxies should have. Therefore, if a CMD of a sky region shows an overdensity of red galaxies, there is a high probability that in this region we can find a galaxy cluster. Another way to find a galaxy cluster is via X-ray emission, that is duo to the hot intracluster medium (Mitchell et al., 1976). Also, many cluster have been detected by their Sunyaev–Zeldovich effect (Sunyaev & Zeldovich, 1980).

Galaxy clusters are formed by hundreds to thousands of galaxies, hot gas, and dark matter. They have typical sizes larger than $1.5h^{-1}$ (where $H_0 = 100\ h\ kms^{-1}\ Mpc^{-1}$, Spergel et al., 2003), and masses greater than $\sim 10^{14} M_{\odot}$. When the mass of a galaxy cluster is estimated by the sum of the masses of the individual galaxies in the cluster, the final mass is not enough to explain the dynamical behaviour of the galaxies. The measured velocity dispersion of the cluster indicates that it should have more matter than what we are observing only with the galaxies. This is known as the missing mass problem and it is an indication of the existence of dark matter (Zwicky, 1937), nowadays the cold dark matter (CDM).

The cluster total mass can be measured using the velocity dispersion of its galaxies (Leonard & King, 2010), that will include all the mass in the cluster, not only the galaxy's luminous mass. Measurements performed with X-Ray show that the intra-cluster space should be formed by a hot gas $(10^7 - 10^8)$K. The hotter the gas is, the greater the potential well of the cluster is, and the mass estimation using the hot gas is analogous to the mass estimated with the velocity dispersion (if the cluster is virialized). The origin of the X-Ray emission is thermal bremsstrahlung (free-free radiation). The emitted

radiation is from the free electrons, that are accelerated by nucleus and protons in the intra-cluster medium. The X-Ray distribution structure can inform the cluster dynamical state; if it is virialized or if the cluster has passed by a disturbed merger process. If the X-Ray morphology distribution is homogeneous, this means that the cluster is virialized, or very close to the state of virilization. If the X-Ray morphology distribution is irregular, this implies that the cluster could be in a stage of a merging process, or smaller groups of galaxies are falling into the cluster causing substructures in the X-Ray distribution.

Clusters of galaxies can have different configurations in their galaxy's spatial distribution, which can also be an indication of their dynamical state. In general, galaxy clusters have a spherical or elliptical form, but there are some interacting clusters, those that are gravitationally interacting with another cluster or group of galaxies, which display a disturbed shape in their galaxy distribution. Galaxy clusters are classified based on the comparison between the relative brightness between the brightest galaxy and the other cluster member galaxies. Bautz & Morgan (1970) separated clusters in three main classes based on this. Type I: a cluster containing a centrally located cD galaxy, which is a giant elliptical galaxy that possesses an extended stellar halo. Type II: a cluster which brightest galaxies are intermediate in appearance between class cD and the Virgo-type giant ellipticals. Finally Type III: a cluster that contains no dominant galaxy. Also, there are clusters with intermediate types between the three classes described here. Figure 1.6 shows examples of the three types of clusters. The left, middle and right images of Figure 1.6 show the cluster Abell 2199, the Coma, and the Virgo clusters, which are Type I, II and III, respectively.

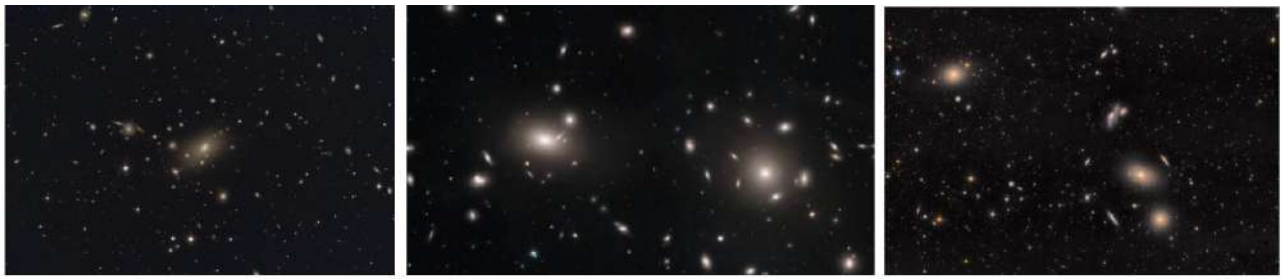

Figure 1.6: Left image shows the cluster Abell 2199 that is a Type I (Image credit: Capella Observatory). Middle image shows the Coma cluster that is a Type II (Image credit: NASA and Australian Telescope National Facility). The right panel shows the Virgo cluster that is a Type III (Image credit: 2020 October 10 - Astronomy Picture of the Day by Fernando Penae).

Another cluster classification was made by Rood & Sastry (1971) who created a "Tuning Fork" diagram of rich clusters of galaxies containing six classes: supergiant (cD), binary (B), line (L), core-halo (C), flat (F) and irregular (I), as shown in Figure 1.7. The supergiant clusters, as the name suggest, contain a cD galaxy. Binary clusters have two supergiant galaxies that are separated by a distance $\leq$ 10 diameters of the largest galaxy. Line clusters have three or more bright galaxies ordered in line with a comparable separation among them, and with numerous fainter members. The core-halo clusters have four or more bright galaxies with a comparable separation, and positioned near the cluster centre. The flat clusters are disposed in a flattened configuration, and contain several bright galaxies. Finally, the irregular clusters do not have an ordered distribution of their galaxy members, this type of clusters have more late-type galaxies, meanwhile cD clusters have more early-type galaxies. Also,

irregular clusters show more substructures and are less dense than other clusters.

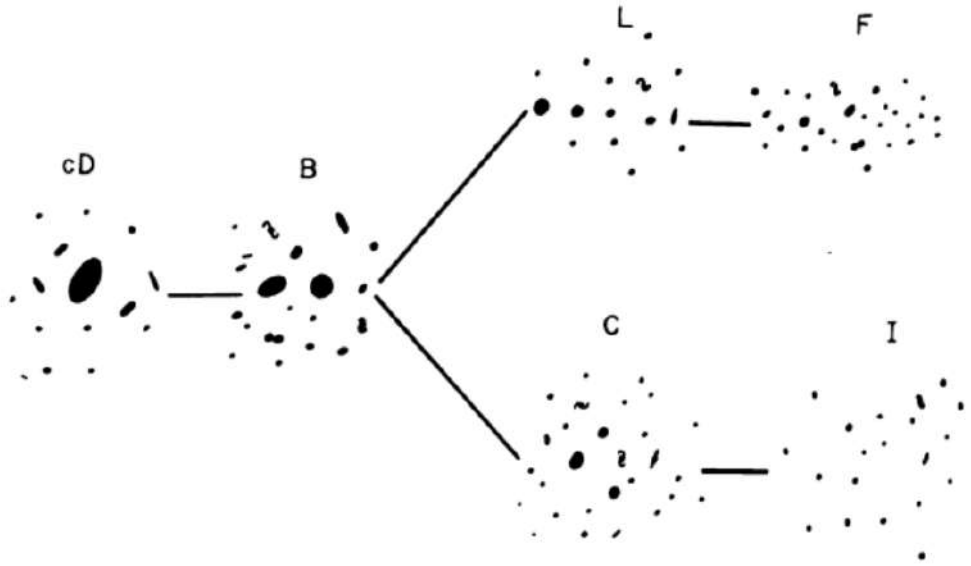

Figure 1.7: Tuning Fork diagram for galaxy clusters proposed by Rood & Sastry (1971). The six classes are shown as: supergiant (cD), binary (B), line (L), core-halo (C), flat (F) and irregular (I) clusters.

Within a cluster, the galaxies inhabiting the core are usually the most massive ones, and most of them are quenched at early times. Late-type galaxies within clusters are often found among the satellites at the outskirts (Dressler et al., 1997, Fasano et al., 2000, Postman et al., 2005, Desai et al., 2007). In general late-type galaxies are the less massive components and are more strongly susceptible to morphological changes due to the influence of the environmental processes.

Galaxies in clusters have high peculiar velocities, then a merger (minor or major) between galaxies is not common. In a galaxy cluster, due to the high density of galaxies, it is expected to occur other types of interactions, as described in subsection 1.4.2. These interactions could temporarily increase the galaxy star formation rate (SFR). Indeed, a concentrated star formation is observed when neighbouring galaxies interact (Moss et al., 1998). Also a tidal interaction could trigger a bar formation in cluster cores (Łokas et al., 2016). In this type of environment a galaxy can suffer other processes that decrease its star formation and could become quenched. Some of this processes are the ram-pressure and stripping of the cold gas (Gunn & Gott, 1972, Abadi et al., 1999, Jaffé et al., 2015, Peng et al., 2015). Due to the loss of gas expelled into the environment the galaxy stops the star formation and over time it becomes redder.

For galaxies in clusters, their outermost part is the one that suffers most from the influence of the environment. For example, Durret et al. (2019) studied the link between brightest cluster galaxy (BCG) properties in the redshift range $0.2 < z < 0.9$. They found that, when modelling the light of the BCGs, with two profiles, the effective radius of their outer component increases with decreasing redshift. This agrees with the growth of BCGs by accretion of smaller galaxies. Another evidence from a stronger influence of the environment in the outer parts of galaxies is found in Gutiérrez et al.

(2004). They performed a bulge-disc decomposition of galaxies in the Coma cluster and in the field, and found that the scale lengths of the discs of Coma spiral galaxies are 30 percent smaller than field galaxies. In this thesis, we are also interested in studying the effect that the environment plays in the components of a galaxy (bulge and disc) separately, which will be discussed in Chapter 5.

1.7 This thesis: the Hydra cluster

The main goal of this thesis is to understand the evolution of galaxies in a dense environment. In particular, we focus on analysing the galaxies in the Hydra cluster and aim to answer the following open questions: How can the environment influence the physical and structural properties of galaxies in different bands? And, how do galaxies' properties change with increasing local density or clustercentric distance? We will study the Hydra galaxies mainly using photometric images from the Southern Photometric Local Universe Survey (S-PLUS, see Section 2). This work has the advantage of using a unique set of 12 filters in the visible range of the spectrum, that allow us to explore how the properties of galaxies change among them. This is an interesting approach since each region of the spectrum provides us with information on different physical mechanisms in galaxies. For instance, by observing in the *J*0660-band we can estimate the galaxy's Hα emission and its star-formation rate. The structural and physical properties of galaxies carry information about their formation and evolution, then observing their behaviour with respect to the environment around them (density and clustercentric distance), gives us clues about the evolutionary processes and physical phenomena that the galaxies are being experiencing.

This thesis aims to explore the structural, physical, and kinematical properties of galaxies in the Hydra cluster (Abell 1060). In this thesis, we consider structural parameters those that can suffer from the effects of the galaxy's projection, such as effective radius, Sérsic index, and b/a. Additionally, the physical parameters are those that do not depend strongly on the galaxy's projection, such as stellar mass, star-formation rate, luminosity, magnitude, and colour. We want to examine the properties of galaxies, and also their wavelength dependence, to observe and understand how and if their properties are being affected by the environment. We choose to study the Hydra cluster because it is a nearby structure located at a distance of $\sim$ 50 Mpc (Misgeld et al., 2011, Arnaboldi et al., 2012) and for which galaxies can be spatially well resolved, making it an ideal laboratory to fulfill our objectives. Hydra is a medium-mass compact cluster (Arnaboldi et al., 2012) with a large fraction of early-type galaxies and at least 50 ultra-compact dwarf galaxies (Misgeld & Hilker, 2011, Misgeld et al., 2011). It is classified as a type III structure (Bautz & Morgan, 1970), which means it has no dominant central member although there are two bright galaxies near to the centre: NGC 3311, a cD galaxy with radial velocity of 3825 km/s, and NGC 3309, an E3 galaxy with radial velocity of 4009 km/s (Ventimiglia et al. 2011 and references therein). Hydra is isolated in redshift space, having no background galaxies up to $\sim$ 8000 km/s (Richter, 1987).

Based on X-ray data, Ventimiglia et al. (2011) have shown evidences that Hydra is a prototype of a dynamically relaxed cluster, showing an isothermal intracluster medium for the most part of the cluster region, indicating that it has not been going through any big merging process during the last few Gyrs (Furusho et al., 2001, Ventimiglia et al., 2011). The cluster virial and X-ray masses are $(5.80 \pm 0.56) \times 10^{14} M_{\odot}$ and $(9.8 \pm 1.3) \times 10^{14} M_{\odot}$ respectively, and the global projected velocity dispersion is 660 ± 52 km/s (Babyk & Vavilova, 2013) with the X-ray centre of the cluster located at $\sim$8.6 kpc northeast of NGC 3311 (Hayakawa et al., 2004, Barbosa et al., 2018), we will use this

galaxy as the central component for practical purposes. In this and the previous paragraph we showed a summary of the main characteristics and works carried out in the Hydra cluster. This thesis comes to contribute with original results about the galaxies' properties (physical and structural), and for the first time it will be presented a panchromatic study, using 12 bands, of the Hydra cluster galaxies.

1.8 Outline of the thesis

This Ph.D. thesis is organised as follows: In Chapter 2 we describe the S-PLUS data used in this work and the Hydra membership selection. Chapter 3 explains how we estimate the structural (Sérsic index, effective radius) and physical (stellar masses, star-formation rates, colours and magnitudes) parameters of galaxies. We also introduce the MEGAMORPH-GALAPAGOS2 project, which was used to model the galaxies with the Sérsic profile and to perform the bulge-disc decomposition. In Chapter 4, we explore the results of fitting the light profile of the galaxies with a single Sérsic profile. We investigate how the structural parameters vary in the 12 S-PLUS filters and determine the dynamic state of the Hydra cluster. In Chapter 5 we explore the bulge-disc decomposition of Hydra galaxies, investigating how the bulge-to-total flux varies in the 12 S-PLUS bands, and we also examine the mass-size plane. In Chapter 6 we present an overview of the work conducted in this thesis. Finally, in Chapter 7 we propose follow up works, based on the results that we obtained in this thesis.

2 Data and Hydra membership selection

In this thesis we study the physical and structural properties of galaxies in the Hydra cluster. We do so mainly by using photometric data from S-PLUS, a survey that observes in 12 photometric bands (see 2.1). This is the first time that a morphological analysis using 12 bands in the visible spectra is presented for Hydra galaxies, and the wide field of view of S-PLUS allows us to investigate, in great detail, any possible variation in the structural parameters and physical properties as a function of wavelength. This work represents a great improvement over most previous studies which use up to eight filters to perform a multiband fitting (La Barbera et al., 2010, Vulcani et al., 2011, Kelvin et al., 2012, Vika et al., 2013, 2014). In this Chapter, we introduce the data used in this thesis and the Hydra membership selection.

2.1 S-PLUS

The Southern Photometric Local Universe Survey (S-PLUS, Mendes de Oliveira et al., 2019), analogous to J-PLUS (Cenarro et al., 2019) in the northern hemisphere, is an ongoing photometric survey in the southern hemisphere. The Survey's objective is to image ∼9300 square degrees of the sky over a 5-yr period of observations since August 2017, when it started. S-PLUS uses the T80Cam installed at the 82.6 cm T80-South telescope located at Cerro Tololo Inter-American Observatory, Chile. The T80Cam has a detector with 9232×9216 10μm-pixels, a plate-scale of 0.55 arcsec pixel^{-1} and an effective field of view of 2 square degrees.

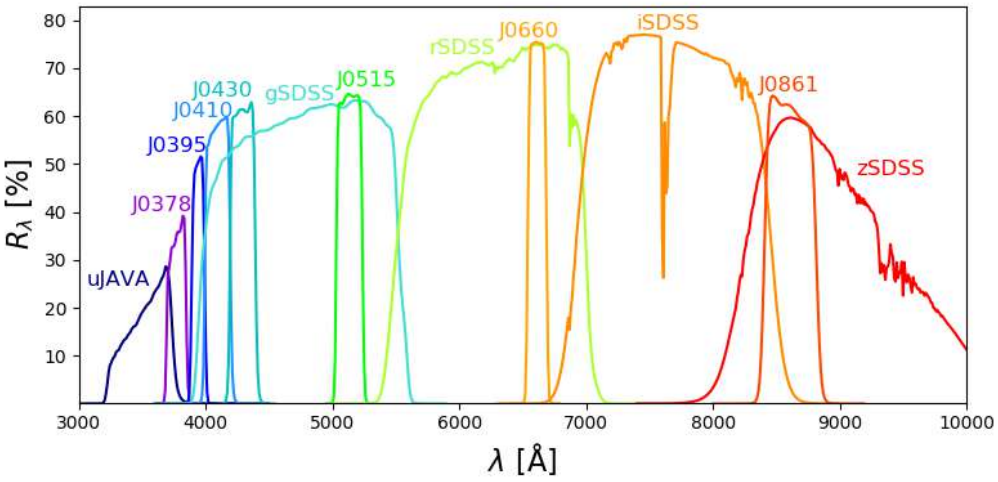

Figure 2.1: The S-PLUS 12-filter system. The y-axis shows the total efficiency of the S-PLUS filters obtained through the multiplication of the average filter transmission curves, the atmospheric transmission, the CCD efficiency, and the primary mirror reflectivity curves.

S-PLUS uses the Javalambre 12-band filter system[1], illustrated in Figure 2.1, composed of 5 broad filters (uJAVA, gSDSS, rSDSS, iSDSS and zSDSS – *ugriz* for simplicity) and 7 narrow-band ones (*J*0378, *J*0395, *J*0410, *J*0430, *J*0515, *J*0660 and *J*0861) strategically positioned in regions of the electromagnetic spectrum that have important stellar features like [OII], Hα H$_\delta$, Mgb and Ca triplets.

[1] https://www.splus.iag.usp.br/instrumentation/

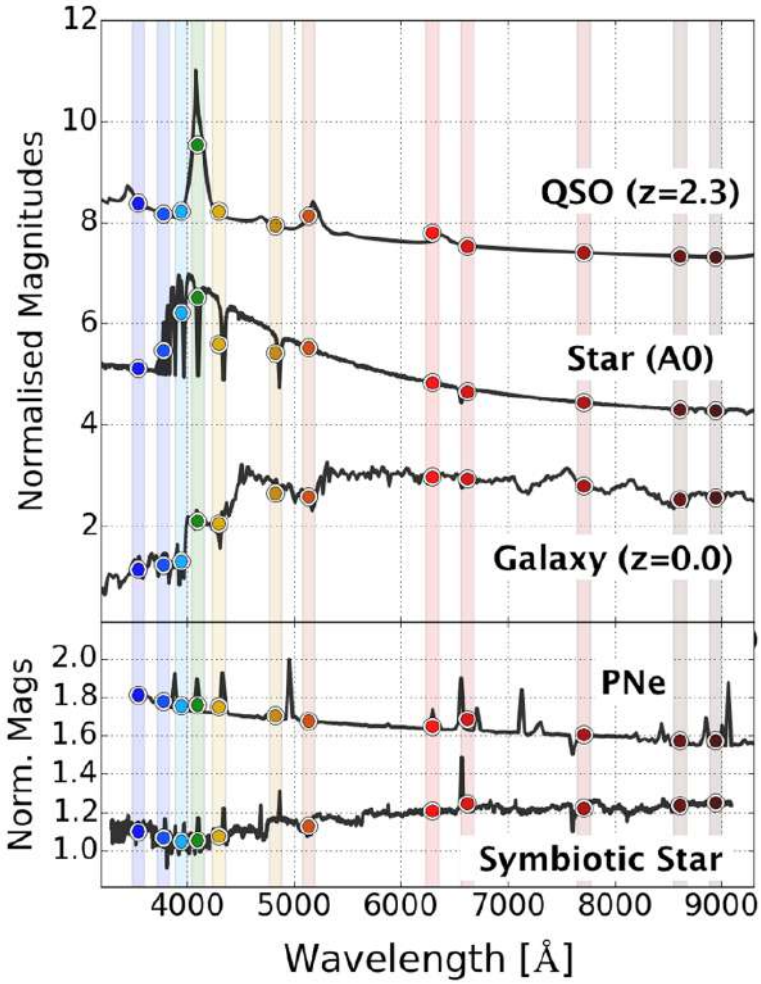

Figure 2.2: Example of different spectra (solid black lines) and their convolution with the S-PLUS 12-filter photometric system (coloured dots). The vertical bands correspond to the effective wavelengths of the S-PLUS filters. Figure 7 of Mendes de Oliveira et al. (2019).

The S-PLUS filter system was built specifically for stellar classification, yet given its spectral richness, it can also be used to analyse the physical properties of galaxies and planetary nebulae (PNe). Figure 2.2 shows an examples of different spectra and their convolution with the S-PLUS 12-filter photometric system. More information about the S-PLUS filters is presented in Table 2.1, where columns 2 and 3 indicate the central wavelengths and the full width at half-maximum (FWHM) of the filters + atmosphere + CCD + transmission curves ($\Delta\lambda$), respectively. Five kinds of sub-surveys were proposed on the S-PLUS: The Main Survey, The Ultra-Short Survey, The Galactic Survey, The Marble Field Survey, and The Variability Fields Survey, as explained below. The Hydra observations were taken as part of the main survey. Columns 4, 5 of Table 2.1 list the filters' total exposure time (of the main survey) and depth, respectively. A relevant comment on each filter is found in Column 6. Figure 2.3 shows in red the total area that will be covered by S-PLUS, as well as the main different optical and near-infrared surveys observed in the southern hemisphere, for comparison.

Table 2.1: S-PLUS filter system and the total exposure times for the Main Survey.

(1)	(2)	(3)	(4)	(5)	(6)
Filter name	λ_{eff} [Å]	$\Delta\lambda$ [Å]	Exp. Time [s]	Depth	Comment
uJAVA	3536	352	681	21.07	Javalambre *u*
J0378	3770	151	660	20.64	[O II]
J0395	3940	103	354	20.11	Ca H+K
J0410	4094	201	177	20.30	Hδ
J0430	4292	201	171	20.38	G-band
gSDSS	4751	1545	99	21.79	SDSS-like *g*
J0515	5133	207	183	20.61	Mgb Triplet
rSDSS	6258	1465	120	21.63	SDSS-like *r*
J0660	6614	147	870	21.36	Hα
iSDSS	7690	1506	138	21.22	SDSS-like *i*
J0861	8611	408	240	20.32	Ca Triplet
zSDSS	8831	1182	168	20.64	SDSS-like *z*

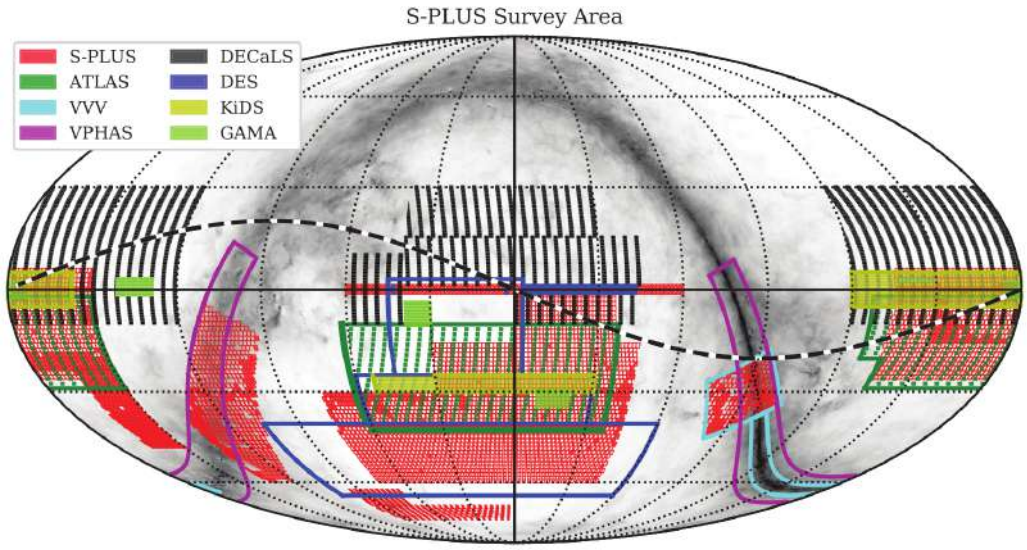

Figure 2.3: Diagram in equatorial coordinates showing some of the main optical and near-infrared surveys in the Southern hemisphere. The area covered by S-PLUS is shown in red. Figure 1 of Mendes de Oliveira et al. (2019).

S-PLUS aims to contribute to the understanding of various scientific questions, therefore it is divided into five sub-surveys according to their specific scientific goals:

The Main Survey (MS) – Mainly motivated by the requirements of extragalactic science, it aims to

match the photometric depth of SDSS, however S-PLUS is, on average, shallower than SDSS. In the Main Survey all images were taken under photometric conditions and seeing from 0.8 to 2.0 arcsec. Each field is observed 3 times with dither offsets of 10 arcsec along the RA direction ($\sim$18 pixels). The total exposure of each filter is shown in the column Exp. Time of Table 2.1.

The Ultra-Short Survey (USS) – This survey has a saturation limit that is brighter than the MS, favouring the study of bright objects. The exposure time of this survey is 1/12th of the MS. A good example of the application of this survey is the study of bright low-metallicity star candidates as done by Placco et al. (2021), who found a new ultra metal-poor star using the narrowband photometry from S-PLUS, and confirmed their finding with Gemini data.

The Galactic Survey (GS) – This survey is observing the Milk Way plane, covering an area of 1420 deg^2. The observations are performed in different epochs, allowing detection of variable sources, including pulsating RR Lyrae and Cepheids. The two GS main studies are: variable stars and stellar open clusters. The first epoch of the GS has the MS exposure times and it is observed in the 12 S-PLUS bands, and is followed by two sets of observations with exposure times of 1/12th of the MS using only the *r*, *i*, and *J*0660 bands.

The Marble Field Survey (MFS) will revisit fields under dark or grey nights, photometric conditions, and seeing > 2 arcsec, including the fields from the Hydra cluster, the M83 galaxy, the Small Magellanic Cloud (SMC) and the Dorado Group. The fact of observing the same field repeatedly will increase the depth of the MS, obtaining data appropriate for the study of galaxy groups and clusters, and their surroundings. However, in this thesis, we do not use data from the MFS because they have not been observed.

The Variability Fields Survey (VFS) will cover the same fields as the MS in non-photometric nights. The targets could be: cataclysmic variables, eclipsing binaries, variable low-mass stars, asteroids, SNe and AGNs, that will be observed repeatedly.

Due to the large coverage on sky of S-PLUS, some regions overlap with other surveys (See Figure 2.3 for some examples of overlap), such as SDSS, Pan-STARRS (Schlafly et al., 2012), DES (Dark Energy Survey Collaboration et al., 2016), and KiDS (de Jong et al., 2015). These surveys are used to calibrate the S-PLUS images. To do so, approximately 1000 stars that have known magnitudes from other surveys are selected in each field, and this information is used to calibrate and to find the zero-point of the 12 filters of each image of the survey. S-PLUS uses templates fitting algorithm from Next Generation Spectral Library (Heap & Lindler, 2007) and the Pickles library (Pickles, 1998) to find the best model that fits the literature photometry. Then the zero-points are determined by convolving the S-PLUS's filters with the best model.

S-PLUS provides photometric redshifts for galaxies brighter than 20 mag (in *r*-band) and $z < 0.5$ (see Molino et al., 2020). The observational strategy was defined to increase depth and reduce noise (the *Petrosian* magnitude limit is $J0395 = 20.11$ – the shallower band – to as deep as $g = 21.79$ with $S/N \geq 3$), while dithering is used to overcome problems with bad pixels. A detailed description of the survey including filter system, calibration method (Almeida-Fernandes et al., 2021), first results and full assessment of its capabilities can be found in Mendes de Oliveira et al. (2019).

In particular, for this thesis work, the depth of the MS is good enough to extract the properties of

the Hydra's galaxies (magnitudes and structural features). This work represents the first analysis of Hydra's galaxies using S-PLUS data.

2.2 S-PLUS observations of Hydra cluster

The region of the Hydra cluster was observed as part of the MS, that is mainly motivated by the requirements of extragalactic science, then all Hydra's images were taken under photometric conditions. In this work we use four S-PLUS fields, covering an area of 1.4 Mpc radius, centred on the Hydra cluster, whose central region is shown in Figure 2.4. Table 2.2 lists the central coordinates of each field.

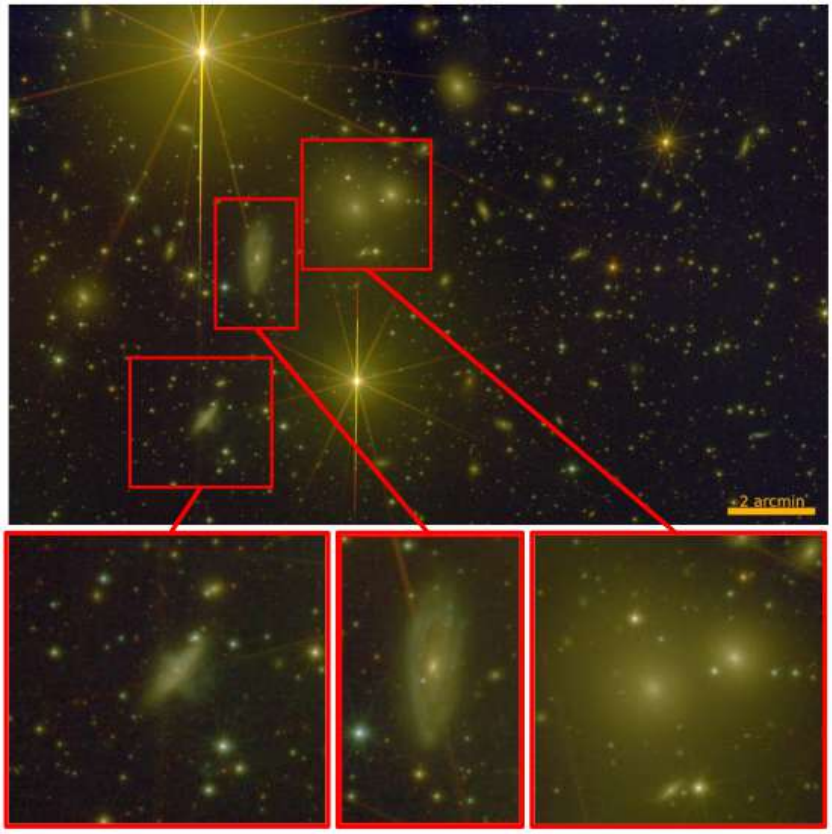

Figure 2.4: Top panel: Hydra central region. Bottom panels: Zoom-ins to some galaxies. Colour composition, using the images of the 12 S-PLUS bands with blue corresponding to $u + J0378 + J0395 + J0410 + J0430$, green to $g + J0515 + r + J0660$ and red to $J0861 + i + z$, made using the software Trilogy (Coe et al., 2012).

2.3 Sample of the Hydra's galaxies analysed in this thesis

We describe here how we determine the membership of the Hydra galaxies, based mainly on kinematics and positions, and then the final sample of galaxies analysed in this thesis, which is selected to be a magnitude-complete sample (16 r-band).

Table 2.2: Central position J2000 of the four S-PLUS fields used in this work.

FIELD	1	2	3	4
RA° (J2000)	157.90	159.47	159.30	157.70
DEC° (J2000)	-26.69	-26.69	-28.08	-28.08

2.3.1 Kinematic selection of Hydra cluster galaxies: Membership determination

We select all galaxies that are gravitationally bound to the cluster and inside $1\,R_{200}$, the radius at which the mean density is two hundred times the critical density of the Universe. To do so, we first select all galaxies with peculiar velocities lower than the cluster escape velocity, which are calculated in the line-of-sight relative to the cluster recessional velocity, as defined by Equation 2.1 (see Harrison, 1974, Jaffé et al., 2015):

$$v_{pec} = c\frac{z - z_{cl}}{1 + z_{cl}} \tag{2.1}$$

where $z_{cl} = 0.012$ (Babyk & Vavilova, 2013) is the cluster redshift, z is the redshift of each galaxy obtained from the NASA/IPAC Extragalactic Database (NED[2]), and c is the speed of light. The cluster escape velocity (v_{esc}), in km/s, is calculated using the Equation 2.2 (Equation 1 in Diaferio, 1999):

$$v_{esc} \simeq 927 \left(\frac{M_{200}}{10^{14} h^{-1} M_{\odot}}\right)^{1/2} \left(\frac{R_{200}}{h^{-1}\mathrm{Mpc}}\right)^{-1/2} \tag{2.2}$$

The determination of the cluster escape velocity depends on the M_{200} (mass within the R_{200}), and R_{200}, which in turn are determined by the velocity dispersion (σ), and h= H_0/100 km s^{-1} Mpc^{-1}. To obtain σ we use only galaxies with radial velocities ranging from 1800 to 6000 km/s, suggested by Ventimiglia et al. (2011). We found a biweight velocity dispersion of 690 ± 28 km/s as defined by the Equation 2.3:

$$\sigma_{BI}^2 = N\frac{\sum_{|u_i|<1}(1-u_i^2)^4(v_{pec,i} - \overline{v})^2}{D(D-1)} \tag{2.3}$$

where $v_{pec,i}$ is the peculiar velocity and $\overline{v}$ is its average, as described in Beers et al. (1990a) and Ruel et al. (2014), and N is the number of members. D is given by Equation 2.4.

$$D = \sum_{|u_i|<1}(1-u_i^2)(1-5u_i^2) \tag{2.4}$$

[2]https://ned.ipac.caltech.edu/

where u_i is defined as shown by Equation 2.5.

$$u_i = \frac{v_i - \overline{v}}{9\mathrm{MAD}(\mathrm{v_i})} \tag{2.5}$$

and $\mathrm{MAD}(\mathrm{v_i})$ is the median absolute deviation of the velocities. The biweight velocity dispersion uncertainty is calculated as in Equation 2.6.

$$\Delta\sigma_{BI} = \frac{C_{BI}\sigma_{BI}}{\sqrt{N-1}} \tag{2.6}$$

where $C_{BI} = 0.92$. After measuring σ (690 ± 28 km/s in our case), we can determine M_{200} and R_{200} following Leonard & King (2010). They use a singular isothermal sphere model profile, assume spherical symmetry, and that the 3D velocity dispersion can be described from the line-of-sight one dimensional velocity dispersion (Gonzalez et al., 2018). The relationships found by Leonard & King (2010) between σ, M_{200} and R_{200} are as follows:

$$M_{200} = \frac{2\sigma^3}{\sqrt{50}GH} \tag{2.7}$$

$$R_{200} = \frac{\sigma}{\sqrt{50}H} \tag{2.8}$$

where G and H are the gravitational and Hubble constants, respectively. We find a $M_{200} = 3.1 \pm 0.4 \times 10^{14} M_\odot$ and $R_{200} = 1.4 \pm 0.1$ Mpc. The errors were estimated using the the *uncertainties* package from *python*. We also calculate M_{200} using the relation between velocity dispersion and M_{200}, as obtained by Munari et al. (2013) for simulated galaxy clusters, and described by Equation 2.9.

$$\frac{\sigma_{D1}}{\mathrm{km\ s^{-1}}} = A_{1D}\left[\frac{h(z)M_{200}}{10^{15}M_\odot}\right]^{\alpha} \tag{2.9}$$

The values of A_{1D} and α for the Equation 2.9 are found in Munari et al. (2013). In Munari et al. (2013), the velocity dispersion in the simulation is determined using Dark Matter particles (DM), subhaloes (SUB) and galaxies (GAL). The three cases consider the contribution of AGN feedback. Using the Equation 2.9 we obtained the following M_{200} masses, in units of $10^{14} M_\odot$, for DM, SUB and GAL, respectively, 3.5 ± 0.4, 3.1 ± 0.3 and 3.3 ± 0.3, which are in agreement with the M_{200} estimated using Equation 2.7, as well as other reported values (e.g., $M_{200} = 3.8 \times 10^{14} M_\odot$ from Comerford & Natarajan, 2007).

Using the calculated $M_{200} = 3.1 \pm 0.4 \times 10^{14} M_\odot$ and $R_{200} = 1.4 \pm 0.1$ Mpc, we obtain $v_{esc} = 1379$ km/s from Equation 2.2, which gives us a sample of 193 galaxies satisfying the criteria to be members of the Hydra Cluster within $1\,R_{200}$. To check our consistency, we use another method to select Hydra members by applying a 3 sigma-clipping to the recessional velocity distribution of the galaxies. For this, we reject galaxies with recessional velocities larger than 3σ which results in a sample of 223 objects located within $1\,R_{200}$. Although both methods provide numbers of cluster members within the

same order of magnitude, ensuring that our choice will not affect the results of this work, we will use the sample selected by the first method to ease further comparisons with other studies.

2.3.2 Final sample of Hydra's cluster galaxies

In order to produce a complete sample of galaxies in Hydra, we performed a cross match between different spectroscopic surveys in the Hydra area from Richter (1987), Stein (1996) and Jones et al. (2004). All these spectroscopic studies are complete for galaxies brighter than ∼16 mag in the *r*-band ($M_r \leq$ -17.5). Therefore, in this thesis we only include the selected galaxies in sect. 2.3.1 that are brighter than 16 mag in the *r*-band, to ensure that a complete sample of galaxies is analysed. Given this, all galaxies analysed here have large S/N, between 24 and 145 (in the *r*-band) with a mean value of 55.

With the aim of producing a clean sample of galaxies with good light profile fits, we remove objects located close to the edge of the images or close to foreground stars. These objects were found in the first run of the morphological analysis developed by MEGAMORPH-GALAPAGOS2 (see Section 3). After removing these objects we obtain a final sample of 81 galaxies brighter than 16 (*r*-band), within $1\,R_{200}$, and with peculiar velocities lower than $v_{esc} = 1379$ km/s. This is the sample of galaxies analysed in this thesis. Figures 2.5 and 2.6 show the distribution of recessional velocities and a CMD respectively, for the selected 81 galaxy members. We note, in Figure 2.6, that most galaxies are located in the red sequence.

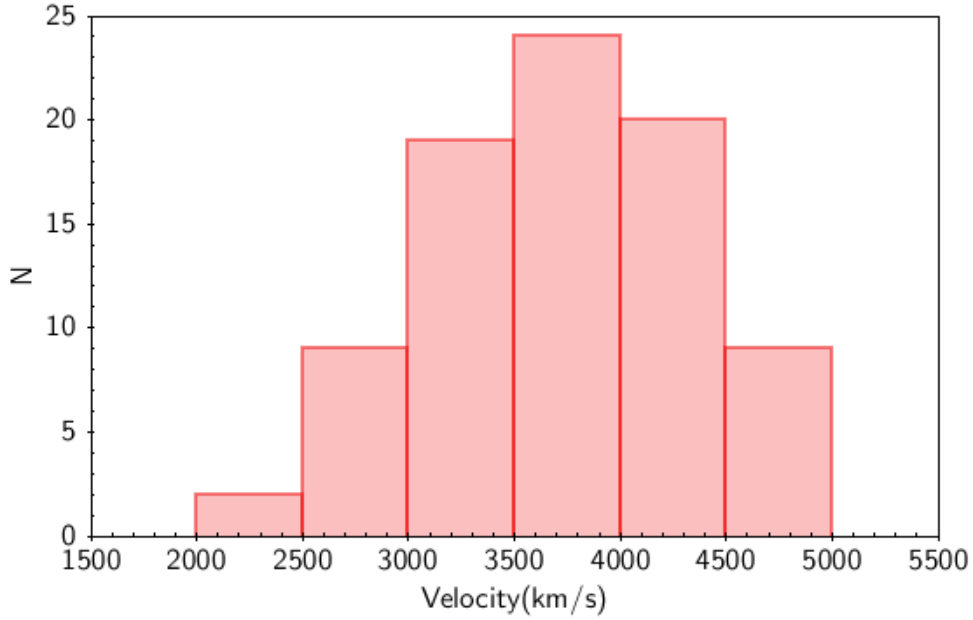

Figure 2.5: Histogram of the velocity distribution for the 81 Hydra Cluster galaxies of our sample. The y-axis shows the number of galaxies at each velocity bin. This represents the final sample of galaxies analysed in this thesis.

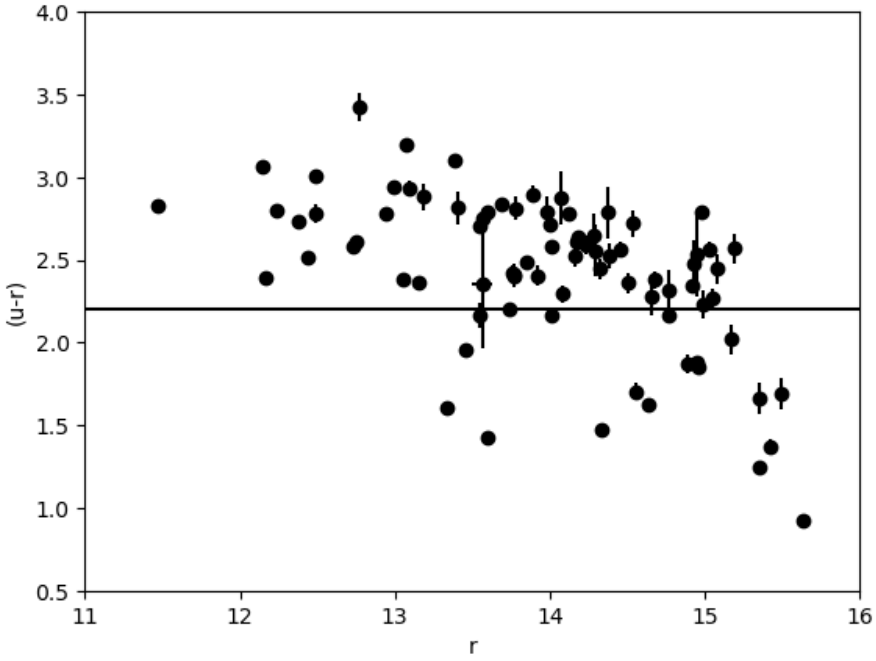

Figure 2.6: Colour magnitude diagram for the galaxies in the Hydra Cluster. The x-axis shows the apparent magnitude in the r-band, and the y-axis shows the colour $(u-r)$. The magnitudes are from GALFITM. The horizontal line is the $(u-r)$ = 2.22, the colour that separates the bimodal CMD colour distribution (Strateva et al., 2001).

3 Methodology

One of the objectives of this thesis is to observe how the galaxies' structural and physical parameters change with environment (density and clustercentric distance) as well as with respect to the S-PLUS filters. In this Chapter we detail how we estimate the physical and structural parameters of the Hydra cluster galaxies.

3.1 Determination of galaxy's structural parameters

The morphological classification of galaxies can be done by visual inspection (e.g., Lintott et al., 2008, Kartaltepe et al., 2015, Simmons et al., 2017). It is, however, extremely costly on human resources to classify over millions of galaxies which are available within modern surveys. For this volume of data we must rely on the computational power we have available and use different approaches to obtain the structural parameters of galaxies, such as Sérsic index (n), effective radius (R_e), bulge-to-total flux (B/T), Gini coefficient and the second-order moment of the brightest 20 percent of the galaxy (Lotz et al., 2004). All these parameters can be used to classify galaxies morphologically, specially considering that morphological analyses can be done from the infrared to the ultraviolet regions of spectra (Gil de Paz et al., 2007, Lotz et al., 2008, Wright et al., 2010, Dobrycheva et al., 2017). Indeed, the Sérsic profile describes how the intensity of a galaxy varies with radius, providing information regarding the morphology of the galaxy (Sérsic, 1963). The use of structural parameters and colours to classify galaxies is the approach we adopt in this thesis, whose motivation is two folded: on one side, automatic classification allows us to perform a morphological analysis from the near infrared to the blue regions of spectra in a consistent way. On the other hand, it will allow us to readily compare our results with future S-PLUS and J-PLUS data, which will deliver multiband information for millions of galaxies (Mendes de Oliveira et al., 2019), as well as with other works that have also performed automatic classification.

In this thesis, we first analyse the galaxies as a whole, to study their global properties (Chapter 4). Then we study their components, bulge and disc separately (Chapter 5). To estimate the Sérsic index (n), effective radius (R_e) and magnitudes (m) in all S-PLUS bands we used the code MEGAMORPH-GALAPAGOS2 (Bamford et al., 2011, Vika et al., 2013, Häußler et al., 2013), which includes SourceExtractor (Bertin & Arnouts, 1996) to identify and to create an input catalogue for the galaxies. The input catalogue contains the preliminary galaxies' position, magnitudes, ellipticity, among others information to run MEGAMORPH-GALAPAGOS2. Appendix A shows the MEGAMORPH-GALAPAGOS2 and SourceExtractor configuration and input files used in this thesis. MEGAMORPH-GALAPAGOS2 performs a multiwavelength two-dimensional fitting using the algorithm GALFITM (Peng et al., 2002, 2010a, Vika et al., 2013). GALFITM extracts structural components from galaxy images by modelling the surface-brightness with different profiles: Nuker law (Lauer et al., 1995), the Sérsic profile, exponential disc, Gaussian or Moffat functions (Moffat, 1969). GALFITM can also be used to model galaxies with two or more components. The main advantage of a simultaneous multiwavelength fitting is an increase in the accuracy of the estimated parameters (Vika et al., 2015). In addition, MEGAMORPH-GALAPAGOS2 allows us to fit all galaxies in a given field simultaneously, which is of great convenience. We note that MEGAMORPH-GALAPAGOS2 was used to perform a multiband fitting in several previous studies (Vika et al., 2013, 2014, 2015, Häußler et al., 2013, Vulcani et al., 2014, Kennedy et al., 2015, Dimauro et al., 2018). In addition, it was tested with simulated galaxies (Häußler et al., 2013). Thus it is a well-tested code. The galaxies analysed here have large S/N, between 24 and 145 (in the r-band) with a mean value of 55, and good imaging

quality, since all images were taken under photometric conditions. Thus we trust that the output parameters provided by MEGAMORPH-GALAPAGOS2 are reliable. Nevertheless, as a sanity check, we tested how well GALFITM recovers the galaxy parameters for our particular data set of S-PLUS.

We generated a set of five simulated galaxies to be modeled by GALFITM. The simulated galaxies were generated in each of all S-PLUS-filters, using the same range of observational parameters as in the observations (S/N, filters and background level). We use a star-forming (SF) spectral energy distribution (SED) and a quiescent (Q) SED to model a realistic wavelength dependence of the flux. On this exercise, we fix the Sérsic index over all wavelength, letting free the total flux. GALFITM allows us to recover the Sérsic index and effective radius with an uncertainty $\sim$4 percent with respect to the value used in the construction of the simulated galaxy. In addition, we perform a linear regression, comparing the magnitudes of the simulated galaxies with respect to the magnitudes found by GALFITM. We find a coefficient of determination of $\sim$1. The coefficient of determination is defined as R^2 = 1 - (SS_{res}/SS_{tot}), where SS_{res} is the sum of residual errors and SS_{tot} is the total errors. Its value ranges from 0 to 1, where 1 corresponds to the maximum correlation. These results confirm that the parameters recovered by the GALFITM models are reliable. Table 3.1 lists the magnitudes in all 12 S-PLUS filters, n_r, $R_{e,r}$ and the SED used in the five simulated galaxies (input simulation) and those recovered by GALFITM (GALFITM output). Figures 3.1, 3.2, 3.3, 3.4 and 3.5, show the 5 modeled galaxies. On these figures, top panels show the simulated galaxies, middle panels show the GALFITM models and bottom panels show the residuals, derived from the subtraction between the top and middle panels.

Table 3.1: Magnitudes for 5 simulated galaxies (Input Model) and its magnitudes recovered by GALFITM (GALFITM output).

Galaxy	*u*	J0378	J0395	J0410	J0430	*g*	J0515	*r*	J0660	*i*	J0861	z	n_r	$R_{e,r}$ (arcsec)	SED
1 Input simulation	13.75	13.53	13.34	13.08	12.59	12.17	11.90	11.52	11.45	11.20	11.04	11.00	2.00	10.00	Q
1 GALFITM output	13.74	13.52	13.33	13.07	12.58	12.16	11.89	11.50	11.44	11.19	11.03	11.00	1.98	10.02	
2 Input simulation	13.75	13.53	13.34	13.08	12.59	12.17	11.90	11.52	11.45	11.20	11.04	11.00	4.00	10.00	Q
2 GALFITM output	13.69	13.47	13.28	13.02	13.53	12.11	11.84	11.46	11.39	11.14	10.98	10.94	3.87	9.96	
3 Input simulation	14.41	14.30	14.11	13.57	13.28	13.20	13.14	13.08	13.08	13.04	13.01	13.00	4.00	20.00	SF
3 GALFITM output	14.34	14.24	14.05	13.50	13.21	13.13	13.08	13.02	13.02	12.98	12.94	12.93	3.85	19.65	
4 Input simulation	14.41	14.30	14.11	13.57	13.28	13.20	13.14	13.08	13.08	13.04	13.01	13.00	5.00	10.00	SF
4 GALFITM output	14.33	14.22	14.03	13.48	13.19	13.11	13.05	13.00	13.00	12.96	12.92	12.92	4.82	9.68	
5 Input simulation	14.41	14.30	14.11	13.57	13.28	13.20	13.14	13.08	13.08	13.04	13.01	13.00	1.00	20.00	SF
5 GALFITM output	14.42	14.31	14.11	13.56	13.27	13.19	13.13	13.08	13.07	13.04	13.00	12.99	0.99	20.01	

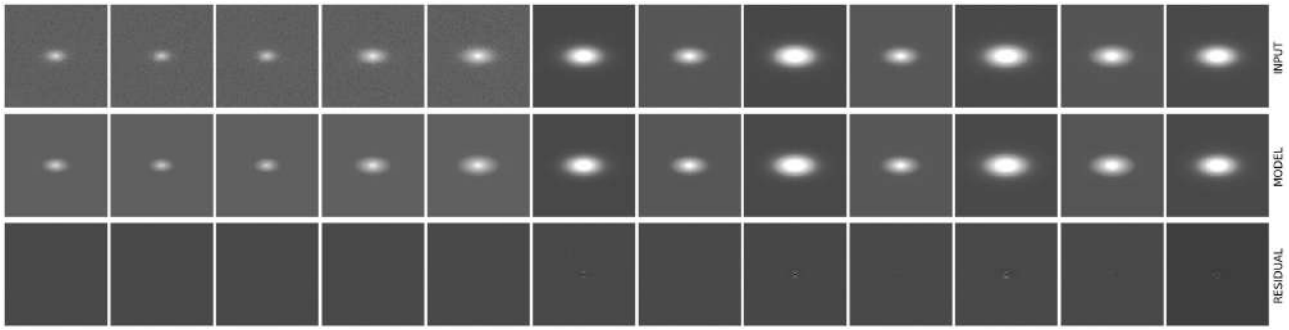

Figure 3.1: Simulated galaxy 1 (top panels), the GALFITM models (middle panels), and the residual image (observed minus modeled – bottom panels).

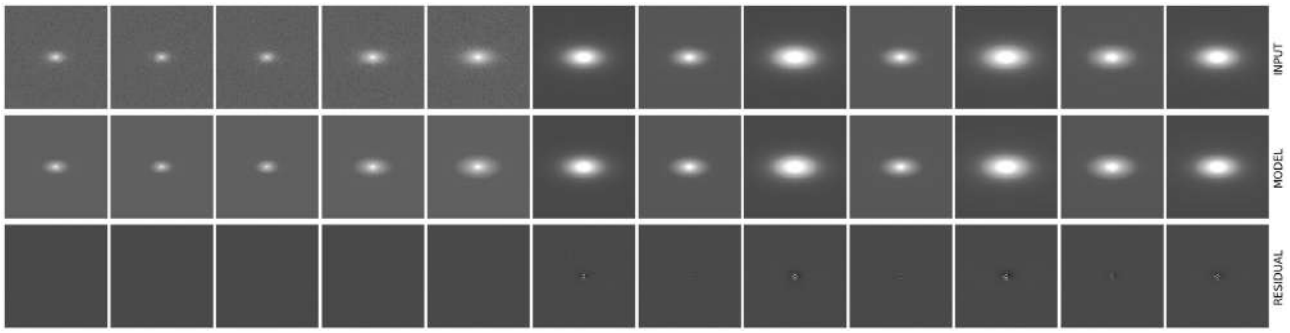

Figure 3.2: Simulated galaxy 2 (top panels), the GALFITM models (middle panels), and the residual image (observed minus modeled – bottom panels)

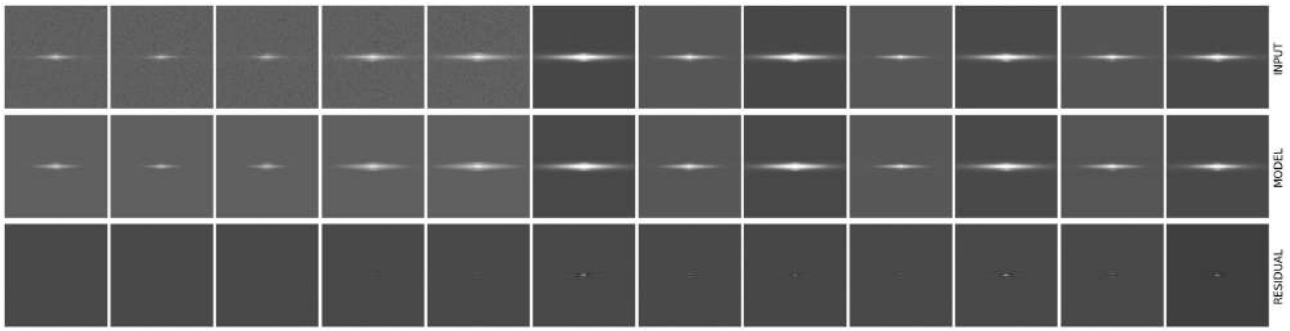

Figure 3.3: Simulated galaxy 3 (top panels), the GALFITM models (middle panels), and the residual image (observed minus modeled – bottom panels).

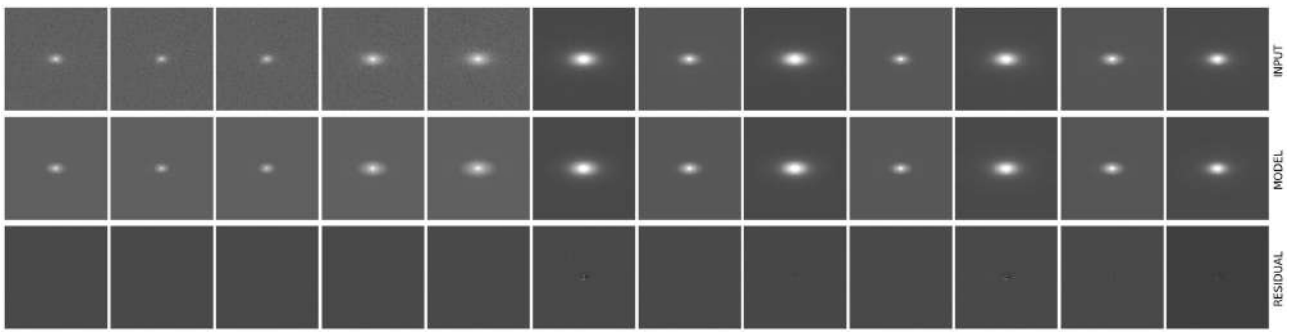

Figure 3.4: Simulated galaxy 4 (top panels), the GALFITM models (middle panels), and the residual image (observed minus modeled – bottom panels).

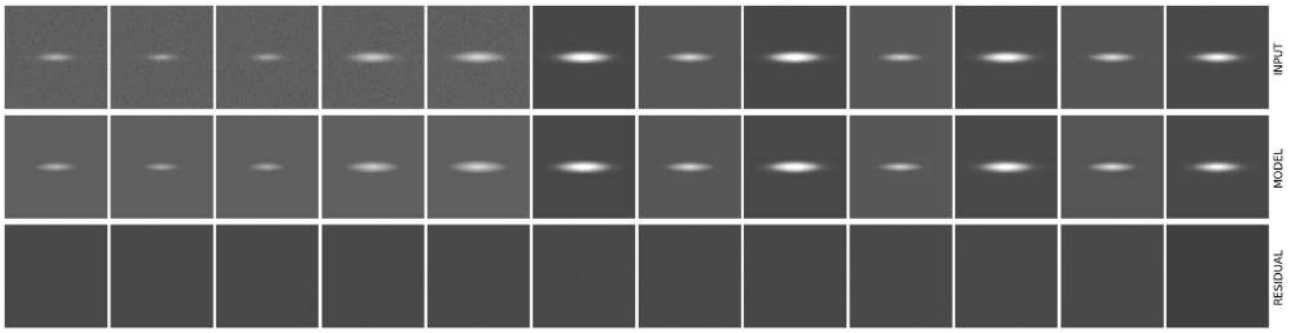

Figure 3.5: Simulated galaxy 5 (top panels), the GALFITM models (middle panels), and the residual image (observed minus modeled – bottom panels).

In this thesis, the centre of each galaxy was determined by SourceExtractor (Bertin & Arnouts, 1996) using a deep detection image, generated for each field as a weighted combination of the *g*, *r*, *i* and *z* broad-band images. For our first analysis in this thesis (Chapter 4) we fit, for each galaxy, a single Sérsic profile simultaneously for images in all filters, by fixing for each filter the central position measured on the detection image. Each parameter to be measured is modeled as a function of wavelength and the degrees of freedom afforded to model each of these parameters are determined by a set of Chebyshev polynomials. This analysis provided us with the following structural parameters: Sérsic index and effective radius (modeled as quadratic functions of wavelength) as well as b/a (the ratio of the major (a) to the minor (b) axes of the galaxy) and position angle (modeled as linear functions of wavelength) (Häußler et al., 2013).

For our second analysis (Chapter 5), we fit each galaxy's profile with the sum of a Sérsic profile (n free) and an exponential profile (n=1). The galaxies were modeled using a linear function of wavelength for the bulge and the disc, as well as b/a and position angle that were obtained by fitting a constant offset from the input values.

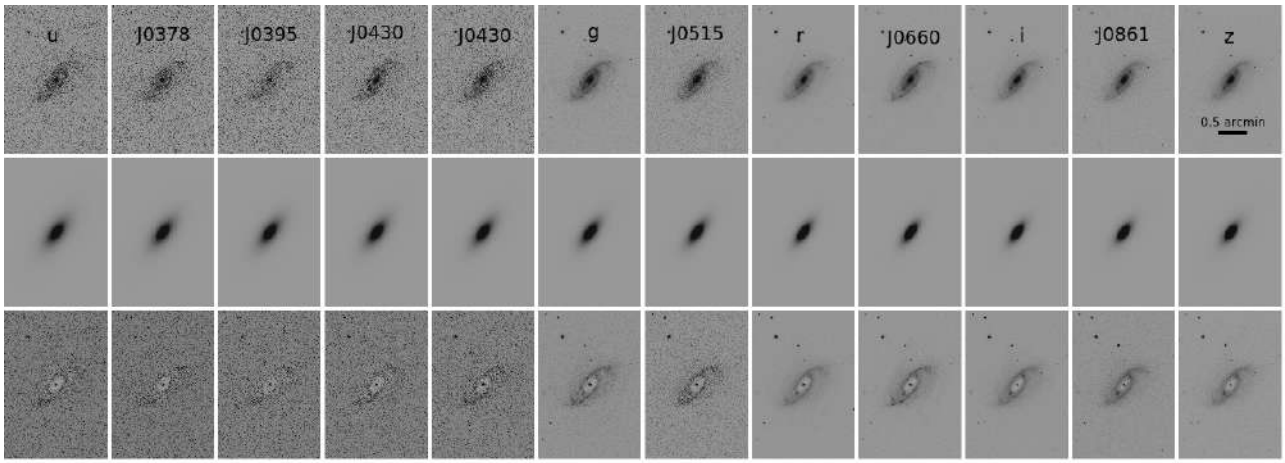

Figure 3.6: Galaxy ESO 437-G 004 as observed by S-PLUS (top panels), the models calculated using GALFITM (middle panels), and the residual image (observed minus modeled – bottom panels).

In order to determine the best fit, GALFITM uses a Levenberg-Marquardt technique, which finds the optimum model by minimising the χ^2. In Figure 3.6 we present the GALFITM output for the galaxy

ESO 437- G 004, as an example, where observed images, models and residuals (the latter derived as the observed image minus the modeled image) are shown in top, middle and bottom panels, respectively, for all filters. We can easily see the spiral arms and substructures in the residual images of this example.

Magnitudes for the 81 analysed galaxies are available in Tables B.1. A short version if this table is available in Table 3.2. The magnitudes of the bulge and the disc for the 52 galaxies that have reliable bulge-disc decomposition (see Chapter 5) are in the Tables B.2 and B.3, respectively. A short version of the two tables are available in Tables 3.4 and 3.3, respectively. The magnitudes shown in all tables are not corrected by Galactic extinction. In this way, it is possible for each investigator to use the correction for extinction they judge necessary. Indeed, for the analysis performed in this thesis, all magnitudes have been corrected for Galactic extinction, by using a Cardelli et al. (1989) law and the maps from Schlegel et al. (1998). The Sérsic indexes for the whole galaxy and the bulge are available in Tables B.4 and B.5, and a short version of these tables are available in Table 3.5 and 3.6, respectively. Finally, the effective radius of the whole galaxy, bulge, and disc are available in Tables B.8, B.9, and B.10, respectively. A short version of the three tables are in Tables 3.7, 3.8, and 3.9, respectively.

Table 3.2: Galaxy' magnitudes estimated in this thesis using MEGAMORPH-GALAPAGOS2 project. Column 1 is the ID of each galaxy, and the columns 2 to 13 are the magnitudes in the 12 S-PLUS filters, without the correction for Galactic extinction. The full version of this table is in the Appendix B of this thesis.

ID	u	J0378	J0395	J0410	J0430	g	J0515	r	J0660	i	J0861	z
1	16.31±0.03	16.02±0.03	15.66±0.03	15.31±0.02	14.92±0.01	14.37±0.01	14.07±0.01	13.56±0.00	13.4 ±0.00	13.14±0.00	12.94±0.00	12.89±0.00
2	17.02±0.05	16.62±0.04	16.32±0.05	16.04±0.04	15.72±0.03	15.25±0.01	14.99±0.01	14.45±0.01	14.24±0.01	14.04±0.01	13.83±0.01	13.79±0.01
⋮	⋮	⋮	⋮	⋮	⋮	⋮	⋮	⋮	⋮	⋮	⋮	⋮
81	16.49±0.02	16.04±0.01	15.63±0.01	15.26±0.01	14.86±0.01	14.27±0.00	13.98±0.00	13.38±0.00	13.24±0.00	12.95±0.00	12.76±0.00	12.63±0.00

Table 3.3: Bulge's magnitudes estimated in this thesis using MEGAMORPH-GALAPAGOS2 project. Column 1 is the ID of each galaxy, and columns 2 to 13 are the magnitudes in the 12 S-PLUS filters, without the correction for Galactic extinction. The full version of this table is in the Appendix B of this thesis.

ID	u	J0378	J0395	J0410	J0430	g	J0515	r	J0660	i	J0861	z
1	17.52±0.16	17.11±0.15	16.7 ±0.16	16.41±0.13	16.19±0.10	15.98±0.05	15.68±0.06	15.03±0.03	14.85±0.03	14.5 ±0.04	14.2 ±0.05	14.11±0.05
2	17.77±0.11	17.35±0.1	17.1 ±0.13	16.77±0.09	16.42±0.07	16.01±0.05	15.7 ±0.05	15.18±0.03	14.96±0.02	14.78±0.02	14.53±0.03	14.51±0.03
⋮	⋮	⋮	⋮	⋮	⋮	⋮	⋮	⋮	⋮	⋮	⋮	⋮
81	17.96±0.05	17.48±0.05	17.25±0.05	16.66±0.04	16.41±0.03	15.81±0.02	15.53±0.02	14.93±0.01	14.79±0.01	14.53±0.01	14.41±0.01	14.34±0.02

Table 3.4: Disc's magnitudes estimated in this thesis using MEGAMORPH-GALAPAGOS2 project. Column 1 is the ID of each galaxy, and columns 2 to 13 are the magnitudes in the 12 S-PLUS filters, without the correction for Galactic extinction. The full version of this table is in the Appendix B of this thesis.

ID	u	J0378	J0395	J0410	J0430	g	J0515	r	J0660	i	J0861	z
1	16.67±0.06	16.43±0.06	16.05±0.06	15.66±0.05	15.21±0.03	14.56±0.01	14.25±0.01	13.74±0.0	13.57±0.0	13.31±0.0	13.1 ±0.0	13.04±0.0
2	17.77±0.15	17.37±0.15	17.13±0.19	16.63±0.13	16.53±0.11	15.91±0.05	15.71±0.06	15.13±0.03	14.94±0.03	14.72±0.02	14.56±0.03	14.47±0.03
⋮	⋮	⋮	⋮	⋮	⋮	⋮	⋮	⋮	⋮	⋮	⋮	⋮
81	17.13±0.05	16.8 ±0.06	16.7 ±0.09	16.03±0.05	15.7 ±0.04	15.15±0.02	14.85±0.02	14.31±0.01	14.2 ±0.01	13.9 ±0.01	13.72±0.01	13.61±0.01

Table 3.5: Galaxy's Sérsic indexes estimated in this thesis using MEGAMORPH-GALAPAGOS2 project. Column 1 is the ID of each galaxy, and the columns 2 to 13 are the Sérsic indexes in the 12 S-PLUS filters. The full version of this table is in the Appendix B of this thesis.

ID	u	J0378	J0395	J0410	J0430	g	J0515	r	J0660	i	J0861	z
1	0.85±0.02	0.88±0.02	0.9 ±0.01	0.91±0.01	0.93±0.01	0.97±0.01	0.99±0.00	1.05±0.00	1.07±0.00	1.11±0.00	1.15±0.00	1.17±0.00
2	1.00±0.04	1.00±0.03	1.00±0.03	1.00±0.02	1.00±0.02	1.02±0.01	1.03±0.01	1.07±0.01	1.08±0.01	1.1±0.00	1.09±0.01	1.06±0.01
⋮	⋮	⋮	⋮	⋮	⋮	⋮	⋮	⋮	⋮	⋮	⋮	⋮
81	4.76±0.08	5.02±0.06	5.15±0.05	5.26±0.04	5.39±0.03	5.67±0.02	5.83±0.02	6.17±0.01	6.24±0.01	6.45±0.01	6.69±0.01	6.88±0.02

Table 3.6: Bulge's Sérsic indexes estimated in this thesis using MEGAMORPH-GALAPAGOS2 project. Column 1 is the ID of each galaxy, and the columns 2 to 13 are the Bulge's Sérsic indexes in the 12 S-PLUS filters. The full version of this table is in the Appendix B of this thesis.

ID	u	J0378	J0395	J0410	J0430	g	J0515	r	J0660	i	J0861	z
1	0.67±0.07	0.82±0.06	0.91±0.05	0.99±0.05	1.11±0.04	1.43±0.04	1.67±0.04	2.53±0.05	2.84±0.05	3.88±0.07	4.92±0.11	5.52±0.15
2	0.6±0.02	0.64±0.02	0.67±0.02	0.68±0.02	0.71±0.01	0.76±0.01	0.79±0.01	0.86±0.0	0.87±0.0	0.89±0.0	0.87±0.0	0.84±0.01
⋮	⋮	⋮	⋮	⋮	⋮	⋮	⋮	⋮	⋮	⋮	⋮	⋮
81	2.32±0.1	2.4±0.08	2.44±0.07	2.48±0.07	2.52±0.06	2.62±0.05	2.68±0.04	2.8±0.03	2.82±0.03	2.83±0.02	2.76±0.03	2.7±0.04

Table 3.7: Galaxy's effective radius (kpc) estimated in this thesis using MEGAMORPH-GALAPAGOS2 project. Column 1 is the ID of each galaxy, and the columns 2 to 13 are the effective radius in the 12 S-PLUS filters. The full version of this table is in the Appendix B of this thesis.

ID	Re_u	Re_{J0378}	Re_{J0395}	Re_{J0410}	Re_{J0430}	Re_g	Re_{J0515}	Re_r	Re_{J0660}	Re_i	Re_{J0861}	Re_z
1	4.2±0.1	4.1±0.1	4.1±0.1	4.1±0.1	4.1±0.1	4.0±0.1	4.0±0.1	4.0±0.1	4.0±0.1	4.1±0.1	4.1±0.1	4.0±0.1
2	3.1±0.1	3.1±0.1	3.0±0.1	3.0±0.1	3.0±0.1	2.9±0.1	2.8±0.1	2.7±0.1	2.7±0.1	2.7±0.1	2.6±0.1	2.5±0.1
⋮	⋮	⋮	⋮	⋮	⋮	⋮	⋮	⋮	⋮	⋮	⋮	⋮
81	3.0±0.1	3.3±0.1	3.5±0.1	3.7±0.1	3.8±0.1	4.2±0.1	4.3±0.1	4.7±0.1	4.7±0.1	5.0±0.1	5.3±0.1	5.7±0.1

Table 3.8: Bulge's effective radius (kpc) estimated in this thesis using MEGAMORPH-GALAPAGOS2 project. Column 1 is the ID of each galaxy, and the columns 2 to 13 are the Bulge's effective radius in the 12 S-PLUS filters. The full version of this table is in the Appendix B of this thesis.

ID	Re_u	Re_{J0378}	Re_{J0395}	Re_{J0410}	Re_{J0430}	Re_g	Re_{J0515}	Re_r	Re_{J0660}	Re_i	Re_{J0861}	Re_z
1	3.3±0.2	3.2 ±0.1	3.1 ±0.1	3.1 ±0.1	3.0 ±0.1	3.0±0.1	3.0 ±0.1	3.4±0.1	3.6 ±0.1	4.5±0.2	5.7 ±0.3	6.5±0.4
2	3.1±0.1	3.0 ±0.1	3.0 ±0.1	3.0 ±0.1	3.0 ±0.1	2.9±0.1	2.9 ±0.1	2.7±0.1	2.7 ±0.1	2.6±0.1	2.5 ±0.1	2.5±0.1
⋮	⋮	⋮	⋮	⋮	⋮	⋮	⋮	⋮	⋮	⋮	⋮	⋮
81	0.5±0.1	0.5 ±0.1	0.5 ±0.1	0.5 ±0.1	0.5 ±0.1	0.5±0.1	0.5 ±0.1	0.5±0.1	0.5 ±0.1	0.5±0.1	0.5 ±0.1	0.5±0.1

Table 3.9: Disc's effective radius (kpc) estimated in this thesis using MEGAMORPH-GALAPAGOS2 project. Column 1 is the ID of each galaxy, and the columns 2 to 13 are the Disc's effective radius in the 12 S-PLUS filters. The full version of this table is in the Appendix B of this thesis.

ID	Re_u	Re_{J0378}	Re_{J0395}	Re_{J0410}	Re_{J0430}	Re_g	Re_{J0515}	Re_r	Re_{J0660}	Re_i	Re_{J0861}	Re_z
1	7.6±0.1	7.6±0.1	7.5±0.1	7.5±0.1	7.5±0.1	7.5±0.1	7.4±0.1	7.4±0.1	7.3±0.1	7.2±0.1	7.2±0.1	7.1±0.1
2	4.2±0.2	4.2±0.1	4.1±0.1	4.1±0.1	4.1±0.1	4.0±0.1	4.0±0.1	3.9±0.1	3.9±0.1	3.8±0.1	3.8±0.1	3.8±0.1
⋮	⋮	⋮	⋮	⋮	⋮	⋮	⋮	⋮	⋮	⋮	⋮	⋮
81	6.1±0.1	6.1±0.1	6.2±0.1	6.2±0.1	6.3±0.1	6.4±0.1	6.4±0.1	6.5±0.1	6.6±0.1	6.6±0.1	6.6±0.1	6.5±0.1

3.2 Estimation of galaxy physical parameters

We are interested in investigating how the galaxies' properties behave in a dense environment. Here we describe how we estimate the galaxies' stellar mass, star formation rate, and specific star formation rate for the Hydra galaxies analysed in this thesis.

3.2.1 Stellar masses

The stellar mass is one of the main properties of a galaxy and it is well correlated with its luminosity (Faber & Gallagher, 1979). Different types of galaxies increase their stellar mass at different rates, e.g. starburst galaxies form stars at higher rates than main sequence galaxies (Papovich et al., 2005). In this thesis, we estimate the masses using luminosity-colour relations and SED fittings, as explained below.

Stellar masses using colours: Bell et al. (2003), using a large sample of 22,679 galaxies observed with the Two Micron All Sky Survey (Skrutskie et al., 1997) and the SDSS, calculated stellar mass-to-light ratio $M_\star/L$ as a function of the $(g-i)$ colour assuming a Salpeter initial mass function (IMF, Salpeter, 1955). In this thesis we use the i-band luminosities, with the $(g-i)$ colour, to estimate the stellar mass of each galaxy following the definition given by Bell et al. (2003), which is shown in the Equation 3.1.

$$\log\ M_\star/L_i = -0.152 + 0.518 \times (g-i) \tag{3.1}$$

We found a median uncertainty of 0.06 dex for the estimated stellar masses for the Hydra galaxies. On the other hand, Taylor et al. (2011) using a sample of galaxies from the Galaxy And Mass Assembly (GAMA) survey have shown that the $(g-i)$ colour can be used to infer $M_\star/L_i$ with a typical uncertainty of $\lesssim 0.1$ dex following the relation shown in Equation 3.2.

$$\log M_\star/L_i = 1.15 + 0.7 \times (g-i) - 0.4 \times M_i \tag{3.2}$$

where M_i is the absolute magnitude in the i-band. The authors used the SSP models from Bruzual & Charlot (2003) and assumed a Chabrier (2003) IMF with a Calzetti et al. (2000a) extinction law, to derive the relationship in Equation 3.2. In this thesis we also use the relation presented in Taylor et al. (2011) to estimate the stellar masses.

Stellar mass using SED fitting: Another way to estimate the stellar mass of a galaxy is using a SED or spectral fitting code (Bruzual A. & Charlot, 1993, Cid Fernandes et al., 2005, da Cunha et al., 2012). These codes use models to fit the SED, allowing us to determine the ages and metallicities of the stellar populations. Then, it is possible to obtain several physical parameters of the galaxy, including its stellar mass.

Given that we have observed each Hydra galaxy with 12 filters, we can construct the SED from those 12 data points. Following this approach, we perform a SED fit for the galaxies detected inside of the S-PLUS field containing the centre of the Hydra Cluster (only one field for a consistency check). The SED fitting process was done using the code PHotometric Analysis for Redshift Estimate (LEPHARE Arnouts et al., 1999, Ilbert et al., 2006) and the stellar population libraries of Bruzual & Charlot (2003) with a Chabrier (2003) IMF. The models have 3 metallicities $0.2\,Z_\odot$, $0.4\,Z_\odot$ and $1\,Z_\odot$ with ages ranging from 0.01 to 13.5 Gyrs.

In Figure 3.7 we compare the resulting masses obtained by the SED fitting method with respect to the masses derived from luminosities and colours. Red dots are the stellar masses estimated using the $(g-i)$ colour relation from Bell et al. (2003). We have scaled the Bell mass-luminosity relation by 0.093 dex to take into account the use of Salpeter IMF rather than a Chabrier IMF, as described in Taylor et al. (2011). Blue dots are the stellar masses estimated using the $(g-i)$ colour relation from Taylor et al. (2011). The stellar masses estimated using Bell et al. (2003) are on average 0.22 dex larger than those estimated via Taylor et al. (2011). When the stellar masses derived from the SED fitting are compared with those derived from the colour relations we find, on average, a percentage error of 1.2 and 2.0 for the masses estimated using the Taylor et al. (2011) and Bell et al. (2003) relations, respectively. In both cases a linear regression of the stellar masses obtained from the two methods provides a good fit, with a coefficient of determination $R^2 = 0.97$, indicating a good linear correlation between the data. Given that the two colour relations show a good correlation with the masses estimated using a SED fitting, and considering that the masses estimated using colours are less time consuming, we therefore use the stellar masses for all the S-PLUS fields obtained from the colour relation by Taylor et al. (2011), which shows the smallest percentage error.

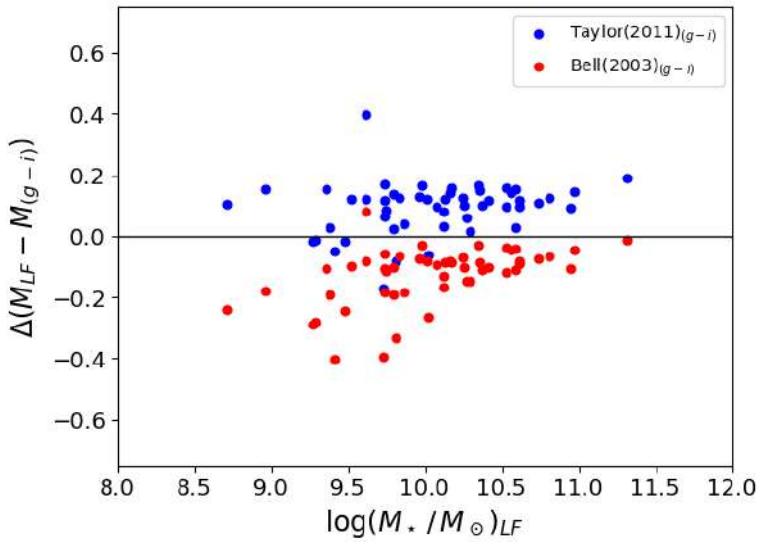

Figure 3.7: Comparison between the stellar masses estimated using colours and using the code LEPHARE for the galaxies in the central S-PLUS field of Hydra. The y-axis shows the difference between the stellar masses calculated with LEPHARE and the colour relation. In red and blue are the masses estimated using the $(g-i)$ colour from Bell et al. (2003) and Taylor et al. (2011), respectively.

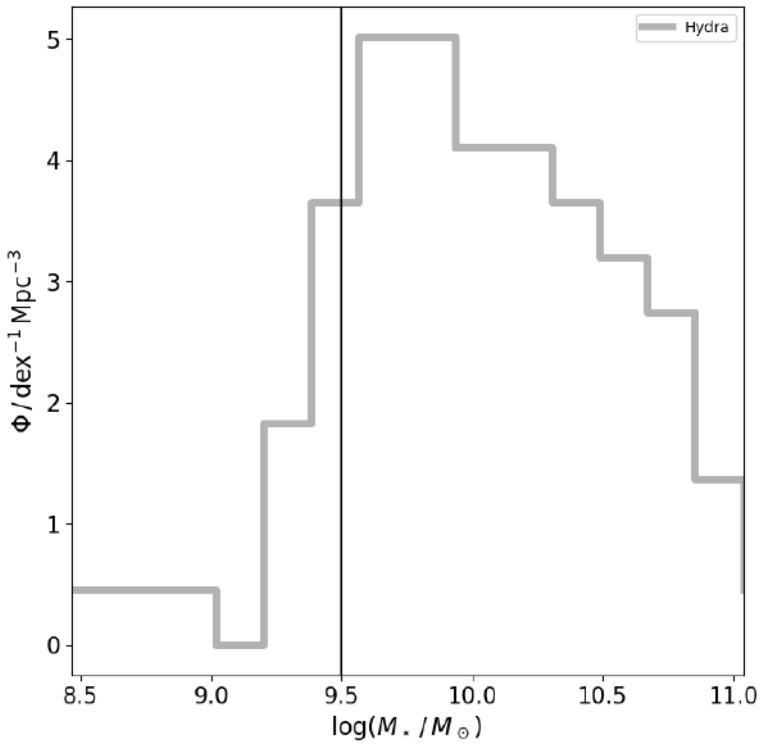

Figure 3.8: Stellar mass function of galaxies brighter than m_r=16 within a sphere with 1.4Mpc of radius centred on Hydra. The grey line corresponds to the 81 galaxies belonging to Hydra selected as indicated in subsection 2.3.1. The black vertical line shows the minimum stellar mass completeness for which our sample is complete ($3.3\times10^9 M_\odot$).

We show the stellar mass function (SMF) of the Hydra galaxies analysed in this thesis as a grey histogram in Figure 3.8. Our sample is complete for stellar masses $\geq 3.3 \times 10^9 M_{\odot}$, which was determined from the colour relation using the faintest magnitude (16 mag in the *r*-band) and the reddest colour of our sample of galaxies. The stellar masses are listed in Table B.6 of the Appendix.

3.2.2 The Star Formation Rate

To further extend our understanding of the galaxies inside the Hydra Cluster and the influence of the environment over the evolutionary path of the members, we need to know how many and what galaxies are star-forming; and for those galaxies, we need to estimate their star formation rate (*SFR*) and specific star formation rate (*sSFR*). For this task we use the *J*0660 narrow band filter, which is centred around the rest frame wavelength of Hα . We note that there are several advantages in using photometric data to determine Hα emission in galaxies. First, the use of S-PLUS data allow us to perform an homogeneous analysis on the Hα emission of galaxies in Hydra, where all the data were observed under similar conditions. In addition, imaging surveys are not biased by the orientation of the slits, as in the case of spectroscopic studies. Furthermore, the S-PLUS will cover a huge area on the sky, and in the near future the photometric redshifts will be available, increasing the number of objects belonging to Hydra for which we will have S-PLUS data. In this way, the same criteria will be used to select and analyse galaxies providing homogeneous data with S-PLUS.

We select the Hα emission line galaxy candidates in our sample based on two criteria: one regarding the equivalent width and the other one regarding a given colour excess for the objects (known as 3Σ cut, Sobral et al. (2012)). For the galaxies to be considered as line emitters, the H_{α} equivalent width (EW_{J0660}) should be greater than 12 Å, as suggested by Vilella-Rojo et al. (2015), who determined that J-PLUS cannot resolve, with a precision of 3σ, $EW_{J0660} < 12$ Å. In this thesis, we use the same criteria given that S-PLUS and J-PLUS use twin telescopes, with the same filter system. Thus we can utilize the same criteria to analyse the galaxies if the objects have the similar photometric conditions. We use the equation 3.3 to determine the galaxies's EW_{J0660}:

$$EW_{J0660} = \Delta_{J0660}(Q-1)\frac{Q-1}{1-Q\varepsilon} \tag{3.3}$$

where Δ_x is defined for any passband x at any wavelength of interest λ_s as

$$\Delta_x \equiv \frac{\int P_x(\lambda)\lambda d\lambda}{P_x(\lambda=\lambda_s)\lambda_s} \tag{3.4}$$

where P_x is the transmission of the passband x as a function of wavelength. $\varepsilon \equiv \Delta_{J0660}/\Delta_r$ and m_r - $m_{J0660} = 2.5\log Q$. The m_r and m_{J0660} are the apparent magnitudes.

The second criteria is based on colour excess. Emission line galaxies are objects with $(r-J0600)$ colour excess greater than zero, i.e. $(r-J0600) > 0$. However, to quantify the colour excess when compared to a random scatter expected for a source with zero colour, we use a 3Σ cut (Sobral et al., 2012). We use Equation 3.5 to define the 3Σ curve (Khostovan et al., 2020):

$$\Sigma = 1 - \frac{10^{-0.4(m_r - m_{J0660})}}{10^{ZP - m_{J0660}} \sqrt{\sigma^2_{J0660} + \sigma^2_r}} \tag{3.5}$$

where σ_{J0660} and σ_r are the rms errors of the apparent magnitudes in $J0660$ and r filters, respectively, and ZP is the photometric zero-point for $J0660$ filter. SourceExtractor (Bertin & Arnouts, 1996) was used in this case to obtain the galaxy photometric errors (σ_{J0660} and σ_r) for the broad-band and narrow-band fluxes measured, for each Hydra's field, with an AUTO aperture around the source. Figure 3.9 shows the application of these selection criteria to all the detected sources in one Hydra field. Only galaxies that obey the 3Σ cut and $\mathrm{EW}_{J0660} > 12$ Å were selected as line emitters. We apply the same selection on all 4 S-PLUS fields analysed in this thesis and find only 10 galaxies in Hydra that meet our selection criteria to be emission line galaxy candidates. The 10 galaxies are shown in Figure 3.10. These galaxies have H_α luminosities between 1.4×10^{40} and 1.5×10^{41} erg/s.

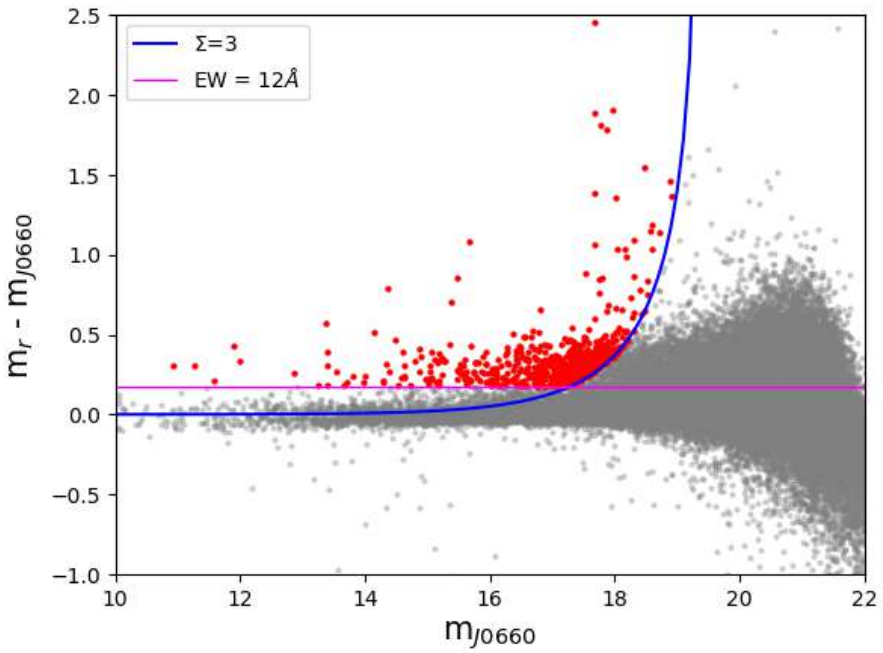

Figure 3.9: m_{J0660} excess as a function of m_{J0660} magnitude. The blue line represents the Σ cut of 3. The magenta horizontal line presents the EW_{J0660} cut of 12 Å. The grey points represent all $m_r - m_{J0660}$ detected sources. The red points are the sources that can be considered to have a narrow-band excess in the field.

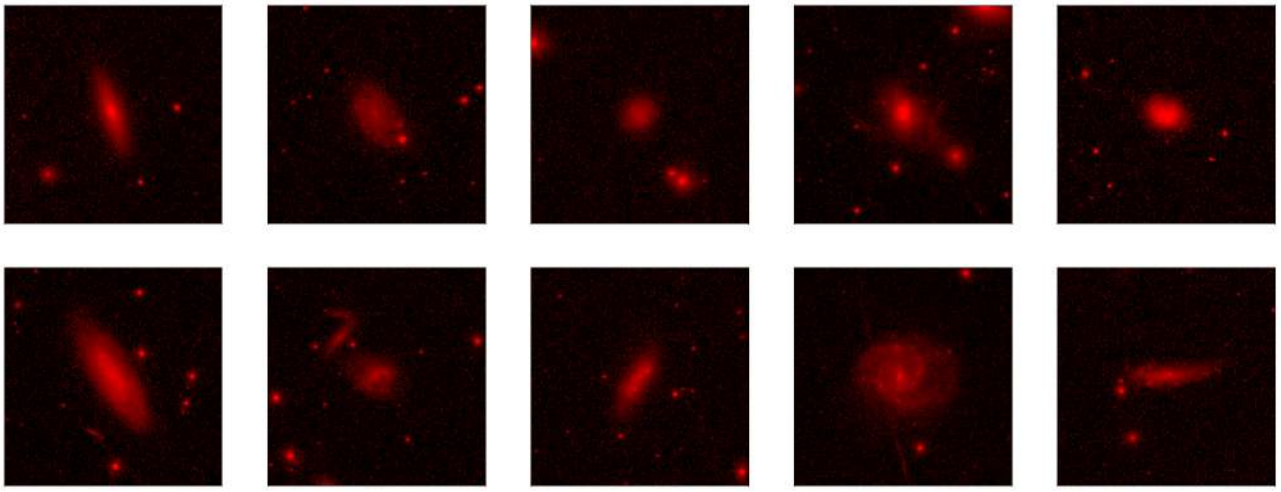

Figure 3.10: Hα images of the 10 star-forming galaxies found in this thesis. All images have a size of 1.8x1.8 arcminute.

To measure the Hα flux on the emission-line selected galaxies, we apply the Three Filter Method (TMF, Pascual et al., 2007) – which has already been successfully implemented to similar data from the J-PLUS survey (Cenarro et al., 2019, Vilella-Rojo et al., 2015) – using the *r* and *i*-bands to trace the linear continuum and *J*0660 to contrast the line. This approach allows us to obtain a "pure" Hα plus [N II] doublet emission. Even though it is impossible to separate the contribution of the [N II] lines from the Hα flux, given the width of the *J*0660 filter, we can use the empirical relations from Vilella-Rojo et al. (2015) to estimate the level of contamination one could expect in this kind of data. Following the relations from the Equation 3.6, we are able to subtract the contribution from [N II] and obtain a pure Hα emission for our galaxies.

$$\log F_{\mathrm{H}\alpha} = \begin{cases} 0.989 \log F_{\mathrm{H}\alpha+[\mathrm{N\,II}]} - 0.193, & \text{if } g-i \leq 0.5 \\ 0.954 \log F_{\mathrm{H}\alpha+[\mathrm{N\,II}]} - 0.753, & \text{if } g-i > 0.5 \end{cases} \tag{3.6}$$

The analysis described above allows us to determine that the sensitivity of the F_{H_α} is 1×10^{-13} erg s^{-1}cm^{-2} which corresponds to a surface brightness of 21 mag/arcsec^{-2}. We use the Hα flux to determine the Hα luminosity, and then the classical relation proposed by Kennicutt (1998), that relates the SFR and luminosity, was used to estimate the SFR. The SFRs obtained from this relation must be corrected for dust attenuation. A common correction arises from the assumption of an extinction A(Hα) = 1 mag, as proposed by Kennicutt (1992). However, this correction overestimates the SFR for galaxies with low Hα luminosities (Hα luminosity of $\lesssim 10^{40.5}$ ergs s^{-1}, Ly et al., 2012), which is the case for some galaxies analysed in this thesis. For this reason, we choose to use the relation between the intrinsic and observed SFR (corrected by the obscuration), which is presented in Hopkins et al. (2001) and updated by Ly et al. (2007). The relation is shown in Equation 3.7:

$$\begin{aligned} \log SFR_{obs}(H_\alpha) &= \log SFR_{int} - 2.360 \\ &\times \log \left[\frac{0.797 \log(SFR_{int}) + 3.786}{2.86} \right] \end{aligned} \tag{3.7}$$

where SFR_{int} and SFR_{obs} are the intrinsic and observed SFR, respectively.

Finally, the $sSFR = SFR/M_{\star}$ for the 10 galaxies that are Hα emitters were estimated by using the SFR and the stellar masses derived in section 3.2.1. Table B.6 in the appendix lists the *sSFRs* (column 6). A *sSFR* threshold is defined empirically to separate star-forming galaxies (SFGs) from the non-star forming ones (NSFGs, Weinmann et al., 2010). We consider a galaxy as star-forming if its $sSFR > 10^{-11}\,\mathrm{yr}^{-1}$, otherwise it will be classified as quiescent following the threshold commonly used in the literature (see for example Wetzel et al., 2012, 2013, 2014). We note, however, that some other studies use different thresholds for the *sSFR* at different redshifts to separate SFG from NSFG, as for example Laganá & Ulmer (2018) and Koyama et al. (2013). Based on these definitions, we found that all 10 galaxies that are Hα emitters are star-forming.

4 An environmental dependence of the physical and structural properties in the Hydra Cluster galaxies [3]

As discussed in Chapter 1, one of the many remarkable and still open questions in extragalactic astronomy is: how do galaxies evolve with/within the environment? Several studies have addressed this issue, generally based on pioneer works, which determined a relation between the environment in which galaxies reside and their physical properties (Oemler, 1974, Davis & Geller, 1976, Butcher & Oemler, 1978, Dressler, 1980, Postman & Geller, 1984, Peng et al., 2010b, Jaffé et al., 2015, Fasano et al., 2015). In particular, as already mentioned in Chapter 1, Dressler (1980) detected an increase in the fraction of elliptical and S0 galaxies (early-type galaxies, or ETGs) as a function of increasing environmental density, while the opposite is observed for spiral galaxies (late-type galaxies, or LTGs) (Gunn & Gott, 1972, Whitmore & Gilmore, 1991, Poggianti et al., 2001, Boselli et al., 2005, Fasano et al., 2015). This indicates that the environment is playing a crucial role on the morphology and stellar formation of galaxies and it is often associated to the star-formation (SF) quenching in the Local Universe. Thus, the environment, in addition to the internal processes described in Chapter 1, is actively participating in the evolution of galaxies.

More recently, using data from the Sloan Digital Sky Survey (SDSS; Abazajian et al. 2009), Liu et al. (2019) compared the fractions of ETGs and LTGs, and the fraction of main sequence galaxies (MSG) and quenched galaxies (QG) relative to different environments (voids, sheets, filaments, and clusters), finding that the star-forming properties of galaxies changed more dramatically than their structural properties. This means that a galaxy will stop forming stars before any morphological change can take place. Liu et al. (2019) also found that the morphological transformation and quenching for low-mass galaxies can be two independent processes, suggesting that the interruption of the SF is determined by the halo mass while the morphological transformation is more correlated with the stellar mass.

While at the present epoch a dense environment plays an important role on the process of star-formation suppression, some recent studies have shown that the environment starts being relevant only at $z < 0.5$ (Hatfield & Jarvis, 2017), when the galaxies have already gotten close enough to trigger the ram-pressure stripping. This stripping process, in addition to the strangulation process that eventually but more slowly quench galaxies, yields to a fast quenching (Rodríguez-Muñoz et al., 2019). These two processes start to be at play when a galaxy falls into the cluster, i.e. when it crosses the virial radius of a massive cluster (Wetzel et al., 2012), which is a key area to understand the processes regulating the evolution of galaxies in clusters. However, to-date there is still a lack of deeper studies of morphological and physical properties of galaxies in clusters, from an homogeneous multi-wavelength point of view (to mention some Liu et al. 2011 and Yan et al. 2014), which is what we aim to do in this Chapter.

In this Chapter, we study the global properties and their environmental dependence of the Hydra's galaxies. To do so, we model the light distribution of galaxies, which we consider here as single-component systems, with a single Sérsic profile, and classify them morphologically as Early and Late-type galaxies, using their Sérsic index (n) and colours. We then analyse the spatial distribution of the different types of galaxies (ETGs and LTGs) in terms of their physical and structural parameters, as well as the behaviour of the different galaxy parameters with respect to the cluster central distance

[3] Based on **Lima-Dias C**, et al., 2021, MNRAS, 500, 1323.

and with the cluster density. We also show the behaviour of n as a function of the 12 S-PLUS filters. In addition, we analyse the cluster's phase-space diagram and explore the presence of substructures in the Hydra cluster via the Dressler-Schectman test (DST, Dressler & Shectman, 1988) and the Density-Based Spatial Clustering (DBSCAN, Ester et al., 1996) algorithm.

4.1 Early-type and Late-type galaxies classification

Based on the physical properties of the stellar populations of ETGs and LTGs, it is straightforward to separate between these two populations using a colour-magnitude diagram (Bell et al., 2004). ETGs have in general much older and redder stellar populations, placing this population in a very well determined position of the diagram separated from the bluer and star-forming LTGs (Lee et al., 2007). Using SDSS data, Vika et al. (2015) combined n_r and the colour cut $(u-r) = 2.3$ to separate these two galaxy classes (see also Park & Choi 2005 for different values of the colour cut). Vika et al. (2015) classified the galaxies with $(u-r) \geq 2.3$ and $n_r \geq 2.5$ as ETGs and galaxies with $(u-r) < 2.3$ and $n_r < 2.5$ as LTGs. Following these parameters to classify our sample, $\sim$ 54 percent of the galaxies (44 objects) are ETGs, whereas $\sim$ 23 percent (19 galaxies) are LTGs.

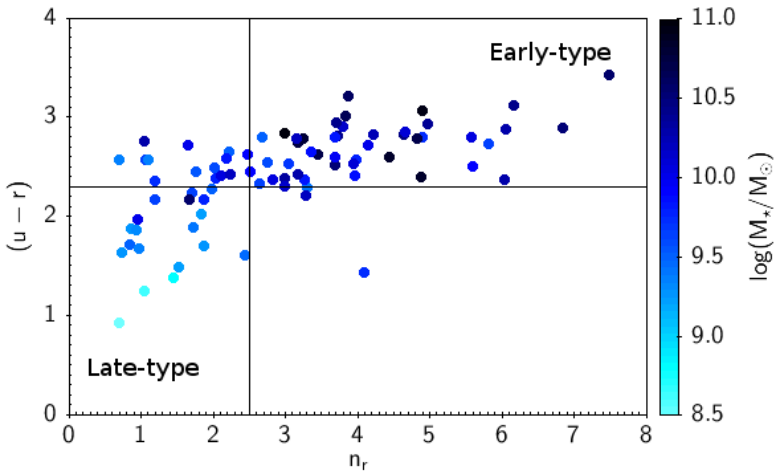

Figure 4.1: Results of the morphological fitting, performed with MegaMorph-GALAPAGOS2. The x-axis shows the Sérsic index in the r-band and the y-axis displays the galaxy $(u-r)$ colour. Symbols are coloured according to the stellar mass of each galaxy, as indicated by the colour bar. The vertical and horizontal lines are at $n_r = 2.5$ and $(u-r) = 2.3$, respectively.

In Figures 4.1 and 4.2 we present the n_r versus the (u-r) colour for the 81 galaxies used in this study, where symbols in the figures are colour-coded by stellar mass and sSFR, respectively. As expected, ETGs (top-right region on each plot) are more massive than LTGs (bottom-left region). In Figure 4.2, we show that some LTGs are forming stars at a level of -10.0<log(sSFR)<-8.8 whereas all the ETGs are quenched. It is interesting to note that there is a population of blue + green ($(u-r)$ <2.3) galaxies in the Hydra cluster that do not present Hα emission at the detection level. The stellar mass function (SMF) of star-forming galaxies (SFGs) and quenched galaxies (NSFGs) is shown in the Figure 4.3, as cyan and orange histograms, respectively. We find that the SFGs are less massive than the NSFGs, where the NSFG have basically the same behaviour of the global SMF, since only 10 galaxies in our sample are SFGs. There is a mix of populations in the top left region in Figures 4.1 and 4.2, which

represents a $\sim$ 17 percent of our sample. This region is called the transition zone [$(u-r) > 2.3$ and $n_r < 2.5$].

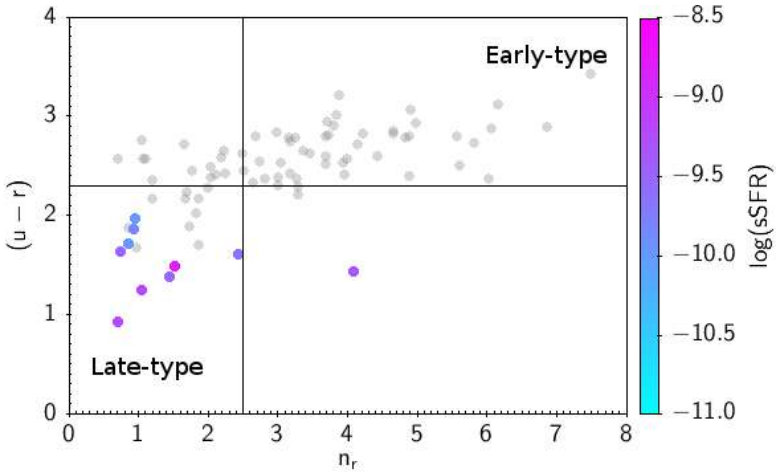

Figure 4.2: Same as Figure 4.1, but colour-coded by the $log(sSFR)$. The grey dots are NSFG.

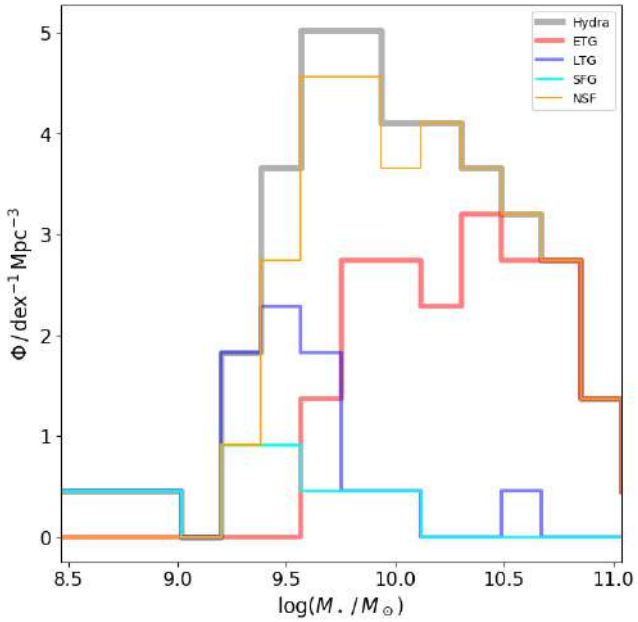

Figure 4.3: Stellar mass function of galaxies brighter than m_r=16 within a sphere with 1.4Mpc of radius centred on Hydra. The grey line represents the 81 galaxies belonging to Hydra selected as indicated in section 2.3.2. The orange and cyan lines are the quenched (NSFGs) and SFGs. The red and blue lines are ETGs and LTGs respectively.

4.2 Spatial distribution: structural and physical parameters

In this subsection we analyse how the morphological and physical parameters change with respect to the distance to the cluster centre as well as a function of the projected local density. For each galaxy

we estimate the projected local density defined as $\Sigma_{10} = 10/A_{10}$, where $A_{10} = \pi R_{10}^2(\mathrm{Mpc})$ is the area of the circle that contains the nearest 10 galaxies and R_{10} is the radio of the circle, as described by Fasano et al. (2015). Each galaxy is in the centre of the circle.

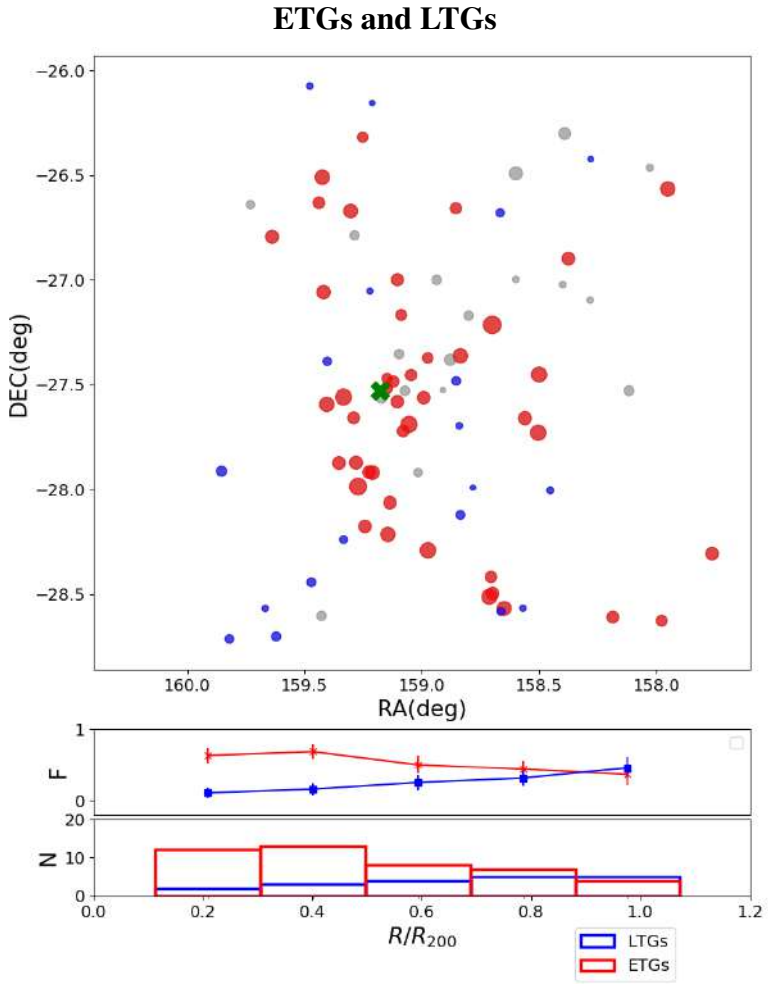

Figure 4.4: Top panel: Hydra's galaxies distribution. The x-axis shows the RA and y-axis shows the DEC in degrees. The radial extension is from the centre up to $\sim R_{200}$. The blue and red dots are the LTGs and ETGs, respectively. The grey dots are the galaxies in the first and fourth quadrants in the Figure 4.1. The size of each circle is proportional to the n_r. The green x symbol is the cluster centre. Middle panel: fraction of LTGs and ETGs in blue and red, respectively, as a function of distance in terms of R_{200}. The error bars are binomial uncertainties with a 68 percent confidence. Bottom panel: histogram of galaxies per R_{200} bin.

The top panel of Figure 4.4 shows the spatial distribution of ETGs and LTGs classified in subsection 4.1. The red and blue dots are the ETGs and LTGs respectively, and the grey dots are the mix of galaxies that do not meet the ETG or LTG definition requirements (first and fourth quadrants in Figure 4.1). The size of each circle is proportional to the n_r. The middle and bottom panels show the radial fraction and histograms of ETGs and LTGs, respectively. The fractions are calculated over the total number of galaxies. We find that the fraction of ETGs is higher than the LTGs fraction, basically for all bins, except at $\sim 0.9R_{200}$, where the behaviour is inverted. We find that ~ 47 percent of the LTGs and ~ 75 percent of the ETGs are inside $0.6R_{200}$. The number of LTG and ETG galaxies

beyond $0.6R_{200}$ is quite similar.

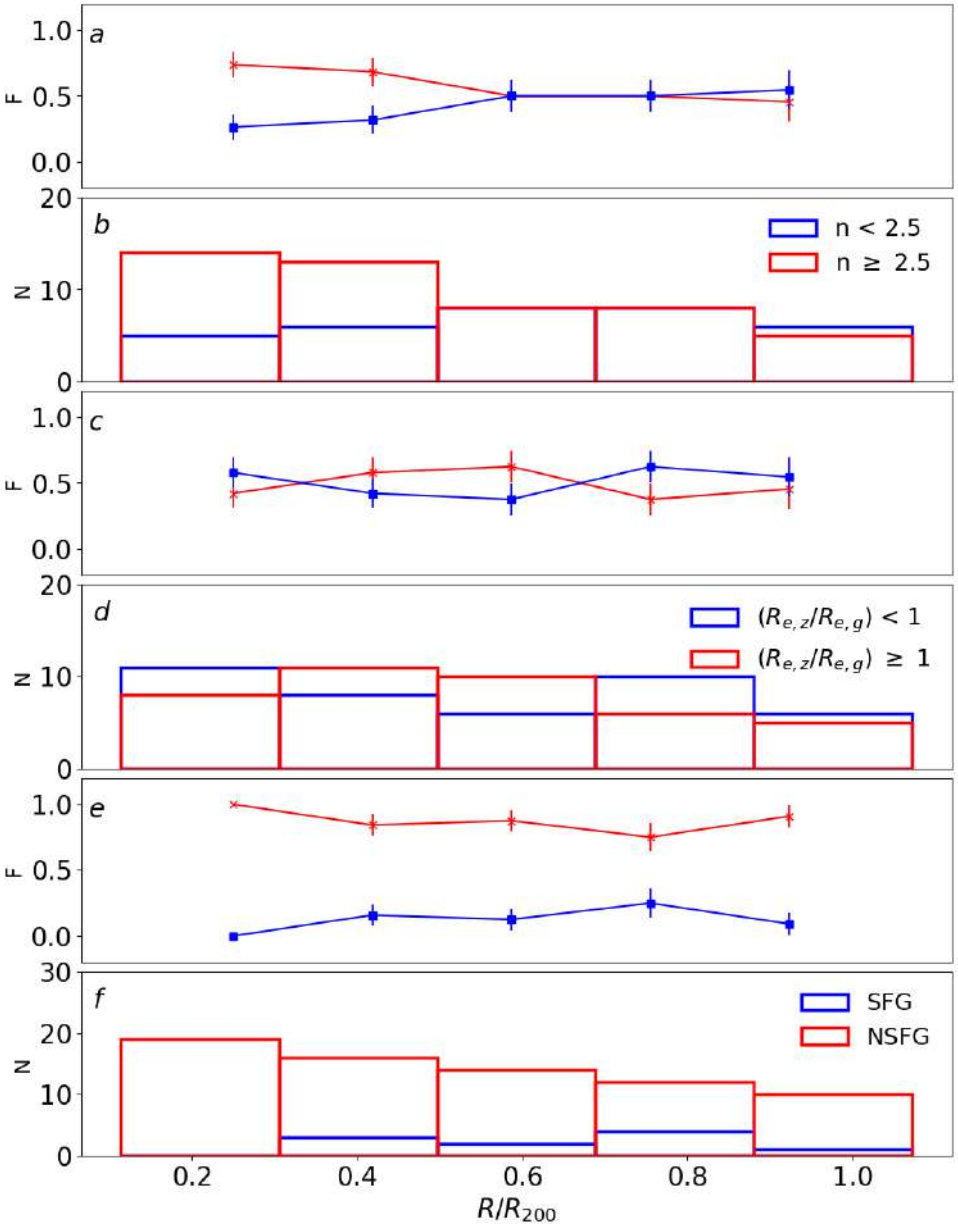

Figure 4.5: The fraction (F) and histogram representing the number of galaxies (N) per R_{200} bin. Panels **a** and **b** show galaxies with $n_r \geq 2.5$ and < 2.5 in red and blue, respectively. Panels **c** and **d** show galaxies with $(R_{e,z}/R_{e,g}) \geq 1$ and < 1 in red and blue, respectively. Finally panels **e** and **f** show NSFG and SFG in red and blue, respectively. The error bars are binomial uncertainties with a 68 percent confidence.

Figure 4.5 shows the radial fraction profiles and histograms for galaxies having n_r larger than 2.5 (red colour) and for galaxies having n_r lower than 2.5 (blue colour), $(R_{e,z}/R_{e,g})$ values larger (red colour) and smaller (blue colour) than 1, and SFG (blue colour), NSFG (red colour) with respect to the clustercentric distance. Panels **a** and **b** show that most galaxies (~ 59 percent) have $n_r \geq 2.5$, and their fraction (panel **a**) is higher than that of galaxies with $n_r < 2.5$ up to $\sim 0.5R_{200}$. For radii larger

than $\sim 0.5R_{200}$ the fractions are basically the same for the two groups of galaxies.

The **c** and **d** panels of Figure 4.5 show the ratio of effective radii in z and g bands $(R_{e,z}/R_{e,g})$. Hydra has 40 galaxies with $(R_{e,z}/R_{e,g}) > 1$ and 41 otherwise, showing a similar fraction for these two cases across all clustercentric distances inside R_{200}. Panels **e** and **f** of Figure 4.5 show the fraction and radial distribution of SFGs and NSFGs. We find that $\sim$ 88 percent of our sample of galaxies in Hydra (71 galaxies) are quenched. These quenched galaxies are found at all distances from the cluster centre, however their number decreases as a function of clustercentric distance. We also find that there are no SFGs in the central bin, i.e. inside $\sim 0.3R_{200}$ of Hydra. Owers et al. (2019), who studied a sample of galaxy clusters at low redshift, also found that the number and the fraction of passive galaxies decrease towards larger clustercentric distances. They found that beyond $0.3R_{200}$ the number of SFGs remains relatively constant, while the fraction of SFGs increases as a function of clustercentric distance. Pallero et al. (2019) studied a sample of galaxy clusters from the EAGLE hydrodynamical simulation. They classified SFGs as we do in this thesis, i.e. star-forming galaxies display log(sSFR) > -11, and found that a cluster as massive as Hydra ($M_{200} > 3\times10^{14}M_{\odot}$) has $\sim$ 90 percent of the galaxies quenched, in agreement with our findings.

We show in Figure 4.6 the distribution of SFGs and NSFGs as a function of projected local density. No SFGs are found in the highest and lowest density bins. The NSFGs dominate at all densities, however after $\sim \log(\Sigma_{10} > 1.2)$ the fraction of NSFG increases towards denser regions, while the fraction of SFG decreases in the same direction.

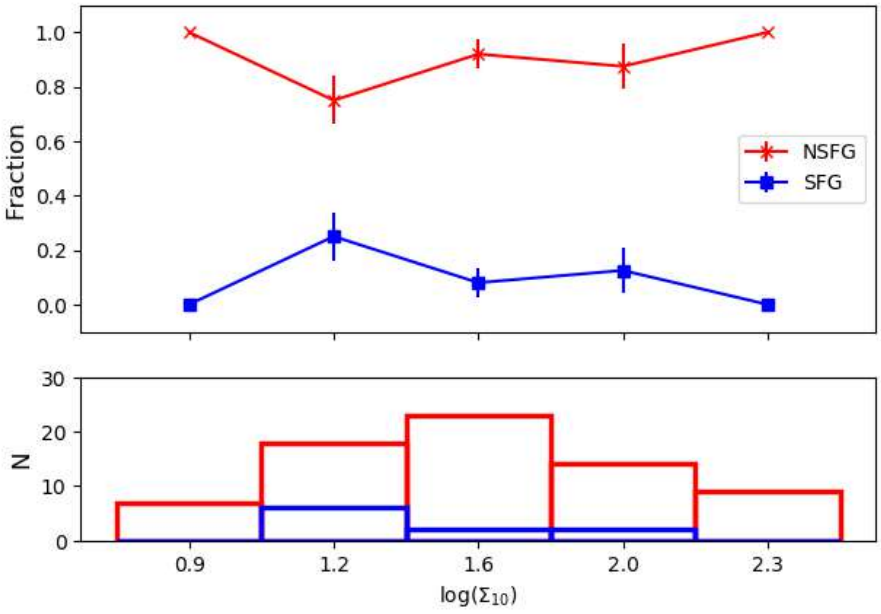

Figure 4.6: SF and NSF-Density relation. Top panel: fraction of SFG and NSFG in blue and red, respectively. The error bars are binomial uncertainties with a 68 percent confidence. Bottom panel: Histograms with the number of galaxies per density bin.

4.3 Behaviour of n as a function of wavelength

The light emitted by a galaxy at different wavelengths has information from different physical phenomena. As an example, stellar populations of different ages and metallicities have emission peaks in different regions of the spectrum. In addition, other contributions such as emission from HII regions, AGN, and planetary nebulae can also be found in a galaxy spectrum. In the case of S-PLUS, each filter is placed in optical strategic regions. Thus, within this context, it is interesting to measure how the Sérsic index (n) changes with respect to each S-PLUS filter, and how each of the n_{filter} behaves as a function of clustercentric distance and density. In order to investigate this, we separate the Hydra galaxies into four groups: i) ETG, ii) LTG, iii) red and iv) blue + green, to facilitate comparisons with other studies. Galaxies with $(u-r) \geq 2.3$ are red (58 galaxies) and galaxies with $(u-r) < 2.3$ are blue + green (23 galaxies). ETGs and LTGs follow the definition provided in Section 4.1.

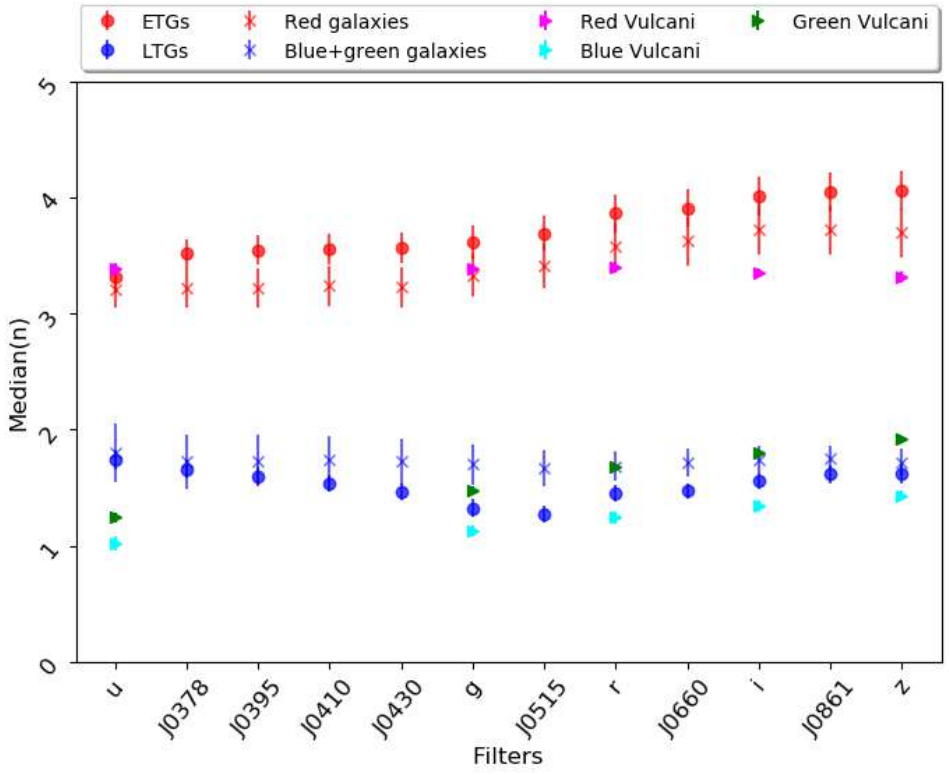

Figure 4.7: Median Sérsic index $\bar{n}$ as a function of the 12 S-PLUS filters. Red symbols represent ETGs and red ($(u-r) \geq$2.3) galaxies, blue symbols represent LTGs and blue + green ($(u-r) < 2.3$) galaxies. The error bars are the standard error of the median $1.253\sigma/\sqrt{N}$, where N is the number of objects. The magenta, green and cyan symbols are the red ($(u-r) \geq 2.1$), green ($1.6 < (u-r) < 2.1$), and blue ($(u-r) \leq 1.6$) galaxies in Vulcani et al. (2014); see Section 4.5 for more details.

Figure 4.7 shows how the median Sérsic index ($\bar{n}$) changes as a function of wavelength. The $\bar{n}$ for red galaxies shows a larger value (13 percent) toward redder filters. The $\bar{n}$ for blue + green galaxies remains constant across all filters. For ETGs, $\bar{n}$ increases with wavelength (18 percent), whereas for LTGs it decreases up to the $J0515$-band, and after that increases its value up to the z-band. The LTGs present a net decrease, from filter u to z, of 7 percent. The $\bar{n}$ values and their uncertainties per filter, estimated by adding the individual uncertainties in quadrature and dividing by the number of galaxies,

for ETGs, LTGs, red and blue + green galaxies are in Table 4.1. Figure 4.7 also shows the median Sérsic index for red ($(u-r) \geq 2.1$), green ($1.6 < (u-r) < 2.1$), and blue ($(u-r) \leq 1.6$) galaxies in Vulcani et al. (2014). They found that the median Sérsic index for blue and green galaxies increases towards redder filters, while the median Sérsic index for red galaxies remains nearly constant in the 5 SDSS filters. The galaxy sample studied by Vulcani et al. (2014) contains field galaxies, then is not a fair comparison to the Hydra galaxies.

Table 4.1: Median of Sérsic index ($\bar{n}$) of the galaxies per filter. The errors were estimated by adding the individual uncertainties in quadrature and divided by the number of galaxies per filter.

GALAXIES	$\bar{n}_u$	$\bar{n}_{J0378}$	$\bar{n}_{J0395}$	$\bar{n}_{J0410}$	$\bar{n}_{J0430}$	$\bar{n}_g$	$\bar{n}_{J0515}$	$\bar{n}_r$	$\bar{n}_{J0660}$	$\bar{n}_i$	$\bar{n}_{j0861}$	$\bar{n}_z$
ETG	3.31±0.03	3.52±0.02	3.55±0.02	3.56±0.02	3.57±0.01	3.62±0.01	3.69±0.01	3.87±0.01	3.91±0.01	4.02±0.01	4.05±0.01	4.06±0.01
LTG	1.74±0.02	1.66±0.01	1.60±0.01	1.54±0.01	1.46±0.01	1.32±0.01	1.27±0.01	1.45±0.01	1.47±0.01	1.56±0.01	1.62±0.01	1.62±0.01
RED	3.21±0.03	3.22±0.02	3.22±0.02	3.24±0.01	3.23±0.01	3.33±0.01	3.41±0.01	3.58±0.01	3.62±0.01	3.72±0.01	3.72±0.01	3.70±0.01
BLUE + GREEN	1.80±0.02	1.72±0.02	1.73±0.01	1.74±0.01	1.72±0.01	1.70±0.01	1.67±0.01	1.68±0.01	1.71±0.01	1.74±0.01	1.75±0.01	1.72±0.01

Figures 4.8 and 4.9 show how $\bar{n}$, for each S-PLUS filter, changes with density (quantified by $\log(\Sigma_{10})$) for red and blue + green galaxies, respectively. The $\bar{n}$ for red galaxies (Figure 4.8), shows an increase up to $\log(\Sigma_{10}) = 1.6$, and then decreases for denser regions. For the blue + green galaxies (Figure 4.9) $\bar{n}$, in general, remains nearly constant at all densities.

Figures 4.10 and 4.11 show the behaviour of $\bar{n}$ for each filter, for red and blue + green galaxies, respectively, but now as a function of the clustercentric distance. For red galaxies, Figure 4.10 shows that, beyond $\sim 0.4 R_{200}$, galaxies show lower $\bar{n}$ values, for all filters. For blue + green galaxies, Figure 4.11 shows that $\bar{n}$ decreases, for all filters, up to $\sim 0.4 R_{200}$, beyond that it remains constant with distance within the uncertainties. These results will be discussed in section 4.5.

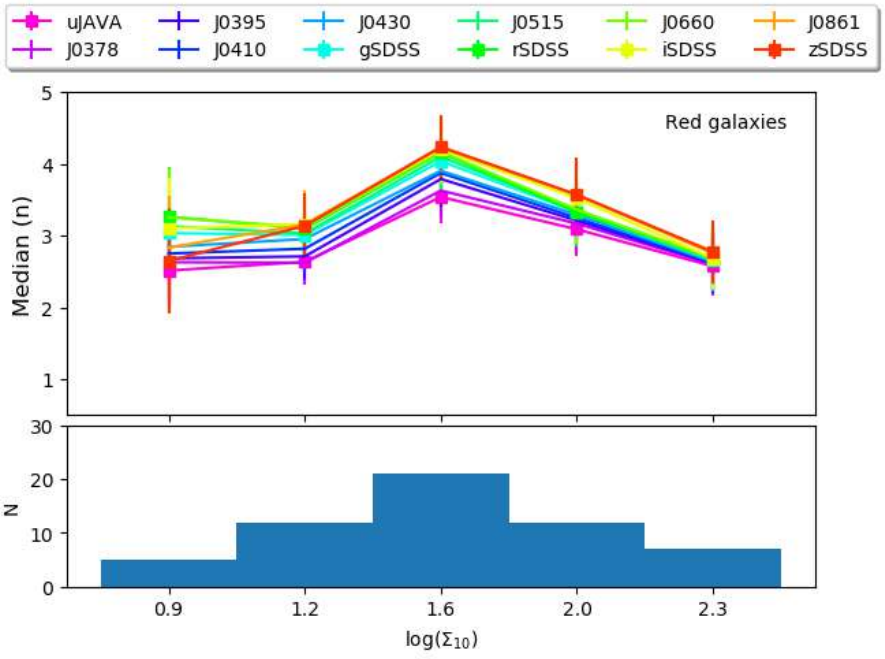

Figure 4.8: Sérsic index - Density relation for red galaxies. The top panel shows the $\bar{n}$, for each S-PLUS filter, with respect to the cluster density. The bottom panel shows a histogram with the number of galaxies per density bin.

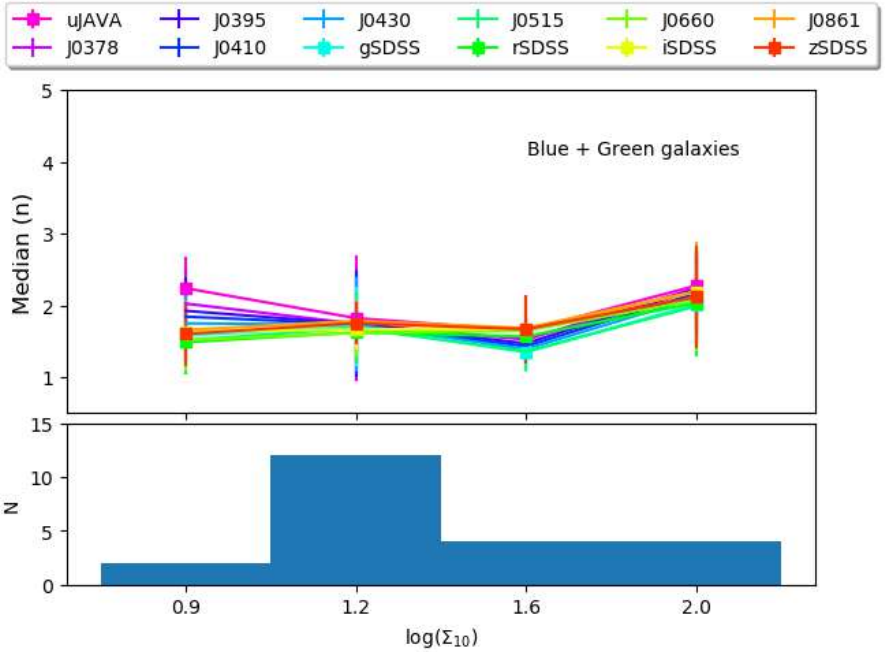

Figure 4.9: Same as Figure 4.8, but for the blue + green galaxies.

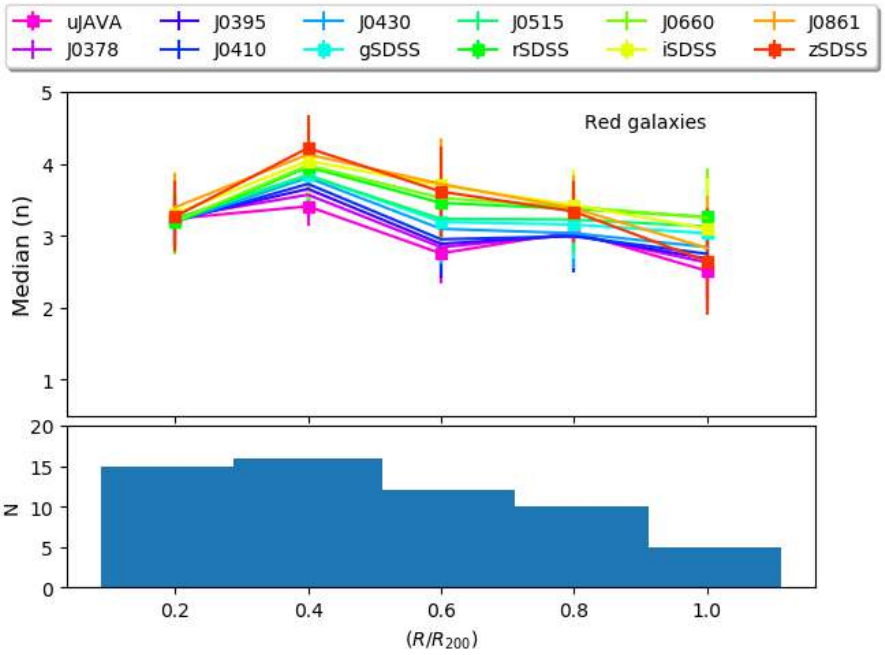

Figure 4.10: Sérsic index - Radius relation for red galaxies. The top panel shows the $\bar{n}$, for each S-PLUS filter, with respect to the clustercentric distance. The bottom panel shows a histogram with the number of galaxies per (R/R_{200}) bin.

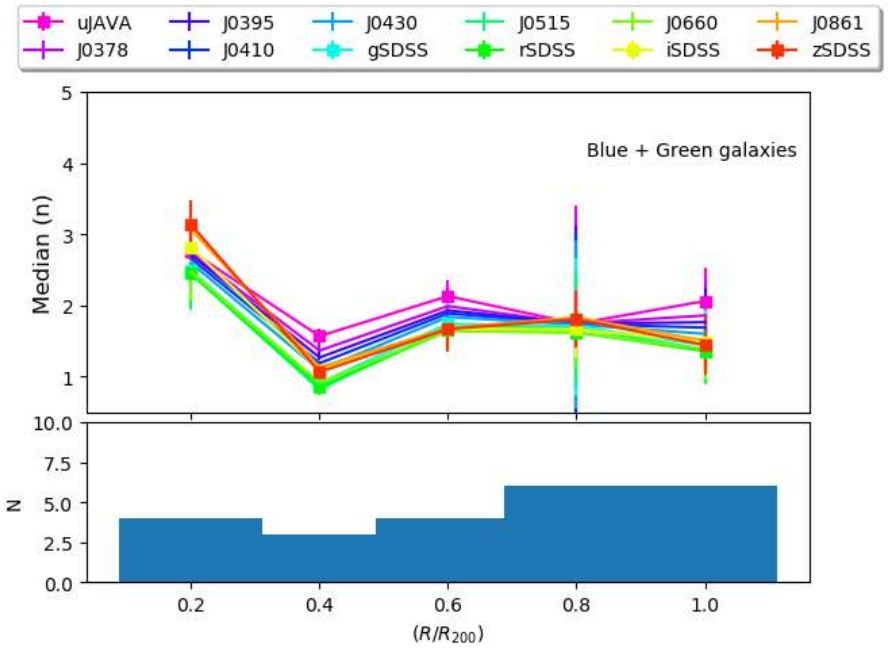

Figure 4.11: Same as Figure 4.10, here for the blue + green galaxies.

4.4 Substructures in the Hydra Cluster and the phase-space diagram

The environment in which a galaxy is embedded may play an important role in determining its morphological (e.g. the n) and physical (e.g. the sSFR) parameters. The presence of substructures in a cluster can influence the parameters mentioned above. To check if this is the case in Hydra, we need to determine whether there are possible substructures within the cluster. The substructures generally have galaxies of different luminosities, thus if we only use galaxies brighter than 16 (r-band) to check for the presence of substructure, we could lose important information. Therefore, we decide to use in this section the galaxies selected in Section 2.3.1, i.e. all the galaxies that have peculiar velocities lower than the escape velocity of the cluster, without considering any cut in magnitude. There is a total of 193 such galaxies in Hydra and we apply the Dressler-Schectman test (DST, Dressler & Shectman, 1988) on those galaxies to search for the existence of possible substructures. The DST estimates a Δ statistic for the cluster by comparing the kinematics of neighbouring galaxies with respect to the kinematics of the cluster. This comparison is done for each galaxy taking into account the N_{nn} nearest neighbours, where we use $N_{nn} = \sqrt{(N_{\rm total})}$ following Pinkney et al. (1996), with $N_{\rm total}$ being the total number of objects in the Hydra cluster. Each galaxy and its N_{nn} neighbours are used to estimate a local mean velocity $\bar{v}_{local}$ and a local velocity dispersion σ_{local}, which are compared with the mean velocity ($\bar{v}$) and velocity dispersion (σ) of the cluster. For each galaxy we then estimate the deviation δ as:

$$\delta_i^2 = (N_{nn}/\sigma^2)[(\bar{v}_{local} - \bar{v})^2 + (\sigma_{local} - \sigma^2)] \tag{4.1}$$

The Δ statistic is then defined as the cumulative deviation; $\Delta = \sum_i^N \delta_i$. If $\Delta/N_{\rm total} > 1$ it means that there probably is a substructure in the cluster (White et al., 2015). For the Hydra cluster, considering an area of $\sim 95'$ of radius and with 193 members, we found a $\Delta/N_{\rm total} = 1.25$. To confirm that

this result is significantly different from a random distribution, and validate the possible existence of substructures in Hydra, we calibrate the Δ statistic by randomly shuffling the velocities using a Monte Carlo simulation. We perform $1x10^5$ iterations: for each of those we calculated the Δ statistic, which we call for simplicity random Δ. We then count the number of configurations for which the random Δ is greater than the original Δ, N(Δ,randoms $> \Delta$), normalised by the number of iterations, N(Δ,randoms), that is

$$P = \frac{N(\Delta, \text{randoms} > \Delta)}{N(\Delta, \text{randoms})} \tag{4.2}$$

If the fraction P is lower than 0.1, we can conclude that the original Δ value is not obtained from a random distribution (White et al., 2015). We find P = 0.016, which is consistent with a possible presence of substructures in the Hydra cluster.

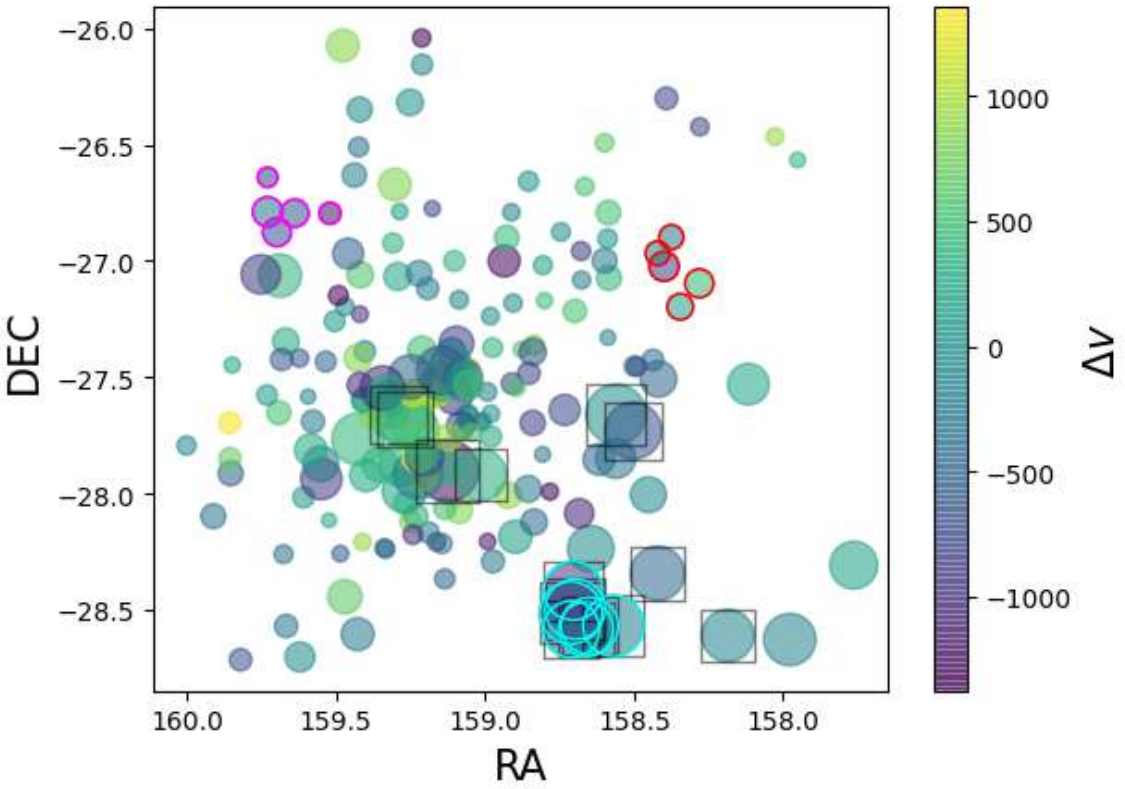

Figure 4.12: Spatial distribution of Hydra galaxies. The size of each circle is proportional to e^{δ}, i.e. bigger dots indicate that the galaxy is in a possible substructure. The galaxies are colour-coded by their peculiar velocity. The galaxies that belong to the different structures identified by `DBSCAN` are enclosed by open circles of different colours. Galaxies with $\delta > 3$ times the standard deviation of δ distribution are enclosed by open black square.

In Figure 4.12 we highlight the possible substructures detected in Hydra, where we show the distribution of the cluster's galaxies where the size of each circle is proportional to e^{δ}. Larger circles indicate a higher probability for a galaxy be part of a kinematical substructure. Each galaxy is colour-coded

by their peculiar velocities with respect to the cluster's median velocity. We found possible substructures, i.e. galaxies with $\delta > 3$ times the standard deviation of δ distribution, in the outer regions of the cluster as well as in the central part. These possible substructures are enclosed by a black open square in Figures 4.12 and 4.14.

We note that Stein (1997) found that Hydra does not present any substructure, by applying the same DST but in an area of $45'$ radius ($\sim$0.67 Mpc), which includes 76 galaxies[4]. To understand this discrepancy we applied the DST in the same area as Stein (1997) using 136 galaxies, and found $\Delta/N_{\rm total} = 1.0$, which is inconclusive in terms of substructures. Therefore, we detect possible new substructures in an unexplored area of Hydra.

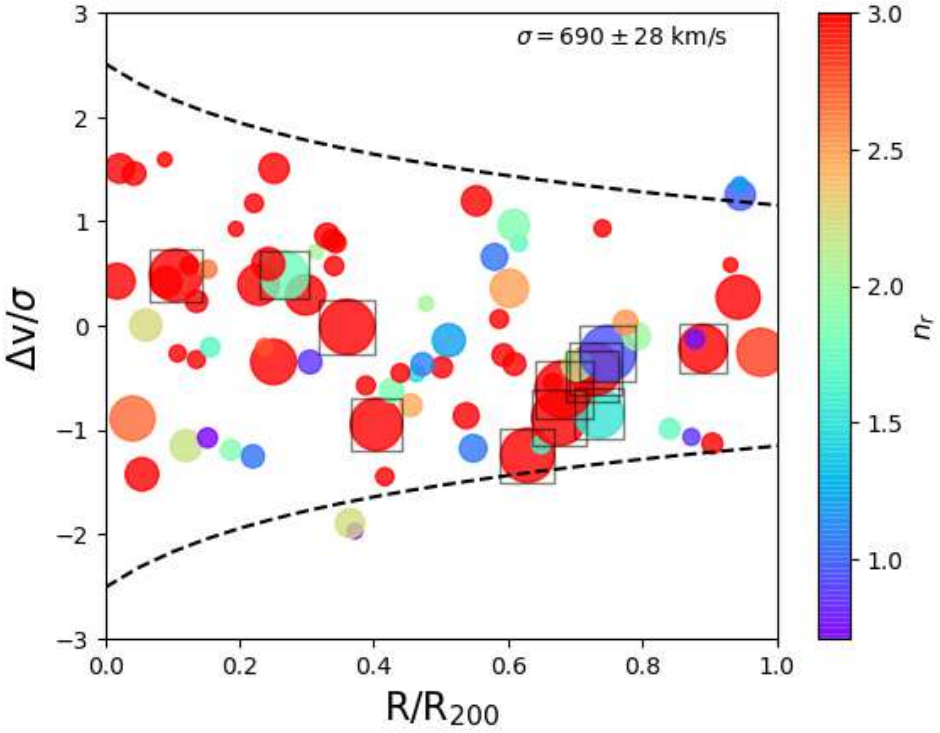

Figure 4.13: The phase-space diagram. The x-axis shows the projected distance from the cluster centre normalised by R_{200}. The y-axis shows the peculiar line-of-sight velocity with respect to the cluster recessional velocity, normalised by the velocity dispersion of the cluster. The dashed lines are the escape velocity defined in Jaffé et al. (2015, see their Equation 2). Each galaxy is colour-coded by n_r. The colour bar saturates at n_r=3, thus all galaxies that have $n_r \geq 2.5$ are in red. The size of each circle is proportional to the δ of the DST. Galaxies with $\delta > 3$ times the standard deviation of δ distribution are enclosed by open black square.

In order to further look into the possibility of substructures, we use a Density-Based Spatial Clustering (DBSCAN, Ester et al., 1996) algorithm. `DBSCAN` takes as input the positions of the objects and the minimum number of objects with a maximum distance between them to be considered as a group/substructure. We adopt a maximum distance of 140 kpc and a minimum of 3 galaxies to

[4]We also note that, using the normality-test, Stein (1997) found that Hydra presents substructures with 1 percent of significance level. See Beers et al. (1990b) for more details.

consider a substructure (Sohn et al., 2015, Olave-Rojas et al., 2018). Using the 193 galaxies, DBSCAN finds the presence of three substructures within R_{200}, one of them in agreement with the possibility of a substructure found with the DST. Each galaxy that belongs to the substructure found by DBSCAN is enclosed by open circles in Figure 4.12. The galaxies that belong to the same structure found by DST are enclosed by cyan open circles; this substructure has 7 galaxies, 2 of them are SFGs.

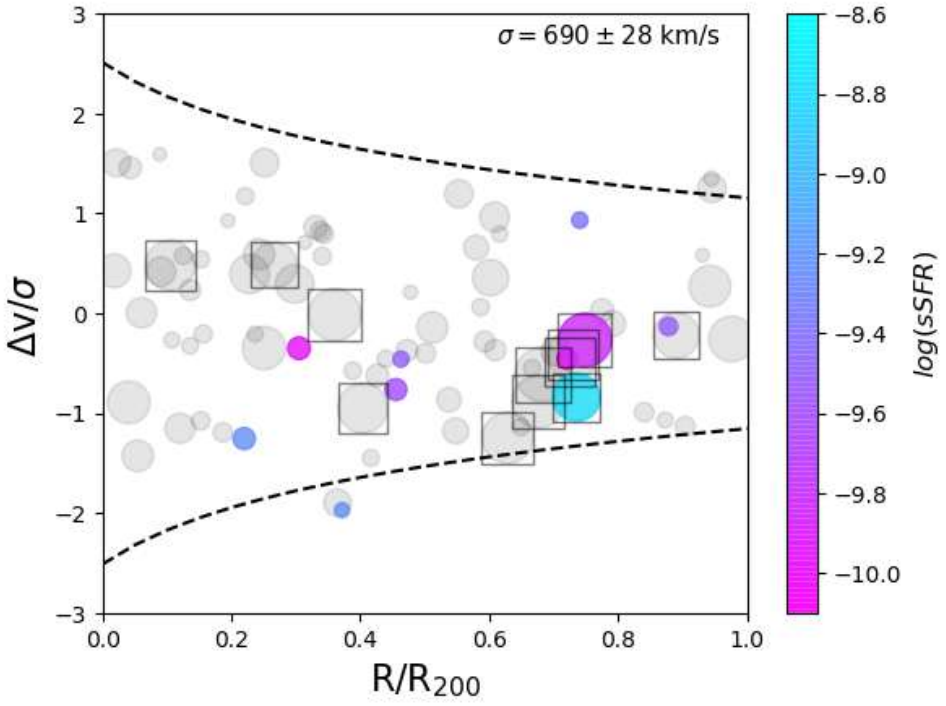

Figure 4.14: Same as Figure 4.13, colour-coded by $\log(sSFR)$. The grey dots are galaxies that do not have Hα emission. Galaxies with $\delta > 3$ times the standard deviation of δ distribution are enclosed by open black square.

Having determined the possible existence of substructures in Hydra, the phase-space diagram (Jaffé et al., 2015), which relates the distance to the cluster centre with the kinematical quantity $\Delta v/\sigma$, could help us to understand the dynamic state of Hydra. We show the phase-space diagram of Hydra in Figures 4.13 and 4.14, where we use the 81 galaxies that have $m_r < 16$. The x-axis is the projected distance from the cluster centre normalised by R_{200} and the y-axis is the peculiar line-of-sight velocity of each galaxy with respect to the cluster recessional velocity, normalised by the velocity dispersion of the cluster. The escape velocity is indicated by the dashed lines and it is obtained based on a Navarro, Frenk & White dark matter profile (Navarro et al., 1996), see Jaffé et al. (2015) for more details. Figures 4.13 and 4.14 show the same diagram colour-coded by n_r and $\log(sSFR)$, respectively, where the circle sizes are proportional to δ. Galaxies with $\delta \geq 3\sigma_\delta$ (the standard deviation of δ distribution) have the largest probability to belonging to a substructure (Girardi et al., 1997, Olave-Rojas et al., 2018). These galaxies are enclosed by open black square in Figures 4.13 and 4.14. We can see that there are galaxies both with high and low n_r in possible substructures (bigger circles). Also, it is clear that some galaxies located in substructures are star forming. We can see from Figure 4.14 that galaxies with larger δ are located beyond $0.6R_{200}$, and also some galaxies are closer to the cluster central region. Figure 4.14 shows the 12 galaxies that have $\delta \geq 3\sigma_\delta$. Four of these galaxies are near to the cluster centre and 8 are beyond $0.6R_{200}$. Two of the 12 galaxies are SFGs and 8 have $n_r \geq 2.5$.

We saw that the DBSCAN algorithm found a substructure with exactly the same galaxies as one of the substructures detected by the DST, and based on the phase-space diagram this substructure lies in front of the cluster centre. We speculate that these galaxies are falling now into the cluster.

4.5 Discussion

We discuss in this section the results that we found in this Chapter, and compare them with previous studies. Also, we discuss few caveats and cautions that should be taken into account when interpreting some of the results presented here.

We find that $\bar{n}$ for ETGs, as well as red galaxies, displays a slight increase towards redder filters (13 percent of its value for red galaxies and 18 percent for ETGs, see Figure 4.7). This result is in agreement with previous studies (La Barbera et al., 2010, Kelvin et al., 2012, Vulcani et al., 2014). For LTGs, we find that $\bar{n}$ decreases, from filter u to z, by 7 percent. However, other studies both in cluster and in field galaxies have found that n increases as a function of wavelength for LTGs (La Barbera et al., 2010, Kelvin et al., 2012, Vulcani et al., 2014, Psychogyios et al., 2019). This behaviour may be due to higher star formation in these galaxies, which is more concentrated in the inner regions. To better compare with Vulcani et al. (2014, hereafter V14) we have included their data points in Figure 4.7. V14 used the filters u, g, r, i, and z from SDSS, and modeled field galaxies with a single Sérsic profile. We note, first, that their sample contains field galaxies and, second, that their colour cuts to separate galaxies as red, blue and green are slightly different than the ones used in this thesis. Nevertheless, the green+blue and LTGs from Hydra show similar values of $\bar{n}$, within the uncertainties, with respect to the green galaxies in V14 for most filters. The $\bar{n}$ value for the u filter is higher for Hydra. For the red galaxies and filters u, g, and r, this thesis and that of V14 show similar values of $\bar{n}$. However, red galaxies in Hydra show a higher value in the filters i and z when compared to the red field galaxies in V14. Overall blue galaxies in Hydra exhibit a higher value of $\bar{n}$ when compared to the blue galaxies of V14. This result is interesting and in agreement with Psychogyios et al. (2019), who found that cluster galaxies always have a higher value of $\bar{n}$, regardless of the filter, when compared to field galaxies. Thus, bearing in mind that a comparison with other studies is not so simple, due to the differences in separating galaxies as ETGs, LTGs, red, green and blue, which likely contribute to differences in the results, there may be actual differences between the $\bar{n}$ values as a function of filter between cluster and field galaxies.

The $\bar{n}$ value for blue + green galaxies remains constant as a function of wavelength. We find that it appears to have a higher value for the bluest filters with respect to the clustercentric distance (Figure 4.11). However, considering the uncertainties, we find no significant change in $\bar{n}$ as a function of distance or wavelength. We can see the same behaviour with respect to the density ($\log(\Sigma_{10})$), where $\bar{n}$ remains constant, considering the uncertainties (Figure 4.9). The $\bar{n}$ for red galaxies is always greater than 2.5, and for blue + green galaxies is generally lower than 2. A similar result was presented in Psychogyios et al. (2019) using 5 filters (u, B, V, J and K). They found that the Sérsic index remains nearly constant as a function of wavelength, for galaxies that belong to a cluster.

Examining the Hydra's SMF we find that the ETGs and NSFGs are more massive and dominate the higher mass end of the global SMF (see Figure 4.3), as expected for a cluster. The lower mass galaxies are mostly LTGs and SFGs and dominate the lower mass end of the SMF. These results are in agreement with previous studies (e.g., Blanton & Moustakas, 2009, Vulcani et al., 2011, Etherington

et al., 2017, van der Burg et al., 2020b). For example, Vulcani et al. (2011) analysed a sample of 21 nearby clusters $(0.04 < z < 0.07)$, finding that the global SMF is dominated by ETGs (Elliptical and S0 galaxies), while the number of Late-type galaxies declines towards the high mass end of the SMF. In the local universe, the high mass end of the SMF is dominated by ETGs both in low and high-dense environments (Blanton & Moustakas, 2009, Bell et al., 2003). The low mass end of the SMF for low-density environments is completely dominated by blue disk galaxies, whereas in high-dense environments there is a mix of ETGs and LTGs (Blanton & Moustakas, 2009). Regarding the red galaxies, with the increase of local density (isolated − poor group − rich group − cluster), the characteristic mass of this population increases. This is because most of the brightest objects are red and located in dense regions. In addition, the blue population declines in importance as the local density increases (Blanton & Moustakas, 2009).

In this thesis we separate galaxies as blue + green ($(u-r) < 2.3$) and red ($(u-r) \geq 2.3$). There is an intermediate zone between the red sequence and the blue cloud, called green valley. These galaxies have typical colours between $1.8 \lesssim (u-r) \lesssim 2.3$ (Schawinski et al., 2014). In Hydra, we find that galaxies with colours $1.8 \lesssim (u-r) < 2.3$ do not present H_α emission at the detection limit used on this thesis (21 mag/arcsec^{-2}). These objects could be transitional galaxies that have lower sSFRs than actively star-forming galaxies of the same mass. The galaxies in the green valley have very low levels of ongoing star formation (log (sSFR) < -10.8, Salim, 2014), and we are not detecting star formation at such a low level. These galaxies do not meet the criteria required to be considered as emission line galaxies, i.e. to have a genuine narrow-band colour excess (above the 3Σ cut and a $EW_{J0660} > 12$ Å). It is possible that these objects have Hα emission below the detection limit of the survey. Perhaps, in some of these galaxies, deeper images will evidence Hα emission. Most of these objects appear located in the outskirts of the cluster, which suggests that these have fallen into the cluster recently; however, these have already suffered the influence of the cluster, and may already have lost some or a considerable amount of their gas, which might be another possibility to explain the absence of Hα emission. We therefore suggest that this population of green galaxies could have stopped their star formation recently due to environmental effects (Peng et al., 2010b, Wright et al., 2019).

As it is well known, the morphology and *SFR* of galaxies are correlated, and the environment likely plays an important role in the evolutionary changes of these parameters (Paulino-Afonso et al., 2019, Pallero et al., 2019, Fasano et al., 2015). In this thesis we study the behaviour of the sSFR with respect to the clustercentric distance and density. We find that ~ 88 percent of the Hydra's galaxies are quenched, based on their Hα emission. However, 23 percent of Hydra galaxies are LTGs, according to our morphological and physical classification. This suggests that, as advocated by Liu et al. (2019), the galactic physical properties (e.g. SFR) of galaxies in a cluster change faster than their structural properties.

The DST we performed in the previous section indicates that Hydra presents substructures with a $\Delta/N_{\rm total} = 1.25$. This value is not too high in comparison with other clusters (see e.g., Olave-Rojas et al. 2018). We also confirm the presence of substructures using the `DBSCAN` algorithm. Interestingly, previous studies have shown that Hydra has an approximately homogeneous X-ray distribution. This observed feature suggests that the cluster has not suffered merging processes recently, and probably is a relaxed system (Fitchett & Merritt, 1988, Furusho et al., 2001, Hayakawa et al., 2004, Łokas et al., 2006). It was also found in other work that Hydra does not present a Gaussian velocity distribution (Fitchett & Merritt, 1988). Combining the previous information with our findings of substructures in Hydra, we conclude that Hydra is perturbed, but not significantly and thus it is very close to become

a virialized system.

4.6 Summary and Conclusions

In this Chapter, we focus on the global properties of a selected sample of 81 Hydra galaxies observed with S-PLUS. We analyse the derived structural and physical parameters of these galaxies and relate these to the environment.

Our main findings are:

1) There is a clear correlation between the single Sérsic index (n_r) and the galaxy stellar mass. Higher values of n_r are found for larger stellar masses. The sSFR has the opposite behaviour, the higher the n_r, the lower is the sSFR, as expected (see Figures 4.1 and 4.2).

2) There is a larger fraction of NSFGs (galaxies with $\log(sSFR) \leq$ -11) than SFGs (galaxies with $\log(sSFR) >$ -11) across all R_{200} and all cluster densities. We find that $\sim$88 percent of our sample of Hydra galaxies can be classified as NSFG.

3) The $\bar{n}$ changes its behaviour with respect to the wavelength depending on the colour of the galaxies. The $\bar{n}$ for red and ETGs present an increase of 13 and 18 percent respectively, towards redder wavelengths. The LTGs show a decrease in $\bar{n}$ (7 percent), from the u to the z band, while the $\bar{n}$ for blue + green galaxies remains constant. Beyond $\sim 0.3R_{200}$, red galaxies show lower $\bar{n}$ values, for all filters, declining as a function of distance from the cluster centre. Additionally, beyond $\sim 0.4R_{200}$, the $\bar{n}$ for blue + green galaxies remains constant for all filters.

4) We find that the Hydra cluster presents possible substructures, as determined from a DST. The `DBSCAN` algorithm found a substructure with exactly the same galaxies as one of the substructures detected by the DST. Two of the galaxies that are in that likely substructure are SFG, and lie in front of the cluster centre, based on the phase-space diagram. We speculate that these galaxies are falling now in to the cluster. However, given that there are few substructures, we conclude that the Hydra cluster is, although perturbed, close to virialization.

5 Bulge-disc decomposition of Hydra galaxies[5]

In the previous Chapter, we focus on studying the structural parameters of galaxies assuming a single component, by fitting a single Sérsic profile for the whole galaxy. However, galaxies are composed of different components; bulge, disc, halo and also occasionally a bar, and we can use the characteristics of these different components to study the galaxies' formation and evolution. The bulge and disc could be formed by different processes, and they have photometric, chemical and kinematic differences. In this Thesis, we focus on the photometric properties to understand the structure of these galaxies. The bulge is a spheroidal component that presents mostly an old and red stellar population generally metal poor, when compared to the disc (Head et al., 2014), and its light profile is well described by a Sérsic profile (Sérsic, 1963). Meanwhile the disc presents a mix of old and young stellar populations, generally more metal rich than the bulge stellar population, and its light profile is well described by an exponential profile (Peng et al., 2010a). Nowadays there are three main scenarios for bulge formation: Monolithic Collapse, Secular Evolution, and Mergers. In the monolithic scenario (Eggen et al., 1962), the gas collapses and creates stars. This process occurs within a short time (1 or 2 Gyr). In the Secular Evolution, the bulges formed after discs and undergo several central starbursts (Bouwens et al., 1999). Finally, galaxy mergers can also form bulges (Brooks & Christensen, 2016). In this case bulges form from gas that underwent substantial merger induced dissipation and from the stars accreted during the merger (Katz, 1992, Brooks & Christensen, 2016).

Matharu et al. (2019) found evidence for size growth of quiescent galaxies in the field, due to minor mergers. Compared with cluster galaxies, they found that quiescent and star-forming cluster galaxies are smaller than their field counterparts. This effect will be seen in the galaxy components, and the outermost part, the disc, will be the most affected due to environmental influence (Hudson et al., 2010). Therefore, studying the different components of galaxies and their variation of structural (Sérsic index, effective radius) and physical parameters, with respect to the clustercentric distance and density, could give some clues about the evolution of galaxies, and this is the goal of this Chapter.

A bulge-disc decomposition of galaxies can be done in a non parametric way (Schade et al., 1995, Ratnatunga et al., 1999) for low redshift galaxies. Galaxies with the bulge-to-total flux (B/T) ≥ 0.5 are bulge-dominated galaxies (early-type galaxies), and galaxies with $B/T < 0.5$ are disc-dominated (late-type galaxies). A pure disc-like galaxy has $B/T = 0$ while a pure bulge-like galaxy has $B/T = 1$. By performing a simultaneously bulge-disc decomposition in the u, g, r, i and z bands for nearby field galaxies, Vika et al. (2014) found that the mean B/T values increase from 0.17 to 0.7 from spiral to elliptical galaxies. Also, they found that the ratio between the effective radius of the bulge and the disc does not vary significantly with the Hubble type. The disc colours are bluer than the bulge colour (Hudson et al., 2010), regardless of the galaxy's morphological type (Kennedy et al., 2016). Also, Kennedy et al. (2016) found that the bulge and the disc are redder for galaxies with redder total colour, meaning it is not just one component that has a redder colour. Additionally, for fainter galaxies the bulge and disc colours are similar. Considering environmental dependence, Lackner & Gunn (2013) found that the disc colour does increase as a function of local density in relatively poor groups. Hudson et al. (2010) found the same result analysing clusters of galaxies.

In this Chapter, we describe the results from the bulge-disc decomposition of Hydra cluster galaxies. We analyse the galaxies' components separately, and in terms of the global properties of the galax-

[5]Based on **Lima-Dias C,** et al., in preparation.

ies analysed in Chapter 4. The structural and physical properties of each component are analysed as a function of the environment (clustercentric distance, density, and probability to belong a substructure). Additionally, we investigate the mass-size relation for the galaxies and their components. All the analysis presented here was carried out with a subsample of the galaxies discussed in Chapter 4. These galaxies are all within $1R_{200}$ from the cluster centre and are brighter than 16 (r-band). However, only those with reliable bulge-disc decomposition are analysed here, as explained below. Additionally, all linear fits presented in this Chapter were performed using python's *seaborn.regplot* package, where the option *robust=True* was used. This option will de-weight outliers, performing more reliable fits.

5.1 Properties of the sample

In the previous Chapter we studied galaxies using a single Sérsic profile. Here, we performed a bulge-disc decomposition, on the 12 S-PLUS bands simultaneously, for the 81 galaxies analysed in Chapter 4. The fit was made by fixing the central galaxy position. We modeled the bulge with a Sérsic profile with a free Sérsic index, and the disc with an exponential profile (n = 1). The structural parameters obtained are the Sérsic index for the bulge and the scale length of the disc (R_s), which we can use to determine the effective radius of the disc as $Re = 1.678 \times R_s$. The Sérsic index and the effective radius were modeled as linear functions of wavelength (for the bulge and the disc). The b/a and the position angle were obtained by fitting a constant offset from the input values. The models were performed using the MEGAMORPH-GALAPAGOS2 project. See Chapter 3 for more details.

Here we restrict our sample to galaxies that meet the following criteria: a) $\chi^2 \leq 1.9$; this was determined with a visual inspection, all galaxies below this χ^2 value from the fitting procedure have visually a good fit; b) $0.1 < (B/T)_r < 0.9$, to guarantee that these galaxies have a separable bulge and disc. This is because galaxies that have only one component like a bulge have a B/T close to 1, and galaxies with one component like a disc have B/T close to 0. For these galaxies it does not make sense to perform a bulge disc decomposition. B/T is determined by the ratio of the bulge flux to the bulge+disc flux; c) bulge effective radius smaller than the effective radius of the disc, to make sure that we are analysing the central part of the galaxy as a bulge, and the disc otherwise; d) effective radius of the bulge lower than 12 kpc. This criterion was taken to ensure that the size of the galaxy has physical meaning. Indeed, galaxies with stellar masses in the range that we are studying here rarely exceed this physical size (Lange et al., 2016, Kennedy et al., 2016, Kuchner et al., 2017, Méndez-Abreu et al., 2021). Finally, we have a sample of 52 galaxies that meet all these selection criteria.

Some properties of the galaxies, as a result of the bulge-disc decomposition, are shown in Figure 5.1. The black, red and blue colours represent the entire galaxy (as analysed in the previous Chapter), the bulge, and the disc component, respectively. Panel **a** of Figure 5.1 shows the Sérsic index distribution in the r-band. The median bulge n_r is smaller than the median n_r for the single Sérsic profile (galaxy modeled as one component), being 2.8 and 3.7 for the bulge and the Single Sérsic profile, respectively. The effective radius (Re) distributions are shown in panel **b**. The median Re values are 2.6, 0.8 and 4.8 kpc for galaxy, bulge, and disc, respectively. Note that the fact that the Re of the bulges are smaller than those of the disc is a consequence of our selection of galaxies, since we are only investigating galaxies where the effective radius of the bulge is smaller than that of the disc. Indeed, in general, observational studies find that the Re of bulges are smaller than the Re of the discs (Gutiérrez et al.,

2004, Head et al., 2014, Kennedy et al., 2016, Méndez-Abreu et al., 2021). In this work, we find that 32 percent of our galaxies were fitted with a larger *Re* for the bulge than for the disc, and we do not analyse these galaxies. However it can happen that a disc is embedded in the inner regions of a bulge-dominated galaxy (Huang et al., 2013), thus presenting a lower value of *Re* in comparison with the *Re* of the bulge.

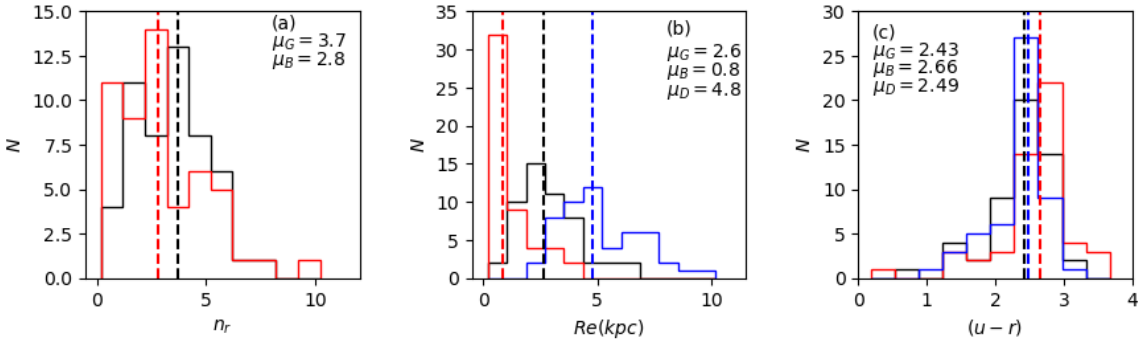

Figure 5.1: Properties of galaxies. The red, blue and black colour represents the bulge, disc, and the whole galaxy, respectively. The μ symbol on each panel is the median of the property distribution. Panel **a** shows the single Sérsic index obtained for the whole galaxy and the bulge's Sérsic index. The median bulge n_r is smaller than the median n_r for the single Sérsic profile. Panel **b** shows the effective radius in kpc. The median *Re* of the bulge is smaller than that of the entire galaxy which is smaller than the median *Re* of the disc. Finally, panel **c** shows the $(u - r)$ colour distribution. In general, the disc and whole galaxy are bluer than the bulge.

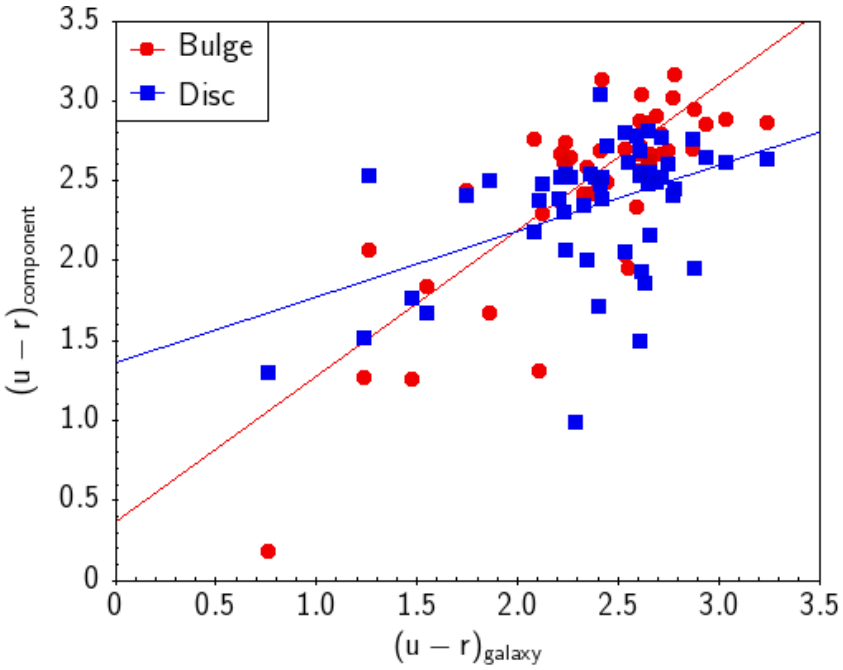

Figure 5.2: The x-axis shows the $(u - r)$ galaxy colour, and the y-axis shows the $(u - r)$ bulge and disc colour. The red dots and blue squares are the bulge and disc, respectively. We can see from this plot that redder galaxies have redder components (bulge and disc). The red and blue lines show the best linear fit for the bulge and disc, respectively.

Panel **c** of Figure 5.1 shows the $(u-r)$ colour distribution for the galaxy, bulge, and disc components. As expected, the median colour of the bulges is redder than that of the discs. However, there are some bluer bulges: 19 out of the 52 galaxies ($\sim$ 37 percent) have the bulge bluer than the disc. We will discuss more about this result later in this Chapter. The median $(u-r)$ colours are 2.43, 2.66, and 2.49 for the galaxy, bulge, and disc, respectively. Figure 5.2 shows the $(u-r)$ colour from the galaxies versus the $(u-r)$ colour from the bulge and disc. We found that redder galaxies have redder components (bulge and disc), which is in agreement with Kennedy et al. (2016). They performed a bulge-disc decomposition in field galaxies using data from the Galaxy And Mass Assembly (GAMA) survey, which includes (*ugriz*) optical bands and the near-IR ($YJHK$) bands.

5.1.1 Bulge-to-total flux ratio

Galaxies that are bulge-dominated have $(B/T)_r \geq 0.5$, while disc-dominated galaxies have $(B/T)_r < 0.5$. Figure 5.3 shows the B/T distribution and its mean value for the 12 S-PLUS filters. The mean B/T does not change significantly with the 12 S-PLUS filters, going from 0.38 to 0.44, having a tendency to be larger for the redder filters. Table 5.1 shows the number and percentage of galaxies with $B/T \geq 0.5$ and $B/T < 0.5$ for each S-PLUS filter. 36 percent of the galaxies are bulge-dominated, using the *r*-band.

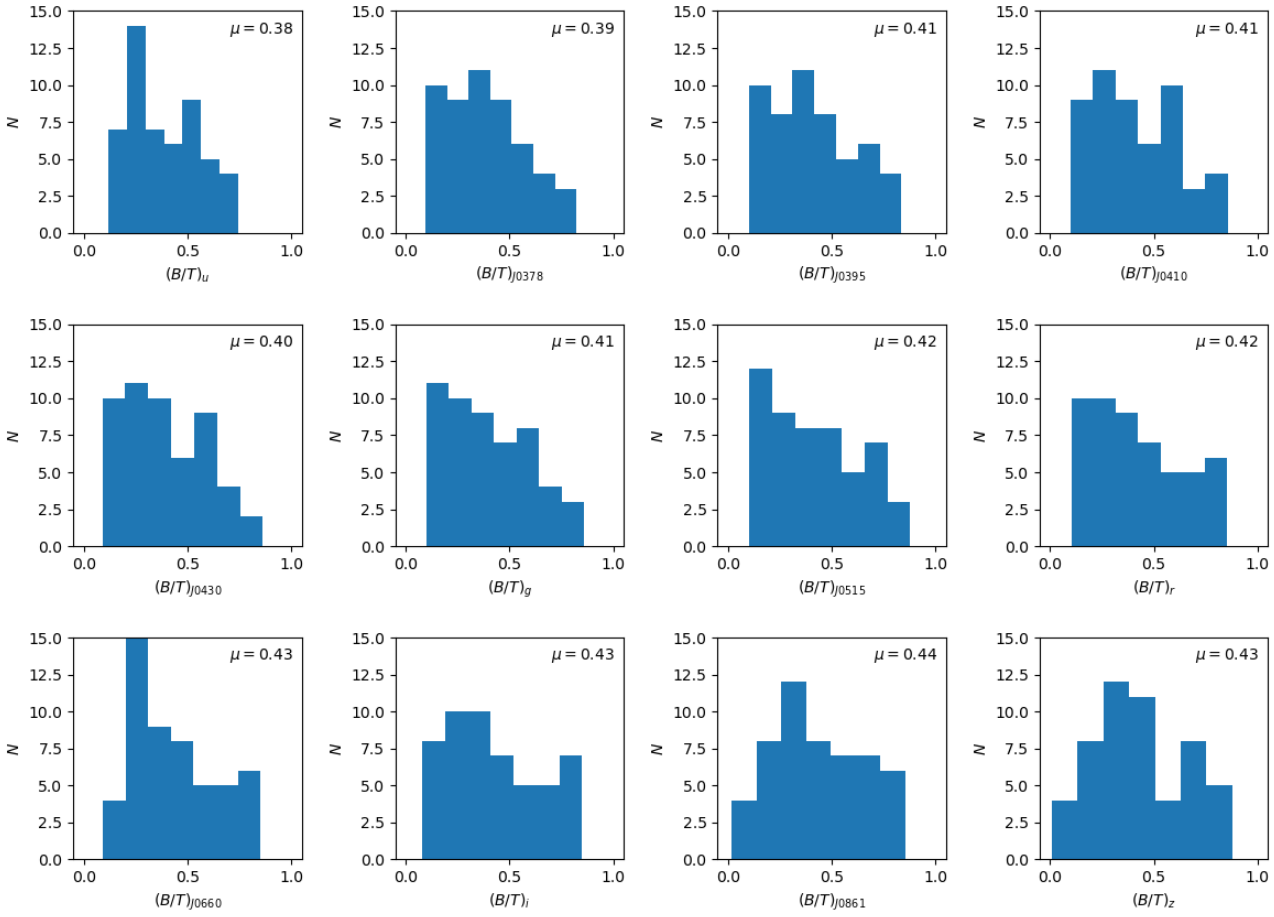

Figure 5.3: B/T histograms for the 12 S-PLUS filters. μ is the B/T median value.

This result may seem surprising due to the fact that the Hydra cluster has a large number of ETGs

and quenched galaxies. However this result is also a consequence of the range of magnitudes of the sample. Fainter galaxies have lower B/T values, and brighter galaxies have higher values of B/T (Head et al., 2014). Figure 5.4 shows the dependence of the $(B/T)_r$ on magnitude. Brighter galaxies have greater (B/T) minimum values. We will discuss these results in the section 5.6.

Table 5.1: Number (N) and percentage (P) of galaxies with $B/T \geq 0.5$ and $B/T < 0.5$ for each S-PLUS filter.

Filter	N ($B/T \geq 0.5$)	P ($B/T \geq 0.5$)	N ($B/T < 0.5$)	P ($B/T < 0.5$)
u	14	27	38	73
*J*0378	15	29	37	71
*J*0395	17	33	35	67
*J*0410	17	33	35	67
*J*0430	17	33	35	67
g	18	35	34	65
*J*0515	19	37	33	63
r	18	35	34	65
*J*0660	19	37	33	63
i	17	33	35	67
*J*0861	19	37	33	63
r	18	35	34	65

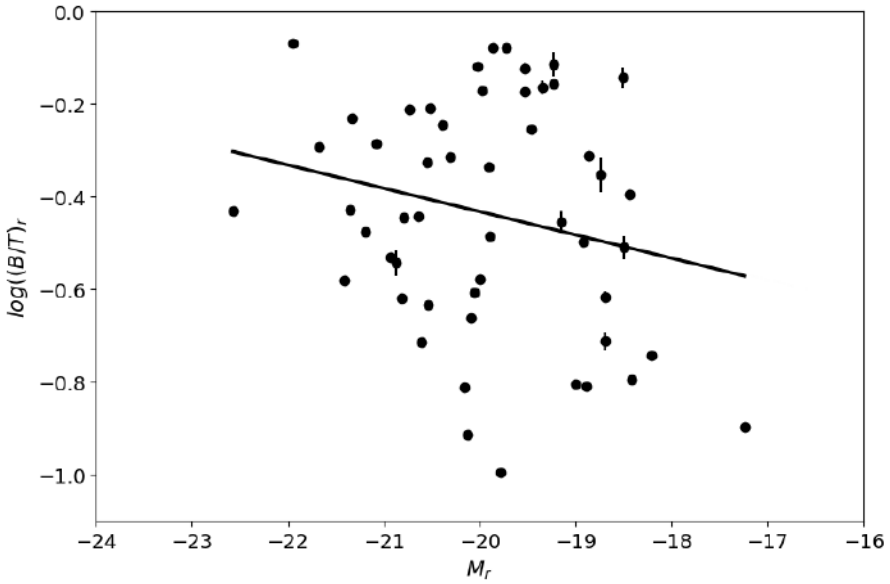

Figure 5.4: The x-axis shows the galaxy's absolute magnitude (*r*-band), and the y-axis shows the $log(B/T)_r$. The black line show the best linear fit, which has a slope of -0.05±0.03.

In the previous Chapter we explored how the Hydra galaxies behave in the $(u-r)$ vs. n_r plane. We

found that galaxies having red colours and large n_r display large stellar masses. Here we show the same plane in Figure 5.5, but now colour-coded by the $(B/T)_r$. Galaxies with low values of $(B/T)_r$ are found at all zones of the $(u-r)$ vs. n_r plane, however, they completely populate the LTGs zone. The galaxies with higher values of $(B/T)_r$ are more concentrated in the ETGs zone [$(u-r) \geq 2.3$ and $n_r \geq 2.5$]. There are no bulge-dominated galaxies in the LTGs zone, and there are only two of them in the transition zone [$(u-r) > 2.3$ and $n_r < 2.5$].

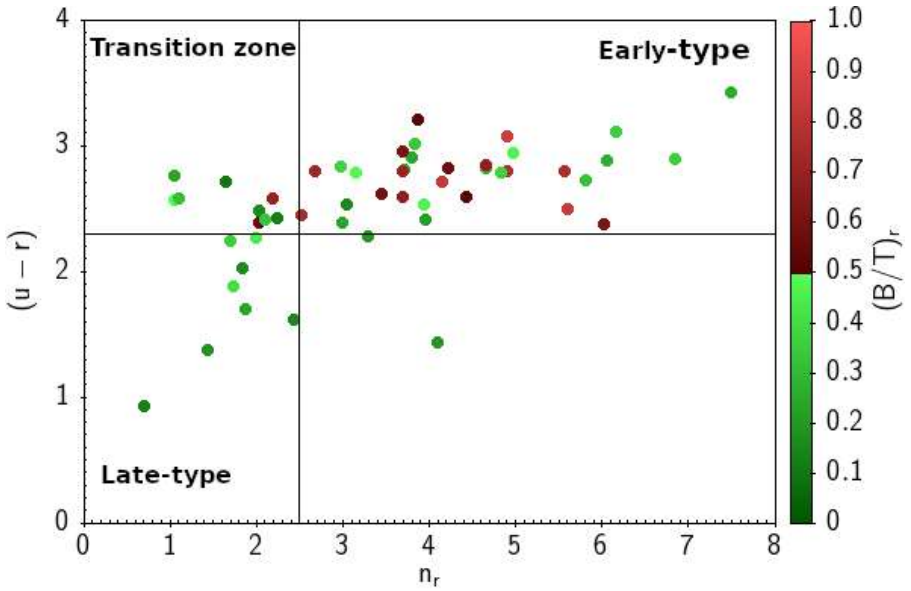

Figure 5.5: The x-axis shows the Sérsic index in the r-band; the y-axis displays the galaxies' $(u-r)$ colour. The colour bar represents the $(B/T)_r$ values of the galaxies. The vertical and horizontal lines are in $n_r = 2.5$ and $(u-r) = 2.3$, respectively.

5.2 Behaviour of n_{bulge} as a function of wavelength

We now explore how the Sérsic index from the bulge is changing with the S-PLUS filters for different types of galaxies. We classify galaxies as: ETGs, LTGs, red and green + blue as in Chapter 4. From the 52 galaxies analysed in this Chapter we classify 8, 33, 10, and 42 as LTGs, ETGs, blue + green, and red galaxies, respectively. A change in the Sérsic index implies a change in the galaxy light profile. Therefore, determining how the Sérsic index from the bulge varies among S-PLUS filters allows us to learn how the different stellar populations of the bulge are distributed (more or less concentrated). Figure 5.6 shows the median of the Sérsic index from the bulge ($\bar{n}_{bulge}$) as a function of the 12 S-PLUS filters for ETGs, LTGs, red, and blue + green galaxies.

The ETGs and red galaxies have the $\bar{n}_{bulge}$ nearly constant from the u to z-band, considering the uncertainties. Also, the ETGs and red galaxies have the $\bar{n}_{bulge}$ almost always greater than 3. The $\bar{n}_{bulge}$ behaves nearly the same for LTGs and blue + green galaxies in the 12 S-PLUS filters, remaining constant from the u-band to the $J0430$-band. After that it has a small drop, and its value starts to rise again. Table 5.2 shows the $\bar{n}_{bulge}$ for the four classes of galaxies.

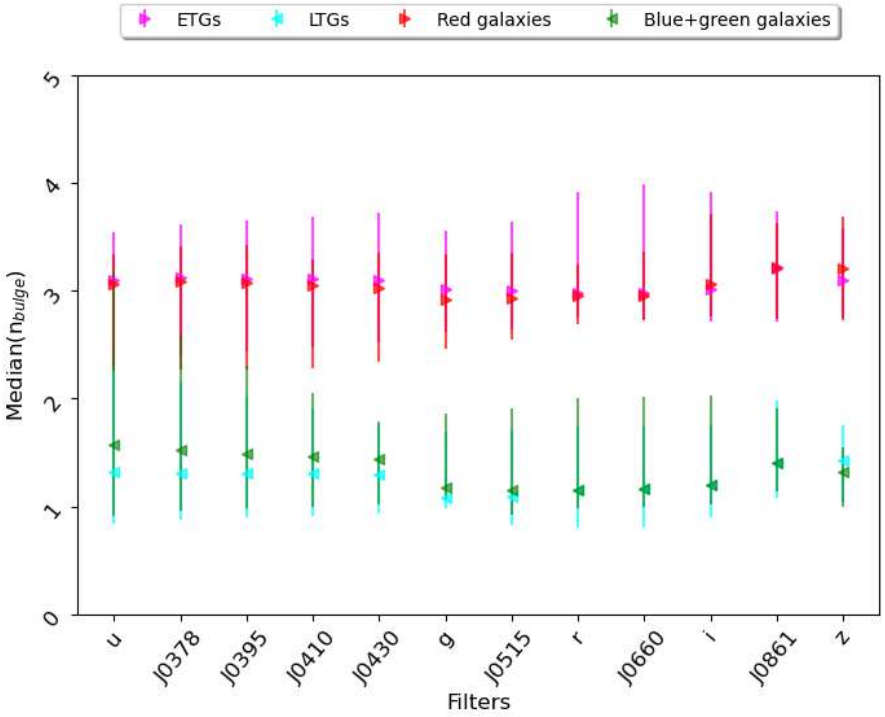

Figure 5.6: Median Sérsic index of the bulges as a function of the 12 S-PLUS filters. Magenta and red symbols represent ETGs and red ($(u-r) \geq 2.3$) galaxies, respectively. Blue and green symbols represent LTGs and blue + green ($(u-r) < 2.3$) galaxies, respectively. The median error was estimated using bootstrapping.

Table 5.2: Median of Sérsic index ($\bar{n}_{bulge}$) of the galaxies per filter. The media's standard error was estimated using Bootstrap with a 95 percent confidence limit.

GALAXIES	$\bar{n}_u$	$\bar{n}_{J0378}$	$\bar{n}_{J0395}$	$\bar{n}_{J0410}$	$\bar{n}_{J0430}$	$\bar{n}_g$	$\bar{n}_{J0515}$	$\bar{n}_r$	$\bar{n}_{J0660}$	$\bar{n}_i$	$\bar{n}_{j0861}$	$\bar{n}_z$
ETG	$3.10\pm^{0.4}_{0.8}$	$3.12\pm^{0.5}_{0.7}$	$3.11\pm^{0.5}_{0.7}$	$3.11\pm^{0.6}_{0.6}$	$3.10\pm^{0.6}_{0.6}$	$3.02\pm^{0.5}_{0.4}$	$3.00\pm^{0.6}_{0.4}$	$2.98\pm^{0.9}_{0.2}$	$2.98\pm^{1.0}_{0.3}$	$3.01\pm^{0.9}_{0.3}$	$3.21\pm^{0.5}_{0.5}$	$3.10\pm^{0.7}_{0.4}$
LTG	$1.32\pm^{1.1}_{0.5}$	$1.31\pm^{0.8}_{0.4}$	$1.30\pm^{0.7}_{0.4}$	$1.30\pm^{0.6}_{0.4}$	$1.29\pm^{0.5}_{0.4}$	$1.08\pm^{0.6}_{0.1}$	$1.09\pm^{0.6}_{0.3}$	$1.15\pm^{0.6}_{0.4}$	$1.16\pm^{0.6}_{0.4}$	$1.20\pm^{0.6}_{0.3}$	$1.40\pm^{0.6}_{0.3}$	$1.43\pm^{0.3}_{0.4}$
RED	$3.06\pm^{0.3}_{0.8}$	$3.09\pm^{0.3}_{0.8}$	$3.07\pm^{0.3}_{0.8}$	$3.05\pm^{0.3}_{0.7}$	$3.02\pm^{0.2}_{0.7}$	$2.92\pm^{0.4}_{0.5}$	$2.93\pm^{0.4}_{0.4}$	$2.96\pm^{0.3}_{0.3}$	$2.95\pm^{0.4}_{0.2}$	$3.06\pm^{0.6}_{0.3}$	$3.22\pm^{0.4}_{0.5}$	$3.20\pm^{0.5}_{0.5}$
BLUE + GREEN	$1.57\pm^{1.6}_{0.7}$	$1.52\pm^{1.1}_{0.6}$	$1.49\pm^{0.8}_{0.5}$	$1.47\pm^{0.6}_{0.5}$	$1.44\pm^{0.3}_{0.4}$	$1.17\pm^{0.7}_{0.1}$	$1.15\pm^{0.8}_{0.2}$	$1.15\pm^{0.9}_{0.2}$	$1.16\pm^{0.9}_{0.2}$	$1.2\pm^{0.8}_{0.2}$	$1.41\pm^{0.5}_{0.3}$	$1.32\pm^{0.2}_{0.3}$

Figure 5.7 shows the relation between the Sérsic index from the single Sérsic profile ($n_{SS,r}$) and that of the bulge ($n_{Bulge,r}$), colour-coded by the $(B/T)_r$ value. We find that the larger the $n_{SS,r}$ value, the larger the $n_{Bulge,r}$ value, although with a large scatter. The best linear fit has a slope of 0.40. It is interesting to note that at a fixed $n_{SS,r}$, galaxies with higher values of $(B/T)_r$ tend to have larger values of $n_{Bulge,r}$, meaning that bulge-dominated galaxies have a more concentrated bulge light profile at a fixed n_{SS}. There are five galaxies marked with an open black square in Figure 5.7 that do not obey the tendency just described. Four of these five galaxies have a bulge much smaller than the disc, in some cases the ratio between the bulge and disc size is ≤ 0.2, and also have a central region much brighter than the disc, thus raising the value of the Sérsic index of the bulge. We found similar results in the 12 S-PLUS filters, which are presented in Appendix C.

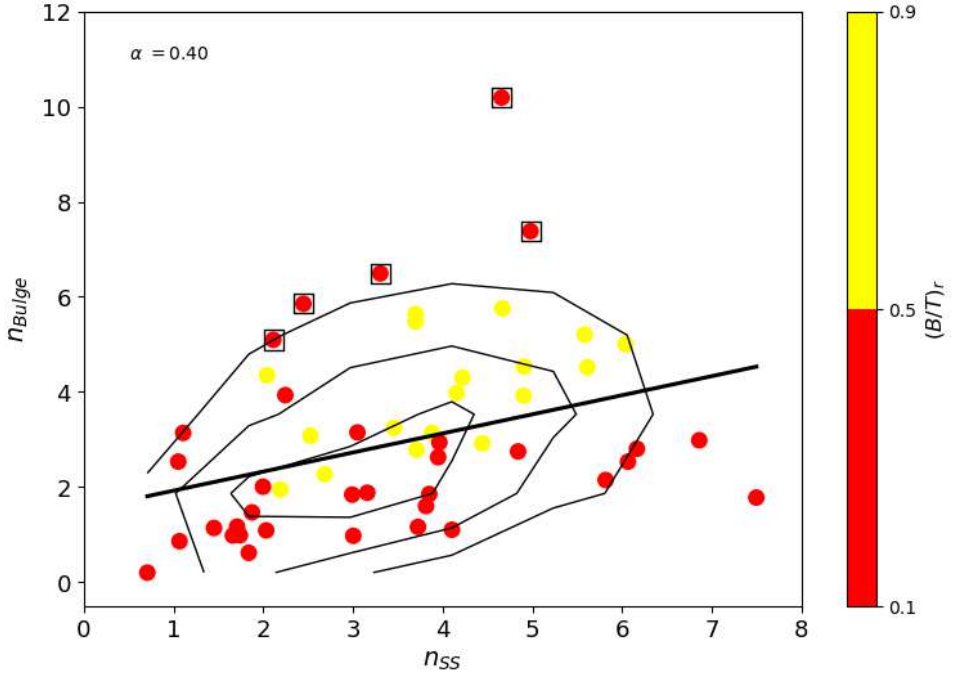

Figure 5.7: $n_{SS,r}$ vs. $n_{Bulge,r}$ plane. Galaxies are colour-coded by their $(B/T)_r$. The black line shows the best linear fit, and the α symbol indicates the slope of the fit. The line contours are the 80th, 50th and 30th percentiles of the respective $n_{SS,r}$ vs. $n_{Bulge,r}$ plane.

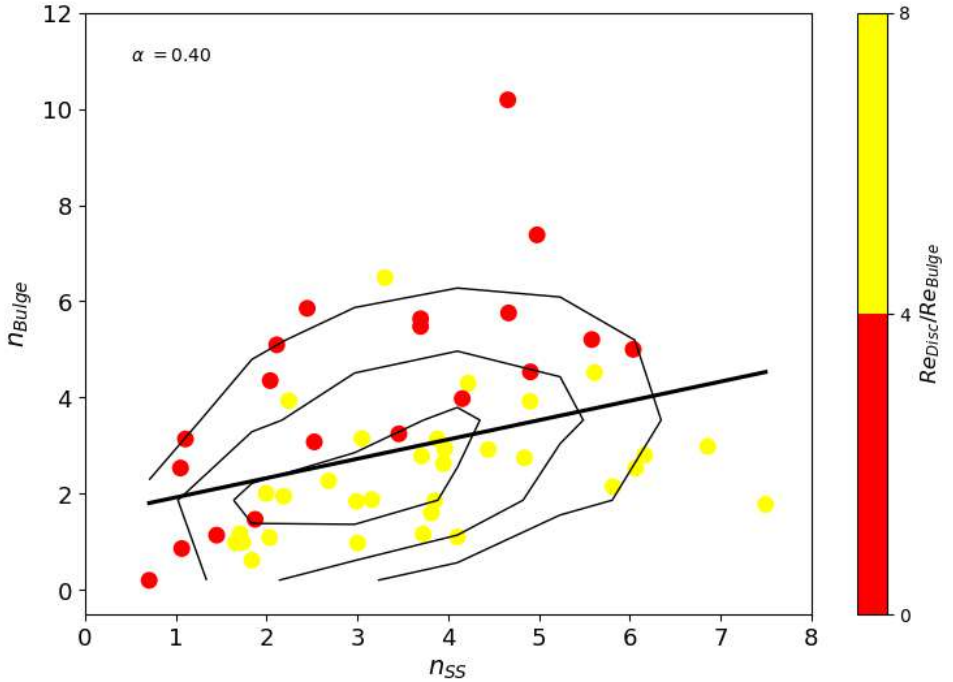

Figure 5.8: Same as Figure 5.7, but now the galaxies are colour-coded by the ratio between the effective radius of the disc to that of the bulge (r-band). The line contours are the 80th, 50th and 30th percentiles of the respective $n_{SS,r}$ vs. $n_{Bulge,r}$ plane.

The ratio between the effective radii of the disc and the bulge, (Re_{Disc}/Re_{Bulge}), indicates how big the

disc compared to the bulge is. Figure 5.8 shows the same $n_{SS,r}$ vs. $n_{Bulge,r}$ plane, but the galaxies are now colour-coded by the Re_{Disc}/Re_{Bulge} ratio. The colour bar saturates at Re_{Disc}/Re_{Bulge} = 8, thus all galaxies that have $Re_{Disc}/Re_{Bulge} \geq 8$ are in yellow. We can see that at a fixed n_{SS}, galaxies with higher values of Re_{Disc}/Re_{Bulge} also have lower values of $n_{Bulge,r}$, meaning that the bigger the effective radius of the disc compared to that of the bulge is, the less concentrated the bulge profile is at a fixed n_{SS}.

5.3 Mass-size Relation

The mass-size relation relates the stellar mass with the effective radius of galaxies. It is a useful tool to analyse galaxy evolution, since the morphological properties of galaxies are related to their formation and interactions. The latter, in the case of galaxies in a cluster, can happen with other galaxies, with the host cluster potential or with both. Figure 5.9 shows the mass-size relation for the 81 Hydra's galaxies analysed in Chapter 4. The galaxy effective radius was estimated in the *r*-band to better compare with other works. We find that galaxies with a higher stellar mass have a larger effective radius. We note that the other S-PLUS filters show the same behaviour seen in Figure 5.9, with only a difference in the slope of this relation such that the mass-size relation slope increases towards redder bands, changing from 0.12±0.05 to 0.21±0.04 from filter *u* to *z*. The mass-size relation for all 12 S-PLUS filters is shown in Appendix D.

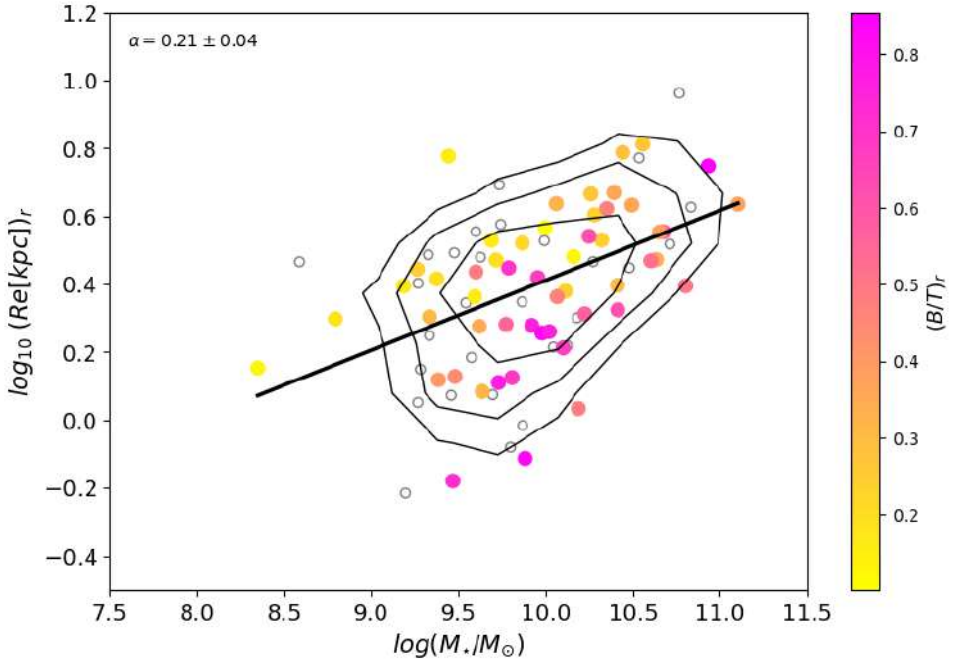

Figure 5.9: Mass-size relation: The x-axis shows the galaxy stellar mass, and the y-axis shows the effective radius. The galaxies are colour-coded by the $(B/T)_r$. The open circles are the galaxies that do not meet the defined criteria for a reliable fit for a galaxy with two components. The black line shows the best linear fit to the 81 galaxies studied in Chapter 4, and the α symbol indicates the slope of the fit. The line contours are the 80th, 50th and 30th percentiles of the respective mass–size distribution.

The galaxies in Figure 5.9, for which a reliable bulge-disc decomposition was made, are colour-coded

by the $(B/T)_r$. We find that at fixed stellar mass, galaxies with lager $(B/T)_r$ are more compact. These galaxies are more compact because they have the same stellar mass in a smaller size. Figure 5.10 is the same as Figure 5.9, but now colour-coded with respect to the galaxy $(u-r)$ colours. For galaxies with $\sim 9.5 \leq log_{10}(M_\star/M_\odot) \leq 10.3$, we find that, at a fixed stellar mass, redder galaxies are generally smaller than bluer galaxies. In addition, it seems that galaxies with different colours have different mass-size relations. The mass-size relation for the redder galaxies is shifted with respect to the relation for bluer galaxies, mostly due to the differences in stellar masses for these different types of galaxies. We will discuss the implications of these results in subsection 5.6.

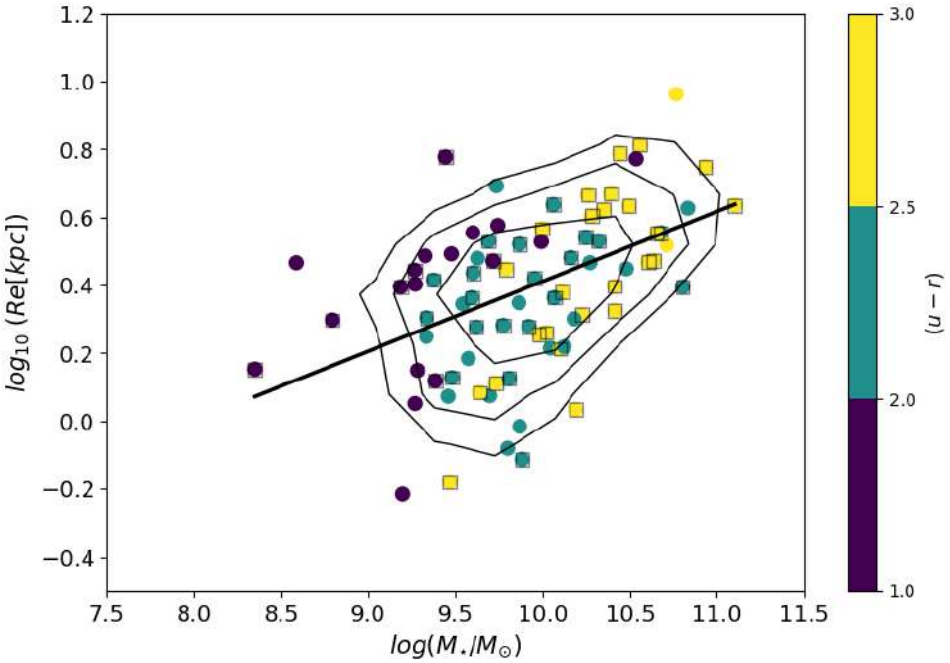

Figure 5.10: Same as Figure 5.9, but symbols now are colour-coded by the galaxy $(u-r)$ colour. This image shows the 81 galaxies used in the previous Chapter. Enclosed by a black open square are the 52 galaxies used in this Chapter.

In what follows we now investigate the mass-size relation, in the *r*-band, of the galactic components separately. We want to examine the variation of the physical sizes of bulge and disc with respect to the galaxy stellar mass, and their connection with the galaxy size growth. Figure 5.11 shows the mass-size relation for the bulge and disc where the galaxies are colour-coded by their $(B/T)_r$. While the bulge's effective radius shows no dependence on the stellar mass of the galaxies, the disc's effective radius has a dependence on the stellar mass of the galaxy, being this larger for galaxies with higher stellar masses. The best linear fit has a slope of 0.18. We saw in Figure 5.9 that the effective radius for the whole galaxy increases with the galaxy stellar mass. Apparently, the galaxy's disc is responsible for this phenomenon. The galaxy absolute magnitude is a proxy for the galaxy stellar mass, then the M_r vs. $log(R_e)$ plane is similar to the mass-size relation. Figure 5.12 shows that plane, where the effective radius of the disc increases towards brighter galaxies, and the bulge's effective radius has no dependence on the absolute magnitude of the galaxy. Additionally, we did not find any relation between $(B/T)_r$ and the components' mass-size relation. The mass-size relation for the galaxies' components in all 12 S-PLUS filters is shown in Appendix D.

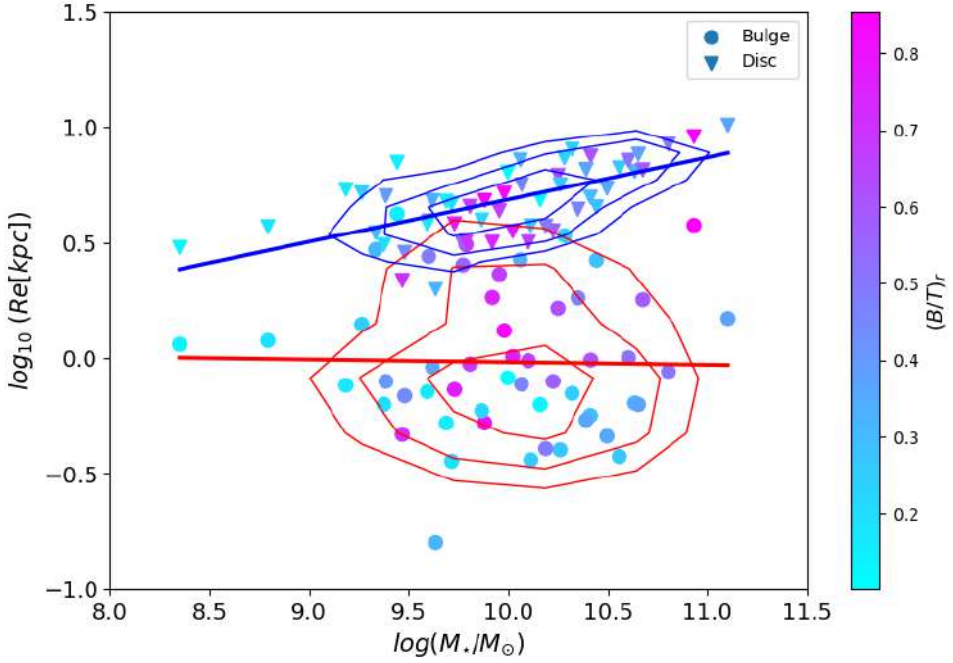

Figure 5.11: Mass-size relation: The x-axis shows the galaxy stellar mass, and the y-axis shows the effective radius from the bulge and disc. The blue and red lines show the best linear fit for the disc and bulge, respectively. The galaxies are colour-coded by the $(B/T)_r$.

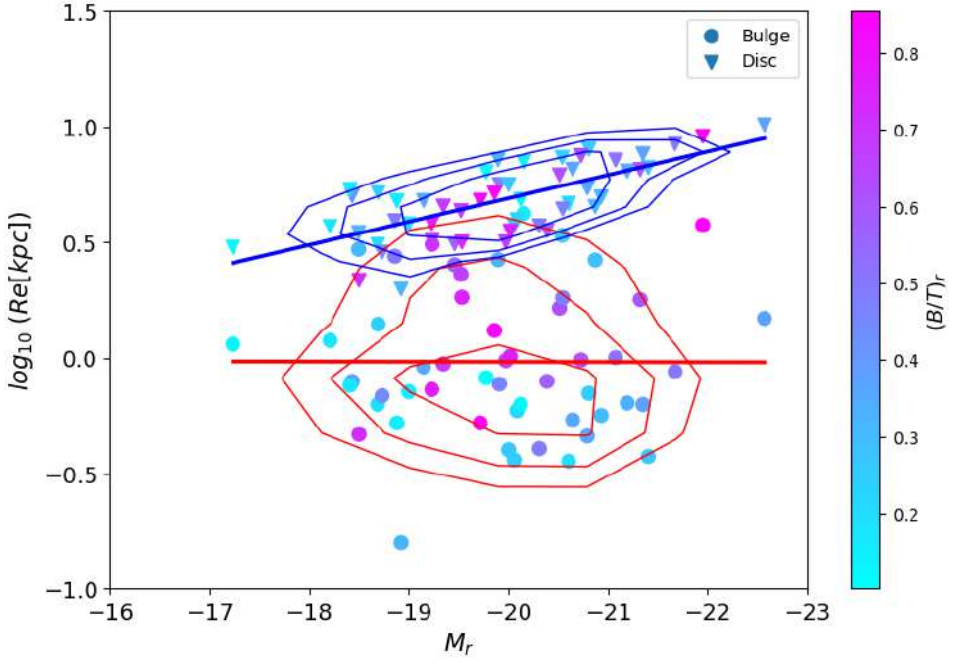

Figure 5.12: The x-axis shows the absolute magnitude in the r-band, and the y-axis shows the effective radius from the bulge and disc. The blue and red lines show the best linear fit for the disc and bulge, respectively. The galaxies are colour-coded by the $(B/T)_r$.

5.4 Colour environmental dependence

In this section we explore the colours of the galaxies as a whole and the colours of the bulge and disc component, and determine whether there is any colour relation with the environment. Figure 5.13 shows the $(u-r)$ colour versus R/R_{200} for the bulge, disc and galaxy. R/R_{200} is the projected distance from the cluster centre. We divide R_{200} into 5 bins, and the median $(u-r)$ colour was estimated in each bin. The best linear fit to the median $(u-r)$ shows that the galaxy, bulge and disc have a small drop in colour, becoming bluer at greater distances from the cluster centre. The slopes are: -0.38±0.28, -0.44±0.17 and -0.47±0.11 for the bulge, disc, and galaxy, respectively. This is not an unexpected result because galaxies that are closer to the centre of the cluster will be more affected by environmental processes, such as harassment, tidal truncation, ram pressure, and starvation.

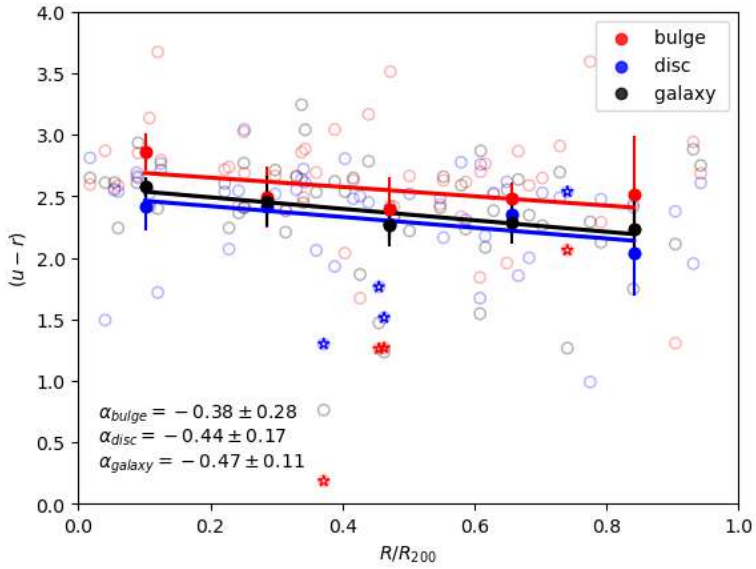

Figure 5.13: $(u-r)$ colour versus R/R_{200} for the bulge (red), disc (blue) and galaxy (black). The open circles are the $(u-r)$ colour for each galaxy and galaxy component. The filled circles are the median $(u-r)$ value in each of the 5 R/R_{200} bins. A linear regression was performed in the median $(u-r)$, and the slope (α) of the linear regression is displayed in the graph. The error bars are the standard error of the median, $1.253\sigma/\sqrt{N}$, where N is the number of objects. The star symbols represent the components of star-forming galaxies.

All these phenomena mentioned previously accelerate the process by which a galaxy stops forming stars, and as a consequence it turns redder, as well as its components (see Figure 5.2). Even so, it is possible to find blue galaxies (Hudson et al., 2010) and/or components (Head et al., 2014) closer to the cluster centre. In the case of this Thesis there are only two discs inside $\sim 0.37R_{200}$ that have $(u-r) < 2$ colours. The reddest discs $[(u-r) > 2.7]$ are located closer to the cluster centre (inside $0.6R_{200}$). There is no preferred location to find the redder bulges. However, the few bluer bulges $[(u-r) < 2.3]$ are beyond $\sim 0.37R_{200}$.

The galaxy's projected local density (Σ_{10}) was estimated in the previous Chapter. Figure 5.14 shows how the colour $(u-r)$, from the bulge, disc and the whole galaxy, changes with respect to the Σ_{10}. The disc median colour remains nearly constant at all densities. However, the bulge and the whole

galaxy becomes redder at higher densities. The bulges show a more accentuated difference in colour. The slopes are: 0.30±0.08, 0.08±0.09 and 0.11± 0.11 for the bulge, disc and galaxy respectively.

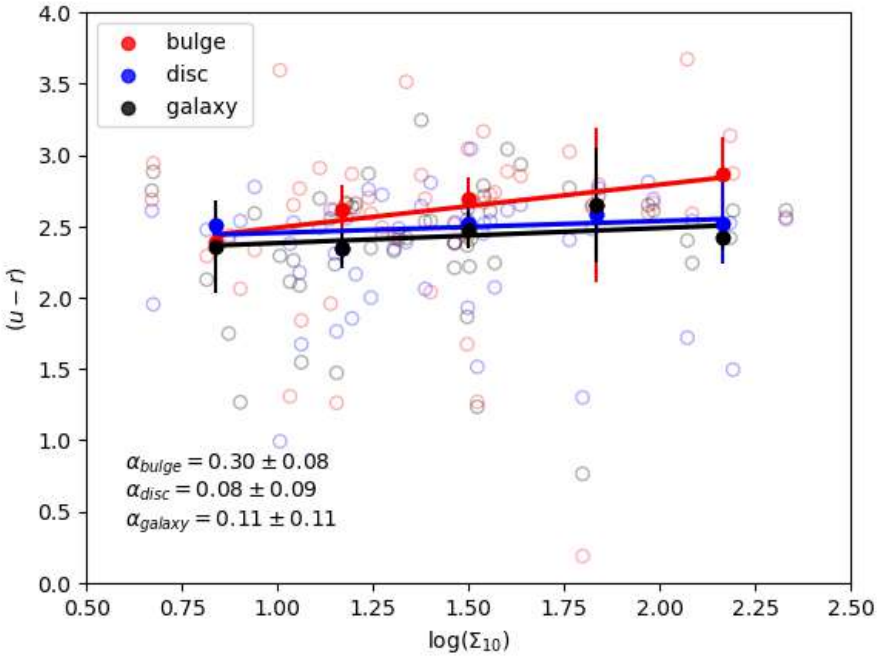

Figure 5.14: $(u-r)$ colour versus $log(\Sigma_{10})$ for the bulge (red), disc (blue) and galaxy (black). The open circles are the $(u-r)$ colour for each galaxy and galaxy component. The filled circles are the median $(u-r)$ value in each of the 5 bins in $log(\Sigma_{10})$. A linear regression was performed in the median $(u-r)$, and the slope (α) of the linear regression is displayed in the graph. The error bars are the standard error of the median, $1.253\sigma/\sqrt{N}$, where N is the number of objects.

In Chapter 4 we found a group of galaxies that apparently is falling recently in Hydra. In this group there are two galaxies that are SFG, but unfortunately these galaxies do not meet the criteria used in this Chapter ($0.1 < B/T < 0.9$, $Re_{disc} > Re_{Bulge}$, and $\chi^2 \geq 1.9$). However, there are four galaxies that are SFGs and meet the criteria used in this Chapter. These galaxies are enclosed by open stars in Figure 5.13. An interesting result is that for these four galaxies the bulge is bluer than the disc, meaning that the star formation is taking place in the central region of the galaxy. The sizes of the bulges (discs) of the four SFGs, from the nearest to the farthest clustercentric distance, are: 1.1 (3.0), 4.2 (7.0), 1.19 (3.7) and 0.36 (4.6) kpc. Thus, the bulges represent a small region in these galaxies. We will discuss these results in section 5.6.

5.5 Dressler–Schectman test: galaxy properties

We performed a DST in the previous Chapter, and found that Hydra is close to virialization, although it still has some perturbation. We know that the greater the δ (hereafter δ_{DST}), from the DST, the higher the probability that the galaxy belongs to a substructure. Then it is interesting to investigate how the properties of galaxies behave in regions that most likely have a substructure.

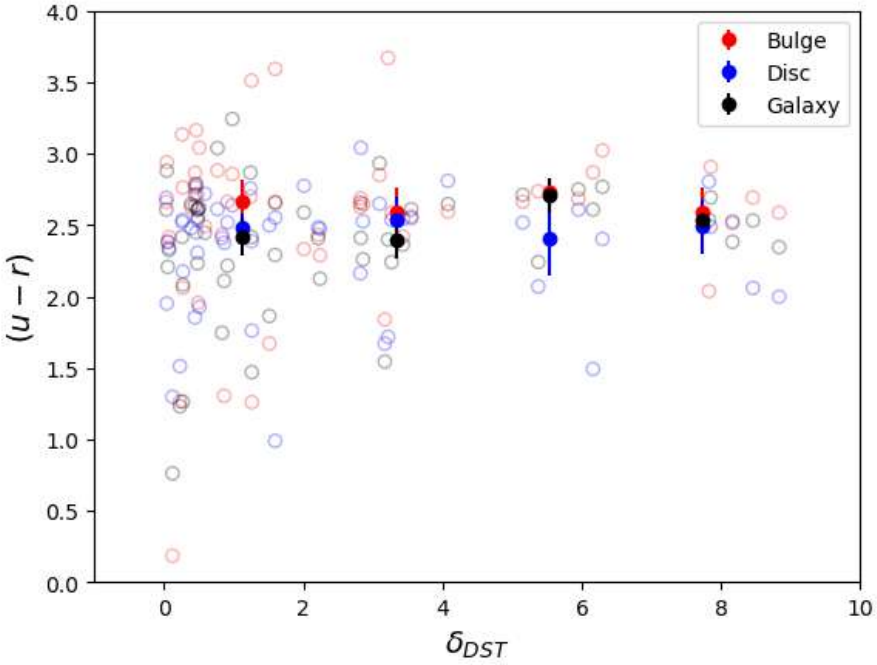

Figure 5.15: $(u-r)$ versus δ_{DST} for the bulge (red), disc (blue) and galaxy (black). The filled circles are the median $(u-r)$ value in 4 δ_{DST} bins. The open circles are the colours and δ_{DST} of each galaxy and its components individually. The error bars are the standard error of the median, $1.253\sigma/\sqrt{N}$, where N is the number of objects.

Figure 5.15 shows the $(u-r)$ colour versus δ_{DST}. We divide δ_{DST} into 4 bins, and the median $(u-r)$ colour was estimated in each bin. The median $(u-r)$ colour, for both galaxies and their components, do not show much difference with respect to δ_{DST}. There are no blue galaxies or components in the highest δ_{DST} bin. Thus, we find that galaxies and their components can be red o blue in regions with lower probability to belong to a substructure (low δ_{DST}), whereas galaxies and components that are in regions with high probability to belong to a substructure (high δ_{DST}) are red. This suggests that probably those galaxies in high δ_{DST} have suffered an environmental quenching process, in which galaxies in groups (or substructures) are preprocessed (Joshi et al., 2017). However, this analysis was done using the 52 galaxies studied in this Chapter. When this same graph is made using the 81 galaxies from Chapter 4, we found that there are 2 blue galaxies in the region of high δ_{DST}. Figure 5.16 shows this result, where galaxies are colour-coded by the Sérsic index from the single Sérsic profile. In this figure, the star symbols represent star-forming galaxies, and galaxies enclosed by an open black square are those that belong to a substructure, as discovered in Chapter 4. Figure 5.16 shows an interesting result, most star-forming galaxies are in low δ_{DST} regions. However, the fraction (8/48) of star-forming galaxies with respect to quenched galaxies in the first δ_{DST} bin (lowest δ_{DST}) is the same as this fraction (2/12) in the highest δ_{DST} bin. One plausible scenario to explain the existence of these 2 SFGs in the substructure is that tidal interactions could be inducing star formation (Byrd & Valtonen, 1990, Moss et al., 1998). For our sample of Hydra' galaxies, we conclude that a region with a high probability of belonging to a substructure is dominated by quenched galaxies. However, due to galaxies interactions, these regions also have a few star-forming galaxies.

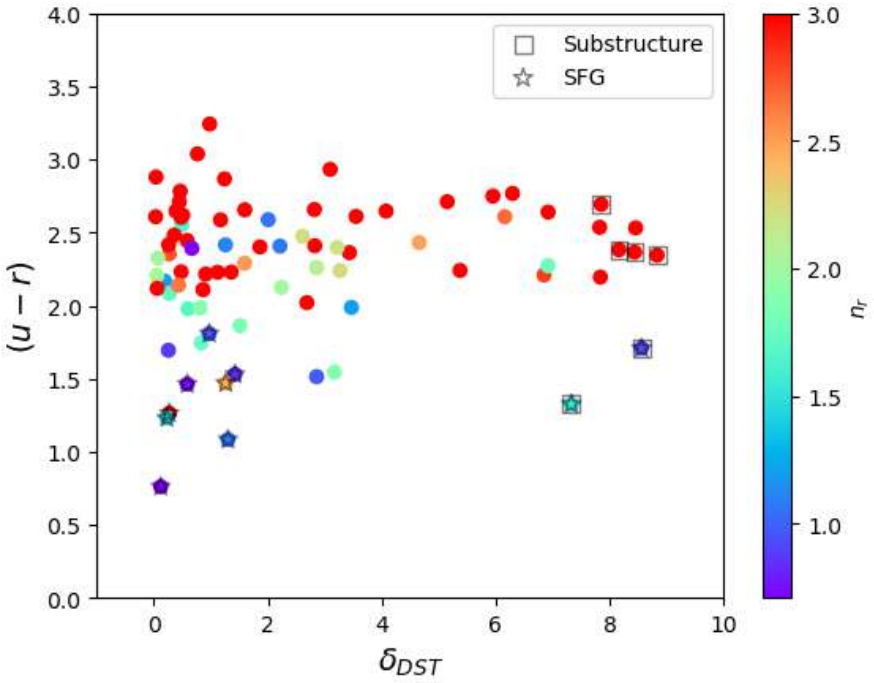

Figure 5.16: Same as Figure 5.15, but now for the 81 galaxies analysed in Chapter 4. The star symbols represent star forming galaxies. Galaxies enclosed by an open black square are those that belong to a substructure, as discovered in Chapter 4. The galaxies are colour-coded by the Sérsic index from the single Sérsic profile.

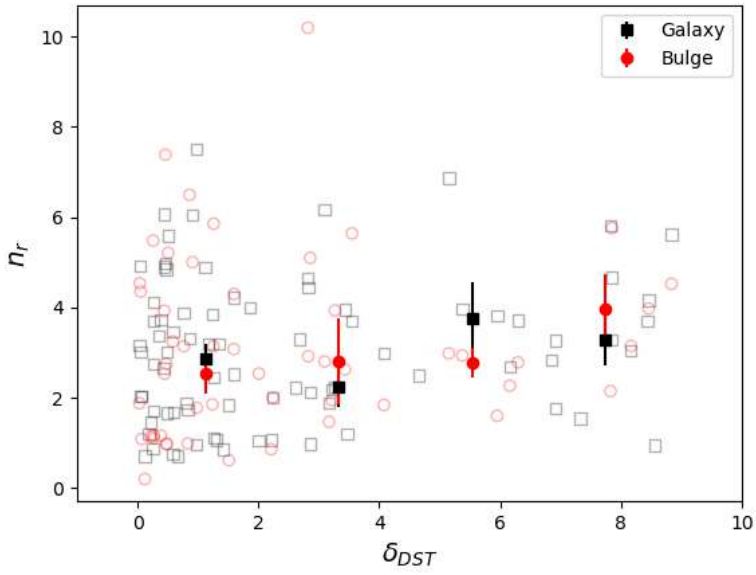

Figure 5.17: n versus δ_{DST} for the bulge and the whole galaxy in the r-band. The open squares represent the 81 galaxies from Chapter 4. The open circles represent the 52 bulges studied in this Chapter. The filled circles are the median n value in 4 δ_{DST} bins. The error bars are the standard error of the median, $1.253\sigma/\sqrt{N}$, where N is the number of objects.

Figure 5.17 shows the plane n_r versus δ_{DST} for the bulge ($n_{Bulge,r}$) and the whole galaxy ($n_{SS,r}$). We will show here the results only for the r-band. However, the other S-PLUS bands show the same

trends as the r-band. We divide δ_{DST} into 4 bins, and the median n was estimated in each bin. The median $n_{SS,r}$ and $n_{Bulge,r}$ show an increase of ∼30 and ∼37 percent, respectively, from the lowest to the highest δ_{DST} bin. Galaxies and bulges show a larger range of n_r values in regions with low probability to belong to a substructure. However, towards higher values of δ_{DST}, n_r starts to show bigger minimum values. Beyond the second δ_{DST} bin n_r is always greater than ∼1.6 for the bulge. There are some galaxies with low n_r values in all δ_{DST}.

Figure 5.18 shows the B/T versus δ_{DST} plane for the u, r and z bands. The median values, as a function of δ_{DST}, were estimated as described for Figure 5.15. The median B/T shows an increase of ~ 45 (u-band), ~ 47 (r-band), and ~ 46 (z-band) percent from the lowest value bin to the highest value bin of δ_{DST}. However, for all δ_{DST} bins the B/T shows a large range of values.

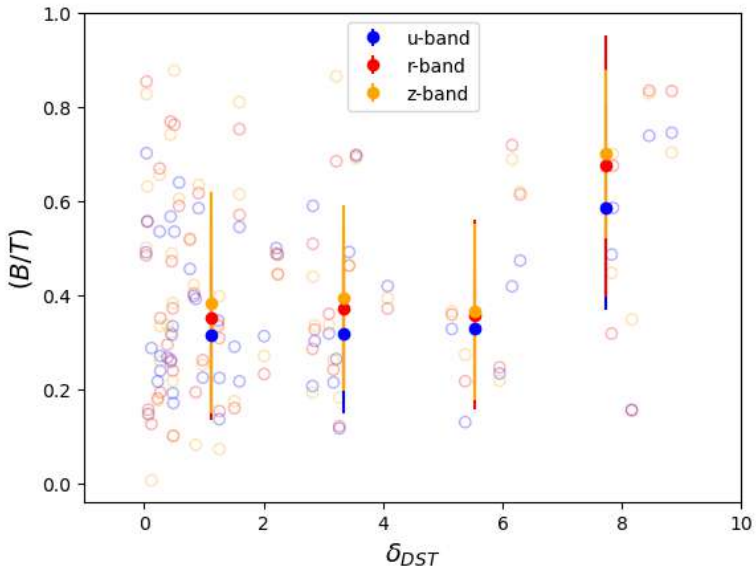

Figure 5.18: B/T versus δ_{DST} for the u-band (blue), r-band (red) and z-band (orange). The filled circles are the median n value in 4 δ_{DST} bins. The open circles represent the B/T values, for the 52 galaxies, in the u (blue), r (red) and, z (orange) bands. The error bars are the standard error of the median, $1.253\sigma/\sqrt{N}$, where N is the number of objects.

5.6 Discussion

In this Chapter, we investigated the behaviour of the physical (colour) and structural (Sérsic index, effective radius, and B/T) properties of the bulge and disc components of Hydra galaxies, as well as their relation with the general properties of the galaxies analysed in Chapter 4. We aimed to examine the properties' variations with respect to the 12 S-PLUS bands and the cluster environment (cluster-centric distance and density).

There exists a relationship between the B/T and absolute magnitude of a galaxy, such that brighter galaxies have higher B/T values (Head et al., 2014), which we also found in Figure 5.4. It is important to keep this in mind that the cut in magnitude we made in our sample can influence the percentage of galaxies that are bulge dominant ($B/T \geq 0.5$). The sample of galaxies analysed here are brighter than $M_r \leq$ -17.5. By studying 192 galaxies in clusters, Barsanti et al. (2021a) found a median $(B/T)_r = 0.52$ (for galaxies with $M_\star > 10^{10} M_\odot$) that is a larger value than our finding for Hy-

dra galaxies (B/T_r= 0.42±0.04). However, Christlein & Zabludoff (2005), studying 1637 galaxies from six nearby clusters (where $\sim$ 80 percent of the galaxies are brighter than $M_R \leq$ -19.2) including the Hydra cluster (A1060), found a median B/T value of 0.36, where 33 percent of the galaxies have $B/T > 0.5$ (R-band). This result is in agreement with what we found in this Thesis, which is that 35 percent of the galaxies are bulge-dominated. We found disc-dominated galaxies in all regions of the $(u-r)$ versus n_r plane. However we do not found bulge-dominated galaxies in the Late-type zone. This result is in agreement with Hudson et al. (2010), who found that the higher the B/T value is, the redder the galaxy's components are. Therefore, the galaxies that are bulge-dominated should occupy the zone of Early-type galaxies (see Figure 5.5).

The mass-size relation of the Hydra's galaxies shows interesting results: at a fixed stellar mass, smaller galaxies have higher values of B/T. This means that smaller galaxies are more compact and have a more spherical shape. These galaxies are more compact because they have the same stellar mass in a smaller size. Additionally, at a fixed stellar mass the most compact galaxies are redder, within the $\sim 9.5 \leq log_{10}(M_\star/M_\odot) \leq 10.3$ range. Apparently, the compact galaxies are older (red colour). Similar results have already been found, since at a fixed stellar mass quenched galaxies (associated with red colour) are smaller than star-forming galaxies (associated with blue colours) (Whitaker et al., 2017, Matharu et al., 2019, Nedkova et al., 2021). This behaviour can be related to the influence of the environment on these galaxies, the ram-pressure stripping of the cold gas is making quenched galaxies more compact (Kuchner et al., 2017).

By studying galaxies from the Coma cluster, Gutiérrez et al. (2004) found that the scale length of the disc in those galaxies is 30 percent smaller than that in spiral galaxies in the field, and they conclude that this may be evidence of environment-driven evolution. We found a relation between the disc size and the galaxy stellar mass: galaxies with a higher stellar mass have a larger disc effective radius. We did not find a relation between the bulge's effective radius and the galaxy stellar mass. A similar trend was found between the sizes of the different components and the galaxy's absolute magnitude (see Figure 5.12). Head et al. (2014) found that the bulge's effective radius of early-type galaxies in the Coma cluster does not depend on the magnitude of the galaxies, being in agreement with the result found in this Thesis. However, other studies of field galaxies found that the bulge's size increases with the galaxy stellar mass. Méndez-Abreu et al. (2021), studying field galaxies, found that the bulge and the disc effective radius increases toward higher stellar masses. Our result might be, then, an environmental consequence.

We found that the bulges, in general, are redder than the discs, with a median $(u-r)$ colour offset of 0.17 mag. Also $\sim$ 36 percent of the galaxies have a bulge bluer than the disc, meaning that some galaxies have a younger stellar population in their central region. A similar result was found by Barsanti et al. (2021b), by studying a sample of cluster galaxies inside $1R_{200}$, who concluded that $\sim$ 34 percent of the galaxies have significantly younger bulges than discs, and $\sim$ 33 percent of the bulges are bluer than the discs. We also found that the bulge, disc and galaxy $(u-r)$ colours become bluer at larger distances from the cluster centre. This result is in agreement with Head et al. (2014) who studied early-type galaxies in the Coma cluster, and found that the bulge and the disc colours of those galaxies also show a slightly drop with respect to the clustercentric distance. However, Barsanti et al. (2021a) found that the bulge colour does not correlate with the environment, although the disc's colour does. Hudson et al. (2010) found a similar result to Barsanti et al. (2021b), where bulge colours are insensitive to the environment, although both studies found a dependence on the colour of the disc with the distance to the centre of the cluster. We also found that the bulge, disc and the whole galaxies

become redder at higher densities. However, the slope of the best linear fit, between the $(u-r)$ colour and the local density, is less steep than the slope of the fit between the colour and the clustercentric distance. Then, the $(u-r)$ colour of the galaxy and its components depends more on the distance to the cluster centre than on the local density.

Generally, after the galaxy falls into a cluster it stops the star formation during its first passage (Lotz et al., 2019). However, due to the pressure exerted by the intracluster medium (ICM) some galaxies can enhance their star formation (Tonnesen & Bryan, 2009). This is probably because the ram pressure from the ICM causes the collapse of dense molecular clouds (Byrd & Valtonen, 1990). Moss et al. (1998) studying the cluster Abell 1367 concluded that compact Hα emission in galaxies is a result of tidally induced star formation, which causes a burst of star formation in the centre of the galaxy, instead of in the outskirt. The interaction could be galaxy-galaxy or galaxy-cluster probably, and the central part of the galaxy is fuelled by disc gas inflow to the nuclear regions (Byrd & Valtonen, 1990). In addition, a study performed by Koopmann et al. (2006) in the Virgo Cluster, found that galaxies in the cluster have a smaller Hα profile when compared to field galaxies, with possibly enhanced activity in the inner discs, and in the galaxy centre. In this Chapter we performed a bulge-disc decomposition for 4 SFGs. All these galaxies have the colour of the bulge bluer than that of the disc, meaning that the star formation is more concentrated in the central part of these galaxy. Indeed 3 of the 4 galaxies have a small bulge effective radius of 1.1, 1.2 and 0.36 kpc. We believe that these four SFGs in Hydra, which all have $M_\star < 10^{9.7} M_\odot$, are going through an outside-in quenching process, where star formation stops first in the outermost parts of the galaxy, but it currently happens in the most central region. This is in agreement with Bluck et al. (2020), who studied low mass satellite galaxies ($M_\star < 10^{9.5}\ M_\odot$) and found evidence of an outside-in quenching process.

5.7 Summary and Conclusions

In this Chapter, we have performed, for the first time, a bulge–disc decomposition of Hydra galaxies simultaneously using the 12 S-PLUS bands. The galaxies were modeled with a free Sérsic profile for the bulge, and an exponential profile for the disc. We used the MEGAMORPH-GALAPAGOS2 project to estimate the structural (Sérsic index and effective radius) and physical (magnitudes) properties of 81 Hydra's galaxies. Only 52 of these galaxies meet the required criteria for a reliable fit for a galaxy with two components ($0.1 < B/T < 0.9$, $Re_{disc} > Re_{bulge}$, and $\chi^2 \geq 1.9$). Then, the results shown here are based on the sample of 52 galaxies. The MEGAMORPH-GALAPAGOS2 project has the advantage of using GALFITM, which, by performing simultaneous multiwavelength bulge-disc decomposition increases the accuracy of the estimated parameters.

Our main findings and conclusions are:

1) The discs are generally bluer than the bulges. The median $(u-r)$ offset separating the colour distributions of the bulges and discs is 0.17 mag. However, there are some galaxies ($\sim$ 36 percent) that have a bulge bluer than the disc. Also, the bulge, disc, and the whole galaxy become redder with local density and to the central part of the cluster, being in agreement with other works. The colour of the bulge, disc, and the whole galaxy are more affected by the clustercentric distance than the local density.

2) Using the 12 S-PLUS bands we found that the median (B/T) grows slightly towards the red-

der filters, and most of the bulge-dominated galaxies ($B/T_r \geq 0.5$) are located in the ETGs zone [$(u-r) \geq 2.3$ and $n_r \geq 2.5$] of the n_r vs. $(u-r)$ plane.

3) ETGs and red galaxies have a similar median Sérsic index for the bulge ($\bar{n}_{Bulge}$), remaining approximately constant among the filters u to z considering the uncertainties. The LTGs and blue + green galaxies have the same behaviour as the ETGs and red galaxies in the filters, remaining nearly constant. However the $\bar{n}_{Bulge}$ for LTG and blue + green galaxies are always lower than $\sim$1.6.

4) Analysing the $n_{SS,r}$ vs. $n_{Bulge,r}$ plane, we found that galaxies with higher values of $n_{Bulge,r}$ have larger values of $(B/T)_r$, at a fixed $n_{SS,r}$. Also galaxies with larger values of $n_{Bulge,r}$, at a fixed $n_{SS,r}$, are more compact.

5) We found a clear galaxy mass-size relation in the 12 S-PLUS filters, and the slope of this relation increases towards redder filters. This mass-size relation shows that, at a fixed stellar mass, galaxies with higher values of $(B/T)_r$ are more compact (have low values of effective radius). Additionally, at a fixed stellar mass, redder galaxies are more compact. Then, it is very likely that the same mechanisms that is quenching the galaxies is also causing its compaction. The bulge's effective radius does not show a dependence on the galaxy stellar mass and the absolute magnitude, however the disc shows an increase in size towards larger stellar masses and lower magnitudes. Thus, it is likely that, for cluster galaxies, the disc component is yielding the galaxy mass-size relation.

6) Analysing the properties of galaxies with respect to the δ_{DST} parameter, we found that the median value of n_{SS}, n_{Bulge}, and $(B/T)_r$ show an increase of ~ 30, ~ 37, and ~ 47 percent, respectively, from the lowest to the highest δ_{DST}. Additionally, the median $(u-r)$ colour for the galaxy and its components do not show much difference with respect to δ_{DST}. We also found that the regions with the high probability of belonging to a substructure are dominated by quenched galaxies. However, due to galaxy interactions, these regions also have a few star-forming galaxies.

7) The star formation, in the 4 star-forming galaxies, is probably concentrated in the centre of the galaxies. Three of these have the effective radius of the bulge smaller than 1.2 kpc (r-band). It is very likely that their star formation is being caused by tidal interaction. In addition, these galaxies are most likely suffering ram pressure stripping and/or harassment events, that could stop the galaxy star-formation from the outside-in, known as outside-in quenching process (Bluck et al., 2020), which will lead the galaxy to become quenched.

6 Summary

The properties of a galaxy reveals its formation and evolution through internal processes and also reflect the external processes that a galaxy has experienced. As an example, the colour gradient of a galaxy can be used to understand its evolution, i.e., when a galaxy has its central region bluer than the outermost region this could be an indication of an outside-in quenching process (Bluck et al., 2020). Thus, modeling the galaxy's light profile can give us clues about its formation and evolution, since elliptical and spiral galaxies have different light profiles, as well as faint and bright galaxies (Peng et al., 2010a, Vika et al., 2014, Vulcani et al., 2014, Vika et al., 2015, Kadowaki et al., 2021). Furthermore, each part of the electromagnetic spectrum reflects different physical phenomena that are occurring in a galaxy: young and hot stars are well observed in the u-band; old and cold stars, in the redder filters. Therefore, analysing the galaxy's light profile in different filters is also a unique opportunity to understand the contribution of different stellar populations have on a galaxy. Additionally, it is already well established that the environment in which galaxies reside plays a role in their evolution, which can be observed in different characteristics of galaxies (morphological type, star formation rate, colour) (Dressler, 1980, Fasano et al., 2015, Jaffé et al., 2015, Olave-Rojas et al., 2018, Liu et al., 2019). Thus, studying the properties of galaxies with respect to the environment they are in can provide us with clues about the different physical processes involved in their evolution.

Considering this context, this thesis focuses on analysing the properties (Sérsic index, effective radius, magnitudes, colour, stellar mass, and sSFR) of galaxies in a dense environment. For this purpose, we chose to study the Hydra cluster (Abell 1060). One of the main advantage of studying this particular cluster is its proximity ($\sim$ 50 Mpc), which enables us to analyse its galaxies in detail. In this thesis We analyse observations from a unique dataset from the S-PLUS survey (Mendes de Oliveira et al., 2019), which provides images in 12 filters in the visible region of the spectrum, thus allowing us to perform a panchromatic study of Hydra galaxies. Here, we are studying galaxies within $1R_{200}$ of the Hydra cluster. The galaxies were selected to have peculiar velocities lower than the cluster escape velocity, providing a sample of 81 galaxies (brighter than 16 in the r-band). We modelled the light distribution of galaxies, using the MEGAMORPH-GALAPAGOS2 project, with a single Sérsic profile (modelling the galaxy as a single component), and also we performed a bulge-disc decomposition modelling the bulge with a Sérsic profile (n free) and the disc with an exponential profile (n = 1). The results obtained in this thesis provide an unprecedented multiwavelength view of Hydra cluster galaxies, significantly improving our understanding of galaxy properties with respect to the environment and wavelength. This thesis generated several catalogues containing physical (stellar mass, star-formation rate, magnitude, and luminosity) and structural (Sérsic index, effective radius, bulge-to-total flux) properties of galaxies that can be used to compare with other clusters and field galaxies. This will help us to understand the evolution of galaxies in clusters in general. Below we summarise our main results presented in this thesis.

In Chapter 4, we study galaxies as a whole with the aim to explore how the structural and physical parameters of the Hydra galaxies change as a function of wavelength and with the cluster environment. We classify the galaxies as early and late-type using the Sérsic index and the $(u-r)$ colour of the galaxies. We found that $\sim$54 percent of the Hydra galaxies analysed in this thesis are early-type and $\sim$23 percent are late-type. Additionally, $\sim$88 percent of the Hydra galaxies, based on this analysis, are quenched ($sSFR < 10^{-11}\,\mathrm{yr}^{-1}$). Examining the Sérsic index variation in the 12 S-PLUS filters for different types of galaxies, we found that the Sérsic index of ETGs increased $\sim$ 18 percent from the u to the z band. This means that the light profile from this type of galaxy is more concentrated

in the redder filters. The Sérsic index of LTGs decreases ~ 7 percent towards redder bands. We also found a relation between the Sérsic index and the galaxy's stellar mass, where galaxies with larger stellar masses have a higher Sérsic index value. This result has also been found with simulations (Tacchella et al., 2016) and observations (Lange et al., 2015). With respect to the cluster environment, we found that the fraction of ETGs decreases towards larger clustercentric distances, while the fraction of LTGs increases in the same direction. We also found that the fraction of star-forming galaxies increases towards higher clustercentric distances, while quenched galaxies behave otherwise.

The dynamic state of a cluster can also influence the evolution of galaxies. For example, galaxies in disturbed, young, massive galaxy clusters have an increase in their star formation activity, which can be triggered by interactions between gas-rich galaxies, shocks, and/or the ICM (Stroe et al., 2017). Therefore, to further investigate the Hydra cluster we performed a Dressler-Schectman test (DST, Dressler & Shectman, 1988), which identifies substructures that are kinematically distinct from the main galaxy cluster. We found that the Hydra cluster is, although perturbed, close to virialization. Additionally, we use the Density-Based Spatial Clustering (`DBSCAN`, Ester et al., 1996) algorithm to identify substructures, and we found three substructures (see Figure 4.12). An interesting result is that one of the substructures found by DST also was identified by `DBSCAN`. This substructure has seven galaxies, some with a high ($n_r > 2.5$) and a low ($n_r < 2.5$) Sérsic index, and two of them are star-forming. We also analyse the position of this substructure in the phase-space diagram. All galaxies that belong to the substructure are inside the area restricted by the cluster escape velocity, which is obtained based on a Navarro, Frenk & White profile (Navarro et al., 1996).

The results exposed so far were carried out by studying the galaxies as a whole, using a single Sérsic profile to model the galaxies' light distribution. However, in general, galaxies have more than one component (bulge and disc), which can be influenced by the environment in different ways. In order to further investigate these components, in Chapter 5 we performed a bulge-disc decomposition of the Hydra galaxies. The bulge was modelled using a free Sérsic profile and the disc was modelled with an exponential profile (n=1). From the 81 galaxies analysed with the single Sérsic profile, only 52 meet the criteria imposed to have a reliable bulge-disc decomposition ($0.1 < B/T < 0.9$, $Re_{disc} > Re_{bulge}$, and $\chi^2 \geq 1.9$). Based on the bulge-disc decomposition we can determine the bulge-to-total flux ratio (B/T) of each galaxy. Many studies use the B/T value to classify galaxies because, in general, ETGd have high B/T and LTGs have low B/T values. However, B/T also has a relation with the magnitude of the galaxy, where brighter galaxies have higher B/T values (Head et al., 2014). We found that the Hydra's galaxies show more disc-dominated galaxies ($B/T < 0.5$) than bulge-dominated galaxies ($B/T \geq 0.5$) in all S-PLUS bands. In the r-band, which is the filter most used in the literature to classify galaxies, we found that 35 percent of our sample of Hydra's galaxies are bulge-dominated, and here we are studying galaxies with absolute magnitude brighter than -17.5 (r-band). This result may seem unexpected since we are analysing galaxies in a cluster, which is dominated by ETGs. However, it is very likely that the cut in magnitude is influencing the percentage of bulge and disc-dominated galaxies. Indeed, as already mentioned in Chapter 5, a similar result was found by Christlein & Zabludoff (2005), who studying galaxies from nearby clusters found a median B/T value of 0.36, where 33 percent of the galaxies have $B/T > 0.5$. In Christlein & Zabludoff (2005) ~ 80 percent of the galaxies are brighter than $M_R \leq$ -19.2.

As we mentioned before, the bulge was modelled with a free Sérsic profile in the 12 S-PLUS bands. Thus, a change in the light profile of the bulge among the filters will be reflected in its Sérsic index. The median bulge's Sérsic index ($\bar{n}_{bulge}$) for the late-type and blue galaxies is smaller than that for

early-type and red galaxies. We also investigated the relation between the Sérsic index of the bulge (n_{bulge}), and the Sérsic index obtained with the single Sérsic profile (n_{SS}). We found that galaxies with higher values of n_{SS} tend to have higher values of n_{bulge}. An interesting result is that at a fixed n_{SS}, galaxies with higher values of $(B/T)_r$ tend to have larger values of $n_{bulge,r}$. In other words, in general, bulge-dominated galaxies have a more concentrated bulge profile at a fixed n_{SS}.

In order to further investigate the galaxies, we explored the mass-size relation [$log(Re)_r$ vs. $log(M_\star/M_\odot)$] which is widely used to study the evolution of galaxies (van Dokkum et al., 2015, Lange et al., 2016, Whitaker et al., 2017, Furlong et al., 2017, Matharu et al., 2019, Nedkova et al., 2021, Méndez-Abreu et al., 2021). We studied the mass-size relation of the Hydra galaxies, first using the galaxies as a whole and then analysing the mass-size relation of each component. By analysing the galaxies as a whole, we found a clear mass-size relation with a slope of 0.20±0.04 (r-band). An interesting observation is that, in general, galaxies with larger B/T values also have a smaller size ($log(Re)$), at a fixed stellar mass. Additionally, the redder galaxies are also smaller at a fixed stellar mass (for galaxies with $\sim 9.5 \leq log(M_\star/M_\odot) \leq 10.3$). This may be the influence of the environment, where the ram-pressure stripping could be making the galaxies more compact and quenched (redder) (Kuchner et al., 2017). We analyse the mass-size relation of the galaxies' components and do not find a dependence on the size of the bulge and the galaxy's stellar mass. However, the disc mass-size relation shows a slope of 0.18±0.03 (r-band). Thus, apparently, the galaxy's disc is responsible for the observed mass-size relation of Hydra galaxies.

Observing the colours of a galaxy and its components can give us clues to understand if only one or both components are responsible for the trends of the whole galaxy colour. Additionally, as previously mentioned in Chapter 1, the environment plays a role in the evolution of galaxies. Thus it is interesting to observe the colours of the galaxies and their components with respect to the environment (density and projected clustercentric distance). Using the $(u-r)$ colour, we found that the bulges are, in general, redder than the discs. Panel c of Fig. 5.1 shows the colour distribution of a galaxy's components. The median $(u-r)$ offset separating the two distributions is 0.17 mag. However, we have some bulges that are bluer than the discs. Additionally, as we saw in Figure 5.2, both components (bulge and disc) are influencing the colour of the whole galaxy; redder galaxies have redder components and bluer galaxies have bluer components. By analysing the colours of galaxies with respect to the environment, we found that the bulge, the disc, and the whole galaxy are bluer towards higher clustercentric distances, and we observe the same behaviour for galaxies and their components in the cluster's less dense regions.

The colours of the different galactic components can also be used to constrain the evolutionary scenario of the galaxies (Pan et al., 2015, Lian et al., 2017). By Comparing the colour of the bulge and the disc we found that $\sim$ 36 percent of galaxies have bulges bluer than discs. Actually, the four star-forming galaxies for which we could make a reliable bulge-disc decomposition, all have the bulge bluer than the disc, and we concluded: apparently, a tidal interaction is inducing star formation in the galaxies' central region, and other environmental effects, such as ram-pressure stripping and/or harassment, are causing the galaxies to stop their star formation from the outside-in.

7 Future Work

We discuss in this Chapter follow-up studies that are based on the work presented in this thesis.

7.1 Outskirts of the Hydra Cluster

Our study of the Hydra Cluster was performed within a $1R_{200}$, which, in general, is the region with the highest density of galaxies in a cluster. However, we also want to study the galaxy preprocessing around the Hydra Cluster. This will allow us to answer questions such as: how many galaxies are falling into the cluster already quenched? what is the structural and physical properties of those galaxies? how do they compare with the galaxies already analysed, in this thesis, in the central region of the cluster? By studying galaxies at distances larger than $1R_{200}$, it will be possible to compare the properties of galaxies that are already heavily influenced by the cluster (galaxies within $1R_{200}$) with galaxies that are still out of this strong cluster influence (galaxies out of $1R_{200}$). S-PLUS will observe a large area around the Hydra cluster including the Antlia cluster and other small groups. Taking advantage of the new S-PLUS data release 4 it will be possible to explore up to $(3-4)R_{200}$, in the Hydra cluster low dense regions. Additionally, with the new data release, we intend to identify a control field sample and analyse its galaxies in the same way as we are analysing the Hydra cluster galaxies. We will then compare the galaxies' properties between field and cluster in an homogeneous way to better understand the influence of the cluster on galaxies.

7.2 SED fitting: ALStar code

The star formation history, age, metallicity, star formation rate, and stellar mass of galaxies can be estimated using SED fitting codes, which model the SED of galaxies by using a base of a simple stellar population or a base of composed stellar population (CSP), to retrieve the galaxies properties. In this thesis, we used the H_α filter to estimate the star-formation rate of the galaxies. However, a SED fitting code could provide better star-formation estimates. We want to understand the bulge, disc, and the whole galaxy formation, evolution, and quenching process. We want to know, for example: did the stellar formation of the bulge and disc of galaxies occur in a single episode, or multiple episodes? What was the moment in the galaxy's life that it stopped its star formation? Did the galaxy's components stop their star formation at the same time? If not, what is the difference between the component's properties compared to galaxies that stopped their star formation at the same time? Also, we want to compare the fraction of star-forming galaxies found using the Three Filter Method with respect to the fraction of star-forming galaxies using a SED fitting code in the Hydra cluster. To do so, we plan to use the ALStar code to estimate the properties of the bulge, disc and the whole galaxy. ALStar is a SED fitting code like STARLIGHT (Cid Fernandes et al., 2005), which performs a SED decomposition in terms of a superposition of CSPs with different ages and metallicities. It uses a non-negative least squares (NNLS) algorithm (Lawson & Hanson 1974) to find the vector that minimises the model's χ^2, and a Monte Carlo simulation to estimate the uncertainties, generating and modeling 100 new SEDs for each galaxy. In addition, to correct for dust attenuation, it uses Calzetti et al. (2000b) law. ALStar has already been tested using 56 filters from J-PAS (Benitez et al., 2014), showing a good result when compared to others SED fitting codes such as BaySeAGal (López Fernández et al., 2018), MUFFIT (Díaz-García et al., 2015) and TGASPEX (González Delgado et al., 2021). However, we are in the process of testing the quality and reliability of this code when using the 12 S-PLUS bands. Figure 7.1 shows an example of a Hydra galaxy, for which a SED fitting was performed using ALStar. For this fit we use a total of 80 CSPs, to model the galaxy, with a range

of ages from 3×10^6 to 14×10^9 yr, and 5 metallicities (0.004, 0.008, 0.017, 0.03, and 0.06). For this galaxy, we find a mean $log(age/yr) = 9.8$, and a mean metallicity $log(Z) = 0.38$. However, more testing needs to be done to validate the estimated parameters using ALStar. It is necessary to have a sample of galaxies with already known parameters from observed spectra (stellar mass, metallicity, and stellar age) in the literature, and determine how well the ALStar retrieves the parameters of the galaxies.

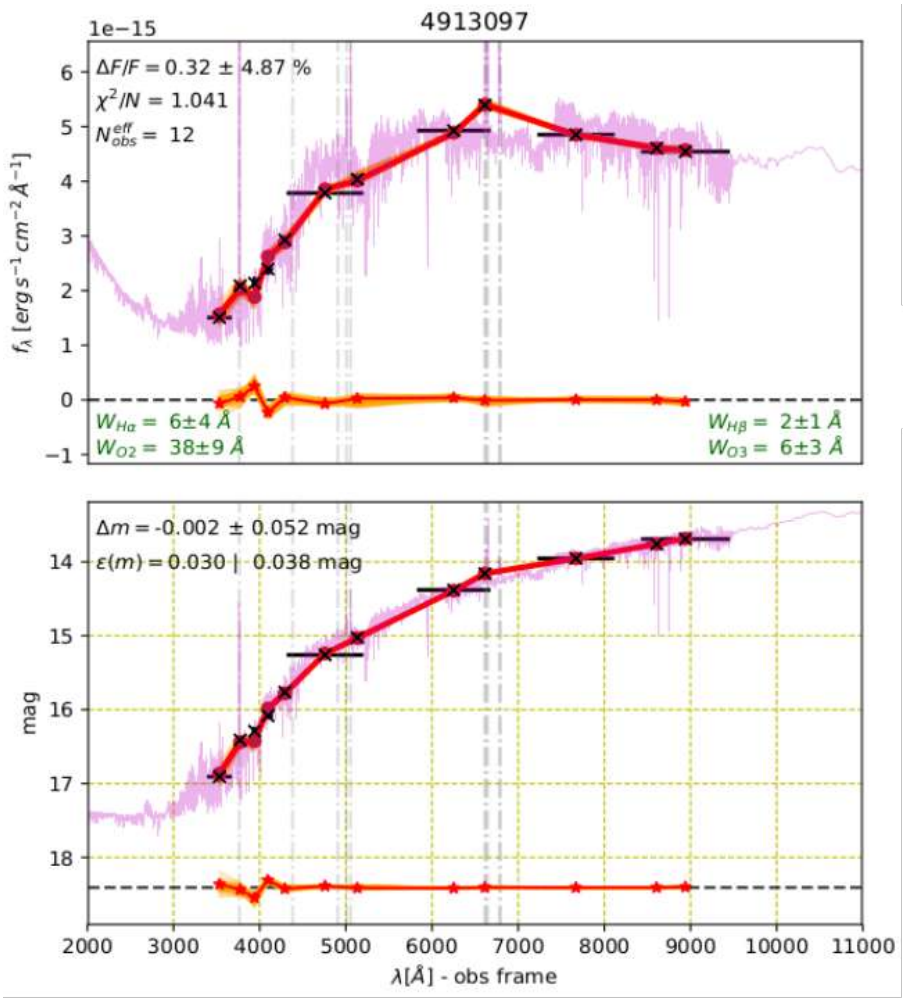

Figure 7.1: A SED fitting example using ALStar of a Hydra galaxy. Top panel shows the modeled spectrum in magenta (created with a base of CSPs), and the black x symbols are the galaxy's fluxes extracted from the S-PLUS magnitudes, calibrated in flux. The model's reduced χ^2 and the equivalent width (W) of the H_α, H_β, $[OII]$, and $[OIII]$ lines are also shown in the top panel. Bottom panel shows same plot as the top panel, but now the galaxy magnitudes are shown on the y-axis. The orange lines are the difference between the galaxy's estimated flux/magnitudes and the model flux/magnitudes.

7.3 Comparison with simulations

We also intend to compare the results obtained in this thesis and future works outlined above, with state-of-the-art hydrodynamical simulations such as IllUSTRIS-TNG (Nelson et al., 2018) and C-EAGLE (Barnes et al., 2018). The Illustris - TNG project consists of three physical simulation box

sizes: 50, 100, and 300 Mpc a side length. The simulation with 300 Mpc (TNG300) enables the study of galaxy clusters. This simulation has groups and clusters with masses between $10^{13} \leq M_{200}/M_{\odot} \leq 10^{15}$, and with a baryon mass particle resolution of $1.1\times10^{7}\ M_{\odot}$. Examples of clusters from TNG300 simulations are shown in Figure 7.2. The C-EAGLE is a suite of 30 cosmological hydrodynamical simulations of massive galaxy clusters (M_{200} from $10^{14}\ M_{\odot}$ to $2.5\ \times10^{15}M_{\odot}$) with a resolution of $2\times10^{6}M_{\odot}$ in mass. Using these simulations, we can study clusters with properties (mass and dynamical state) similar to the Hydra cluster. We will analyse simulations to see if we find consistent results with what we found for Hydra; e.g. percentage of blue, red, ETGs, LTGS, bulge- and disc-dominated galaxies, star-forming and quenched galaxies, as well as the behaviour of the galaxies' properties with respect to the cluster environment. Furthermore, we will trace back and try to understand the evolutionary processes (environmental or internal) responsible for the observed properties of the cluster galaxies in the simulations, which, in turn, will help us understand the evolution of Hydra galaxies.

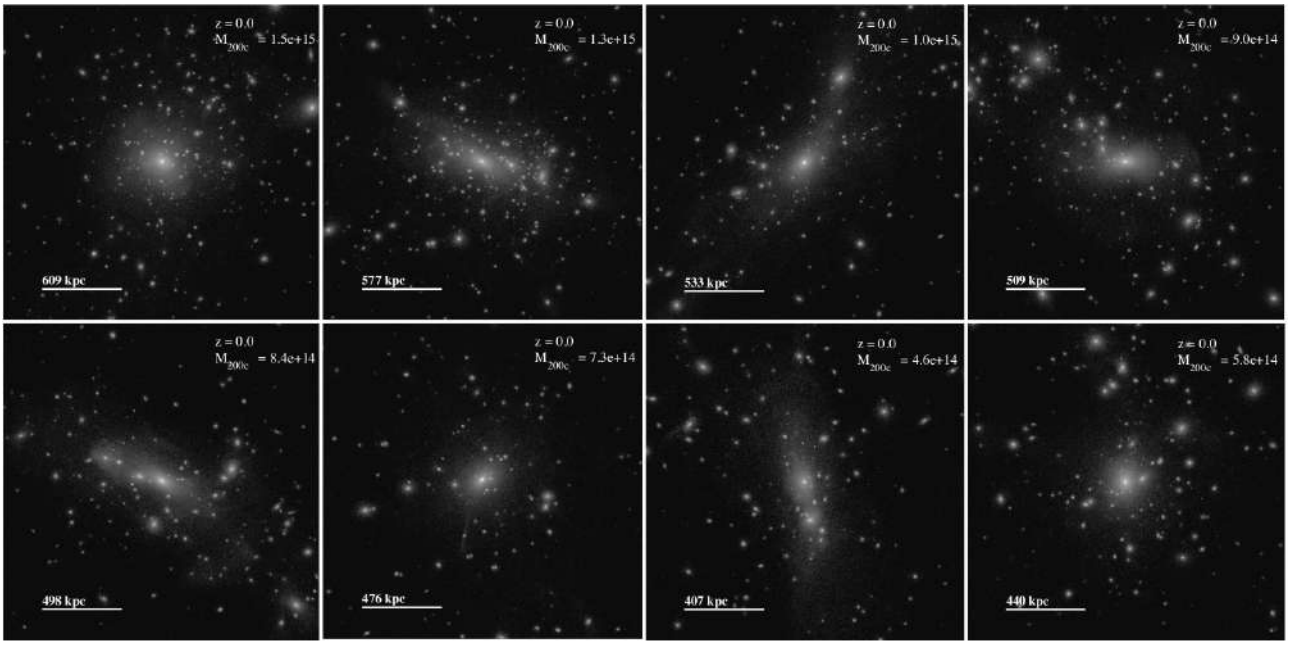

Figure 7.2: Galaxy clusters from the IllUSTRIS-TNG300 simulations. Figure extracted from Pillepich et al. (2018).

Bibliography

Abadi M. G., Moore B., Bower R. G., 1999, MNRAS, 308, 947

Abazajian K. N., et al., 2009, ApJS, 182, 543

Aguerri J. A. L., Méndez-Abreu J., Corsini E. M., 2009, A&A, 495, 491

Almeida-Fernandes F., et al., 2021, arXiv e-prints, p. arXiv:2104.00020

Arnaboldi M., Ventimiglia G., Iodice E., Gerhard O., Coccato L., 2012, A&A, 545, A37

Arnouts S., Cristiani S., Moscardini L., Matarrese S., Lucchin F., Fontana A., Giallongo E., 1999, MNRAS, 310, 540

Babyk I. V., Vavilova I. B., 2013, Odessa Astronomical Publications, 26, 175

Bamford S. P., Häußler B., Rojas A., Borch A., 2011, in Evans I. N., Accomazzi A., Mink D. J., Rots A. H., eds, Astronomical Society of the Pacific Conference Series Vol. 442, Astronomical Data Analysis Software and Systems XX. p. 479

Barbosa C. E., Arnaboldi M., Coccato L., Gerhard O., Mendes de Oliveira C., Hilker M., Richtler T., 2018, A&A, 609, A78

Barnes L. A., et al., 2018, MNRAS, 477, 3727

Barsanti S., et al., 2021a, ApJ, 906, 100

Barsanti S., et al., 2021b, ApJ, 911, 21

Bautz L. P., Morgan W. W., 1970, ApJ, 162, L149

Beers T. C., Flynn K., Gebhardt K., 1990a, AJ, 100, 32

Beers T. C., Flynn K., Gebhardt K., 1990b, AJ, 100, 32

Bell E. F., McIntosh D. H., Katz N., Weinberg M. D., 2003, ApJS, 149, 289

Bell E. F., et al., 2004, ApJ, 608, 752

Benitez N., et al., 2014, arXiv e-prints, p. arXiv:1403.5237

Bertin E., Arnouts S., 1996, A&AS, 117, 393

Blanton M. R., Moustakas J., 2009, ARA&A, 47, 159

Bluck A. F. L., et al., 2020, MNRAS, 499, 230

Boselli A., et al., 2005, ApJ, 629, L29

Bouwens R., Cayón L., Silk J., 1999, ApJ, 516, 77

Brammer G. B., et al., 2009, ApJ, 706, L173

Brooks A., Christensen C., 2016, in Laurikainen E., Peletier R., Gadotti D., eds, Astrophysics and Space Science Library Vol. 418, Galactic Bulges. p. 317 (arXiv:1511.04095), doi:10.1007/978-3-319-19378-6_12

Bruzual G., Charlot S., 2003, MNRAS, 344, 1000

Bruzual A. G., Charlot S., 1993, ApJ, 405, 538

Butcher H., Oemler A. J., 1978, ApJ, 226, 559

Byrd G., Valtonen M., 1990, ApJ, 350, 89

Calzetti D., Armus L., Bohlin R. C., Kinney A. L., Koornneef J., Storchi-Bergmann T., 2000a, ApJ, 533, 682

Calzetti D., Armus L., Bohlin R. C., Kinney A. L., Koornneef J., Storchi-Bergmann T., 2000b, ApJ, 533, 682

Cardelli J. A., Clayton G. C., Mathis J. S., 1989, ApJ, 345, 245

Cenarro A. J., et al., 2019, A&A, 622, A176

Ceverino D., Klypin A., 2009, ApJ, 695, 292

Chabrier G., 2003, PASP, 115, 763

Christlein D., Zabludoff A. I., 2005, ApJ, 621, 201

Cid Fernandes R., Mateus A., Sodré L., Stasińska G., Gomes J. M., 2005, MNRAS, 358, 363

Coe D., et al., 2012, ApJ, 757, 22

Comerford J. M., Natarajan P., 2007, MNRAS, 379, 190

Dark Energy Survey Collaboration et al., 2016, MNRAS, 460, 1270

Davis M., Geller M. J., 1976, ApJ, 208, 13

Dekel A., Silk J., 1986, ApJ, 303, 39

Desai V., et al., 2007, ApJ, 660, 1151

Diaferio A., 1999, MNRAS, 309, 610

Díaz-García L. A., Cenarro A. J., López-Sanjuan C., 2015, in Highlights of Spanish Astrophysics VIII. pp 366–366

Dimauro P., et al., 2018, MNRAS, 478, 5410

Dobrycheva D. V., Vavilova I. B., Melnyk O. V., Elyiv A. A., 2017, preprint, (arXiv:1712.08955)

Dressler A., 1980, ApJ, 236, 351

Dressler A., Shectman S. A., 1988, AJ, 95, 985

Dressler A., et al., 1997, ApJ, 490, 577

Duc P.-A., Bournaud F., 2008, ApJ, 673, 787

Duc P. A., Mirabel I. F., 1999, in Barnes J. E., Sanders D. B., eds, Vol. 186, Galaxy Interactions at Low and High Redshift. p. 61

Durret F., Tarricq Y., Márquez I., Ashkar H., Adami C., 2019, A&A, 622, A78

Eggen O. J., Lynden-Bell D., Sandage A. R., 1962, ApJ, 136, 748

Ester M., Kriegel H.-P., Sander J., Xu X., 1996, in Proceedings of the Second International Conference on Knowledge Discovery and Data Mining. KDD'96. AAAI Press, pp 226–231, http://dl.acm.org/citation.cfm?id=3001460.3001507

Etherington J., et al., 2017, MNRAS, 466, 228

Faber S. M., Gallagher J. S., 1979, ARA&A, 17, 135

Faber S. M., Jackson R. E., 1976, ApJ, 204, 668

Fall S. M., Efstathiou G., 1980, MNRAS, 193, 189

Fasano G., Poggianti B. M., Couch W. J., Bettoni D., Kjærgaard P., Moles M., 2000, ApJ, 542, 673

Fasano G., et al., 2015, MNRAS, 449, 3927

Fitchett M., Merritt D., 1988, ApJ, 335, 18

Fraternali F., Binney J. J., 2008, MNRAS, 386, 935

Furlong M., et al., 2017, MNRAS, 465, 722

Furusho T., et al., 2001, PASJ, 53, 421

Gabor J. M., Davé R., 2015, MNRAS, 447, 374

Gadotti D. A., 2009, MNRAS, 393, 1531

Gil de Paz A., et al., 2007, ApJS, 173, 185

Girardi M., Escalera E., Fadda D., Giuricin G., Mardirossian F., Mezzetti M., 1997, ApJ, 482, 41

González Delgado R. M., et al., 2021, A&A, 649, A79

Gonzalez E. J., et al., 2018, A&A, 611, A78

Gott J. R. I., Thuan T. X., 1976, APJ, 204, 649

Graham A. W., 2013, Elliptical and Disk Galaxy Structure and Modern Scaling Laws. pp 91–140, doi:10.1007/978-94-007-5609-0_2

Gunn J. E., Gott J. Richard I., 1972, ApJ, 176, 1

Gutiérrez C. M., Trujillo I., Aguerri J. A. L., Graham A. W., Caon N., 2004, ApJ, 602, 664

Harrison E. R., 1974, ApJ, 191, L51

Hatfield P. W., Jarvis M. J., 2017, MNRAS, 472, 3570

Häußler B., et al., 2013, MNRAS, 430, 330

Hayakawa A., Furusho T., Yamasaki N. Y., Ishida M., Ohashi T., 2004, PASJ, 56, 743

Head J. T. C. G., Lucey J. R., Hudson M. J., Smith R. J., 2014, MNRAS, 440, 1690

Heap S. R., Lindler D. J., 2007, in Vallenari A., Tantalo R., Portinari L., Moretti A., eds, Astronomical Society of the Pacific Conference Series Vol. 374, From Stars to Galaxies: Building the Pieces to Build Up the Universe. p. 409

Hopkins A. M., Connolly A. J., Haarsma D. B., Cram L. E., 2001, AJ, 122, 288

Hopkins P. F., Cox T. J., Kereš D., Hernquist L., 2008, ApJS, 175, 390

Huang S., Ho L. C., Peng C. Y., Li Z.-Y., Barth A. J., 2013, ApJ, 766, 47

Hubble E., 1926, Contributions from the Mount Wilson Observatory / Carnegie Institution of Washington, 324, 1

Hubble E. P., 1936, Realm of the Nebulae

Hudson M. J., Stevenson J. B., Smith R. J., Wegner G. A., Lucey J. R., Simard L., 2010, MNRAS, 409, 405

Ilbert O., et al., 2006, A&A, 457, 841

Jaffé Y. L., Smith R., Candlish G. N., Poggianti B. M., Sheen Y.-K., Verheijen M. A. W., 2015, MNRAS, 448, 1715

Jeans J. H., 1902, Philosophical Transactions of the Royal Society of London Series A, 199, 1

Jones D. H., et al., 2004, MNRAS, 355, 747

Joshi G. D., Wadsley J., Parker L. C., 2017, MNRAS, 468, 4625

Kadowaki J., Zaritsky D., Donnerstein R. L., RS P., Karunakaran A., Spekkens K., 2021, arXiv e-prints, p. arXiv:2110.00015

Kaiser N., 1984, ApJ, 284, L9

Kartaltepe J. S., et al., 2015, ApJS, 221, 11

Katz N., 1992, ApJ, 391, 502

Kelvin L. S., et al., 2012, MNRAS, 421, 1007

Kennedy R., et al., 2015, MNRAS, 454, 806

Kennedy R., et al., 2016, MNRAS, 460, 3458

Kennicutt Robert C. J., 1992, ApJ, 388, 310

Kennicutt Jr. R. C., 1998, ApJ, 498, 541

Khostovan A. A., et al., 2020, MNRAS, 493, 3966

Koopmann R. A., Haynes M. P., Catinella B., 2006, AJ, 131, 716

Kormendy J., Bender R., 1996, ApJ, 464, L119

Kormendy J., Kennicutt Robert C. J., 2004, ARA&A, 42, 603

Kormendy J., Fisher D. B., Cornell M. E., Bender R., 2009, ApJS, 182, 216

Koyama Y., et al., 2013, MNRAS, 434, 423

Kuchner U., Ziegler B., Verdugo M., Bamford S., Häußler B., 2017, A&A, 604, A54

La Barbera F., de Carvalho R. R., de La Rosa I. G., Lopes P. A. A., Kohl-Moreira J. L., Capelato H. V., 2010, MNRAS, 408, 1313

Lacey C., Cole S., 1993, MNRAS, 262, 627

Lackner C. N., Gunn J. E., 2013, MNRAS, 428, 2141

Laganá T. F., Ulmer M. P., 2018, MNRAS, 475, 523

Lange R., et al., 2015, MNRAS, 447, 2603

Lange R., et al., 2016, MNRAS, 462, 1470

Larson R. B., 1976, MNRAS, 176, 31

Larson R. B., Tinsley B. M., Caldwell C. N., 1980, ApJ, 237, 692

Lauer T. R., et al., 1995, AJ, 110, 2622

Lee J. H., Lee M. G., Kim T., Hwang H. S., Park C., Choi Y.-Y., 2007, ApJ, 663, L69

Leonard A., King L. J., 2010, Monthly Notices of the Royal Astronomical Society, 405, 1854

Lian J., Yan R., Blanton M., Kong X., 2017, MNRAS, 472, 4679

Lintott C. J., et al., 2008, MNRAS, 389, 1179

Liu S.-F., et al., 2011, AJ, 141, 99

Liu C., Hao L., Wang H., Yang X., 2019, ApJ, 878, 69

Łokas E. L., Wojtak R., Gottlöber S., Mamon G. A., Prada F., 2006, MNRAS, 367, 1463

Łokas E. L., Ebrová I., del Pino A., Sybilska A., Athanassoula E., Semczuk M., Gajda G., Fouquet S., 2016, ApJ, 826, 227

López Fernández R., et al., 2018, A&A, 615, A27

Lotz J. M., Primack J., Madau P., 2004, AJ, 128, 163

Lotz J. M., et al., 2008, ApJ, 672, 177

Lotz J. M., Jonsson P., Cox T. J., Croton D., Primack J. R., Somerville R. S., Stewart K., 2011, ApJ, 742, 103

Lotz M., Remus R.-S., Dolag K., Biviano A., Burkert A., 2019, MNRAS, 488, 5370

Ly C., et al., 2007, ApJ, 657, 738

Ly C., Malkan M. A., Kashikawa N., Ota K., Shimasaku K., Iye M., Currie T., 2012, ApJ, 747, L16

Matharu J., et al., 2019, MNRAS, 484, 595

McNab K., et al., 2021, , 508, 157

Mendes de Oliveira C., et al., 2019, MNRAS, p. 2048

Méndez-Abreu J., de Lorenzo-Cáceres A., Sánchez S. F., 2021, MNRAS, 504, 3058

Misgeld I., Hilker M., 2011, MNRAS, 414, 3699

Misgeld I., Mieske S., Hilker M., Richtler T., Georgiev I. Y., Schuberth Y., 2011, A&A, 531, A4

Mitchell R. J., Culhane J. L., Davison P. J. N., Ives J. C., 1976, MNRAS, 175, 29P

Moffat A. F. J., 1969, A&A, 3, 455

Molino A., et al., 2020, MNRAS, 499, 3884

Moore B., Katz N., Lake G., Dressler A., Oemler A., 1996, Nature, 379, 613

Moore B., Lake G., Katz N., 1998, ApJ, 495, 139

Moore B., Lake G., Quinn T., Stadel J., 1999, MNRAS, 304, 465

Moss C., Whittle M., Pesce J. E., 1998, MNRAS, 300, 205

Munari E., Biviano A., Borgani S., Murante G., Fabjan D., 2013, MNRAS, 430, 2638

Navarro J. F., Frenk C. S., White S. D. M., 1996, ApJ, 462, 563

Nedkova K. V., et al., 2021, MNRAS, 506, 928

Nelson D., et al., 2018, MNRAS, 475, 624

Nyland K., et al., 2018, ApJ, 859, 23

Oemler Augustus J., 1974, ApJ, 194, 1

Olave-Rojas D., Cerulo P., Demarco R., Jaffé Y. L., Mercurio A., Rosati P., Balestra I., Nonino M., 2018, MNRAS, 479, 2328

Owers M. S., et al., 2019, ApJ, 873, 52

Pallero D., Gómez F. A., Padilla N. D., Torres-Flores S., Demarco R., Cerulo P., Olave-Rojas D., 2019, MNRAS, 488, 847

Pan Z., Li J., Lin W., Wang J., Fan L., Kong X., 2015, ApJ, 804, L42

Papovich C., Dickinson M., Giavalisco M., Conselice C. J., Ferguson H. C., 2005, ApJ, 631, 101

Park C., Choi Y.-Y., 2005, ApJ, 635, L29

Pascual S., Gallego J., Zamorano J., 2007, PASP, 119, 30

Paulino-Afonso A., et al., 2019, A&A, 630, A57

Peebles P. J. E., 1965, ApJ, 142, 1317

Peng C. Y., Ho L. C., Impey C. D., Rix H.-W., 2002, AJ, 124, 266

Peng C. Y., Ho L. C., Impey C. D., Rix H.-W., 2010a, AJ, 139, 2097

Peng Y.-j., et al., 2010b, ApJ, 721, 193

Peng Y., Maiolino R., Cochrane R., 2015, Nature, 521, 192

Pickles A. J., 1998, PASP, 110, 863

Pillepich A., et al., 2018, MNRAS, 475, 648

Pinkney J., Roettiger K., Burns J. O., Bird C. M., 1996, ApJS, 104, 1

Placco V. M., et al., 2021, ApJ, 912, L32

Poggianti B. M., et al., 2001, ApJ, 562, 689

Postman M., Geller M. J., 1984, ApJ, 281, 95

Postman M., et al., 2005, ApJ, 623, 721

Psychogyios A., et al., 2019, arXiv e-prints, p. arXiv:1909.03256

Ratnatunga K. U., Griffiths R. E., Ostrand er E. J., 1999, AJ, 118, 86

Richter O. G., 1987, A&AS, 67, 237

Rodríguez-Muñoz L., et al., 2019, MNRAS, 485, 586

Rood H. J., Sastry G. N., 1971, PASP, 83, 313

Ruel J., et al., 2014, ApJ, 792, 45

Salim S., 2014, Serbian Astronomical Journal, 189, 1

Salpeter E. E., 1955, ApJ, 121, 161

Schade D., Lilly S. J., Crampton D., Hammer F., Le Fevre O., Tresse L., 1995, ApJ, 451, L1

Schawinski K., et al., 2014, MNRAS, 440, 889

Schlafly E. F., et al., 2012, ApJ, 756, 158

Schlegel D. J., Finkbeiner D. P., Davis M., 1998, ApJ, 500, 525

Sérsic J. L., 1963, Boletin de la Asociacion Argentina de Astronomia La Plata Argentina, 6, 41

Simmons B. D., et al., 2017, MNRAS, 464, 4420

Skrutskie M. F., et al., 1997, The Two Micron All Sky Survey (2MASS): Overview and Status.. p. 25, doi:10.1007/978-94-011-5784-1˙4

Smith R., et al., 2015, MNRAS, 454, 2502

Sobral D., Best P. N., Matsuda Y., Smail I., Geach J. E., Cirasuolo M., 2012, MNRAS, 420, 1926

Sohn J., Hwang H. S., Geller M. J., Diaferio A., Rines K. J., Lee M. G., Lee G.-H., 2015, Journal of Korean Astronomical Society, 48, 381

Spergel D. N., et al., 2003, ApJS, 148, 175

Spergel D. N., et al., 2007, ApJS, 170, 377

Stein P., 1996, A&AS, 116, 203

Stein P., 1997, A&A, 317, 670

Stewart K. R., Kaufmann T., Bullock J. S., Barton E. J., Maller A. H., Diemand J., Wadsley J., 2011, ApJ, 735, L1

Strateva I., et al., 2001, AJ, 122, 1861

Stroe A., Sobral D., Paulino-Afonso A., Alegre L., Calhau J., Santos S., van Weeren R., 2017, MNRAS, 465, 2916

Sunyaev R. A., Zeldovich I. B., 1980, ARA&A, 18, 537

Tacchella S., Dekel A., Carollo C. M., Ceverino D., DeGraf C., Lapiner S., Mandelker N., Primack J. R., 2016, MNRAS, 458, 242

Taylor E. N., et al., 2011, MNRAS, 418, 1587

Tonnesen S., Bryan G. L., 2009, ApJ, 694, 789

Toomre A., Toomre J., 1972, ApJ, 178, 623

Tully R. B., Fisher J. R., 1977, A&A, 500, 105

Ventimiglia G., Arnaboldi M., Gerhard O., 2011, A&A, 528, A24

Vika M., Bamford S. P., Häußler B., Rojas A. L., Borch A., Nichol R. C., 2013, MNRAS, 435, 623

Vika M., Bamford S. P., Häußler B., Rojas A. L., 2014, MNRAS, 444, 3603

Vika M., Vulcani B., Bamford S. P., Häußler B., Rojas A. L., 2015, A&A, 577, A97

Vilella-Rojo G., et al., 2015, A&A, 580, A47

Vulcani B., et al., 2011, MNRAS, 412, 246

Vulcani B., et al., 2014, ApJ, 797, 62

Wang J., et al., 2011, MNRAS, 412, 1081

Weinmann S. M., Kauffmann G., von der Linden A., De Lucia G., 2010, MNRAS, 406, 2249

Wetzel A. R., Tinker J. L., Conroy C., 2012, MNRAS, 424, 232

Wetzel A. R., Tinker J. L., Conroy C., van den Bosch F. C., 2013, MNRAS, 432, 336

Wetzel A. R., Tinker J. L., Conroy C., van den Bosch F. C., 2014, MNRAS, 439, 2687

Whitaker K. E., et al., 2017, ApJ, 838, 19

White S. D. M., Rees M. J., 1978, MNRAS, 183, 341

White J. A., et al., 2015, MNRAS, 453, 2718

Whitmore B. C., Gilmore D. M., 1991, ApJ, 367, 64

Wright E. L., et al., 2010, AJ, 140, 1868

Wright R. J., Lagos C. d. P., Davies L. J. M., Power C., Trayford J. W., Wong O. I., 2019, MNRAS, 487, 3740

Yan P.-F., Yuan Q.-R., Zhang L., Zhou X., 2014, AJ, 147, 106

York D. G., et al., 2000, AJ, 120, 1579

Zwicky F., 1937, ApJ, 86, 217

da Cunha E., Charlot S., Dunne L., Smith D., Rowlands K., 2012, in Tuffs R. J., Popescu C. C., eds, IAU Symposium Vol. 284, The Spectral Energy Distribution of Galaxies - SED 2011. pp 292–296 (arXiv:1111.3961), doi:10.1017/S1743921312009283

de Jong J. T. A., et al., 2015, A&A, 582, A62

van Dokkum P. G., et al., 2015, ApJ, 813, 23

van der Burg R. F. J., et al., 2020a, A&A, 638, A112

van der Burg R. F. J., et al., 2020b, A&A, 638, A112

Appendices

A MEGAMORPH-GALAPAGOS2 setup

Here we present the MEGAMORPH-GALAPAGOS2 setup used to model the galaxies in this thesis. MEGAMORPH-GALAPAGOS2 includes SourceExtractor (Bertin & Arnouts, 1996) to identify and to create an input catalogue for the galaxies. Table A.1 shows the configuration file needed to run SourceExtractor, and Table A.2 shows the input catalogue to run MEGAMORPH-GALAPAGOS2, obtained as an output from SourceExtractor, which contains the preliminary galaxies' position, magnitudes, ellipticity, among other information. Additionally, Table A.3 indicates the main settings of MEGAMORPH-GALAPAGOS2.

Table A.1: SourceExtractor configuration file.

		comments
CATALOG_NAME	sextractor.cat	
CATALOG_TYPE	ASCII_HEAD	ASCII_HEAD,ASCII,FITS_1.0 or FITS_LDAC
PARAMETERS_NAME	gala.param	
DETECT_TYPE	CCD	CCD or PHOTO
DETECT_MINAREA	4	minimum number of pixels above threshold
DETECT_THRESH	1.1	sigmas or threshold, ZP in mag.arcsec-2
ANALYSIS_THRESH	3.	sigmas or threshold, ZP in mag.arcsec-2
FILTER	Y	apply filter for detection (Y or N)?
FILTER_NAME	gauss_3.0_5x5.conv	
DEBLEND_NTHRESH	64	Number of deblending sub-thresholds
DEBLEND_MINCONT	0.0002	Minimum contrast parameter for deblending
CLEAN	Y	Clean spurious detections? (Y or N)?
CLEAN_PARAM	1.	Cleaning efficiency
PHOT_APERTURES	2,4,6	MAG_APER aperture diameter(s) in pixels
PHOT_AUTOPARAMS	1.0,1.0	1.0,1.0 MAG_AUTO parameters: Kron_fact,min_radius
PHOT_PETROPARAMS	3.0,2.0	
MAG_ZEROPOINT	20	magnitude zero-point
MAG_GAMMA	4.0	gamma of emulsion (for photographic scans)
GAIN	130.383	detector gain in e-/ADU.
PIXEL_SCALE	0.55	size of pixel in arcsec
SEEING_FWHM	1.8	stellar FWHM in arcsec
STARNNW_NAME	default.nnw	
BACK_SIZE	50	Background mesh: size or width, height
BACK_FILTERSIZE	7	Background filter: size or width, height
BACKPHOTO_TYPE	LOCAL	can be GLOBAL or LOCAL
BACKPHOTO_THICK	48	thickness of the background LOCAL annulus
MEMORY_OBJSTACK	15000	number of objects in stack
MEMORY_PIXSTACK	2600000	number of pixels in stack
MEMORY_BUFSIZE	4600	number of lines in buffer
CHECKIMAGE_TYPE	APERTURES,SEGMENTATION	IMAGE-TYPE RETURNED
WEIGHT_TYPE	MAP_WEIGHT,MAP_WEIGHT	Since there is no background

Table A.2: Output parameters from SourceExtractor. Column one shows the parameter names and column two shows the parameter description.

PARAMETER	comments
NUMBER	Running object number
X_IMAGE	Pixel x coordinate of the isophotal image centroid
Y_IMAGE	Pixel y coordinate of the isophotal image centroid
CXX_IMAGE	Isophotal image Cxx ellipse parameter
CYY_IMAGE	Isophotal image Cyy ellipse parameter
CXY_IMAGE	Isophotal image Cxy ellipse parameter
THETA_IMAGE	Isophotal image position angle
THETA_WORLD	Position angle (CCW/world-x)
ELLIPTICITY	1 - B_IMAGE / A_IMAGE
KRON_RADIUS	Kron radius
A_IMAGE	Isophotal image major axis
B_IMAGE	Isophotal image minor axis
ALPHA_J2000	J2000 right ascension of the isophotal image centroid
DELTA_J2000	J2000 declination of the isophotal image centroid
BACKGROUND	Background level at the position of the centroid
FLUX_BEST	Best of FLUX AUTO and FLUX ISOCOR
FLUXERR_BEST	RMS error for BEST flux
MAG_BEST	Best of MAG AUTO and MAG ISOCOR
MAGERR_BEST	RMS error for MAG BEST
FLUX_RADIUS	Radius enclosing a specified fraction of the flux
ISOAREA_IMAGE	Isophotal area above Analysis threshold
FWHM_IMAGE	FWHM assuming a gaussian core
FLAGS	Source extraction flags
CLASS_STAR	Star/galaxy classifier

Table A.3: MEGAMORPH-GALAPAGOS2 settings

PARAMETER	comments
SKY PREPARATION	
execute	execute the sky preparation and GALFIT block ('execute' = true)
skymap	output object/sky-mapfile (file_name)
outsky	output filename for sky values (file_name)
1.5	scale factor by which SEx isophote is enlarged (for skymap)
2.0	scale factor by which SEx isophote is enlarged (for neighbours)
10	additional offset to scale factor
10	distance between individual sky isophotes
20	width of individual sky isophotes
10	gap between sextractor isophote and inner sky isophote
2.5	cut below which objects are considered as contributing
4	nobj_max; max number of allowed contributing sources
1.4	power by which the flux_radius is raised to convert to Re
15	calculate the slope of the sky from the x last determinations
0.48	zeropoint in log(fwhm_image) vs. mag_best below which object is star
5	magnitude faint end limit for secondaries when fitting galaxies
2	magnitude faint end limit for secondaries when fitting stars
1	number of neighbouring frames (see Barden 2012 for details)
1	maximum number of parallel processes (see Barden 2012 for details)
300	minimum distance (in arcseconds) between sources processed in parallel
80	minimum distance (in arcseconds) to already blocked objects
galaxies.txt	optional list containing primary targets (format: RA DEC)
1.0	search/correlation radius for the above list [arcsec]
GALFIT SETUP	
galfitm-1.2.1-linux-x86_64	Galfit executable including path
obj	object file preposition (file_name)
gf	preposition for GALFIT output files (file_name)
PSF.fits	PSF filename including path
128	convolution box size
0.55	plate scale of the images [arcsec/pixel]
400	constraint max Re
-8	constraint min magnitude deviation (minus)
8	constraint max magnitude deviation (plus)
0.2	constraint min sersic index
12	constraint max sersic index
4.0	GALFIT version string
input,model,residual,psf	string used to define the format of the galfit output files
240	time (in minutes) after which galfit processes are killed
0,0,12,3,3,2,2	x,y,mag,re,n,AR,PA order of Chebyshev polynomials
B/D DECOMPOSITION SETUP	
execute	execute the B/D fitting block
F01) 0,0,12,2,2,1,1	x,y,mag,re,n,AR,PA order of Chebyshev polynomials for BULGE
F02) 0,0,12,2,-1,1,1	x,y,mag,re,n,AR,PA order of Chebyshev polynomials
F03) bd1	additinal output label

B Data Tables

In this appendix, we present the tables with the photometric information of each galaxy and its components, as well as the parameters determined in this thesis. Details about how these parameters were determined are found in Section 3. Tables B.1, B.2, and B.3 list the galaxy, bulge and disc magnitudes, respectively. Tables B.4 and B.5 list the galaxy and the bulge Sérsic indexes, respectively. Table B.6 indicates the physical parameters (stellar mass, H_α luminosity, and specific star-formation rate) and the names in other catalogues of the 81 galaxies from Chapter 4. Table B.7 lists the B/T of the 52 galaxies analysed in Chapter 5. Finally, Tables B.8, B.9 and B.10 show the effective radius of the galaxies, bulge, and disc, respectively. Note that the parameters related to the bulge-disc decomposition refer to a subsample of 52 galaxies, for which we could reliably obtain a bulge-disc fit decomposition (see Chapter 5). Each galaxy has a unique ID, that remains unchanged in all the tables presented here, thus one can relate the general properties of a galaxy with a given ID with those of the bulge-disc decomposition by looking at the same ID in the corresponding tables.

Table B.1: Galaxy's magnitudes estimated in this thesis using the MEGAMORPH-GALAPAGOS2 project. Column 1 is the ID of each galaxy, and the columns 2 to 13 are the magnitudes in the 12 S-PLUS filters, without the correction for Galactic extinction.

ID	u	J0378	J0395	J0410	J0430	g	J0515	r	J0660	i	J0861	z
1	16.31±0.03	16.02±0.03	15.66±0.03	15.31±0.02	14.92±0.01	14.37±0.01	14.07±0.01	13.56±0.00	13.4 ±0.00	13.14±0.00	12.94±0.00	12.89±0.00
2	17.02±0.05	16.62±0.04	16.32±0.05	16.04±0.04	15.72±0.03	15.25±0.01	14.99±0.01	14.45±0.01	14.24±0.01	14.04±0.01	13.83±0.01	13.79±0.01
3	17.76±0.09	17.38±0.08	17.09±0.09	16.74±0.06	16.34±0.04	15.95±0.02	15.67±0.02	15.19±0.01	15.08±0.01	14.87±0.01	14.68±0.01	14.66±0.01
4	15.49±0.02	15.12±0.02	15.0 ±0.02	14.27±0.01	13.99±0.01	13.36±0.01	13.07±0.00	12.48±0.00	12.31±0.00	12.03±0.00	11.82±0.00	11.77±0.00
5	15.21±0.04	14.85±0.03	14.54±0.02	14.16±0.02	13.67±0.01	13.04±0.01	12.76±0.01	12.15±0.00	11.99±0.00	11.69±0.00	11.5 ±0.00	11.44±0.01
6	15.02±0.03	14.67±0.03	14.46±0.03	14.15±0.02	13.95±0.02	13.68±0.02	13.56±0.02	13.59±0.01	13.33±0.01	13.25±0.01	12.91±0.01	12.97±0.01
7	17.27±0.04	16.91±0.03	16.61±0.03	16.31±0.03	16.0 ±0.02	15.65±0.01	15.35±0.01	14.92±0.01	14.72±0.01	14.57±0.01	14.4 ±0.01	14.36±0.01
8	16.76±0.06	16.49±0.05	16.22±0.05	16.0 ±0.04	15.79±0.04	15.49±0.02	15.29±0.02	14.89±0.01	14.63±0.01	14.51±0.01	14.34±0.01	14.33±0.01
9	16.93±0.11	16.62±0.09	16.33±0.08	16.05±0.07	15.76±0.05	15.37±0.03	15.13±0.03	14.66±0.01	14.48±0.01	14.33±0.01	14.15±0.01	14.11±0.02
10	16.2 ±0.09	15.65±0.04	15.4 ±0.04	14.63±0.03	14.39±0.02	13.69±0.02	13.36±0.02	12.77±0.01	12.63±0.01	12.48±0.01	12.26±0.01	12.23±0.02
11	17.05±0.05	16.78±0.05	16.47±0.05	16.17±0.04	15.85±0.03	15.45±0.01	15.14±0.01	14.67±0.01	14.54±0.01	14.3 ±0.01	14.06±0.01	14.06±0.01
12	17.48±0.25	17.1 ±0.19	16.98±0.18	16.74±0.16	16.36±0.12	15.75±0.07	15.51±0.06	14.95±0.04	14.8 ±0.03	14.54±0.04	14.32±0.05	14.31±0.07
13	16.25±0.05	15.85±0.05	15.55±0.05	15.39±0.04	15.29±0.03	15.11±0.01	14.89±0.02	14.55±0.01	14.28±0.01	14.2 ±0.01	14.05±0.01	14.14±0.02
14	16.59±0.07	16.3 ±0.05	16.23±0.05	15.44±0.04	15.25±0.03	14.61±0.02	14.38±0.02	13.78±0.01	13.64±0.01	13.38±0.01	13.15±0.01	13.11±0.02
15	15.36±0.03	15.08±0.03	14.89±0.03	14.57±0.02	14.14±0.02	13.61±0.01	13.33±0.01	12.75±0.01	12.59±0.01	12.29±0.01	12.05±0.01	12.03±0.01
16	16.82±0.03	16.55±0.03	16.23±0.03	15.88±0.02	15.45±0.02	14.95±0.01	14.71±0.01	14.18±0.01	14.05±0.01	13.83±0.01	13.63±0.01	13.64±0.01
17	17.41±0.14	17.11±0.12	16.83±0.12	16.55±0.10	16.22±0.07	15.68±0.03	15.45±0.03	14.93±0.02	14.8 ±0.02	14.54±0.02	14.35±0.02	14.31±0.03
18	16.85±0.16	16.39±0.12	16.27±0.11	16.02±0.09	15.64±0.07	15.13±0.04	14.89±0.03	14.3 ±0.02	14.16±0.02	13.89±0.02	13.74±0.02	13.78±0.03
19	17.22±0.08	16.84±0.07	16.68±0.08	16.48±0.07	16.2 ±0.05	15.72±0.02	15.47±0.03	14.99±0.02	14.85±0.02	14.63±0.02	14.44±0.02	14.48±0.03
20	16.22±0.10	15.74±0.06	15.44±0.06	15.11±0.05	14.73±0.04	14.3 ±0.03	14.09±0.03	13.41±0.02	13.15±0.02	13.02±0.02	12.84±0.02	12.81±0.03
21	16.26±0.04	15.97±0.04	15.77±0.04	15.2 ±0.03	14.91±0.02	14.39±0.01	14.13±0.01	13.55±0.00	13.37±0.00	13.14±0.00	12.92±0.01	12.86±0.01
22	15.43±0.04	15.16±0.03	14.91±0.03	14.61±0.03	14.25±0.02	13.78±0.01	13.52±0.01	13.05±0.01	12.9 ±0.01	12.65±0.01	12.42±0.01	12.41±0.01
23	15.1 ±0.03	14.7 ±0.02	14.63±0.02	14.35±0.02	13.87±0.01	13.25±0.01	13.06±0.01	12.37±0.00	12.22±0.00	11.91±0.00	11.69±0.00	11.65±0.01
24	17.16±0.15	16.77±0.11	16.6 ±0.10	16.27±0.08	15.79±0.06	15.18±0.03	14.98±0.03	14.38±0.02	14.26±0.02	13.99±0.02	13.8 ±0.02	13.78±0.03
25	16.77±0.06	16.49±0.05	16.3 ±0.05	16.02±0.05	15.64±0.03	15.13±0.02	14.87±0.02	14.32±0.01	14.17±0.01	13.87±0.01	13.63±0.01	13.59±0.01
26	16.26±0.02	15.88±0.02	15.62±0.02	15.44±0.02	15.3 ±0.02	15.15±0.01	14.9 ±0.01	14.63±0.01	14.29±0.01	14.45±0.01	14.3 ±0.01	14.3 ±0.01
27	17.02±0.09	16.52±0.08	16.42±0.09	16.35±0.08	16.23±0.07	15.92±0.03	15.78±0.03	15.35±0.02	15.1 ±0.01	15.07±0.02	14.89±0.02	14.92±0.03
28	15.92±0.38	15.42±0.31	15.4 ±0.36	15.22±0.3	14.88±0.23	14.32±0.10	14.1 ±0.12	13.56±0.06	13.41±0.06	13.2 ±0.07	12.95±0.08	12.94±0.10
29	15.27±0.06	14.74±0.05	14.69±0.05	14.47±0.04	14.07±0.03	13.46±0.01	13.2 ±0.01	12.49±0.01	12.28±0.01	12.0 ±0.01	11.76±0.01	11.77±0.01
30	16.78±0.05	16.4 ±0.04	16.14±0.04	15.77±0.03	15.3 ±0.02	14.72±0.01	14.43±0.01	13.89±0.01	13.73±0.01	13.47±0.01	13.23±0.01	13.18±0.01
31	16.78±0.03	16.46±0.03	16.14±0.02	15.81±0.02	15.44±0.02	14.92±0.01	14.66±0.01	14.17±0.01	14.05±0.01	13.83±0.01	13.64±0.01	13.6 ±0.01
32	16.82±0.04	16.3 ±0.03	16.3 ±0.04	16.25±0.04	16.1 ±0.03	15.74±0.01	15.55±0.02	14.95±0.01	14.69±0.01	14.58±0.01	14.39±0.01	14.3 ±0.01
33	17.32±0.06	17.06±0.06	16.67±0.06	16.39±0.04	16.13±0.04	15.77±0.02	15.47±0.02	15.05±0.01	14.93±0.01	14.66±0.01	14.5 ±0.01	14.46±0.01
34	15.81±0.01	15.3 ±0.01	15.1 ±0.01	15.05±0.01	15.06±0.01	14.8 ±0.01	14.43±0.01	14.33±0.00	13.5 ±0.00	14.18±0.00	13.82±0.01	13.58±0.01
35	16.53±0.03	16.04±0.03	15.85±0.03	15.56±0.02	15.14±0.02	14.56±0.01	14.29±0.01	13.69±0.00	13.55±0.00	13.28±0.00	13.12±0.00	13.06±0.01
36	16.81±0.03	16.44±0.02	16.14±0.03	15.96±0.02	15.83±0.02	15.58±0.01	15.36±0.01	14.96±0.00	14.65±0.00	14.69±0.01	14.56±0.01	14.48±0.01
37	16.17±0.04	15.68±0.03	15.6 ±0.04	15.42±0.03	15.1 ±0.02	14.57±0.01	14.33±0.01	13.77±0.00	13.59±0.00	13.33±0.00	13.11±0.00	13.01±0.01
38	15.41±0.01	15.05±0.01	14.81±0.02	14.62±0.01	14.43±0.01	14.12±0.00	13.91±0.01	13.45±0.00	13.19±0.00	13.09±0.00	12.93±0.00	12.87±0.00
39	16.34±0.02	16.01±0.02	15.73±0.02	15.42±0.02	15.05±0.02	14.59±0.01	14.35±0.01	13.85±0.00	13.73±0.00	13.47±0.00	13.36±0.00	13.37±0.00
40	17.19±0.10	16.98±0.09	16.53±0.09	16.28±0.08	16.16±0.06	16.0 ±0.03	15.8 ±0.03	15.5 ±0.02	15.38±0.02	15.15±0.02	15.01±0.02	14.95±0.03
41	14.95±0.01	14.56±0.01	14.43±0.01	14.17±0.01	13.76±0.01	13.24±0.00	13.01±0.00	12.44±0.00	12.32±0.00	12.01±0.00	11.85±0.00	11.79±0.00
42	16.91±0.08	16.41±0.06	16.29±0.06	16.08±0.05	15.76±0.04	15.26±0.02	15.02±0.02	14.38±0.01	14.16±0.01	13.95±0.01	13.76±0.01	13.69±0.01
43	15.52±0.03	15.1 ±0.03	15.03±0.02	14.83±0.02	14.47±0.02	13.93±0.01	13.72±0.01	13.16±0.01	13.02±0.01	12.74±0.01	12.61±0.01	12.57±0.01
44	16.8 ±0.05	16.35±0.04	16.1 ±0.04	16.0 ±0.03	15.96±0.03	15.77±0.01	15.62±0.02	15.42±0.01	15.08±0.01	15.23±0.01	15.1 ±0.02	15.07±0.02
45	16.02±0.05	15.56±0.03	15.32±0.03	14.99±0.02	14.54±0.02	13.97±0.01	13.7 ±0.01	13.1 ±0.01	12.92±0.01	12.67±0.01	12.52±0.01	12.44±0.01
46	17.19±0.09	16.72±0.07	16.6 ±0.08	16.46±0.07	16.24±0.05	15.79±0.02	15.62±0.03	15.17±0.01	15.0 ±0.01	14.86±0.01	14.7 ±0.02	14.59±0.02

Continued on next page

Table B.1 – continued from previous page

ID	u	J0378	J0395	J0410	J0430	g	J0515	r	J0660	i	J0861	z
47	15.03±0.01	14.58±0.01	14.31±0.01	13.78±0.01	13.53±0.01	13.02±0.00	12.77±0.00	12.23±0.00	12.08±0.00	11.83±0.00	11.68±0.00	11.59±0.00
48	16.55±0.02	16.21±0.02	16.03±0.02	15.97±0.02	15.99±0.02	15.9 ±0.01	15.74±0.01	15.63±0.01	15.18±0.01	15.43±0.01	15.26±0.01	15.19±0.02
49	16.27±0.03	15.8 ±0.02	15.67±0.02	14.96±0.02	14.67±0.01	13.99±0.01	13.7 ±0.01	13.07±0.00	12.91±0.00	12.63±0.00	12.45±0.00	12.32±0.00
50	16.93±0.05	16.43±0.04	16.31±0.06	16.17±0.04	15.95±0.03	15.52±0.01	15.26±0.01	14.77±0.01	14.59±0.01	14.38±0.01	14.17±0.01	14.12±0.01
51	16.06±0.08	15.65±0.05	15.43±0.05	15.11±0.04	14.67±0.03	14.09±0.02	13.8 ±0.01	13.18±0.01	13.03±0.01	12.72±0.01	12.56±0.01	12.49±0.01
52	17.53±0.09	17.22±0.08	16.9 ±0.09	16.63±0.07	16.34±0.05	15.81±0.02	15.52±0.02	15.08±0.01	14.97±0.01	14.7 ±0.01	14.51±0.01	14.4 ±0.02
53	15.31±0.02	14.8 ±0.02	14.77±0.02	14.57±0.01	14.19±0.01	13.58±0.01	13.35±0.01	12.73±0.00	12.56±0.00	12.26±0.00	12.09±0.00	12.03±0.00
54	16.33±0.06	15.94±0.05	15.77±0.05	15.27±0.04	15.02±0.03	14.59±0.02	14.32±0.01	13.92±0.01	13.78±0.01	13.62±0.01	13.48±0.01	13.37±0.01
55	16.69±0.06	16.23±0.05	16.12±0.05	15.91±0.04	15.56±0.03	14.99±0.01	14.75±0.01	14.16±0.01	14.02±0.01	13.72±0.01	13.6 ±0.01	13.56±0.01
56	15.93±0.02	15.56±0.02	15.44±0.02	14.73±0.01	14.48±0.01	13.84±0.01	13.6 ±0.00	12.99±0.00	12.83±0.00	12.54±0.00	12.37±0.00	12.27±0.00
57	14.94±0.04	14.42±0.03	14.15±0.03	13.99±0.03	13.85±0.02	13.65±0.01	13.55±0.01	13.34±0.01	13.18±0.01	13.24±0.01	13.09±0.01	12.96±0.01
58	16.82±0.06	16.33±0.05	16.25±0.05	16.03±0.04	15.67±0.03	15.09±0.02	14.85±0.01	14.23±0.01	14.06±0.01	13.76±0.01	13.61±0.01	13.57±0.01
59	16.77±0.09	16.34±0.07	16.12±0.06	15.81±0.05	15.39±0.04	14.83±0.02	14.58±0.02	13.98±0.01	13.83±0.01	13.55±0.01	13.36±0.01	13.28±0.02
60	14.55±0.02	14.12±0.02	14.09±0.02	13.89±0.01	13.53±0.01	12.98±0.01	12.77±0.01	12.16±0.00	12.01±0.00	11.7 ±0.00	11.52±0.00	11.46±0.01
61	16.71±0.04	16.36±0.03	16.19±0.03	15.63±0.02	15.4 ±0.02	14.82±0.01	14.55±0.01	14.0 ±0.00	13.87±0.00	13.61±0.00	13.42±0.00	13.36±0.01
62	16.86±0.06	16.33±0.05	16.36±0.05	16.2 ±0.04	15.86±0.03	15.27±0.02	15.06±0.02	14.5 ±0.01	14.37±0.01	14.13±0.01	13.98±0.01	13.92±0.01
63	16.95±0.16	16.45±0.12	16.33±0.10	16.09±0.08	15.71±0.07	15.05±0.04	14.74±0.03	14.07±0.02	13.91±0.02	13.58±0.02	13.47±0.02	13.45±0.03
64	16.93±0.13	16.55±0.10	16.34±0.09	16.05±0.07	15.65±0.06	15.11±0.03	14.85±0.02	14.28±0.01	14.13±0.01	13.85±0.02	13.68±0.02	13.61±0.03
65	16.6 ±0.04	16.14±0.03	15.91±0.04	15.88±0.03	15.93±0.03	15.68±0.01	15.48±0.02	15.35±0.01	14.98±0.01	15.22±0.01	15.14±0.02	15.14±0.02
66	17.25±0.08	16.89±0.06	16.56±0.05	16.25±0.04	15.9 ±0.03	15.41±0.02	15.11±0.02	14.53±0.01	14.38±0.01	14.14±0.01	13.96±0.01	13.91±0.01
67	15.72±0.04	15.27±0.03	15.04±0.03	14.74±0.02	14.35±0.02	13.81±0.01	13.52±0.01	12.94±0.00	12.79±0.00	12.51±0.00	12.33±0.00	12.27±0.01
68	17.08±0.12	16.58±0.10	16.28±0.10	16.02±0.08	15.77±0.06	15.44±0.03	15.12±0.03	14.77±0.01	14.64±0.01	14.4 ±0.01	14.19±0.02	14.11±0.02
69	15.7 ±0.07	15.35±0.06	15.28±0.06	15.09±0.05	14.8 ±0.04	14.42±0.02	14.19±0.02	13.54±0.01	13.31±0.01	12.82±0.02	12.52±0.02	12.39±0.03
70	16.38±0.05	15.83±0.04	15.85±0.05	15.72±0.04	15.44±0.03	14.92±0.01	14.69±0.01	14.08±0.01	13.94±0.01	13.67±0.01	13.52±0.01	13.49±0.01
71	15.94±0.02	15.44±0.01	15.53±0.01	15.4 ±0.02	15.06±0.01	14.4 ±0.00	14.25±0.00	13.74±0.00	13.61±0.00	13.35±0.00	13.18±0.00	13.11±0.00
72	16.18±0.07	15.71±0.06	15.68±0.08	15.19±0.05	14.98±0.04	14.5 ±0.02	14.23±0.02	13.77±0.01	13.63±0.01	13.33±0.01	13.15±0.01	13.08±0.02
73	16.58±0.03	16.13±0.02	15.95±0.03	15.68±0.02	15.31±0.01	14.8 ±0.01	14.57±0.01	14.01±0.00	13.86±0.00	13.57±0.00	13.39±0.00	13.32±0.00
74	14.29±0.02	13.9 ±0.01	13.61±0.01	13.28±0.01	12.85±0.01	12.28±0.01	12.04±0.00	11.47±0.00	11.32±0.00	11.03±0.00	10.85±0.00	10.75±0.00
75	16.9 ±0.01	16.52±0.00	16.19±0.00	15.86±0.00	15.5 ±0.00	14.95±0.00	14.64±0.00	14.12±0.00	13.97±0.00	13.7 ±0.00	13.53±0.00	13.44±0.00
76	16.17±0.04	15.76±0.03	15.71±0.04	15.55±0.03	15.27±0.02	14.77±0.01	14.57±0.01	14.01±0.00	13.87±0.00	13.6 ±0.00	13.43±0.01	13.38±0.01
77	16.39±0.04	16.0 ±0.03	15.68±0.03	15.35±0.02	14.96±0.02	14.44±0.01	14.15±0.01	13.6 ±0.00	13.46±0.00	13.24±0.01	13.09±0.01	13.03±0.01
78	17.76±0.04	17.46±0.03	17.22±0.04	16.6 ±0.02	16.39±0.02	15.8 ±0.01	15.53±0.01	14.98±0.00	14.83±0.00	14.56±0.00	14.4 ±0.00	14.31±0.01
79	17.6 ±0.04	17.26±0.04	16.93±0.05	16.62±0.03	16.27±0.02	15.82±0.01	15.53±0.01	15.03±0.00	14.88±0.00	14.66±0.00	14.5 ±0.01	14.45±0.01
80	16.17±0.05	15.73±0.04	15.68±0.04	15.49±0.04	15.15±0.03	14.59±0.01	14.35±0.01	13.75±0.01	13.55±0.00	13.3 ±0.01	13.1 ±0.01	13.03±0.01
81	16.49±0.02	16.04±0.01	15.63±0.01	15.26±0.01	14.86±0.01	14.27±0.00	13.98±0.00	13.38±0.00	13.24±0.00	12.95±0.00	12.76±0.00	12.63±0.00

Table B.2: Bulge's magnitudes estimated in this thesis using the MEGAMORPH-GALAPAGOS2 project. Column 1 is the ID of each galaxy, and columns 2 to 13 are the magnitudes in the 12 S-PLUS filters, without the correction for Galactic extinction.

ID	u	J0378	J0395	J0410	J0430	g	J0515	r	J0660	i	J0861	z
1	17.52±0.16	17.11±0.15	16.7 ±0.16	16.41±0.13	16.19±0.10	15.98±0.05	15.68±0.06	15.03±0.03	14.85±0.03	14.5 ±0.04	14.2 ±0.05	14.11±0.05
2	17.77±0.11	17.35±0.1	17.1 ±0.13	16.77±0.09	16.42±0.07	16.01±0.05	15.7 ±0.05	15.18±0.03	14.96±0.02	14.78±0.02	14.53±0.03	14.51±0.03
3	19.95±0.51	18.65±0.32	19.02±0.68	18.9 ±0.63	18.4 ±0.47	17.84±0.22	17.5 ±0.29	16.29±0.12	16.34±0.14	15.73±0.16	15.36±0.2	15.29±0.21
4	16.7 ±0.03	16.34±0.02	16.22±0.02	15.49±0.02	15.24±0.02	14.63±0.01	14.36±0.01	13.86±0.01	13.7 ±0.01	13.44±0.01	13.2 ±0.01	13.15±0.01
5	15.63±0.07	15.18±0.05	15.18±0.05	14.33±0.04	14.04±0.04	13.36±0.03	13.08±0.02	12.51±0.02	12.36±0.02	12.09±0.01	11.91±0.02	11.87±0.02
6	17.82±0.04	17.48±0.04	17.2 ±0.04	17.02±0.04	16.8 ±0.03	16.41±0.02	16.2 ±0.02	15.6 ±0.01	15.02±0.01	15.15±0.01	14.81±0.01	14.62±0.01
9	18.21±0.15	18.34±0.17	17.79±0.17	17.52±0.15	17.38±0.15	17.06±0.14	17.0 ±0.14	16.74±0.13	16.53±0.13	16.86±0.09	17.0 ±0.04	17.14±0.02
10	17.78±0.03	17.45±0.03	17.28±0.04	16.54±0.03	16.31±0.02	15.66±0.01	15.34±0.01	14.74±0.01	14.58±0.01	14.39±0.01	14.1 ±0.01	14.12±0.01
11	17.75±0.19	17.24±0.17	16.98±0.19	16.73±0.16	16.46±0.13	16.07±0.06	15.71±0.06	15.19±0.03	15.05±0.03	14.79±0.03	14.54±0.04	14.43±0.04
14	17.48±0.06	17.18±0.06	17.12±0.08	16.32±0.05	16.1 ±0.05	15.47±0.03	15.27±0.03	14.66±0.02	14.55±0.02	14.25±0.02	13.98±0.02	13.91±0.02
15	16.21±0.06	15.96±0.06	15.98±0.06	15.21±0.05	14.9 ±0.05	14.32±0.04	14.05±0.03	13.55±0.02	13.42±0.02	13.16±0.02	12.89±0.03	12.83±0.03
17	19.65±0.3	19.7 ±0.38	19.04±0.32	18.31±0.21	18.43±0.21	17.81±0.11	17.6 ±0.11	17.08±0.06	17.03±0.06	16.73±0.05	16.47±0.07	16.55±0.09
19	19.03±0.39	19.07±0.44	18.26±0.32	17.87±0.25	17.71±0.24	17.03±0.15	16.72±0.13	16.12±0.09	15.96±0.09	15.8 ±0.08	15.63±0.1	15.66±0.14
20	18.1 ±0.5	17.92±0.44	17.41±0.42	17.07±0.39	16.77±0.36	16.31±0.29	16.15±0.25	15.32±0.15	14.98±0.13	14.98±0.1	14.93±0.11	15.24±0.09
21	18.24±0.17	18.29±0.2	18.19±0.23	17.48±0.16	17.03±0.13	16.7 ±0.09	16.66±0.08	16.13±0.04	16.04±0.04	15.81±0.04	15.46±0.05	15.42±0.07
22	17.43±0.03	17.12±0.03	17.12±0.04	16.27±0.02	16.02±0.02	15.45±0.01	15.17±0.01	14.66±0.0	14.53±0.0	14.35±0.0	14.12±0.01	14.12±0.01
24	17.81±0.27	17.5 ±0.22	17.17±0.2	16.77±0.17	16.27±0.15	15.64±0.1	15.43±0.08	14.79±0.05	14.68±0.05	14.39±0.04	14.21±0.05	14.2 ±0.07
25	18.4 ±0.19	17.73±0.14	17.52±0.12	16.7 ±0.11	16.58±0.09	15.72±0.05	15.33±0.05	14.65±0.03	14.5 ±0.02	14.15±0.02	13.83±0.02	13.75±0.03
30	18.53±0.08	18.16±0.08	18.2 ±0.08	17.41±0.06	17.12±0.05	16.48±0.04	16.2 ±0.03	15.7 ±0.02	15.6 ±0.02	15.38±0.02	15.18±0.02	15.18±0.02
32	18.39±0.05	18.03±0.06	17.68±0.07	17.3 ±0.05	17.19±0.04	16.76±0.02	16.44±0.02	15.82±0.01	15.47±0.01	15.42±0.01	15.2 ±0.01	15.13±0.01
33	18.42±0.23	18.08±0.2	17.72±0.2	17.46±0.18	17.21±0.17	16.78±0.14	16.43±0.13	15.99±0.12	15.86±0.12	15.57±0.11	15.39±0.11	15.37±0.12
35	17.29±0.04	16.77±0.04	16.56±0.04	15.96±0.03	15.73±0.03	15.15±0.02	14.82±0.01	14.24±0.01	14.1 ±0.01	13.84±0.01	13.68±0.01	13.59±0.01
37	17.83±0.14	17.42±0.13	17.31±0.17	16.6 ±0.11	16.44±0.1	15.91±0.06	15.62±0.05	15.05±0.02	14.89±0.02	14.56±0.02	14.34±0.03	14.25±0.03
39	16.81±0.04	16.43±0.04	16.29±0.04	15.61±0.03	15.4 ±0.03	14.86±0.02	14.58±0.02	14.08±0.01	13.98±0.01	13.78±0.01	13.74±0.01	13.76±0.01
40	19.05±0.22	18.68±0.21	18.73±0.31	18.54±0.26	18.14±0.19	17.6 ±0.11	17.38±0.11	17.07±0.07	17.0 ±0.07	16.75±0.07	16.62±0.11	16.44±0.13
42	19.32±0.23	19.09±0.24	18.43±0.23	18.16±0.21	18.07±0.2	17.73±0.16	17.41±0.14	16.66±0.07	16.18±0.06	15.87±0.07	15.34±0.08	15.07±0.09
43	16.62±0.03	16.25±0.02	16.13±0.03	15.44±0.02	15.16±0.02	14.58±0.01	14.34±0.01	13.81±0.01	13.67±0.01	13.42±0.01	13.27±0.01	13.17±0.01
44	18.65±0.12	18.17±0.11	17.97±0.13	17.67±0.1	17.77±0.1	17.67±0.06	17.4 ±0.07	17.25±0.04	16.74±0.04	17.08±0.06	17.01±0.1	17.02±0.12
45	17.56±0.13	16.96±0.1	16.89±0.09	16.22±0.07	15.94±0.06	15.23±0.04	14.9 ±0.03	14.25±0.02	14.02±0.02	13.78±0.02	13.66±0.02	13.61±0.03

Continued on next page

Table B.2 – continued from previous page

ID	u	J0378	J0395	J0410	J0430	g	J0515	r	J0660	i	J0861	z
46	18.98±0.1	18.65±0.1	18.26±0.12	18.06±0.09	18.0 ±0.08	17.78±0.05	17.55±0.05	17.15±0.02	16.8 ±0.02	16.79±0.03	16.59±0.04	16.5 ±0.05
47	16.49±0.01	16.01±0.01	15.69±0.01	15.18±0.01	14.99±0.01	14.49±0.0	14.25±0.0	13.71±0.0	13.53±0.0	13.26±0.0	13.06±0.0	12.94±0.0
48	18.06±0.13	18.08±0.16	17.61±0.16	17.62±0.15	17.9 ±0.18	17.77±0.09	17.55±0.1	17.72±0.05	16.6 ±0.03	18.07±0.15	19.65±1.08	20.55±2.32
49	17.04±0.03	16.63±0.03	16.51±0.03	15.74±0.02	15.52±0.02	14.87±0.01	14.6 ±0.01	14.0 ±0.01	13.82±0.01	13.54±0.01	13.35±0.01	13.27±0.01
51	17.58±0.05	17.18±0.04	17.07±0.04	16.38±0.03	16.15±0.03	15.54±0.02	15.26±0.02	14.74±0.01	14.6 ±0.01	14.33±0.01	14.14±0.01	14.04±0.01
53	16.41±0.03	16.02±0.03	15.76±0.02	15.21±0.02	14.95±0.02	14.36±0.02	14.09±0.01	13.55±0.01	13.4 ±0.01	13.17±0.01	13.04±0.01	12.99±0.01
54	18.85±0.12	18.3 ±0.11	18.12±0.11	17.66±0.09	17.38±0.08	16.81±0.06	16.45±0.05	15.95±0.03	15.78±0.03	15.46±0.03	15.24±0.03	15.14±0.04
55	17.67±0.12	17.22±0.11	17.05±0.11	16.81±0.1	16.45±0.09	15.86±0.06	15.6 ±0.05	15.09±0.03	14.94±0.03	14.68±0.02	14.51±0.03	14.41±0.03
56	16.82±0.03	16.39±0.03	16.18±0.03	15.49±0.02	15.23±0.02	14.55±0.02	14.27±0.01	13.62±0.01	13.45±0.01	13.15±0.01	12.98±0.01	12.9 ±0.01
57	17.04±0.06	16.88±0.07	16.43±0.08	16.23±0.07	16.17±0.06	16.05±0.05	15.84±0.05	15.65±0.04	15.42±0.04	15.88±0.04	16.12±0.04	16.12±0.03
58	18.01±0.11	17.63±0.09	17.01±0.1	16.66±0.06	16.27±0.05	15.65±0.02	15.3 ±0.02	14.7 ±0.01	14.52±0.01	14.27±0.01	14.17±0.01	14.11±0.02
59	17.18±0.12	16.81±0.1	16.63±0.11	15.99±0.08	15.79±0.07	15.23±0.04	15.0 ±0.03	14.44±0.02	14.3 ±0.02	14.05±0.02	13.9 ±0.02	13.82±0.03
61	17.15±0.05	16.73±0.04	16.66±0.04	16.04±0.04	15.8 ±0.03	15.15±0.02	14.86±0.02	14.28±0.01	14.14±0.01	13.89±0.01	13.71±0.01	13.65±0.01
63	18.88±0.1	18.41±0.08	18.24±0.08	17.64±0.07	17.46±0.06	16.82±0.04	16.5 ±0.03	15.93±0.02	15.76±0.02	15.42±0.02	15.19±0.02	15.05±0.03
66	18.32±0.06	18.13±0.06	17.8 ±0.07	17.24±0.05	17.15±0.05	16.74±0.04	16.48±0.03	16.1 ±0.01	15.94±0.01	15.66±0.02	15.28±0.02	15.09±0.03
67	17.17±0.03	16.76±0.03	16.57±0.03	15.91±0.02	15.67±0.02	15.11±0.01	14.81±0.01	14.28±0.01	14.13±0.01	13.88±0.01	13.67±0.01	13.58±0.01
73	18.28±0.24	17.55±0.18	17.26±0.16	16.61±0.14	16.37±0.12	15.59±0.08	15.21±0.06	14.43±0.03	14.23±0.02	13.84±0.02	13.6 ±0.02	13.49±0.02
74	15.38±0.02	15.02±0.02	14.96±0.02	14.22±0.02	13.96±0.02	13.36±0.01	13.14±0.01	12.61±0.01	12.47±0.01	12.19±0.01	11.96±0.01	11.83±0.01
75	17.82±0.03	17.45±0.03	17.24±0.04	16.66±0.03	16.46±0.02	15.85±0.02	15.53±0.02	14.98±0.01	14.82±0.01	14.54±0.01	14.36±0.01	14.27±0.01
77	17.28±0.07	16.9 ±0.06	16.53±0.05	16.01±0.04	15.71±0.03	15.09±0.02	14.73±0.02	14.07±0.01	13.9 ±0.01	13.6 ±0.01	13.37±0.01	13.26±0.01
78	18.41±0.09	17.92±0.08	17.62±0.08	16.99±0.06	16.84±0.06	16.21±0.05	15.9 ±0.04	15.36±0.04	15.2 ±0.04	14.94±0.03	14.8 ±0.04	14.73±0.05
80	18.97±0.21	18.84±0.22	18.48±0.24	18.19±0.2	17.88±0.17	17.26±0.13	16.95±0.12	16.2 ±0.06	15.8 ±0.05	15.6 ±0.05	15.26±0.06	15.1 ±0.06
81	17.96±0.05	17.48±0.05	17.25±0.05	16.66±0.04	16.41±0.03	15.81±0.02	15.53±0.02	14.93±0.01	14.79±0.01	14.53±0.01	14.41±0.01	14.34±0.02

Table B.3: Disc's magnitudes estimated in this thesis using the MEGAMORPH-GALAPAGOS2 project. Column 1 is the ID of each galaxy, and columns 2 to 13 are the magnitudes in the 12 S-PLUS filters, without the correction for Galactic extinction.

ID	u	J0378	J0395	J0410	J0430	g	J0515	r	J0660	i	J0861	z
1	16.67±0.06	16.43±0.06	16.05±0.06	15.66±0.05	15.21±0.03	14.56±0.01	14.25±0.01	13.74±0.0	13.57±0.0	13.31±0.0	13.1 ±0.0	13.04±0.0
2	17.77±0.15	17.37±0.15	17.13±0.19	16.63±0.13	16.53±0.11	15.91±0.05	15.71±0.06	15.13±0.03	14.94±0.03	14.72±0.02	14.56±0.03	14.47±0.03
3	17.95±0.11	17.99±0.2	17.32±0.16	16.86±0.12	16.51±0.08	16.11±0.03	15.83±0.04	15.42±0.02	15.27±0.02	15.08±0.01	14.88±0.02	14.84±0.01
4	16.01±0.03	15.7 ±0.03	15.63±0.04	14.9 ±0.03	14.6 ±0.02	14.0 ±0.01	13.76±0.01	13.11±0.0	12.96±0.0	12.7 ±0.0	12.51±0.0	12.43±0.01
5	16.56±0.19	16.75±0.25	16.12±0.16	15.89±0.18	16.04±0.2	15.32±0.11	15.23±0.11	14.43±0.06	14.25±0.05	13.97±0.05	13.82±0.06	13.57±0.07
6	16.75±0.05	16.35±0.05	16.22±0.07	15.63±0.04	15.37±0.03	14.91±0.01	14.57±0.01	14.05±0.0	13.92±0.0	13.66±0.0	13.48±0.01	13.49±0.01
9	17.73±0.08	17.19±0.06	16.92±0.08	16.66±0.06	16.39±0.05	15.99±0.02	15.67±0.03	15.19±0.02	15.07±0.02	14.79±0.01	14.59±0.01	14.53±0.01
10	16.44±0.05	16.08±0.06	15.88±0.08	15.23±0.05	15.13±0.04	14.47±0.01	14.19±0.02	13.62±0.01	13.5 ±0.01	13.22±0.0	13.08±0.01	12.94±0.01
11	18.0 ±0.12	17.98±0.17	17.46±0.16	17.01±0.12	16.6 ±0.08	16.15±0.03	15.85±0.04	15.44±0.02	15.34±0.02	15.16±0.02	14.94±0.03	15.01±0.03
14	17.68±0.07	17.38±0.08	17.29±0.11	16.52±0.07	16.39±0.06	15.77±0.02	15.48±0.03	14.97±0.02	14.81±0.02	14.61±0.01	14.44±0.02	14.42±0.02
15	16.84±0.1	16.32±0.09	16.22±0.11	15.55±0.08	15.4 ±0.07	14.85±0.05	14.54±0.05	13.95±0.03	13.78±0.03	13.53±0.03	13.36±0.03	13.3 ±0.04
17	17.76±0.12	17.27±0.11	17.55±0.22	16.8 ±0.12	16.66±0.1	16.02±0.03	15.79±0.04	15.26±0.01	15.1 ±0.01	14.88±0.01	14.74±0.02	14.62±0.02
19	17.78±0.16	17.02±0.1	17.48±0.26	16.87±0.17	16.53±0.11	16.15±0.07	15.86±0.07	15.45±0.05	15.35±0.05	15.09±0.04	14.9 ±0.05	14.91±0.06
20	16.65±0.04	16.22±0.03	15.89±0.04	15.59±0.03	15.29±0.03	14.98±0.02	14.77±0.02	14.33±0.01	14.17±0.01	14.02±0.01	13.85±0.02	13.69±0.02
21	16.53±0.04	16.12±0.04	15.91±0.05	15.4 ±0.03	15.2 ±0.03	14.63±0.01	14.32±0.01	13.76±0.0	13.57±0.0	13.33±0.0	13.14±0.01	13.07±0.01
22	15.87±0.03	15.51±0.04	15.35±0.05	14.84±0.03	14.69±0.03	14.18±0.01	13.86±0.01	13.41±0.0	13.27±0.0	13.02±0.0	12.82±0.01	12.74±0.0
24	18.11±0.41	17.51±0.26	17.7 ±0.42	17.59±0.47	17.26±0.43	16.78±0.3	16.46±0.22	16.1 ±0.16	15.88±0.14	15.8 ±0.15	15.52±0.16	15.34±0.18
25	17.01±0.12	17.02±0.15	17.49±0.3	16.99±0.24	16.39±0.13	16.36±0.1	16.3 ±0.13	15.87±0.06	15.68±0.06	15.49±0.05	15.37±0.07	15.33±0.08
30	17.24±0.04	16.83±0.04	16.82±0.06	16.09±0.03	15.86±0.03	15.31±0.01	15.02±0.01	14.49±0.01	14.29±0.01	14.04±0.01	13.87±0.01	13.8 ±0.01
32	17.94±0.14	17.71±0.16	17.23±0.2	17.06±0.15	16.54±0.09	16.1 ±0.02	15.89±0.04	15.4 ±0.01	15.33±0.02	15.04±0.01	14.94±0.02	14.79±0.02
33	18.36±0.35	17.96±0.29	17.54±0.29	17.21±0.22	16.91±0.18	16.48±0.13	16.21±0.13	15.75±0.11	15.64±0.11	15.45±0.12	15.3 ±0.12	15.13±0.12
35	17.67±0.05	17.42±0.07	17.62±0.14	16.7 ±0.06	16.41±0.04	15.78±0.02	15.63±0.02	15.04±0.01	14.92±0.01	14.68±0.01	14.52±0.01	14.51±0.02
37	16.93±0.03	16.62±0.04	16.43±0.06	15.86±0.03	15.65±0.03	15.1 ±0.01	14.83±0.01	14.27±0.0	14.07±0.0	13.82±0.0	13.61±0.01	13.51±0.01
39	17.98±0.17	18.02±0.25	18.06±0.4	17.56±0.28	16.92±0.15	16.55±0.09	16.44±0.1	15.84±0.04	15.74±0.04	15.25±0.04	14.83±0.03	14.7 ±0.03
40	17.65±0.1	17.59±0.13	16.7 ±0.1	16.39±0.07	16.43±0.07	16.43±0.04	16.22±0.05	15.83±0.02	15.69±0.02	15.53±0.02	15.36±0.03	15.32±0.04
42	17.49±0.05	17.15±0.05	16.89±0.07	16.54±0.05	16.1 ±0.04	15.62±0.02	15.38±0.02	14.82±0.01	14.75±0.01	14.49±0.01	14.39±0.02	14.39±0.03
43	17.0 ±0.06	16.7 ±0.07	16.72±0.11	16.0 ±0.06	15.78±0.05	15.16±0.02	14.92±0.02	14.33±0.01	14.22±0.01	13.92±0.01	13.82±0.01	13.78±0.02
44	17.26±0.05	16.79±0.05	16.59±0.07	16.41±0.05	16.15±0.04	15.99±0.02	15.8 ±0.03	15.61±0.01	15.36±0.01	15.46±0.01	15.37±0.03	15.35±0.03
45	16.73±0.04	16.41±0.04	16.36±0.05	15.65±0.03	15.35±0.02	14.87±0.01	14.68±0.01	14.13±0.01	14.03±0.01	13.78±0.01	13.65±0.01	13.56±0.01
46	18.01±0.15	17.61±0.16	17.43±0.22	16.81±0.12	16.63±0.1	16.04±0.02	15.82±0.04	15.36±0.01	15.31±0.01	15.06±0.01	14.95±0.02	14.82±0.02
47	15.4 ±0.01	15.02±0.01	14.85±0.02	14.31±0.01	14.0 ±0.01	13.51±0.0	13.28±0.0	12.77±0.0	12.65±0.0	12.41±0.0	12.29±0.0	12.2 ±0.0
48	17.08±0.04	16.51±0.04	16.51±0.06	16.35±0.05	16.11±0.04	16.03±0.02	15.85±0.03	15.63±0.01	15.44±0.01	15.41±0.01	15.23±0.02	15.18±0.01
49	16.85±0.05	16.48±0.05	16.4 ±0.07	15.99±0.05	15.59±0.03	14.99±0.01	14.72±0.02	14.08±0.01	13.93±0.01	13.65±0.01	13.55±0.01	13.36±0.01
51	16.8 ±0.04	16.51±0.05	16.45±0.08	15.7 ±0.04	15.5 ±0.03	14.96±0.02	14.72±0.02	14.12±0.01	14.0 ±0.01	13.7 ±0.01	13.56±0.01	13.45±0.01
53	16.81±0.07	16.37±0.07	16.76±0.16	15.63±0.06	15.34±0.05	14.58±0.02	14.25±0.02	13.59±0.01	13.44±0.01	13.07±0.01	12.86±0.01	12.73±0.01
54	16.79±0.03	16.51±0.03	16.35±0.05	15.81±0.03	15.58±0.02	15.21±0.01	14.99±0.01	14.56±0.01	14.4 ±0.01	14.27±0.01	14.18±0.01	14.09±0.01
55	17.63±0.17	17.19±0.16	16.9 ±0.17	16.56±0.12	16.16±0.09	15.75±0.06	15.53±0.06	14.93±0.03	14.84±0.03	14.49±0.03	14.34±0.03	14.25±0.03
56	16.7 ±0.06	16.44±0.06	16.7 ±0.12	15.77±0.06	15.47±0.04	14.91±0.03	14.72±0.03	14.13±0.02	14.04±0.02	13.76±0.02	13.6 ±0.02	13.43±0.02
57	15.7 ±0.02	15.09±0.02	14.8 ±0.03	14.59±0.02	14.41±0.02	14.21±0.01	14.08±0.01	13.8 ±0.0	13.64±0.0	13.61±0.0	13.47±0.01	13.38±0.01
58	18.17±0.11	17.62±0.1	18.24±0.28	16.94±0.08	16.85±0.07	16.27±0.03	16.1 ±0.03	15.47±0.01	15.37±0.01	15.08±0.01	14.87±0.02	14.81±0.02
59	18.08±0.17	17.7 ±0.16	17.86±0.3	17.3 ±0.17	16.89±0.11	16.24±0.04	16.0 ±0.05	15.35±0.02	15.22±0.02	14.93±0.02	14.75±0.02	14.7 ±0.03

Continued on next page

Table B.3 – continued from previous page

ID	u	J0378	J0395	J0410	J0430	g	J0515	r	J0660	i	J0861	z
61	18.29±0.2	18.4 ±0.3	17.41±0.19	17.12±0.15	16.89±0.12	16.78±0.08	16.58±0.09	16.05±0.04	16.01±0.04	15.69±0.04	15.52±0.06	15.37±0.07
63	17.74±0.08	17.3 ±0.08	17.31±0.13	16.57±0.07	16.27±0.05	15.68±0.02	15.39±0.02	14.81±0.01	14.68±0.01	14.42±0.01	14.3 ±0.02	14.24±0.02
66	18.26±0.1	17.79±0.09	17.84±0.17	17.23±0.1	16.76±0.06	16.2 ±0.03	15.95±0.03	15.28±0.01	15.16±0.01	14.92±0.01	14.83±0.02	14.86±0.03
67	16.43±0.03	16.06±0.04	15.73±0.05	15.33±0.03	15.07±0.02	14.57±0.01	14.24±0.01	13.72±0.01	13.59±0.01	13.31±0.0	13.13±0.01	13.07±0.01
73	17.17±0.09	16.95±0.13	16.94±0.17	16.2 ±0.11	15.97±0.1	15.63±0.09	15.57±0.09	15.28±0.07	15.31±0.07	15.33±0.08	15.51±0.1	15.51±0.1
74	15.03±0.03	14.43±0.02	14.4 ±0.03	13.76±0.02	13.6 ±0.02	12.96±0.01	12.66±0.01	12.04±0.01	11.92±0.01	11.62±0.01	11.48±0.01	11.37±0.01
75	17.78±0.08	17.3 ±0.07	17.1 ±0.1	16.62±0.06	16.25±0.04	15.71±0.02	15.43±0.02	14.92±0.01	14.8 ±0.01	14.52±0.01	14.36±0.02	14.28±0.02
77	17.44±0.13	16.97±0.09	17.19±0.16	16.56±0.1	16.3 ±0.08	15.81±0.04	15.75±0.05	15.34±0.03	15.35±0.03	15.23±0.02	15.25±0.03	15.4 ±0.04
78	18.05±0.12	18.56±0.29	18.79±0.53	18.39±0.42	17.47±0.17	17.08±0.13	17.06±0.16	16.38±0.11	16.31±0.12	15.99±0.11	15.75±0.11	15.6 ±0.13
80	16.78±0.03	16.38±0.03	16.1 ±0.04	15.77±0.03	15.36±0.02	14.85±0.01	14.58±0.01	14.06±0.01	13.94±0.01	13.69±0.01	13.55±0.01	13.48±0.01
81	17.13±0.05	16.8 ±0.06	16.7 ±0.09	16.03±0.05	15.7 ±0.04	15.15±0.02	14.85±0.02	14.31±0.01	14.2 ±0.01	13.9 ±0.01	13.72±0.01	13.61±0.01

Table B.4: Galaxy's Sérsic indexes estimated in this thesis using the MEGAMORPH-GALAPAGOS2 project. Column 1 is the ID of each galaxy, and the columns 2 to 13 are the Sérsic indexes in the 12 S-PLUS filters.

ID	u	J0378	J0395	J0410	J0430	g	J0515	r	J0660	i	J0861	z
1	0.85±0.02	0.88±0.02	0.9 ±0.01	0.91±0.01	0.93±0.01	0.97±0.01	0.99±0.00	1.05±0.00	1.07±0.00	1.11±0.00	1.15±0.00	1.17±0.00
2	1.00±0.04	1.00±0.03	1.00±0.03	1.00±0.02	1.00±0.02	1.02±0.01	1.03±0.01	1.07±0.01	1.08±0.01	1.1±0.00	1.09±0.01	1.06±0.01
3	1.08±0.08	1.05±0.06	1.04±0.05	1.03±0.05	1.03±0.04	1.03±0.02	1.04±0.02	1.11±0.01	1.13±0.01	1.19±0.01	1.18±0.01	1.13±0.01
4	3.51±0.06	3.53±0.05	3.54±0.04	3.56±0.03	3.58±0.03	3.64±0.02	3.69±0.01	3.85±0.01	3.9 ±0.01	4.01±0.01	4.04±0.01	4.01±0.01
5	4.00±0.09	4.14±0.06	4.21±0.05	4.27±0.05	4.35±0.04	4.53±0.02	4.64±0.02	4.91±0.01	4.97±0.01	5.08±0.01	5.09±0.01	5.06±0.02
6	10.27±0.15	9.22±0.12	8.68±0.10	8.23±0.09	7.66±0.08	6.41±0.05	5.69±0.04	4.1±0.02	3.8 ±0.02	3.31±0.02	3.31±0.01	3.42±0.02
7	0.81±0.03	0.88±0.02	0.91±0.02	0.94±0.02	0.97±0.01	1.05±0.01	1.10±0.01	1.20±0.01	1.22±0.01	1.28±0.01	1.33±0.01	1.37±0.01
8	1.58±0.05	1.4 ±0.04	1.32±0.03	1.25±0.03	1.17±0.02	1.02±0.01	0.95±0.01	0.87±0.01	0.87±0.01	0.92±0.01	0.93±0.01	0.9±0.01
9	3.45±0.22	3.52±0.17	3.54±0.15	3.56±0.13	3.57±0.10	3.55±0.06	3.51±0.05	3.31±0.03	3.23±0.02	3.07±0.02	3.10±0.02	3.21±0.03
10	4.43±0.17	5.23±0.13	5.61±0.11	5.92±0.10	6.29±0.08	6.96±0.07	7.26±0.06	7.5±0.04	7.42±0.03	6.98±0.04	6.69±0.04	6.7±0.06
11	2.14±0.10	2.07±0.08	2.05±0.07	2.03±0.06	2.01±0.05	1.98±0.03	1.98±0.02	2.04±0.01	2.07±0.01	2.16±0.01	2.17±0.02	2.13±0.02
12	2.19±0.3	2.29±0.22	2.33±0.19	2.38±0.16	2.43±0.13	2.54±0.08	2.61±0.07	2.75±0.05	2.78±0.04	2.82±0.05	2.8 ±0.06	2.79±0.08
13	1.34±0.04	1.16±0.03	1.08±0.03	1.01±0.02	0.94±0.02	0.82±0.01	0.79±0.01	0.86±0.01	0.91±0.01	1.08±0.01	1.13±0.01	1.08±0.01
14	3.52±0.23	3.64±0.17	3.7 ±0.14	3.75±0.12	3.81±0.10	3.95±0.06	4.03±0.05	4.22±0.04	4.26±0.04	4.36±0.04	4.42±0.04	4.45±0.06
15	3.21±0.08	3.19±0.06	3.18±0.05	3.18±0.04	3.18±0.03	3.22±0.02	3.26±0.02	3.46±0.01	3.53±0.01	3.69±0.01	3.72±0.01	3.67±0.02
16	2.08±0.07	2.12±0.05	2.14±0.04	2.15±0.04	2.17±0.03	2.2±0.02	2.21±0.01	2.23±0.01	2.22±0.01	2.2±0.01	2.18±0.01	2.17±0.02
17	2.22±0.14	2.15±0.10	2.12±0.09	2.09±0.07	2.07±0.06	2.02±0.03	2.01±0.03	2.03±0.02	2.05±0.01	2.1±0.02	2.09±0.02	2.05±0.03
18	3.24±0.35	3.29±0.26	3.33±0.22	3.37±0.19	3.42±0.15	3.56±0.09	3.67±0.07	3.99±0.05	4.08±0.05	4.2±0.05	4.06±0.06	3.87±0.08
19	1.8 ±0.08	1.77±0.06	1.75±0.05	1.74±0.05	1.72±0.04	1.7±0.02	1.7 ±0.02	1.71±0.01	1.72±0.01	1.75±0.01	1.74±0.01	1.72±0.02
20	2.04±0.13	2.45±0.09	2.66±0.08	2.84±0.07	3.07±0.06	3.6±0.06	3.91±0.05	4.66±0.04	4.82±0.04	5.08±0.05	5.05±0.05	4.94±0.08
21	1.73±0.06	1.72±0.05	1.72±0.04	1.72±0.03	1.71±0.03	1.7±0.02	1.69±0.01	1.66±0.01	1.65±0.01	1.63±0.01	1.62±0.01	1.62±0.01
22	3.22±0.06	3.18±0.05	3.16±0.04	3.15±0.04	3.13±0.03	3.08±0.02	3.06±0.01	3.0±0.01	2.99±0.01	2.96±0.01	2.93±0.01	2.91±0.01
23	2.67±0.05	2.73±0.04	2.77±0.03	2.8 ±0.03	2.84±0.02	2.93±0.01	3.00±0.01	3.19±0.01	3.24±0.01	3.35±0.01	3.38±0.01	3.36±0.01
24	3.83±0.27	3.94±0.20	4.01±0.17	4.07±0.14	4.15±0.11	4.35±0.07	4.49±0.05	4.9±0.04	5.01±0.04	5.26±0.04	5.34±0.05	5.31±0.07
25	2.43±0.10	2.40±0.07	2.39±0.06	2.39±0.05	2.39±0.04	2.4±0.02	2.42±0.02	2.53±0.01	2.57±0.01	2.69±0.01	2.77±0.02	2.79±0.02
26	0.62±0.01	0.62±0.01	0.62±0.01	0.62±0.01	0.63±0.01	0.65±0.00	0.67±0.00	0.75±0.00	0.77±0.00	0.86±0.00	0.93±0.01	0.96±0.01
27	1.74±0.10	1.5 ±0.07	1.39±0.06	1.31±0.05	1.21±0.04	1.03±0.02	0.97±0.02	0.98±0.01	1.02±0.01	1.16±0.01	1.19±0.02	1.11±0.02
28	2.51±0.91	2.63±0.69	2.68±0.59	2.72±0.51	2.77±0.42	2.85±0.27	2.87±0.22	2.83±0.16	2.79±0.15	2.64±0.15	2.55±0.16	2.54±0.21
29	2.39±0.10	2.58±0.08	2.67±0.07	2.75±0.06	2.84±0.05	3.03±0.03	3.13±0.02	3.26±0.02	3.25±0.01	3.1±0.01	2.83±0.01	2.65±0.02
30	3.13±0.13	3.33±0.10	3.43±0.08	3.5 ±0.07	3.59±0.06	3.73±0.04	3.79±0.03	3.82±0.02	3.8 ±0.02	3.81±0.02	4.02±0.03	4.26±0.04
31	2.25±0.07	2.33±0.05	2.37±0.04	2.40±0.04	2.43±0.03	2.48±0.02	2.5 ±0.02	2.49±0.02	2.48±0.01	2.49±0.02	2.62±0.02	2.75±0.02
32	2.38±0.09	2.21±0.07	2.14±0.06	2.07±0.05	2.00±0.04	1.85±0.03	1.79±0.02	1.74±0.01	1.75±0.01	1.81±0.01	1.82±0.01	1.78±0.02
33	2.74±0.13	2.54±0.10	2.45±0.09	2.38±0.07	2.29±0.06	2.13±0.03	2.06±0.03	2.0±0.02	2.01±0.01	2.1±0.02	2.13±0.02	2.1±0.02
34	1.69±0.03	1.72±0.02	1.73±0.02	1.74±0.01	1.74±0.01	1.71±0.01	1.67±0.01	1.54±0.00	1.51±0.00	1.58±0.01	1.93±0.01	2.27±0.01
35	3.75±0.14	3.93±0.11	4.02±0.09	4.09±0.08	4.19±0.06	4.38±0.04	4.48±0.03	4.67±0.02	4.68±0.02	4.64±0.02	4.5 ±0.02	4.39±0.03
36	0.99±0.03	0.96±0.02	0.95±0.02	0.94±0.01	0.93±0.01	0.92±0.01	0.92±0.01	0.95±0.00	0.96±0.00	1.02±0.01	1.07±0.01	1.1±0.01
37	2.6 ±0.08	2.51±0.06	2.47±0.05	2.43±0.05	2.39±0.04	2.29±0.02	2.23±0.02	2.11±0.01	2.09±0.01	2.05±0.01	2.04±0.01	2.04±0.01
38	1.36±0.02	1.23±0.01	1.17±0.01	1.12±0.01	1.07±0.01	0.97±0.00	0.94±0.00	0.96±0.00	0.99±0.00	1.1±0.00	1.15±0.00	1.13±0.00
39	6.95±0.15	6.57±0.11	6.41±0.10	6.27±0.09	6.12±0.07	5.84±0.05	5.73±0.04	5.61±0.02	5.6 ±0.02	5.39±0.02	4.75±0.02	4.12±0.02
40	2.81±0.15	2.59±0.11	2.49±0.10	2.41±0.08	2.31±0.07	2.11±0.04	2.01±0.03	1.88±0.02	1.87±0.02	1.9±0.02	1.92±0.02	1.89±0.03
41	3.55±0.03	3.55±0.02	3.55±0.02	3.56±0.02	3.57±0.01	3.6±0.01	3.62±0.01	3.7±0.01	3.72±0.01	3.76±0.01	3.72±0.01	3.66±0.01
42	2.02±0.13	2.22±0.10	2.32±0.08	2.40±0.07	2.5 ±0.06	2.72±0.04	2.83±0.03	3.05±0.02	3.08±0.02	3.09±0.02	3.05±0.02	3.01±0.03
43	3.77±0.07	4.22±0.05	4.45±0.04	4.64±0.04	4.87±0.03	5.34±0.02	5.59±0.02	6.04±0.02	6.09±0.02	6.1±0.02	6.01±0.02	5.97±0.03
44	1.75±0.06	1.66±0.04	1.62±0.04	1.58±0.03	1.54±0.02	1.47±0.02	1.44±0.02	1.45±0.01	1.47±0.01	1.56±0.01	1.62±0.02	1.62±0.03
45	3.54±0.12	3.78±0.09	3.91±0.08	4.01±0.07	4.15±0.05	4.44±0.03	4.6 ±0.03	4.98±0.02	5.06±0.02	5.19±0.02	5.21±0.02	5.2±0.03
46	2.42±0.16	2.3 ±0.12	2.24±0.10	2.20±0.09	2.14±0.07	2.02±0.04	1.96±0.03	1.84±0.02	1.82±0.02	1.79±0.02	1.75±0.02	1.71±0.03
47	2.84±0.04	2.95±0.03	3.01±0.02	3.07±0.02	3.14±0.01	3.3±0.01	3.41±0.01	3.73±0.01	3.81±0.01	4.05±0.01	4.23±0.01	4.31±0.01
48	1.57±0.03	1.37±0.02	1.27±0.02	1.19±0.02	1.09±0.01	0.91±0.01	0.82±0.01	0.71±0.01	0.71±0.00	0.79±0.01	0.86±0.01	0.87±0.01
49	2.96±0.07	3.14±0.06	3.22±0.05	3.3 ±0.04	3.39±0.03	3.57±0.02	3.67±0.02	3.88±0.01	3.92±0.01	4.02±0.01	4.12±0.01	4.21±0.02
50	1.84±0.05	1.68±0.04	1.6 ±0.04	1.54±0.03	1.46±0.02	1.32±0.01	1.26±0.01	1.21±0.01	1.22±0.01	1.29±0.01	1.32±0.01	1.29±0.01
51	5.08±0.18	5.36±0.13	5.5 ±0.11	5.63±0.09	5.79±0.07	6.14±0.05	6.35±0.04	6.86±0.03	6.97±0.02	7.2±0.03	7.26±0.03	7.25±0.04
52	2.27±0.13	2.17±0.10	2.12±0.08	2.08±0.07	2.03±0.06	1.92±0.03	1.86±0.02	1.77±0.01	1.76±0.01	1.8±0.01	1.88±0.01	1.93±0.02
53	3.3 ±0.07	3.51±0.05	3.61±0.04	3.7 ±0.04	3.81±0.03	4.04±0.02	4.17±0.02	4.44±0.01	4.49±0.01	4.59±0.01	4.62±0.01	4.64±0.02

Continued on next page

Table B.4 – continued from previous page

ID	u	J0378	J0395	J0410	J0430	g	J0515	r	J0660	i	J0861	z
54	3.73±0.19	3.81±0.14	3.85±0.12	3.87±0.10	3.9 ±0.08	3.95±0.05	3.97±0.04	3.96±0.02	3.96±0.02	3.99±0.02	4.14±0.03	4.3±0.04
55	3.12±0.17	3.24±0.12	3.3 ±0.10	3.36±0.09	3.43±0.07	3.6±0.04	3.7 ±0.03	3.95±0.03	4.00±0.02	4.06±0.03	3.98±0.03	3.88±0.04
56	4.16±0.08	4.02±0.06	3.96±0.05	3.91±0.05	3.85±0.04	3.75±0.02	3.71±0.02	3.71±0.01	3.74±0.01	3.84±0.01	3.88±0.01	3.86±0.01
57	2.56±0.06	2.56±0.05	2.56±0.04	2.56±0.04	2.56±0.03	2.54±0.02	2.52±0.02	2.45±0.01	2.43±0.01	2.44±0.01	2.54±0.01	2.65±0.02
58	2.96±0.15	3.03±0.11	3.08±0.09	3.12±0.08	3.17±0.06	3.31±0.04	3.41±0.03	3.7±0.02	3.77±0.02	3.94±0.02	3.95±0.02	3.89±0.03
59	3.24±0.15	3.32±0.11	3.36±0.09	3.4 ±0.08	3.44±0.07	3.53±0.04	3.58±0.03	3.7±0.02	3.73±0.02	3.81±0.02	3.93±0.02	4.01±0.03
60	3.3 ±0.04	3.63±0.03	3.79±0.03	3.92±0.02	4.09±0.02	4.42±0.01	4.59±0.01	4.89±0.01	4.94±0.01	5.01±0.01	5.11±0.01	5.22±0.02
61	3.95±0.15	3.99±0.11	4.00±0.10	4.02±0.08	4.03±0.07	4.07±0.04	4.10±0.03	4.16±0.02	4.17±0.02	4.2±0.02	4.22±0.02	4.24±0.03
62	5.49±0.36	4.92±0.27	4.65±0.23	4.44±0.20	4.18±0.16	3.7±0.09	3.49±0.07	3.28±0.04	3.31±0.04	3.47±0.04	3.45±0.04	3.27±0.05
63	4.13±0.26	4.37±0.20	4.5 ±0.17	4.62±0.15	4.77±0.13	5.15±0.08	5.4 ±0.07	6.07±0.05	6.23±0.05	6.55±0.05	6.56±0.05	6.44±0.08
64	3.21±0.17	3.20±0.12	3.19±0.11	3.19±0.09	3.19±0.07	3.21±0.04	3.24±0.03	3.36±0.02	3.41±0.02	3.56±0.02	3.68±0.02	3.73±0.03
65	1.68±0.05	1.48±0.04	1.38±0.03	1.31±0.03	1.23±0.02	1.09±0.01	1.04±0.01	1.06±0.01	1.10±0.01	1.22±0.01	1.18±0.01	1.07±0.02
66	4.88±0.35	5.02±0.26	5.10±0.22	5.17±0.19	5.25±0.15	5.44±0.09	5.55±0.07	5.82±0.05	5.87±0.05	5.94±0.05	5.88±0.05	5.8±0.07
67	3.6 ±0.11	3.83±0.08	3.94±0.07	4.04±0.06	4.15±0.05	4.41±0.03	4.55±0.02	4.84±0.02	4.89±0.02	4.95±0.02	4.92±0.02	4.89±0.02
68	2.88±0.23	2.85±0.17	2.83±0.15	2.82±0.13	2.8 ±0.11	2.75±0.06	2.72±0.04	2.65±0.02	2.64±0.02	2.64±0.02	2.72±0.03	2.79±0.04
69	1.54±0.07	1.39±0.05	1.32±0.04	1.28±0.03	1.24±0.02	1.22±0.01	1.27±0.01	1.68±0.01	1.86±0.01	2.46±0.02	2.93±0.02	3.1±0.04
70	3.19±0.14	3.10±0.10	3.06±0.09	3.03±0.08	2.99±0.06	2.94±0.04	2.94±0.03	3.01±0.02	3.05±0.02	3.17±0.02	3.20±0.02	3.17±0.03
71	2.87±0.06	3.00±0.04	3.07±0.03	3.11±0.02	3.17±0.02	3.27±0.02	3.3 ±0.02	3.29±0.01	3.27±0.01	3.2±0.02	3.23±0.01	3.32±0.02
72	4.02±0.25	3.81±0.19	3.71±0.16	3.63±0.14	3.54±0.11	3.35±0.07	3.27±0.05	3.19±0.03	3.20±0.03	3.31±0.03	3.4 ±0.03	3.42±0.05
73	2.3 ±0.06	2.26±0.05	2.24±0.04	2.23±0.03	2.21±0.03	2.19±0.02	2.18±0.01	2.19±0.01	2.20±0.01	2.24±0.01	2.25±0.01	2.23±0.01
74	3.32±0.03	3.26±0.03	3.23±0.02	3.20±0.02	3.17±0.02	3.1±0.01	3.06±0.01	2.99±0.01	2.98±0.01	2.98±0.01	3.00±0.01	3.02±0.01
75	3.31±0.04	3.29±0.03	3.28±0.02	3.28±0.02	3.27±0.01	3.24±0.01	3.22±0.01	3.16±0.01	3.15±0.00	3.14±0.01	3.19±0.01	3.24±0.01
76	2.65±0.06	2.46±0.05	2.36±0.04	2.29±0.03	2.20±0.03	2.03±0.02	1.96±0.01	1.88±0.01	1.89±0.01	1.96±0.01	1.98±0.01	1.94±0.01
77	4.36±0.16	4.61±0.12	4.73±0.10	4.84±0.09	4.96±0.07	5.22±0.04	5.36±0.03	5.58±0.03	5.6 ±0.02	5.52±0.02	5.35±0.02	5.24±0.03
78	2.57±0.14	2.6 ±0.10	2.61±0.09	2.62±0.08	2.63±0.06	2.66±0.04	2.67±0.03	2.68±0.02	2.69±0.02	2.68±0.02	2.68±0.02	2.69±0.02
79	0.6 ±0.03	0.61±0.02	0.62±0.02	0.63±0.02	0.63±0.01	0.66±0.01	0.67±0.01	0.71±0.00	0.72±0.00	0.75±0.00	0.75±0.00	0.75±0.01
80	1.94±0.07	1.91±0.06	1.9 ±0.05	1.9 ±0.04	1.9 ±0.03	1.95±0.02	2.00±0.01	2.25±0.01	2.34±0.01	2.6±0.01	2.75±0.01	2.77±0.02
81	4.76±0.08	5.02±0.06	5.15±0.05	5.26±0.04	5.39±0.03	5.67±0.02	5.83±0.02	6.17±0.01	6.24±0.01	6.45±0.01	6.69±0.01	6.88±0.02

Table B.5: Bulge's Sérsic indexes estimated in this thesis using the MEGAMORPH-GALAPAGOS2 project. Column 1 is the ID of each galaxy, and the columns 2 to 13 are the Bulge's Sérsic indexes in the 12 S-PLUS filters.

ID	u	J0378	J0395	J0410	J0430	g	J0515	r	J0660	i	J0861	z
1	0.67±0.07	0.82±0.06	0.91±0.05	0.99±0.05	1.11±0.04	1.43±0.04	1.67±0.04	2.53±0.05	2.84±0.05	3.88±0.07	4.92±0.11	5.52±0.15
2	0.6±0.02	0.64±0.02	0.67±0.02	0.68±0.02	0.71±0.01	0.76±0.01	0.79±0.01	0.86±0.0	0.87±0.0	0.89±0.0	0.87±0.0	0.84±0.01
3	0.2±0.22	0.55±0.19	0.74±0.18	0.91±0.18	1.13±0.17	1.68±0.19	2.04±0.21	3.14±0.3	3.46±0.34	4.39±0.44	5.14±0.55	5.51±0.62
4	1.73±0.03	1.75±0.03	1.76±0.02	1.76±0.02	1.77±0.02	1.8±0.01	1.81±0.01	1.85±0.01	1.86±0.01	1.89±0.01	1.91±0.01	1.91±0.01
5	3.54±0.08	3.7±0.07	3.78±0.07	3.85±0.06	3.94±0.05	4.14±0.04	4.26±0.03	4.53±0.02	4.59±0.02	4.66±0.02	4.6±0.03	4.53±0.04
6	1.55±0.06	1.47±0.05	1.43±0.05	1.39±0.04	1.35±0.04	1.26±0.03	1.2±0.02	1.1±0.01	1.09±0.01	1.12±0.01	1.22±0.01	1.3±0.01
9	11.99±1.83	11.4±1.65	11.07±1.56	10.77±1.47	10.37±1.37	9.37±1.14	8.68±1.0	6.49±0.66	5.81±0.58	3.69±0.36	1.83±0.18	0.84±0.14
10	1.49±0.05	1.54±0.04	1.56±0.04	1.58±0.04	1.61±0.03	1.67±0.02	1.7±0.02	1.78±0.01	1.79±0.01	1.8±0.01	1.78±0.01	1.74±0.02
11	3.87±0.5	3.96±0.44	4.01±0.4	4.05±0.37	4.1±0.34	4.2±0.26	4.26±0.21	4.35±0.12	4.36±0.11	4.28±0.12	4.12±0.15	4.0±0.18
14	4.5±0.28	4.45±0.23	4.43±0.21	4.41±0.19	4.38±0.17	4.33±0.12	4.31±0.09	4.3±0.06	4.31±0.06	4.4±0.06	4.55±0.07	4.66±0.09
15	3.1±0.12	3.1±0.1	3.11±0.09	3.11±0.08	3.12±0.08	3.14±0.06	3.16±0.05	3.25±0.03	3.28±0.03	3.39±0.03	3.51±0.04	3.58±0.06
17	0.93±0.15	0.95±0.13	0.97±0.11	0.98±0.1	0.99±0.09	1.03±0.07	1.04±0.05	1.09±0.03	1.09±0.03	1.1±0.03	1.08±0.04	1.07±0.06
19	0.91±0.1	0.96±0.09	0.98±0.08	1.0±0.07	1.02±0.06	1.07±0.05	1.1±0.04	1.17±0.02	1.18±0.02	1.18±0.02	1.14±0.03	1.1±0.04
20	11.95±3.85	11.95±3.44	11.94±3.22	11.91±3.03	11.85±2.78	11.62±2.22	11.38±1.87	10.19±1.0	9.68±0.81	7.72±0.46	5.49±0.38	4.11±0.38
21	1.26±0.09	1.21±0.08	1.19±0.07	1.17±0.06	1.14±0.06	1.08±0.04	1.04±0.03	0.98±0.02	0.97±0.02	0.99±0.02	1.05±0.02	1.11±0.03
22	1.06±0.02	1.05±0.02	1.04±0.02	1.04±0.01	1.03±0.01	1.01±0.01	1.0±0.01	0.97±0.0	0.97±0.0	0.95±0.0	0.95±0.0	0.95±0.01
24	3.03±0.45	3.15±0.38	3.22±0.34	3.28±0.31	3.35±0.28	3.53±0.2	3.64±0.16	3.92±0.1	3.99±0.1	4.15±0.1	4.21±0.12	4.21±0.16
25	1.46±0.1	1.68±0.08	1.8±0.08	1.9±0.07	2.03±0.06	2.35±0.05	2.54±0.04	3.08±0.04	3.22±0.04	3.55±0.05	3.74±0.07	3.79±0.09
30	1.75±0.12	1.73±0.1	1.71±0.09	1.7±0.08	1.69±0.07	1.66±0.05	1.64±0.04	1.6±0.02	1.59±0.02	1.57±0.02	1.57±0.03	1.57±0.03
32	0.77±0.04	0.8±0.03	0.82±0.03	0.83±0.03	0.85±0.02	0.9±0.02	0.92±0.01	0.99±0.01	1.0±0.01	1.02±0.01	1.01±0.01	1.0±0.01
33	1.64±0.17	1.7±0.14	1.73±0.13	1.76±0.12	1.79±0.1	1.87±0.08	1.91±0.06	2.01±0.06	2.02±0.06	2.03±0.06	1.99±0.06	1.95±0.08
35	6.1±0.27	6.11±0.23	6.11±0.21	6.1±0.2	6.09±0.17	6.05±0.13	6.0±0.1	5.76±0.05	5.65±0.04	5.24±0.04	4.76±0.04	4.46±0.05
37	5.8±0.54	5.72±0.46	5.67±0.42	5.63±0.38	5.57±0.34	5.44±0.24	5.35±0.19	5.1±0.09	5.02±0.08	4.81±0.08	4.65±0.08	4.58±0.11
39	4.11±0.16	4.26±0.14	4.33±0.13	4.38±0.12	4.45±0.1	4.57±0.08	4.61±0.06	4.52±0.03	4.42±0.03	3.92±0.03	3.21±0.03	2.73±0.03
40	1.59±0.17	1.57±0.14	1.56±0.13	1.55±0.12	1.53±0.11	1.51±0.08	1.49±0.06	1.47±0.04	1.47±0.04	1.48±0.04	1.52±0.05	1.55±0.07
42	4.28±1.06	4.09±0.92	3.99±0.85	3.9±0.79	3.8±0.71	3.56±0.53	3.43±0.42	3.15±0.18	3.11±0.15	3.12±0.15	3.31±0.17	3.47±0.17
43	4.99±0.11	4.99±0.09	4.99±0.09	5.0±0.08	5.0±0.07	5.0±0.06	5.0±0.05	5.0±0.02	5.0±0.02	4.98±0.02	4.95±0.03	4.94±0.04
44	1.05±0.08	1.05±0.06	1.06±0.06	1.06±0.05	1.07±0.04	1.08±0.03	1.09±0.03	1.14±0.02	1.16±0.02	1.22±0.03	1.29±0.05	1.34±0.07
45	6.36±0.48	6.57±0.41	6.68±0.38	6.77±0.35	6.88±0.31	7.12±0.23	7.23±0.18	7.38±0.09	7.36±0.09	7.06±0.09	6.54±0.09	6.15±0.11
46	0.75±0.06	0.72±0.05	0.71±0.04	0.7±0.04	0.69±0.04	0.66±0.03	0.64±0.02	0.62±0.01	0.61±0.01	0.63±0.01	0.67±0.02	0.7±0.02
47	0.7±0.01	0.75±0.01	0.78±0.01	0.81±0.01	0.84±0.0	0.93±0.0	0.99±0.0	1.16±0.0	1.21±0.0	1.36±0.0	1.49±0.0	1.55±0.0
48	3.19±0.17	2.6±0.13	2.3±0.12	2.05±0.1	1.74±0.08	1.08±0.05	0.74±0.03	0.2±0.01	0.21±0.01	0.78±0.06	1.96±0.15	2.85±0.22
49	2.65±0.06	2.72±0.05	2.75±0.04	2.79±0.04	2.83±0.04	2.92±0.03	2.98±0.02	3.14±0.01	3.18±0.01	3.27±0.01	3.31±0.02	3.32±0.02
51	3.1±0.12	3.08±0.1	3.07±0.09	3.06±0.09	3.04±0.08	3.02±0.05	3.0±0.04	2.98±0.02	2.98±0.02	3.01±0.02	3.06±0.03	3.1±0.04
53	3.24±0.05	3.21±0.04	3.19±0.04	3.17±0.04	3.15±0.03	3.1±0.03	3.06±0.02	2.92±0.02	2.87±0.01	2.71±0.01	2.56±0.01	2.47±0.02
54	3.21±0.28	3.17±0.24	3.15±0.22	3.13±0.21	3.11±0.19	3.05±0.14	3.02±0.11	2.94±0.06	2.92±0.05	2.88±0.05	2.87±0.07	2.87±0.08

Continued on next page

Table B.5 – continued from previous page

ID	u	J0378	J0395	J0410	J0430	g	J0515	r	J0660	i	J0861	z
55	2.66±0.2	2.66±0.17	2.66±0.16	2.66±0.14	2.66±0.13	2.65±0.09	2.65±0.07	2.63±0.04	2.62±0.04	2.6±0.04	2.57±0.04	2.56±0.05
56	2.31±0.04	2.38±0.04	2.42±0.03	2.45±0.03	2.49±0.03	2.58±0.02	2.64±0.02	2.78±0.01	2.82±0.01	2.88±0.01	2.89±0.01	2.88±0.02
57	12.0±0.38	11.24±0.33	10.83±0.31	10.47±0.29	9.99±0.26	8.83±0.21	8.07±0.18	5.85±0.13	5.22±0.12	3.46±0.08	2.14±0.06	1.52±0.07
58	4.16±0.28	4.36±0.24	4.47±0.22	4.56±0.2	4.68±0.18	4.95±0.13	5.1±0.1	5.48±0.06	5.55±0.06	5.66±0.06	5.6±0.07	5.51±0.1
59	4.83±0.46	4.97±0.39	5.04±0.35	5.1±0.32	5.17±0.28	5.34±0.2	5.43±0.16	5.64±0.09	5.67±0.08	5.67±0.08	5.56±0.09	5.45±0.13
61	3.54±0.11	3.62±0.09	3.65±0.09	3.69±0.08	3.73±0.07	3.82±0.05	3.87±0.04	3.98±0.02	3.99±0.02	3.98±0.02	3.9±0.02	3.82±0.03
63	2.12±0.19	2.14±0.16	2.16±0.15	2.17±0.14	2.19±0.12	2.26±0.09	2.31±0.07	2.53±0.04	2.62±0.03	2.92±0.05	3.24±0.07	3.43±0.09
66	3.93±0.39	3.61±0.33	3.45±0.3	3.31±0.27	3.14±0.24	2.76±0.16	2.55±0.12	2.15±0.06	2.11±0.06	2.24±0.06	2.68±0.08	3.05±0.12
67	3.19±0.08	3.12±0.07	3.09±0.07	3.05±0.06	3.01±0.06	2.92±0.04	2.87±0.03	2.75±0.02	2.72±0.02	2.69±0.02	2.72±0.02	2.75±0.02
73	1.51±0.08	1.57±0.07	1.6±0.06	1.63±0.06	1.66±0.05	1.75±0.04	1.8±0.03	1.95±0.02	1.99±0.01	2.09±0.01	2.15±0.01	2.18±0.01
74	2.21±0.02	2.15±0.02	2.12±0.02	2.09±0.02	2.06±0.01	1.98±0.01	1.94±0.01	1.84±0.01	1.82±0.01	1.82±0.01	1.87±0.01	1.92±0.01
75	1.58±0.05	1.63±0.05	1.65±0.04	1.67±0.04	1.7±0.03	1.76±0.03	1.79±0.02	1.88±0.01	1.9±0.01	1.93±0.01	1.92±0.02	1.91±0.02
77	3.45±0.19	3.72±0.16	3.85±0.15	3.97±0.14	4.13±0.12	4.48±0.09	4.69±0.07	5.21±0.04	5.32±0.04	5.5±0.04	5.47±0.04	5.38±0.05
78	1.59±0.09	1.7±0.08	1.76±0.07	1.81±0.07	1.87±0.06	2.01±0.04	2.1±0.04	2.27±0.03	2.29±0.03	2.29±0.03	2.19±0.04	2.09±0.04
80	6.61±0.96	6.22±0.84	6.02±0.77	5.84±0.72	5.61±0.65	5.08±0.48	4.76±0.39	3.93±0.16	3.74±0.12	3.35±0.1	3.25±0.11	3.3±0.13
81	2.32±0.1	2.4±0.08	2.44±0.07	2.48±0.07	2.52±0.06	2.62±0.05	2.68±0.04	2.8±0.03	2.82±0.03	2.83±0.02	2.76±0.03	2.7±0.04

Table B.6: Physical parameters of the galaxies. Column 1 is the ID of each galaxy, columns 2 and 3 are the right ascension and declination respectively. The stellar mass calculated with the $(g-i)$ colour presented in Taylor et al. (2011) is in column 4. The H_α luminosity and sSFR are in the columns 5 and 6, respectively. Column 7 lists the galaxies catalogue name.

ID	RA° J2000	DEC° J2000	$\log(M_*/M_\odot)$	$L_{H\alpha}$ 10^{39}ergs^{-1}	$\log(sSFR/yr)$	Identifier
1	158.281	-27.096	10.3±0.05	24 ±4	0.0±0.0	ESO 501- G 010
2	158.400	-27.023	9.62±0.05	12 ±2	0.0±0.0	ESO 501- G 014
3	158.599	-26.998	9.35±0.05	1±1	0.0±0.0	2MASX J10342375-2659537
4	158.375	-26.898	10.65±0.05	50 ±7	0.0±0.0	ESO 501- G 013
5	157.952	-26.565	10.96±0.05	70 ±13	0.0±0.0	ESO 501- G 003
6	158.599	-26.492	9.74±0.05	128±16	-9.37±0.07	ESO 501- G 017
7	158.027	-26.465	9.72±0.05	21 ±3	0.0±0.0	2MASX J10320651-2627531
8	158.279	-26.423	9.29±0.05	13 ±2	0.0±0.0	2MFGC 08182
9	158.391	-26.301	9.4 ±0.05	9±2	0.0±0.0	2MASX J10333391-2618030
10	158.699	-27.214	10.58±0.05	63 ±16	0.0±0.0	ESO 501- G 020
11	158.801	-27.170	9.8 ±0.05	5±2	0.0±0.0	2MASX J10351214-2710106
12	159.087	-27.167	9.6 ±0.08	4±5	0.0±0.0	2MASX J10362089-2709599
13	159.221	-27.053	9.5 ±0.05	28 ±4	-9.97±0.07	ESO 501- G 041
14	159.419	-27.058	10.25±0.05	11 ±7	0.0±0.0	2MASX J10374052-2703284
15	159.103	-27.000	10.7±0.05	42 ±9	0.0±0.0	ESO 501- G 035
16	158.936	-27.000	9.48±0.05	2±1	0.0±0.0	2MASX J10354469-2700006
17	159.286	-26.787	9.62±0.06	2±3	0.0±0.0	2MASX J10370873-2647141
18	159.639	-26.794	9.76±0.06	3±4	0.0±0.0	2MASX J10383325-2647389
19	158.665	-26.679	9.64±0.06	6±3	0.0±0.0	2MASX J10343967-2640457
20	159.303	-26.671	10.46±0.06	110±21	0.0±0.0	ESO 501- G 045
21	159.730	-26.640	10.02±0.05	18 ±2	0.0±0.0	ESO 501- G 066
22	158.854	-26.657	10.34±0.05	26 ±6	0.0±0.0	ESO 501- G 025
23	159.439	-26.631	10.73±0.05	31 ±7	0.0±0.0	ESO 501- G 056
24	159.424	-26.510	9.75±0.06	1±4	0.0±0.0	2MASX J10374180-2630344
25	159.252	-26.318	9.94±0.05	7±3	0.0±0.0	2MASX J10370041-2619051
26	159.211	-26.155	9.29±0.05	45 ±5	-9.5 ±0.07	2MASX J10365073-2609192
27	159.477	-26.074	9.35±0.06	22 ±4	0.0±0.0	ESO 501- G 060
28	157.978	-28.627	10.06±0.12	20 ±31	0.0±0.0	2MASX J10315459-2837374
29	158.186	-28.610	10.79±0.05	75 ±12	0.0±0.0	ESO 436- G 034
30	157.763	-28.307	10.13±0.05	13 ±4	0.0±0.0	2MASX J10310304-2818256
31	158.117	-27.529	9.9 ±0.05	7±3	0.0±0.0	ESO 501- G 005
32	159.821	-28.714	9.4 ±0.05	13 ±2	0.0±0.0	2MASX J10391697-2842489
33	159.621	-28.702	9.5 ±0.05	2±1	0.0±0.0	2MASX J10382906-2842068
34	158.661	-28.583	9.22±0.05	147±17	-8.77±0.06	ESO 436-IG 042
35	158.649	-28.568	10.12±0.05	7±2	0.0±0.0	2MASX J10343568-2834048
36	158.569	-28.568	9.3 ±0.05	25 ±3	-9.82±0.07	2MASX J10341656-2834057
37	159.428	-28.604	10.08±0.05	17 ±2	0.0±0.0	ESO 437- G 017
38	159.668	-28.569	10.01±0.05	64 ±7	-10.01±0.06	ESO 437- G 025
39	158.712	-28.513	9.9 ±0.05	2±2	0.0±0.0	ESO 436- G 045
40	159.471	-28.443	9.28±0.06	1±2	0.0±0.0	2MASX J10375302-2826344
41	158.698	-28.496	10.5±0.05	3±3	0.0±0.0	ESO 436- G 044
42	158.704	-28.418	9.71±0.05	13 ±2	0.0±0.0	ESO 437- G 001
43	158.973	-28.291	10.27±0.05	13 ±4	0.0±0.0	2MASX J10355363-2817269
44	159.333	-28.239	8.81±0.05	19 ±2	-9.49±0.07	2MASX J10371989-2814201
45	159.145	-28.215	10.37±0.05	35 ±5	0.0±0.0	ESO 437- G 009

Continued on next page

Table B.6 – continued from previous page

ID	RA° J2000	DEC° J2000	$\log(M_\star/M_\odot)$	$L_{H\alpha}$ 10^{39}ergs^{-1}	$\log(sSFR/yr)$	Identifier
46	158.835	-28.122	9.21±0.05	6±1	0.0±0.0	2MASX J10352060-2807205
47	159.242	-28.176	10.43±0.05	33 ±4	0.0±0.0	ESO 437- G 015
48	158.782	-27.991	8.37±0.05	15 ±2	-9.21±0.07	2MASX J10350772-2759286
49	159.135	-28.064	10.63±0.05	37 ±5	0.0±0.0	ESO 437- G 008
50	158.452	-28.005	9.63±0.05	10 ±2	0.0±0.0	ESO 436- G 036
51	159.271	-27.986	10.52±0.05	19 ±7	0.0±0.0	GALEXASC J103705.17-275908.9
52	159.016	-27.919	9.57±0.05	1±2	0.0±0.0	2MASX J10360386-2755079
53	159.211	-27.919	10.83±0.05	56 ±9	0.0±0.0	GALEXASC J103650.45-275508.0
54	159.280	-27.872	9.89±0.05	17 ±4	0.0±0.0	GALEXASC J103707.24-275220.1
55	159.353	-27.874	10.09±0.05	9±3	0.0±0.0	2MASX J10372477-2752261
56	159.225	-27.917	10.44±0.05	21 ±3	0.0±0.0	GALEXASC J103654.00-275500.8
57	159.854	-27.913	9.46±0.05	51 ±7	-9.6 ±0.08	ESO 437- G 032
58	158.992	-27.562	9.98±0.05	9±2	0.0±0.0	2MASX J10355816-2733449
59	159.104	-27.582	9.81±0.05	4±2	0.0±0.0	2MASX J10362490-2734542
60	159.406	-27.594	10.86±0.05	50 ±8	0.0±0.0	NGC 3316
61	158.560	-27.660	10.01±0.05	7±2	0.0±0.0	2MASX J10341443-2739347
62	159.290	-27.658	9.82±0.05	4±3	0.0±0.0	2MASX J10370969-2739281
63	159.054	-27.689	10.28±0.06	12 ±9	0.0±0.0	2MASX J10361305-2741189
64	159.079	-27.721	9.89±0.06	6±4	0.0±0.0	2MASX J10361893-2743169
65	158.840	-27.696	8.61±0.05	22 ±3	-9.22±0.07	ESO 501- G 022
66	158.503	-27.729	9.66±0.05	5±2	0.0±0.0	2MASX J10340065-2743456
67	158.836	-27.362	10.68±0.05	40 ±8	0.0±0.0	ESO 501- G 021
68	158.975	-27.372	9.65±0.06	5±3	0.0±0.0	2MASX J10355389-2722199
69	159.404	-27.388	10.56±0.05	19 ±8	0.0±0.0	ESO 501- G 052
70	158.879	-27.381	10.15±0.05	10 ±3	0.0±0.0	2MASX J10353083-2722496
71	159.172	-27.561	10.21±0.05	12 ±2	0.0±0.0	2MASX J10364122-2733392
72	159.121	-27.484	10.3±0.05	11 ±8	0.0±0.0	2MASX J10362905-2729022
73	159.096	-27.354	9.83±0.05	5±1	0.0±0.0	2MASX J10362306-2721152
74	159.149	-27.518	11.13±0.05	78 ±16	0.0±0.0	NGC 3309
75	159.046	-27.454	10.21±0.05	15 ±2	0.0±0.0	2MASX J10361101-2727149
76	158.853	-27.482	9.77±0.05	4±1	0.0±0.0	ESO 501- G 026
77	158.499	-27.452	10.05±0.05	11 ±2	0.0±0.0	2MASX J10335976-2727066
78	159.148	-27.470	9.49±0.05	3±1	0.0±0.0	2MASX J10363551-2728122
79	158.910	-27.526	9.36±0.05	3±1	0.0±0.0	2MASX J10353827-2731346
80	159.072	-27.530	10.19±0.05	30 ±4	0.0±0.0	NGC 3307
81	159.333	-27.560	10.42±0.05	10 ±2	0.0±0.0	ESO 501- G 049

Table B.7: B/T estimated in this thesis. Column 1 is the ID of each galaxy, and columns 2 to 13 are the B/T in the 12 S-PLUS filters.

ID	u	J0378	J0395	J0410	J0430	g	J0515	r	J0660	i	J0861	z
1	0.31±0.03	0.35±0.03	0.36±0.04	0.33±0.03	0.29±0.02	0.21±0.01	0.21±0.01	0.23±0.01	0.24±0.0	0.25±0.01	0.27±0.01	0.27±0.01
2	0.5±0.04	0.5±0.04	0.51±0.05	0.47±0.04	0.52±0.03	0.48±0.02	0.5±0.02	0.49±0.01	0.5±0.01	0.49±0.01	0.5±0.01	0.49±0.01
3	0.14±0.06	0.35±0.08	0.17±0.09	0.13±0.07	0.15±0.06	0.17±0.03	0.18±0.04	0.31±0.02	0.27±0.02	0.35±0.03	0.39±0.04	0.4±0.05
4	0.35±0.01	0.36±0.01	0.37±0.01	0.37±0.01	0.36±0.01	0.36±0.0	0.36±0.0	0.33±0.0	0.34±0.0	0.34±0.0	0.35±0.0	0.34±0.0
5	0.7±0.04	0.81±0.04	0.71±0.03	0.81±0.03	0.86±0.02	0.86±0.01	0.88±0.01	0.85±0.01	0.85±0.01	0.85±0.01	0.85±0.01	0.83±0.01
6	0.27±0.01	0.26±0.01	0.29±0.02	0.22±0.01	0.21±0.01	0.2±0.0	0.18±0.0	0.19±0.0	0.27±0.0	0.2±0.0	0.23±0.0	0.26±0.0
9	0.39±0.04	0.26±0.03	0.31±0.04	0.31±0.03	0.29±0.03	0.27±0.03	0.23±0.02	0.19±0.02	0.21±0.02	0.13±0.01	0.1±0.0	0.08±0.0
10	0.23±0.01	0.22±0.01	0.22±0.01	0.23±0.01	0.25±0.01	0.25±0.0	0.26±0.0	0.26±0.0	0.27±0.0	0.25±0.0	0.28±0.0	0.25±0.0
11	0.56±0.05	0.67±0.05	0.61±0.05	0.56±0.04	0.53±0.03	0.52±0.02	0.53±0.02	0.56±0.01	0.57±0.01	0.59±0.01	0.59±0.01	0.63±0.01
14	0.55±0.02	0.55±0.02	0.54±0.03	0.55±0.02	0.57±0.02	0.57±0.01	0.55±0.01	0.57±0.01	0.56±0.01	0.58±0.0	0.6±0.01	0.62±0.01
15	0.64±0.03	0.58±0.02	0.56±0.03	0.58±0.02	0.61±0.02	0.62±0.01	0.61±0.01	0.59±0.01	0.58±0.01	0.59±0.01	0.61±0.01	0.61±0.01
17	0.15±0.04	0.1±0.03	0.2±0.06	0.2±0.04	0.16±0.03	0.16±0.01	0.16±0.01	0.16±0.01	0.14±0.01	0.15±0.01	0.17±0.01	0.14±0.01
19	0.24±0.07	0.13±0.05	0.33±0.08	0.29±0.06	0.25±0.05	0.31±0.03	0.31±0.03	0.35±0.02	0.36±0.02	0.34±0.02	0.34±0.02	0.33±0.03
20	0.21±0.08	0.17±0.06	0.2±0.06	0.2±0.06	0.2±0.05	0.23±0.05	0.22±0.04	0.29±0.03	0.32±0.03	0.29±0.02	0.27±0.02	0.19±0.01
21	0.17±0.02	0.12±0.02	0.11±0.02	0.13±0.02	0.16±0.02	0.13±0.01	0.1±0.01	0.1±0.0	0.09±0.0	0.09±0.0	0.11±0.0	0.1±0.01
22	0.19±0.01	0.18±0.01	0.16±0.01	0.21±0.01	0.23±0.01	0.24±0.0	0.23±0.0	0.24±0.0	0.24±0.0	0.23±0.0	0.23±0.0	0.22±0.0
24	0.57±0.11	0.5±0.08	0.62±0.1	0.68±0.1	0.71±0.09	0.74±0.06	0.72±0.04	0.77±0.03	0.75±0.02	0.78±0.02	0.77±0.03	0.74±0.03
25	0.22±0.04	0.34±0.04	0.49±0.07	0.57±0.06	0.46±0.04	0.64±0.02	0.71±0.03	0.75±0.01	0.75±0.01	0.77±0.01	0.81±0.01	0.81±0.01
30	0.23±0.02	0.23±0.01	0.22±0.02	0.23±0.01	0.24±0.01	0.25±0.01	0.25±0.01	0.25±0.0	0.23±0.0	0.23±0.0	0.23±0.0	0.22±0.0
32	0.4±0.03	0.43±0.04	0.4±0.05	0.44±0.04	0.36±0.02	0.35±0.01	0.38±0.01	0.4±0.0	0.47±0.0	0.41±0.0	0.44±0.01	0.42±0.0
33	0.49±0.1	0.47±0.08	0.46±0.08	0.44±0.06	0.43±0.06	0.43±0.04	0.45±0.04	0.44±0.04	0.45±0.04	0.47±0.04	0.48±0.04	0.45±0.04
35	0.59±0.02	0.65±0.02	0.73±0.03	0.66±0.01	0.65±0.01	0.64±0.01	0.68±0.01	0.68±0.0	0.68±0.0	0.68±0.0	0.69±0.0	0.7±0.0
37	0.3±0.03	0.33±0.03	0.31±0.03	0.34±0.02	0.33±0.02	0.32±0.01	0.33±0.01	0.33±0.01	0.32±0.0	0.34±0.0	0.34±0.01	0.34±0.01
39	0.75±0.03	0.81±0.04	0.84±0.05	0.86±0.03	0.8±0.02	0.83±0.01	0.85±0.01	0.83±0.01	0.84±0.01	0.79±0.01	0.73±0.01	0.7±0.01
40	0.22±0.04	0.27±0.04	0.13±0.04	0.12±0.03	0.17±0.03	0.25±0.02	0.26±0.02	0.24±0.01	0.23±0.01	0.24±0.01	0.24±0.02	0.26±0.02
42	0.16±0.03	0.14±0.03	0.2±0.03	0.18±0.03	0.14±0.02	0.13±0.02	0.13±0.02	0.16±0.01	0.21±0.01	0.22±0.01	0.29±0.02	0.35±0.02
43	0.59±0.01	0.6±0.02	0.63±0.02	0.63±0.01	0.64±0.01	0.63±0.0	0.63±0.01	0.62±0.0	0.62±0.0	0.61±0.0	0.62±0.0	0.64±0.0
44	0.22±0.02	0.22±0.02	0.22±0.02	0.24±0.02	0.18±0.02	0.18±0.01	0.19±0.01	0.18±0.01	0.22±0.01	0.18±0.01	0.18±0.01	0.18±0.02
45	0.32±0.03	0.38±0.02	0.38±0.02	0.37±0.02	0.37±0.01	0.42±0.01	0.45±0.01	0.47±0.0	0.5±0.0	0.5±0.0	0.5±0.0	0.49±0.01
46	0.29±0.03	0.28±0.03	0.32±0.05	0.24±0.03	0.22±0.02	0.17±0.01	0.17±0.01	0.16±0.0	0.2±0.0	0.17±0.0	0.18±0.01	0.18±0.01
47	0.27±0.0	0.29±0.0	0.32±0.0	0.31±0.0	0.29±0.0	0.29±0.0	0.29±0.0	0.3±0.0	0.31±0.0	0.31±0.0	0.33±0.0	0.34±0.0
48	0.29±0.03	0.19±0.02	0.27±0.03	0.24±0.03	0.16±0.02	0.17±0.01	0.17±0.01	0.13±0.01	0.25±0.0	0.08±0.01	0.02±0.02	0.01±0.01
49	0.46±0.01	0.47±0.01	0.47±0.02	0.56±0.01	0.52±0.01	0.53±0.0	0.53±0.0	0.52±0.0	0.52±0.0	0.53±0.0	0.55±0.0	0.52±0.0
51	0.33±0.01	0.35±0.01	0.36±0.02	0.35±0.01	0.35±0.01	0.37±0.01	0.38±0.01	0.36±0.0	0.36±0.0	0.36±0.0	0.37±0.0	0.37±0.0
53	0.59±0.02	0.58±0.02	0.72±0.03	0.6±0.01	0.59±0.01	0.55±0.01	0.54±0.01	0.51±0.0	0.51±0.0	0.48±0.0	0.46±0.0	0.44±0.0
54	0.13±0.01	0.16±0.01	0.16±0.02	0.15±0.01	0.16±0.01	0.19±0.01	0.21±0.01	0.22±0.0	0.22±0.0	0.25±0.0	0.27±0.01	0.27±0.01
55	0.49±0.05	0.49±0.04	0.47±0.05	0.44±0.04	0.43±0.03	0.47±0.02	0.48±0.02	0.46±0.01	0.48±0.01	0.46±0.01	0.46±0.01	0.46±0.01
56	0.47±0.01	0.51±0.02	0.62±0.03	0.57±0.01	0.56±0.01	0.58±0.01	0.6±0.01	0.61±0.0	0.63±0.0	0.64±0.0	0.64±0.0	0.62±0.01
57	0.22±0.01	0.16±0.01	0.18±0.01	0.18±0.01	0.17±0.01	0.16±0.01	0.16±0.01	0.15±0.01	0.16±0.01	0.11±0.0	0.08±0.0	0.07±0.0
58	0.54±0.04	0.5±0.03	0.76±0.05	0.57±0.02	0.63±0.02	0.64±0.01	0.68±0.01	0.67±0.0	0.69±0.0	0.68±0.0	0.66±0.0	0.66±0.01
59	0.7±0.04	0.69±0.04	0.76±0.05	0.77±0.03	0.73±0.02	0.72±0.01	0.72±0.01	0.7±0.0	0.7±0.0	0.69±0.0	0.69±0.01	0.69±0.01
61	0.74±0.04	0.82±0.04	0.67±0.04	0.73±0.03	0.73±0.02	0.82±0.01	0.83±0.01	0.84±0.01	0.85±0.01	0.84±0.0	0.84±0.01	0.83±0.01
63	0.26±0.02	0.27±0.02	0.3±0.03	0.27±0.02	0.25±0.01	0.26±0.01	0.27±0.01	0.26±0.0	0.27±0.0	0.29±0.0	0.31±0.01	0.32±0.01
66	0.49±0.03	0.42±0.03	0.51±0.04	0.5±0.03	0.41±0.02	0.38±0.01	0.38±0.01	0.32±0.0	0.33±0.0	0.34±0.0	0.4±0.01	0.45±0.01
67	0.33±0.01	0.34±0.01	0.31±0.01	0.37±0.01	0.37±0.01	0.38±0.0	0.37±0.0	0.37±0.0	0.38±0.0	0.37±0.0	0.38±0.0	0.38±0.0
73	0.27±0.05	0.37±0.05	0.43±0.05	0.41±0.04	0.41±0.03	0.51±0.03	0.58±0.02	0.69±0.01	0.73±0.01	0.8±0.01	0.85±0.01	0.87±0.01
74	0.42±0.01	0.37±0.01	0.37±0.01	0.4±0.01	0.42±0.01	0.41±0.0	0.39±0.0	0.37±0.0	0.38±0.0	0.37±0.0	0.39±0.0	0.39±0.0
75	0.49±0.02	0.47±0.02	0.47±0.02	0.49±0.02	0.45±0.01	0.47±0.01	0.48±0.01	0.49±0.0	0.5±0.0	0.5±0.0	0.5±0.0	0.5±0.01
77	0.54±0.03	0.51±0.02	0.65±0.03	0.62±0.02	0.63±0.02	0.66±0.01	0.72±0.01	0.76±0.0	0.79±0.0	0.82±0.0	0.85±0.0	0.88±0.0
78	0.42±0.04	0.64±0.06	0.75±0.09	0.78±0.07	0.64±0.04	0.69±0.03	0.74±0.03	0.72±0.02	0.74±0.02	0.73±0.02	0.71±0.02	0.69±0.03
80	0.12±0.02	0.09±0.02	0.1±0.02	0.1±0.02	0.09±0.01	0.1±0.01	0.1±0.01	0.12±0.01	0.15±0.01	0.15±0.01	0.17±0.01	0.18±0.01
81	0.32±0.02	0.35±0.02	0.38±0.02	0.36±0.01	0.34±0.01	0.35±0.01	0.35±0.01	0.36±0.0	0.37±0.0	0.36±0.0	0.35±0.0	0.34±0.0

Table B.8: Galaxy's effective radius (kpc) estimated in this thesis using the MEGAMORPH-GALAPAGOS2 project. Column 1 is the ID of each galaxy, and the columns 2 to 13 are the effective radius in the 12 S-PLUS filters.

ID	Re_u	Re_{J0378}	Re_{J0395}	Re_{J0410}	Re_{J0430}	Re_g	Re_{J0515}	Re_r	Re_{J0660}	Re_i	Re_{J0861}	Re_z
1	4.2±0.1	4.1±0.1	4.1±0.1	4.1±0.1	4.1±0.1	4.0±0.1	4.0±0.1	4.0±0.1	4.0±0.1	4.1±0.1	4.1±0.1	4.0±0.1
2	3.1±0.1	3.1±0.1	3.0±0.1	3.0±0.1	3.0±0.1	2.9±0.1	2.8±0.1	2.7±0.1	2.7±0.1	2.7±0.1	2.6±0.1	2.5±0.1
3	1.9±0.1	1.9±0.1	1.9±0.1	1.9±0.1	1.9±0.1	1.9±0.1	2.0±0.1	2.0±0.1	2.0±0.1	2.1±0.1	2.1±0.1	2.0±0.1
4	2.7±0.1	2.7±0.1	2.7±0.1	2.7±0.1	2.7±0.1	2.8±0.1	2.8±0.1	3.0±0.1	3.0±0.1	3.1±0.1	3.1±0.1	3.0±0.1
5	4.5±0.2	4.6±0.2	4.7±0.1	4.7±0.1	4.8±0.1	5.0±0.1	5.2±0.1	5.6±0.1	5.7±0.1	5.9±0.1	5.9±0.1	5.7±0.1
6	30.4±0.9	24.6±0.8	21.8±0.7	19.5±0.6	16.6±0.5	10.9±0.3	7.9±0.2	3.0±0.1	2.4±0.1	2.5±0.1	2.9±0.1	2.5±0.1
7	1.1±0.1	1.1±0.1	1.1±0.1	1.1±0.1	1.2±0.1	1.2±0.1	1.2±0.1	1.2±0.1	1.2±0.1	1.2±0.1	1.2±0.1	1.2±0.1
8	3.6±0.1	3.3±0.1	3.2±0.1	3.1±0.1	3.0±0.1	2.7±0.1	2.6±0.1	2.5±0.1	2.5±0.1	2.6±0.1	2.6±0.1	2.6±0.1

Continued on next page

Table B.8 – continued from previous page

ID	Re_u	Re_{J0378}	Re_{J0395}	Re_{J0410}	Re_{J0430}	Re_g	Re_{J0515}	Re_r	Re_{J0660}	Re_i	Re_{J0861}	Re_z
9	2.5±0.3	2.6±0.2	2.6±0.2	2.6±0.2	2.7±0.1	2.7±0.1	2.7±0.1	2.6±0.1	2.6±0.1	2.5±0.1	2.4±0.1	2.5±0.1
10	2.7±0.3	3.8±0.2	4.4±0.2	4.8±0.2	5.3±0.2	6.2±0.2	6.5±0.2	6.5±0.1	6.3±0.1	5.4±0.1	5.0±0.1	5.1±0.1
11	2.3±0.1	2.1±0.1	2.1±0.1	2.0±0.1	2.0±0.1	1.9±0.1	1.9±0.1	1.9±0.1	1.9±0.1	2.0±0.1	2.1±0.1	2.1±0.1
12	1.6±0.3	1.6±0.2	1.6±0.2	1.5±0.1	1.5±0.1	1.5±0.1	1.5±0.1	1.5±0.1	1.5±0.1	1.6±0.1	1.6±0.1	1.6±0.1
13	4.5±0.1	4.0±0.1	3.8±0.1	3.7±0.1	3.5±0.1	3.2±0.1	3.1±0.1	3.1±0.1	3.2±0.1	3.4±0.1	3.4±0.1	3.2±0.1
14	2.1±0.2	2.1±0.2	2.0±0.1	2.0±0.1	2.0±0.1	2.0±0.1	2.0±0.1	2.1±0.1	2.1±0.1	2.1±0.1	2.2±0.1	2.2±0.1
15	4.1±0.2	3.9±0.1	3.7±0.1	3.7±0.1	3.6±0.1	3.4±0.1	3.4±0.1	3.6±0.1	3.7±0.1	4.0±0.1	4.1±0.1	4.0±0.1
16	1.4±0.1	1.3±0.1	1.3±0.1	1.3±0.1	1.3±0.1	1.2±0.1	1.2±0.1	1.2±0.1	1.2±0.1	1.2±0.1	1.1±0.1	1.1±0.1
17	2.6±0.2	2.5±0.2	2.5±0.1	2.4±0.1	2.4±0.1	2.3±0.1	2.3±0.1	2.3±0.1	2.3±0.1	2.4±0.1	2.5±0.1	2.5±0.1
18	4.4±0.9	4.3±0.6	4.3±0.5	4.2±0.5	4.2±0.4	4.3±0.2	4.4±0.2	4.9±0.1	5.1±0.1	5.3±0.1	5.0±0.2	4.6±0.2
19	2.4±0.1	2.3±0.1	2.2±0.1	2.1±0.1	2.1±0.1	2.0±0.1	1.9±0.1	1.9±0.1	1.9±0.1	2.0±0.1	2.0±0.1	1.9±0.1
20	3.1±0.3	3.5±0.2	3.7±0.2	3.9±0.2	4.2±0.2	4.8±0.2	5.2±0.2	6.1±0.1	6.3±0.1	6.7±0.2	6.5±0.2	6.1±0.3
21	3.9±0.2	3.9±0.1	3.9±0.1	3.9±0.1	3.9±0.1	3.8±0.1	3.8±0.1	3.7±0.1	3.7±0.1	3.6±0.1	3.5±0.1	3.5±0.1
22	5.4±0.2	4.9±0.1	4.7±0.1	4.5±0.1	4.3±0.1	3.9±0.1	3.7±0.1	3.4±0.1	3.4±0.1	3.4±0.1	3.5±0.1	3.4±0.1
23	3.1±0.1	3.1±0.1	3.1±0.1	3.0±0.1	3.0±0.1	3.0±0.1	3.1±0.1	3.3±0.1	3.4±0.1	3.6±0.1	3.6±0.1	3.5±0.1
24	1.3±0.2	1.3±0.1	1.2±0.1	1.2±0.1	1.2±0.1	1.2±0.1	1.3±0.1	1.3±0.1	1.3±0.1	1.3±0.1	1.3±0.1	1.3±0.1
25	2.3±0.1	2.2±0.1	2.1±0.1	2.1±0.1	2.0±0.1	1.9±0.1	1.9±0.1	1.9±0.1	1.9±0.1	2.1±0.1	2.2±0.1	2.3±0.1
26	1.2±0.1	1.2±0.1	1.2±0.1	1.2±0.1	1.2±0.1	1.1±0.1	1.1±0.1	1.1±0.1	1.1±0.1	1.1±0.1	1.1±0.1	1.2±0.1
27	3.7±0.2	3.5±0.2	3.4±0.2	3.3±0.1	3.2±0.1	3.1±0.1	3.0±0.1	3.1±0.1	3.1±0.1	3.2±0.1	3.0±0.1	2.7±0.1
28	2.0±0.9	1.9±0.7	1.9±0.6	1.9±0.5	1.8±0.4	1.8±0.3	1.7±0.2	1.6±0.1	1.6±0.1	1.6±0.1	1.6±0.1	1.6±0.2
29	8.4±0.6	8.6±0.4	8.6±0.4	8.7±0.3	8.8±0.3	9.0±0.2	9.1±0.1	9.2±0.1	9.1±0.1	8.5±0.1	7.5±0.1	6.6±0.1
30	2.1±0.1	2.1±0.1	2.2±0.1	2.2±0.1	2.3±0.1	2.3±0.1	2.4±0.1	2.4±0.1	2.4±0.1	2.5±0.1	2.6±0.1	2.8±0.1
31	1.0±0.1	1.0±0.1	1.0±0.1	1.0±0.1	1.0±0.1	1.0±0.1	1.0±0.1	1.0±0.1	1.0±0.1	1.0±0.1	1.0±0.1	1.0±0.1
32	1.7±0.1	1.6±0.1	1.6±0.1	1.6±0.1	1.5±0.1	1.4±0.1	1.4±0.1	1.3±0.1	1.3±0.1	1.3±0.1	1.3±0.1	1.2±0.1
33	1.9±0.1	1.7±0.1	1.6±0.1	1.6±0.1	1.5±0.1	1.4±0.1	1.4±0.1	1.3±0.1	1.4±0.1	1.4±0.1	1.5±0.1	1.5±0.1
34	0.7±0.1	0.7±0.1	0.7±0.1	0.7±0.1	0.7±0.1	0.7±0.1	0.7±0.1	0.6±0.1	0.6±0.1	0.6±0.1	0.8±0.1	1.0±0.1
35	1.6±0.1	1.6±0.1	1.6±0.1	1.6±0.1	1.6±0.1	1.6±0.1	1.6±0.1	1.6±0.1	1.6±0.1	1.6±0.1	1.5±0.1	1.5±0.1
36	1.4±0.1	1.4±0.1	1.4±0.1	1.4±0.1	1.4±0.1	1.4±0.1	1.4±0.1	1.4±0.1	1.4±0.1	1.4±0.1	1.5±0.1	1.5±0.1
37	4.6±0.2	4.6±0.2	4.6±0.1	4.6±0.1	4.5±0.1	4.5±0.1	4.5±0.1	4.3±0.1	4.3±0.1	4.2±0.1	4.1±0.1	4.1±0.1
38	4.5±0.1	4.2±0.1	4.1±0.1	4.0±0.1	3.9±0.1	3.6±0.1	3.5±0.1	3.4±0.1	3.4±0.1	3.4±0.1	3.3±0.1	3.3±0.1
39	1.4±0.1	1.2±0.1	1.2±0.1	1.1±0.1	1.0±0.1	0.9±0.1	0.9±0.1	0.8±0.1	0.8±0.1	0.7±0.1	0.6±0.1	0.5±0.1
40	5.2±0.4	4.7±0.3	4.4±0.2	4.2±0.2	3.9±0.2	3.4±0.1	3.2±0.1	2.8±0.1	2.8±0.1	2.8±0.1	2.9±0.1	2.8±0.1
41	3.5±0.1	3.3±0.1	3.2±0.1	3.1±0.1	3.0±0.1	2.9±0.1	2.8±0.1	2.8±0.1	2.8±0.1	2.9±0.1	2.9±0.1	2.7±0.1
42	3.1±0.2	3.1±0.2	3.2±0.2	3.2±0.1	3.2±0.1	3.3±0.1	3.3±0.1	3.4±0.1	3.4±0.1	3.3±0.1	3.2±0.1	3.0±0.1
43	3.3±0.1	3.3±0.1	3.3±0.1	3.2±0.1	3.3±0.1	3.3±0.1	3.3±0.1	3.5±0.1	3.5±0.1	3.5±0.1	3.3±0.1	3.0±0.1
44	2.4±0.1	2.3±0.1	2.2±0.1	2.2±0.1	2.2±0.1	2.1±0.1	2.0±0.1	2.0±0.1	2.0±0.1	2.0±0.1	2.1±0.1	2.1±0.1
45	3.4±0.2	3.5±0.2	3.6±0.1	3.6±0.1	3.7±0.1	3.9±0.1	4.0±0.1	4.2±0.1	4.2±0.1	4.3±0.1	4.2±0.1	4.1±0.1
46	2.9±0.3	2.8±0.2	2.7±0.2	2.7±0.1	2.7±0.1	2.6±0.1	2.5±0.1	2.5±0.1	2.5±0.1	2.5±0.1	2.6±0.1	2.6±0.1
47	2.2±0.1	2.3±0.1	2.3±0.1	2.3±0.1	2.3±0.1	2.4±0.1	2.4±0.1	2.5±0.1	2.5±0.1	2.5±0.1	2.6±0.1	2.6±0.1
48	2.3±0.1	2.1±0.1	2.0±0.1	1.9±0.1	1.8±0.1	1.6±0.1	1.5±0.1	1.4±0.1	1.4±0.1	1.5±0.1	1.6±0.1	1.7±0.1
49	1.9±0.1	2.1±0.1	2.2±0.1	2.3±0.1	2.4±0.1	2.7±0.1	2.8±0.1	2.9±0.1	3.0±0.1	3.0±0.1	3.1±0.1	3.1±0.1
50	4.8±0.1	4.5±0.1	4.4±0.1	4.3±0.1	4.1±0.1	3.9±0.1	3.8±0.1	3.6±0.1	3.6±0.1	3.6±0.1	3.5±0.1	3.3±0.1
51	3.2±0.2	3.3±0.2	3.3±0.1	3.4±0.1	3.4±0.1	3.6±0.1	3.8±0.1	4.3±0.1	4.4±0.1	4.7±0.1	4.7±0.1	4.5±0.1
52	2.7±0.2	2.7±0.1	2.6±0.1	2.6±0.1	2.5±0.1	2.4±0.1	2.4±0.1	2.2±0.1	2.2±0.1	2.2±0.1	2.3±0.1	2.4±0.1
53	2.7±0.1	2.7±0.1	2.6±0.1	2.6±0.1	2.6±0.1	2.5±0.1	2.5±0.1	2.5±0.1	2.5±0.1	2.4±0.1	2.3±0.1	2.2±0.1
54	3.8±0.3	3.8±0.3	3.8±0.2	3.8±0.2	3.8±0.2	3.7±0.1	3.6±0.1	3.3±0.1	3.2±0.1	3.1±0.1	3.2±0.1	3.3±0.1
55	2.3±0.2	2.2±0.1	2.2±0.1	2.2±0.1	2.2±0.1	2.1±0.1	2.2±0.1	2.3±0.1	2.4±0.1	2.5±0.1	2.5±0.1	2.3±0.1
56	2.3±0.1	2.3±0.1	2.2±0.1	2.2±0.1	2.2±0.1	2.1±0.1	2.1±0.1	2.1±0.1	2.1±0.1	2.1±0.1	2.1±0.1	2.1±0.1
57	8.8±0.4	8.5±0.3	8.4±0.2	8.2±0.2	8.0±0.2	7.5±0.1	7.1±0.1	6.0±0.1	5.7±0.1	5.3±0.1	5.6±0.1	6.1±0.1
58	2.7±0.2	2.5±0.1	2.5±0.1	2.4±0.1	2.4±0.1	2.4±0.1	2.4±0.1	2.6±0.1	2.7±0.1	2.9±0.1	2.8±0.1	2.6±0.1
59	2.5±0.2	2.5±0.1	2.6±0.1	2.6±0.1	2.6±0.1	2.7±0.1	2.7±0.1	2.8±0.1	2.8±0.1	2.9±0.1	3.0±0.1	3.1±0.1
60	4.9±0.1	4.6±0.1	4.6±0.1	4.5±0.1	4.4±0.1	4.3±0.1	4.2±0.1	4.2±0.1	4.3±0.1	4.4±0.1	4.3±0.1	4.1±0.1
61	2.0±0.1	2.0±0.1	1.9±0.1	1.9±0.1	1.9±0.1	1.9±0.1	1.8±0.1	1.8±0.1	1.8±0.1	1.8±0.1	1.8±0.1	1.8±0.1
62	0.9±0.1	0.9±0.1	0.9±0.1	0.8±0.1	0.8±0.1	0.8±0.1	0.8±0.1	0.8±0.1	0.8±0.1	0.8±0.1	0.8±0.1	0.7±0.1
63	2.7±0.3	2.7±0.3	2.8±0.2	2.8±0.2	2.9±0.2	3.3±0.1	3.6±0.1	4.6±0.1	4.9±0.1	5.5±0.1	5.2±0.1	4.6±0.1
64	2.2±0.2	2.1±0.1	2.1±0.1	2.1±0.1	2.1±0.1	2.1±0.1	2.1±0.1	2.2±0.1	2.3±0.1	2.4±0.1	2.4±0.1	2.4±0.1
65	3.2±0.1	3.1±0.1	3.0±0.1	3.0±0.1	2.9±0.1	2.9±0.1	2.9±0.1	2.9±0.1	3.0±0.1	3.0±0.1	3.0±0.1	2.8±0.1
66	1.1±0.1	1.1±0.1	1.1±0.1	1.1±0.1	1.1±0.1	1.1±0.1	1.2±0.1	1.2±0.1	1.2±0.1	1.3±0.1	1.2±0.1	1.2±0.1
67	3.1±0.2	3.1±0.1	3.1±0.1	3.2±0.1	3.2±0.1	3.3±0.1	3.3±0.1	3.6±0.1	3.6±0.1	3.7±0.1	3.7±0.1	3.5±0.1
68	4.1±0.5	3.9±0.4	3.8±0.3	3.7±0.3	3.6±0.2	3.4±0.1	3.2±0.1	3.0±0.1	3.0±0.1	3.0±0.1	3.1±0.1	3.2±0.1
69	9.2±0.5	7.9±0.3	7.3±0.3	6.8±0.2	6.3±0.1	5.5±0.1	5.3±0.1	5.9±0.1	6.4±0.1	8.4±0.1	10.0±0.2	10.5±0.3
70	1.6±0.1	1.5±0.1	1.5±0.1	1.5±0.1	1.5±0.1	1.5±0.1	1.5±0.1	1.7±0.1	1.7±0.1	1.8±0.1	1.7±0.1	1.6±0.1
71	2.5±0.1	2.4±0.1	2.4±0.1	2.3±0.1	2.3±0.1	2.1±0.1	2.1±0.1	2.0±0.1	2.0±0.1	2.0±0.1	1.9±0.1	1.8±0.1
72	4.8±0.5	4.3±0.3	4.1±0.3	3.9±0.3	3.7±0.2	3.3±0.1	3.1±0.1	2.9±0.1	3.0±0.1	3.1±0.1	3.2±0.1	3.2±0.1
73	1.7±0.1	1.6±0.1	1.5±0.1	1.5±0.1	1.5±0.1	1.4±0.1	1.4±0.1	1.3±0.1	1.3±0.1	1.4±0.1	1.4±0.1	1.3±0.1
74	5.7±0.1	5.4±0.1	5.3±0.1	5.2±0.1	5.0±0.1	4.7±0.1	4.6±0.1	4.3±0.1	4.3±0.1	4.2±0.1	4.3±0.1	4.3±0.1
75	1.1±0.1	1.1±0.1	1.1±0.1	1.1±0.1	1.1±0.1	1.1±0.1	1.1±0.1	1.1±0.1	1.1±0.1	1.1±0.1	1.1±0.1	1.1±0.1
76	4.9±0.2	4.6±0.1	4.4±0.1	4.3±0.1	4.2±0.1	3.9±0.1	3.8±0.1	3.8±0.1	3.8±0.1	4.0±0.1	3.9±0.1	3.8±0.1
77	1.6±0.1	1.6±0.1	1.7±0.1	1.7±0.1	1.7±0.1	1.8±0.1	1.8±0.1	1.8±0.1	1.8±0.1	1.8±0.1	1.7±0.1	1.6±0.1
78	0.7±0.1	0.7±0.1	0.7±0.1	0.7±0.1	0.7±0.1	0.7±0.1	0.7±0.1	0.7±0.1	0.7±0.1	0.7±0.1	0.6±0.1	0.6±0.1
79	1.8±0.1	1.8±0.1	1.8±0.1	1.8±0.1	1.8±0.1	1.8±0.1	1.8±0.1	1.8±0.1	1.8±0.1	1.8±0.1	1.8±0.1	1.8±0.1
80	3.4±0.1	3.3±0.1	3.2±0.1	3.2±0.1	3.1±0.1	3.0±0.1	3.0±0.1	3.0±0.1	3.1±0.1	3.2±0.1	3.2±0.1	3.1±0.1
81	3.0±0.1	3.3±0.1	3.5±0.1	3.7±0.1	3.8±0.1	4.2±0.1	4.3±0.1	4.7±0.1	4.7±0.1	5.0±0.1	5.3±0.1	5.7±0.1

Table B.9: Bulge's effective radius (kpc) estimated in this thesis using the MEGAMORPH-GALAPAGOS2 project. Column 1 is the ID of each galaxy, and the columns 2 to 13 are the Bulge's effective radius in the 12 S-PLUS filters.

ID	Re_u	Re_{J0378}	Re_{J0395}	Re_{J0410}	Re_{J0430}	Re_g	Re_{J0515}	Re_r	Re_{J0660}	Re_i	Re_{J0861}	Re_z
1	3.3±0.2	3.2 ±0.1	3.1 ±0.1	3.1 ±0.1	3.0 ±0.1	3.0±0.1	3.0 ±0.1	3.4±0.1	3.6 ±0.1	4.5±0.2	5.7 ±0.3	6.5±0.4
2	3.1±0.1	3.0 ±0.1	3.0 ±0.1	3.0 ±0.1	3.0 ±0.1	2.9±0.1	2.9 ±0.1	2.7±0.1	2.7 ±0.1	2.6±0.1	2.5 ±0.1	2.5±0.1
3	0.6±0.1	0.7 ±0.1	0.8 ±0.1	0.9 ±0.1	1.0 ±0.2	1.3±0.2	1.6 ±0.3	2.9±0.6	3.5 ±0.7	5.3±1.4	7.4 ±2.3	8.7±2.8
4	0.7±0.1	0.7 ±0.1	0.7 ±0.1	0.7 ±0.1	0.7 ±0.1	0.7±0.1	0.7 ±0.1	0.6±0.1	0.6 ±0.1	0.6±0.1	0.6 ±0.1	0.6±0.1
5	2.9±0.2	3.1 ±0.2	3.1 ±0.2	3.2 ±0.2	3.3 ±0.1	3.5±0.1	3.6 ±0.1	3.8±0.1	3.8 ±0.1	3.8±0.1	3.6 ±0.1	3.5±0.1
6	0.4±0.1	0.4 ±0.1	0.4 ±0.1	0.4 ±0.1	0.4 ±0.1	0.4±0.1	0.4 ±0.1	0.4±0.1	0.4 ±0.1	0.4±0.1	0.4 ±0.1	0.5±0.1
9	1.9±0.7	1.7 ±0.6	1.6 ±0.5	1.5 ±0.5	1.4 ±0.5	1.2±0.4	1.0 ±0.3	0.6±0.2	0.5 ±0.1	0.3±0.1	0.2 ±0.1	0.1±0.1
10	0.4±0.1	0.4 ±0.1	0.4 ±0.1	0.4 ±0.1	0.4 ±0.1	0.4±0.1	0.4 ±0.1	0.4±0.1	0.4 ±0.1	0.4±0.1	0.4 ±0.1	0.4±0.1
11	2.3±0.5	2.4 ±0.5	2.4 ±0.4	2.4 ±0.4	2.4 ±0.4	2.4±0.3	2.4 ±0.2	2.5±0.1	2.6 ±0.1	2.6±0.1	2.7 ±0.2	2.8±0.2
14	1.0±0.1	0.9 ±0.1	0.9 ±0.1	0.9 ±0.1	0.9 ±0.1	0.8±0.1	0.8 ±0.1	0.8±0.1	0.8 ±0.1	0.8±0.1	0.9 ±0.1	1.0±0.1
15	2.2±0.1	2.1 ±0.1	2.1 ±0.1	2.0 ±0.1	2.0 ±0.1	1.9±0.1	1.9 ±0.1	1.8±0.1	1.8 ±0.1	1.8±0.1	2.0 ±0.1	2.1±0.1
17	0.8±0.1	0.8 ±0.1	0.7 ±0.1	0.7 ±0.1	0.7 ±0.1	0.7±0.1	0.7 ±0.1	0.7±0.1	0.7 ±0.1	0.7±0.1	0.7 ±0.1	0.7±0.1
19	0.8±0.1	0.8 ±0.1	0.8 ±0.1	0.8 ±0.1	0.8 ±0.1	0.9±0.1	0.9 ±0.1	0.9±0.1	0.9 ±0.1	0.9±0.1	0.9 ±0.1	0.9±0.1
20	3.3±3.8	3.3 ±3.4	3.3 ±3.2	3.3 ±3.0	3.3 ±2.7	3.2±2.1	3.1 ±1.8	2.6±0.9	2.5 ±0.7	1.8±0.3	1.0 ±0.2	0.6±0.1
21	1.2±0.1	1.2 ±0.1	1.1 ±0.1	1.1 ±0.1	1.1 ±0.1	1.0±0.1	0.9 ±0.1	0.8±0.1	0.8 ±0.1	0.8±0.1	0.8 ±0.1	0.8±0.1
22	0.8±0.1	0.8 ±0.1	0.8 ±0.1	0.8 ±0.1	0.8 ±0.1	0.7±0.1	0.7 ±0.1	0.7±0.1	0.7 ±0.1	0.7±0.1	0.7 ±0.1	0.7±0.1
24	0.7±0.2	0.7 ±0.2	0.7 ±0.1	0.7 ±0.1	0.7 ±0.1	0.7±0.1	0.7 ±0.1	0.7±0.1	0.7 ±0.1	0.7±0.1	0.7 ±0.1	0.7±0.1
25	0.7±0.1	0.9 ±0.1	0.9 ±0.1	1.0 ±0.1	1.1 ±0.1	1.3±0.1	1.4 ±0.1	1.8±0.1	1.9 ±0.1	2.3±0.1	2.6 ±0.1	2.8±0.1
30	0.4±0.1	0.4 ±0.1	0.4 ±0.1	0.4 ±0.1	0.4 ±0.1	0.4±0.1	0.4 ±0.1	0.4±0.1	0.4 ±0.1	0.3±0.1	0.3 ±0.1	0.3±0.1
32	0.8±0.1	0.8 ±0.1	0.8 ±0.1	0.8 ±0.1	0.8 ±0.1	0.8±0.1	0.8 ±0.1	0.8±0.1	0.8 ±0.1	0.8±0.1	0.8 ±0.1	0.8±0.1
33	0.6±0.1	0.6 ±0.1	0.6 ±0.1	0.6 ±0.1	0.6 ±0.1	0.7±0.1	0.7 ±0.1	0.7±0.1	0.7 ±0.1	0.7±0.1	0.6 ±0.1	0.6±0.1
35	1.1±0.1	1.1 ±0.1	1.1 ±0.1	1.0 ±0.1	1.0 ±0.1	1.0±0.1	1.0 ±0.1	1.0±0.1	1.0 ±0.1	0.9±0.1	0.8 ±0.1	0.8±0.1
37	3.1±0.7	3.0 ±0.6	3.0 ±0.5	3.0 ±0.5	2.9 ±0.4	2.9±0.3	2.8 ±0.2	2.7±0.1	2.6 ±0.1	2.5±0.1	2.5 ±0.1	2.5±0.1
39	0.6±0.1	0.6 ±0.1	0.6 ±0.1	0.6 ±0.1	0.6 ±0.1	0.6±0.1	0.6 ±0.1	0.5±0.1	0.5 ±0.1	0.4±0.1	0.4 ±0.1	0.3±0.1
40	1.7±0.2	1.6 ±0.2	1.6 ±0.1	1.6 ±0.1	1.6 ±0.1	1.5±0.1	1.5 ±0.1	1.4±0.1	1.4 ±0.1	1.4±0.1	1.4 ±0.1	1.5±0.1
42	0.7±0.2	0.7 ±0.2	0.6 ±0.2	0.6 ±0.2	0.6 ±0.1	0.5±0.1	0.5 ±0.1	0.5±0.1	0.6 ±0.1	0.7±0.1	1.0 ±0.1	1.2±0.1
43	2.0±0.1	2.0 ±0.1	1.9 ±0.1	1.9 ±0.1	1.9 ±0.1	1.8±0.1	1.8 ±0.1	1.6±0.1	1.6 ±0.1	1.5±0.1	1.5 ±0.1	1.5±0.1
44	1.3±0.1	1.3 ±0.1	1.2 ±0.1	1.2 ±0.1	1.2 ±0.1	1.2±0.1	1.2 ±0.1	1.2±0.1	1.2 ±0.1	1.1±0.1	1.1 ±0.1	1.0±0.1
45	1.2±0.3	1.3 ±0.2	1.3 ±0.2	1.4 ±0.2	1.5 ±0.2	1.6±0.1	1.7 ±0.1	1.8±0.1	1.8 ±0.1	1.7±0.1	1.5 ±0.1	1.4±0.1
46	0.7±0.1	0.7 ±0.1	0.7 ±0.1	0.7 ±0.1	0.7 ±0.1	0.7±0.1	0.7 ±0.1	0.8±0.1	0.8 ±0.1	0.8±0.1	0.8 ±0.1	0.9±0.1
47	0.7±0.1	0.6 ±0.1	0.6 ±0.1	0.6 ±0.1	0.6 ±0.1	0.6±0.1	0.6 ±0.1	0.6±0.1	0.6 ±0.1	0.5±0.1	0.5 ±0.1	0.5±0.1
48	2.3±0.2	2.1 ±0.2	2.0 ±0.1	1.9 ±0.1	1.8 ±0.1	1.5±0.1	1.4 ±0.1	1.1±0.1	1.1 ±0.1	1.2±0.1	1.5 ±0.2	1.7±0.2
49	0.9±0.1	0.9 ±0.1	1.0 ±0.1	1.0 ±0.1	1.0 ±0.1	1.0±0.1	1.0 ±0.1	1.0±0.1	1.0 ±0.1	1.0±0.1	1.0 ±0.1	1.0±0.1
51	0.5±0.1	0.5 ±0.1	0.5 ±0.1	0.5 ±0.1	0.5 ±0.1	0.5±0.1	0.5 ±0.1	0.5±0.1	0.5 ±0.1	0.4±0.1	0.5 ±0.1	0.5±0.1
53	1.2±0.1	1.2 ±0.1	1.1 ±0.1	1.1 ±0.1	1.1 ±0.1	1.0±0.1	1.0 ±0.1	0.9±0.1	0.8 ±0.1	0.7±0.1	0.7 ±0.1	0.6±0.1
54	0.5±0.1	0.5 ±0.1	0.5 ±0.1	0.5 ±0.1	0.6 ±0.1	0.6±0.1	0.6 ±0.1	0.6±0.1	0.6 ±0.1	0.6±0.1	0.6 ±0.1	0.7±0.1
55	0.9±0.1	0.9 ±0.1	0.9 ±0.1	0.9 ±0.1	0.9 ±0.1	0.8±0.1	0.8 ±0.1	0.8±0.1	0.8 ±0.1	0.7±0.1	0.7 ±0.1	0.7±0.1
56	0.8±0.1	0.8 ±0.1	0.8 ±0.1	0.8 ±0.1	0.9 ±0.1	0.9±0.1	0.9 ±0.1	1.0±0.1	1.0 ±0.1	1.0±0.1	1.0 ±0.1	1.0±0.1
57	14.6±1.3	13.1±1.2	12.4±1.1	11.7±1.0	10.8±0.9	8.8±0.7	7.5 ±0.6	4.2±0.3	3.4 ±0.2	1.6±0.1	0.9 ±0.1	0.8±0.1
58	1.4±0.2	1.5 ±0.2	1.6 ±0.2	1.7 ±0.2	1.8 ±0.1	2.0±0.1	2.1 ±0.1	2.3±0.1	2.3 ±0.1	2.3±0.1	2.2 ±0.1	2.0±0.1
59	2.8±0.5	2.9 ±0.5	2.9 ±0.4	2.9 ±0.4	3.0 ±0.3	3.0±0.2	3.1 ±0.2	3.1±0.1	3.1 ±0.1	3.0±0.1	2.9 ±0.1	2.7±0.2
61	1.2±0.1	1.2 ±0.1	1.2 ±0.1	1.3 ±0.1	1.3 ±0.1	1.3±0.1	1.3 ±0.1	1.3±0.1	1.3 ±0.1	1.3±0.1	1.2 ±0.1	1.2±0.1
63	0.4±0.1	0.4 ±0.1	0.4 ±0.1	0.4 ±0.1	0.4 ±0.1	0.4±0.1	0.4 ±0.1	0.4±0.1	0.4 ±0.1	0.5±0.1	0.5 ±0.1	0.5±0.1
66	0.3±0.1	0.3 ±0.1	0.3 ±0.1	0.3 ±0.1	0.2 ±0.1	0.2±0.1	0.2 ±0.1	0.2±0.1	0.2 ±0.1	0.2±0.1	0.2 ±0.1	0.3±0.1
67	0.7±0.1	0.7 ±0.1	0.7 ±0.1	0.7 ±0.1	0.7 ±0.1	0.7±0.1	0.7 ±0.1	0.6±0.1	0.6 ±0.1	0.6±0.1	0.6 ±0.1	0.6±0.1
73	0.5±0.1	0.6 ±0.1	0.6 ±0.1	0.6 ±0.1	0.7 ±0.1	0.8±0.1	0.8 ±0.1	0.9±0.1	1.0 ±0.1	1.1±0.1	1.1 ±0.1	1.2±0.1
74	2.0±0.1	1.9 ±0.1	1.9 ±0.1	1.8 ±0.1	1.8 ±0.1	1.7±0.1	1.6 ±0.1	1.5±0.1	1.5 ±0.1	1.4±0.1	1.5 ±0.1	1.5±0.1
75	0.4±0.1	0.4 ±0.1	0.4 ±0.1	0.4 ±0.1	0.4 ±0.1	0.4±0.1	0.4 ±0.1	0.4±0.1	0.4 ±0.1	0.4±0.1	0.4 ±0.1	0.4±0.1
77	0.5±0.1	0.6 ±0.1	0.6 ±0.1	0.7 ±0.1	0.7 ±0.1	0.8±0.1	0.9 ±0.1	1.0±0.1	1.1 ±0.1	1.2±0.1	1.2 ±0.1	1.3±0.1
78	0.4±0.1	0.4 ±0.1	0.4 ±0.1	0.4 ±0.1	0.4 ±0.1	0.4±0.1	0.4 ±0.1	0.5±0.1	0.5 ±0.1	0.5±0.1	0.4 ±0.1	0.4±0.1
80	0.9±0.2	0.8 ±0.2	0.8 ±0.2	0.8 ±0.2	0.8 ±0.2	0.7±0.1	0.7 ±0.1	0.6±0.1	0.6 ±0.1	0.6±0.1	0.6 ±0.1	0.7±0.1
81	0.5±0.1	0.5 ±0.1	0.5 ±0.1	0.5 ±0.1	0.5 ±0.1	0.5±0.1	0.5 ±0.1	0.5±0.1	0.5 ±0.1	0.5±0.1	0.5 ±0.1	0.5±0.1

Table B.10: Disc's effective radius (kpc) estimated in this thesis using the MEGAMORPH-GALAPAGOS2 project. Column 1 is the ID of each galaxy, and the columns 2 to 13 are the Disc's effective radius in the 12 S-PLUS filters.

ID	Re_u	Re_{J0378}	Re_{J0395}	Re_{J0410}	Re_{J0430}	Re_g	Re_{J0515}	Re_r	Re_{J0660}	Re_i	Re_{J0861}	Re_z
1	7.6±0.1	7.6±0.1	7.5±0.1	7.5±0.1	7.5±0.1	7.5±0.1	7.4±0.1	7.4±0.1	7.3±0.1	7.2±0.1	7.2±0.1	7.1±0.1
2	4.2±0.2	4.2±0.1	4.1±0.1	4.1±0.1	4.1±0.1	4.0±0.1	4.0±0.1	3.9±0.1	3.9±0.1	3.8±0.1	3.8±0.1	3.8±0.1
3	3.8±0.1	3.8±0.1	3.8±0.1	3.7±0.1	3.7±0.1	3.6±0.1	3.6±0.1	3.5±0.1	3.5±0.1	3.4±0.1	3.5±0.1	3.5±0.1
4	7.1±0.1	7.0±0.1	6.9±0.1	6.9±0.1	6.8±0.1	6.7±0.1	6.6±0.1	6.4±0.1	6.4±0.1	6.3±0.1	6.4±0.1	6.4±0.1
5	14.2±0.8	13.4±0.7	13.0±0.6	12.7±0.6	12.2±0.5	11.2±0.4	10.5±0.3	9.1±0.1	8.8±0.1	8.4±0.1	8.7±0.1	9.1±0.2
6	5.5±0.1	5.3±0.1	5.3±0.1	5.2±0.1	5.1±0.1	5.0±0.1	4.9±0.1	4.7±0.1	4.6±0.1	4.6±0.1	4.7±0.1	4.8±0.1
9	3.2±0.1	3.2±0.1	3.2±0.1	3.2±0.1	3.2±0.1	3.2±0.1	3.1±0.1	3.1±0.1	3.1±0.1	3.0±0.1	2.9±0.1	2.9±0.1

Continued on next page

Table B.10 – continued from previous page

ID	Re_u	Re_{J0378}	Re_{J0395}	Re_{J0410}	Re_{J0430}	Re_g	Re_{J0515}	Re_r	Re_{J0660}	Re_i	Re_{J0861}	Re_z
10	7.4±0.2	7.3±0.2	7.2±0.2	7.2±0.1	7.1±0.1	7.0±0.1	6.9±0.1	6.7±0.1	6.6±0.1	6.5±0.1	6.4±0.1	6.4±0.1
11	3.3±0.1	3.3±0.1	3.3±0.1	3.2±0.1	3.2±0.1	3.2±0.1	3.1±0.1	3.1±0.1	3.1±0.1	3.1±0.1	3.2±0.1	3.3±0.1
14	3.4±0.1	3.4±0.1	3.4±0.1	3.4±0.1	3.4±0.1	3.5±0.1	3.5±0.1	3.6±0.1	3.6±0.1	3.6±0.1	3.6±0.1	3.6±0.1
15	6.9±0.2	6.9±0.2	6.8±0.1	6.8±0.1	6.8±0.1	6.7±0.1	6.7±0.1	6.5±0.1	6.5±0.1	6.4±0.1	6.3±0.1	6.2±0.1
17	3.9±0.2	3.9±0.2	3.9±0.1	3.9±0.1	3.8±0.1	3.8±0.1	3.8±0.1	3.8±0.1	3.8±0.1	3.9±0.1	4.0±0.1	4.0±0.1
19	4.5±0.4	4.5±0.4	4.6±0.3	4.6±0.3	4.6±0.3	4.7±0.2	4.7±0.2	4.8±0.1	4.8±0.1	4.8±0.1	4.8±0.2	4.8±0.2
20	5.1±0.1	5.0±0.1	5.0±0.1	4.9±0.1	4.9±0.1	4.7±0.1	4.7±0.1	4.5±0.1	4.5±0.1	4.5±0.1	4.6±0.1	4.7±0.1
21	7.5±0.2	7.4±0.2	7.3±0.2	7.2±0.1	7.1±0.1	6.9±0.1	6.7±0.1	6.4±0.1	6.3±0.1	6.1±0.1	6.2±0.1	6.2±0.1
22	9.9±0.2	9.6±0.1	9.5±0.1	9.3±0.1	9.2±0.1	8.8±0.1	8.6±0.1	8.0±0.1	7.9±0.1	7.6±0.1	7.6±0.1	7.7±0.1
24	3.6±0.4	3.6±0.3	3.6±0.3	3.6±0.3	3.6±0.2	3.6±0.2	3.7±0.1	3.8±0.1	3.9±0.1	4.1±0.1	4.3±0.2	4.5±0.3
25	5.2±0.3	4.9±0.2	4.7±0.2	4.6±0.2	4.4±0.2	4.0±0.2	3.8±0.1	3.2±0.1	3.0±0.1	2.9±0.1	2.9±0.1	3.0±0.1
30	3.7±0.1	3.7±0.1	3.7±0.1	3.7±0.1	3.7±0.1	3.7±0.1	3.7±0.1	3.7±0.1	3.7±0.1	3.7±0.1	3.7±0.1	3.7±0.1
32	6.3±0.3	6.1±0.2	6.0±0.2	5.9±0.2	5.8±0.2	5.6±0.1	5.4±0.1	5.0±0.1	4.9±0.1	4.7±0.1	4.6±0.1	4.5±0.1
33	3.7±0.2	3.6±0.2	3.5±0.1	3.4±0.1	3.4±0.1	3.2±0.1	3.1±0.1	2.9±0.1	2.8±0.1	2.8±0.1	3.0±0.1	3.1±0.1
35	2.9±0.1	2.9±0.1	2.9±0.1	2.9±0.1	3.0±0.1	3.0±0.1	3.1±0.1	3.2±0.1	3.2±0.1	3.3±0.1	3.4±0.1	3.4±0.1
37	8.0±0.1	7.9±0.1	7.8±0.1	7.8±0.1	7.7±0.1	7.5±0.1	7.5±0.1	7.2±0.1	7.1±0.1	7.0±0.1	7.0±0.1	7.0±0.1
39	6.0±0.5	5.9±0.5	5.9±0.4	5.8±0.4	5.7±0.4	5.5±0.3	5.4±0.2	4.8±0.1	4.6±0.1	4.0±0.1	3.4±0.1	3.0±0.1
40	7.2±0.3	6.9±0.3	6.7±0.3	6.6±0.2	6.4±0.2	6.0±0.2	5.7±0.1	5.2±0.1	5.1±0.1	5.0±0.1	5.2±0.1	5.4±0.1
42	5.2±0.1	5.2±0.1	5.1±0.1	5.1±0.1	5.0±0.1	5.0±0.1	4.9±0.1	4.8±0.1	4.7±0.1	4.7±0.1	4.8±0.1	4.8±0.1
43	5.8±0.1	5.9±0.1	5.9±0.1	6.0±0.1	6.0±0.1	6.1±0.1	6.1±0.1	6.2±0.1	6.2±0.1	6.1±0.1	5.9±0.1	5.7±0.1
44	3.6±0.1	3.6±0.1	3.6±0.1	3.6±0.1	3.6±0.1	3.6±0.1	3.6±0.1	3.7±0.1	3.7±0.1	3.8±0.1	3.8±0.1	3.8±0.1
45	4.7±0.1	4.6±0.1	4.6±0.1	4.6±0.1	4.6±0.1	4.5±0.1	4.5±0.1	4.4±0.1	4.4±0.1	4.4±0.1	4.5±0.1	4.5±0.1
46	5.9±0.3	5.8±0.3	5.7±0.3	5.7±0.2	5.7±0.2	5.6±0.2	5.5±0.1	5.4±0.1	5.3±0.1	5.3±0.1	5.4±0.1	5.5±0.1
47	5.0±0.1	4.9±0.1	4.9±0.1	4.9±0.1	4.9±0.1	4.9±0.1	4.9±0.1	5.0±0.1	5.0±0.1	5.1±0.1	5.2±0.1	5.3±0.1
48	2.9±0.1	2.9±0.1	2.9±0.1	2.9±0.1	3.0±0.1	3.0±0.1	3.0±0.1	3.0±0.1	3.0±0.1	2.9±0.1	2.8±0.1	2.8±0.1
49	6.9±0.1	6.9±0.1	6.9±0.1	7.0±0.1	7.0±0.1	7.0±0.1	7.1±0.1	7.2±0.1	7.2±0.1	7.3±0.1	7.3±0.1	7.4±0.1
51	5.8±0.1	5.7±0.1	5.7±0.1	5.6±0.1	5.6±0.1	5.5±0.1	5.5±0.1	5.4±0.1	5.4±0.1	5.5±0.1	5.6±0.1	5.6±0.1
53	7.8±0.1	8.0±0.1	8.0±0.1	8.1±0.1	8.1±0.1	8.3±0.1	8.4±0.1	8.4±0.1	8.4±0.1	8.2±0.1	7.8±0.1	7.5±0.1
54	4.3±0.1	4.2±0.1	4.2±0.1	4.2±0.1	4.1±0.1	4.1±0.1	4.0±0.1	4.0±0.1	3.9±0.1	4.0±0.1	4.0±0.1	4.1±0.1
55	6.0±0.4	5.9±0.4	5.9±0.3	5.8±0.3	5.8±0.3	5.7±0.2	5.7±0.2	5.6±0.1	5.6±0.1	5.7±0.1	5.9±0.1	6.0±0.1
56	8.1±0.2	8.0±0.2	7.9±0.2	7.9±0.2	7.8±0.2	7.7±0.1	7.6±0.1	7.5±0.1	7.5±0.1	7.4±0.1	7.5±0.1	7.6±0.1
57	8.8±0.1	8.6±0.1	8.4±0.1	8.3±0.1	8.2±0.1	7.8±0.1	7.6±0.1	7.0±0.1	6.9±0.1	6.6±0.1	6.6±0.1	6.6±0.1
58	4.2±0.1	4.2±0.1	4.2±0.1	4.2±0.1	4.2±0.1	4.3±0.1	4.3±0.1	4.3±0.1	4.3±0.1	4.4±0.1	4.4±0.1	4.4±0.1
59	3.4±0.2	3.3±0.1	3.3±0.1	3.3±0.1	3.3±0.1	3.3±0.1	3.2±0.1	3.2±0.1	3.2±0.1	3.3±0.1	3.4±0.1	3.4±0.1
61	6.2±0.4	6.0±0.4	5.9±0.3	5.8±0.3	5.7±0.3	5.4±0.2	5.3±0.2	5.2±0.1	5.2±0.1	5.4±0.1	5.9±0.1	6.3±0.2
63	4.6±0.2	4.7±0.2	4.8±0.2	4.9±0.1	5.0±0.1	5.2±0.1	5.3±0.1	5.6±0.1	5.7±0.1	5.9±0.1	6.0±0.1	6.1±0.1
66	2.4±0.1	2.3±0.1	2.3±0.1	2.2±0.1	2.2±0.1	2.1±0.1	2.1±0.1	2.0±0.1	2.0±0.1	2.0±0.1	2.2±0.1	2.3±0.1
67	7.2±0.1	7.3±0.1	7.3±0.1	7.3±0.1	7.3±0.1	7.4±0.1	7.5±0.1	7.6±0.1	7.7±0.1	7.8±0.1	7.9±0.1	7.9±0.1
73	2.9±0.2	3.1±0.1	3.2±0.1	3.3±0.1	3.5±0.1	3.8±0.1	4.0±0.1	4.5±0.1	4.7±0.1	5.0±0.1	5.1±0.1	5.1±0.2
74	12.5±0.2	12.1±0.2	11.9±0.1	11.8±0.1	11.5±0.1	11.1±0.1	10.8±0.1	10.2±0.1	10.1±0.1	9.9±0.1	10.1±0.1	10.3±0.1
75	4.0±0.1	4.0±0.1	3.9±0.1	3.9±0.1	3.9±0.1	3.8±0.1	3.8±0.1	3.7±0.1	3.7±0.1	3.8±0.1	3.8±0.1	3.9±0.1
77	3.5±0.1	3.5±0.1	3.5±0.1	3.5±0.1	3.5±0.1	3.5±0.1	3.5±0.1	3.5±0.1	3.5±0.1	3.5±0.1	3.4±0.1	3.4±0.1
78	3.2±0.2	3.0±0.2	2.9±0.2	2.9±0.1	2.8±0.1	2.6±0.1	2.4±0.1	2.2±0.1	2.1±0.1	2.1±0.1	2.2±0.1	2.3±0.1
80	5.0±0.1	5.0±0.1	5.0±0.1	4.9±0.1	4.9±0.1	4.9±0.1	4.9±0.1	4.8±0.1	4.8±0.1	4.8±0.1	4.8±0.1	4.9±0.1
81	6.1±0.1	6.1±0.1	6.2±0.1	6.2±0.1	6.3±0.1	6.4±0.1	6.4±0.1	6.5±0.1	6.6±0.1	6.6±0.1	6.6±0.1	6.5±0.1

C The plane n_{SS} versus n_{Bulge}

In Chapter 5 we discussed the plane n_{SS} versus n_{Bulge} in the r-band, and we found that galaxies with high values of the Sérsic index, from the single Sérsic profile, have a larger Sérsic index for the bulge. Here, in Figure C.1, we show the plane n_{SS} versus n_{Bulge} in the 12 S-PLUS bands. The slope of this relation increases towards the redder filters, having its highest values in the g and $J0515$ filters. Table C.1 lists the slope of this relation in each S-PLUS band.

Table C.1: Slope of best linear regression of n_{galaxy} versus n_{bulge} in the 12 S-PLUS bands.

u	J0378	J0395	J0410	J0430	g	J0515	r	J0660	i	J0861	z
0.24±0.25	0.32±0.25	0.35±0.25	0.36±0.24	0.39±0.23	0.41 ±0.21	0.41±0.20	0.40±0.16	0.39±0.15	0.37±0.15	0.36±0.12	0.33±0.13

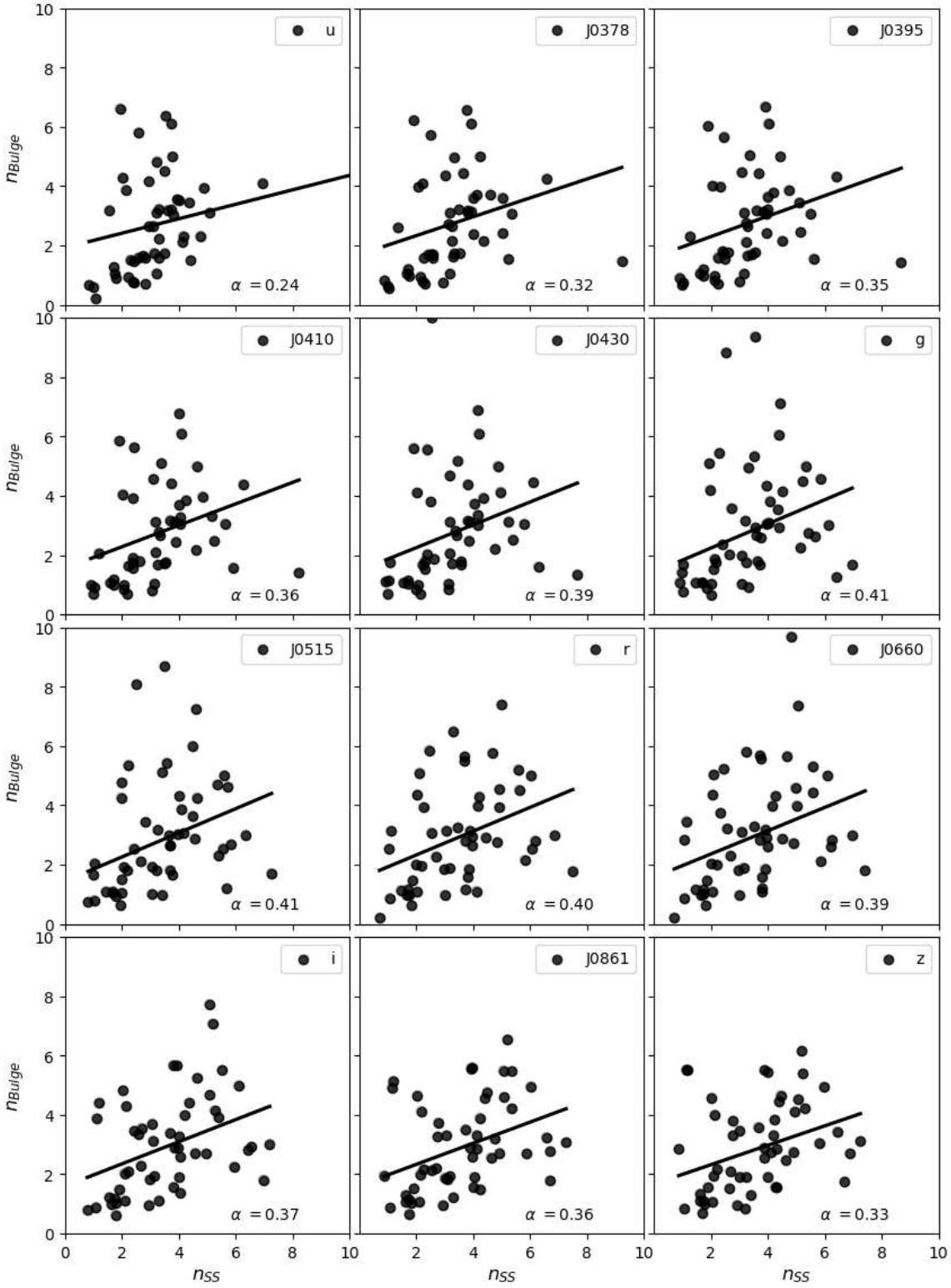

Figure C.1: The plane n_{SS} versus n_{Bulge} for the 12 S-PLUS bands. The black lines show the best linear fit, and the α symbol indicates the slope of the fit.

D Mass-size and Magnitude-size relation in the 12 S-PLUS bands

In the main body of the thesis we show the results of the mass-size relation for the *r*-band. Here, we present these results in the 12 S-PLUS bands. Figures D.1, D.2, and D.3 show the mass-size relation for the entire galaxy, bulge, and disc, respectively. For each filter we found the best linear fit using the python's *seaborn.regplot* package, where the option *robust=True* was used. This setup will de-weight outliers performing more reliable adjustments.

Table D.1: Regression slope of the mass-size relation for the galaxy (column 2), bulge (column 3) and disc (column 4) in the 12 S-PLUS filters.

Filter	Galaxy	Bulge	Disc
u	0.12±0.05	0.00±0.09	0.18±0.04
*J*0378	0.14±0.05	-0.01±0.09	0.19±0.04
*J*0395	0.14±0.05	-0.01±0.08	0.19±0.04
*J*0410	0.15±0.05	-0.01±0.08	0.19±0.04
*J*0430	0.16±0.05	-0.01±0.08	0.19±0.03
g	0.17±0.05	-0.01±0.08	0.19±0.03
*J*0515	0.18±0.05	-0.01±0.08	0.19±0.03
r	0.20±0.04	-0.01±0.08	0.18±0.03
*J*0660	0.21±0.04	-0.01±0.08	0.18±0.03
i	0.21±0.04	-0.01±0.08	0.18±0.03
*J*0861	0.20±0.04	-0.02±0.09	0.18±0.03
z	0.20±0.04	-0.04±0.09	0.18±0.03

The slope of the galaxy mass-size relation, using the 81 galaxies, increases towards redder bands, going from 0.12 to 0.21. To analyse the bulge and disc mass-size relation we used 52 galaxies, which are those that meet the criteria used in chapter 5 ($0.1 < B/T < 0.9$, $Re_{disc} > Re_{bulge}$, and $\chi^2 \geq 1.9$). The bulge's effective radius does not show any significant dependence on the stellar mass of the galaxy in all filters. The slope of the disc mass-size relation remains basically unchanged for all filters, being 0.18 or 0.19. Columns 2, 3, and 4 of Table D.1 show the slope of the best linear fit (in the 12 S-PLUS bands) for the galaxy, the bulge and the disc, respectively.

Table D.2: Regression slope of the magnitude-size relation in the galaxy (column 2), bulge (column 3) and disc (column 4) in the 12 S-PLUS filters.

Filter	Galaxy	Bulge	Disc
u	-0.13±0.03	-0.07±0.05	-0.14±0.02
*J*0378	-0.13±0.03	-0.06±0.05	-0.13±0.02
*J*0395	-0.14±0.03	-0.06±0.05	-0.13±0.02
*J*0410	-0.13±0.03	-0.03±0.05	-0.13±0.02
*J*0430	-0.12±0.03	-0.03±0.05	-0.12±0.02
g	-0.11±0.02	-0.01±0.04	-0.11±0.02
*J*0515	-0.11±0.02	0.00±0.04	-0.11±0.02
r	-0.11±0.02	0.00±0.04	-0.10±0.01
*J*0660	-0.11±0.02	0.01±0.04	-0.10±0.01
i	-0.10±0.02	0.01±0.04	-0.10±0.01
*J*0861	-0.10±0.02	0.02±0.04	-0.10±0.01
z	-0.10±0.02	0.02±0.04	-0.10±0.01

Knowing that the absolute magnitude is a proxy for stellar mass, we also show here the magnitude-size relation. Figures D.4, D.5, and D.6 show the result for the entire galaxy, bulge, and disc, respectively. The magnitude-size relation has similar trends found for the mass-size relation in the 12-SPLUS bands. Brighter galaxies have a larger effective radius than fainter galaxies. However, the slopes of this relations are not stepper towards red filters, as we observed in the mass-size relation. The same behaviour is seen in the effective radius of the disc. The size of the bulge does not vary significantly with the absolute magnitude of the galaxy. The slopes of the magnitude-size relation in the 12 S-PLUS bands are indicated in Table D.2. Columns 2, 3, and 4 show the slopes for the galaxy, the bulge, and the disc, respectively.

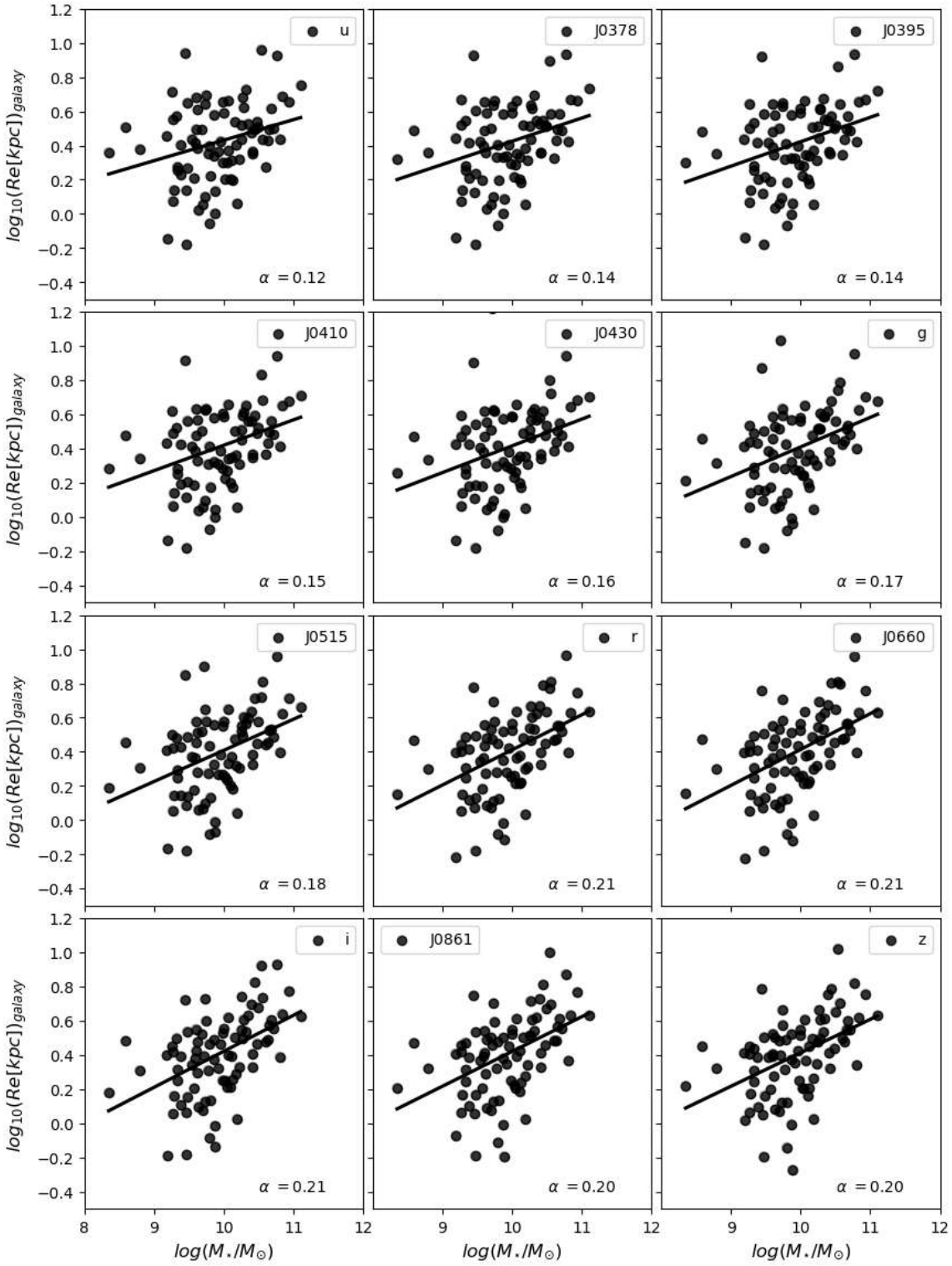

Figure D.1: Galaxy mass-size relation for the 12 S-PLUS bands. x-axis and y-axis show the galaxy' stellar mass and the galaxy's $log_{10}(Re[kpc])$, respectively. The black lines show the best linear fit, and the α symbol indicates the slope of the fit.

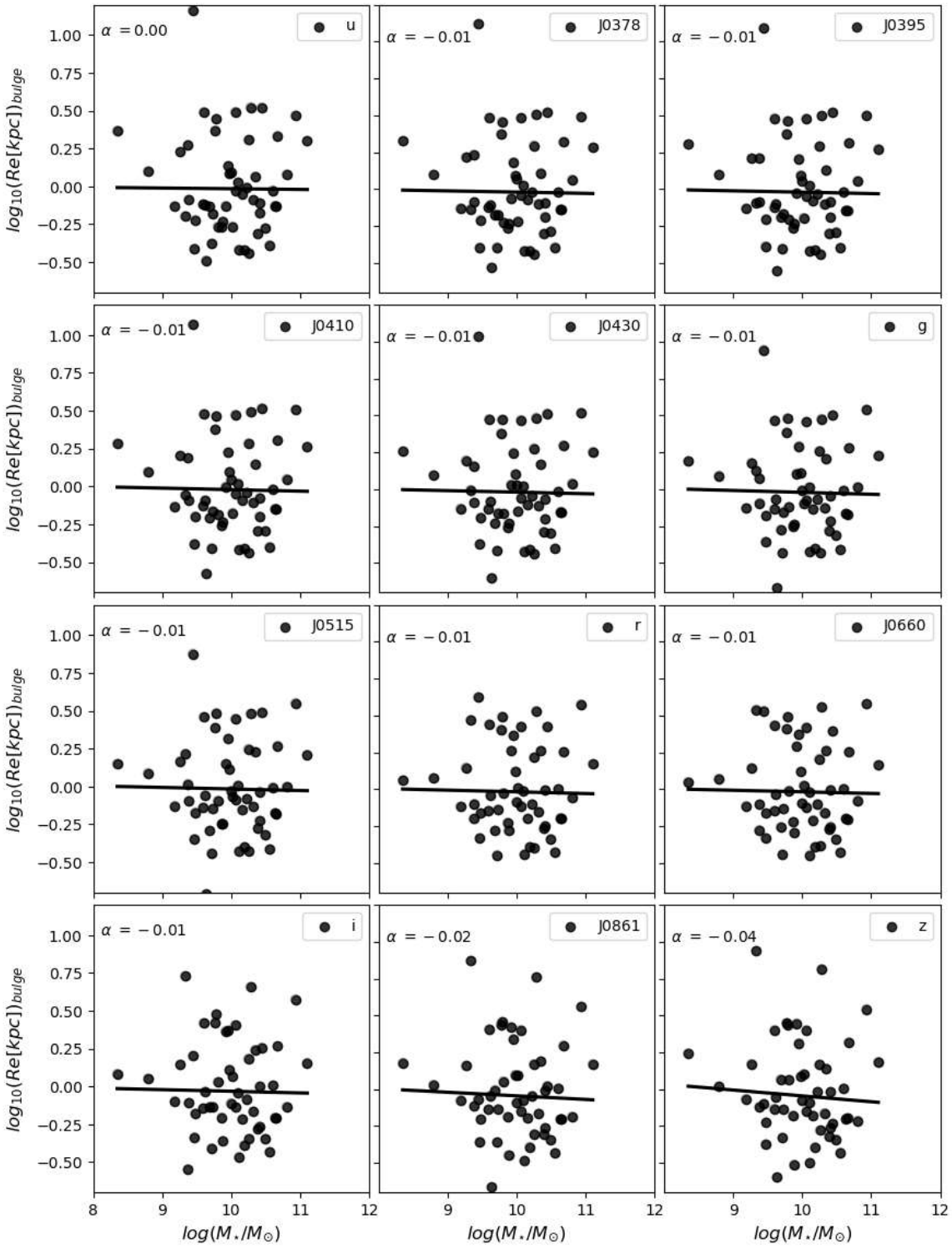

Figure D.2: Bulge mass-size relation in the 12 S-PLUS bands. x-axis and y-axis show the galaxy's stellar mass and the bulge's $log_{10}(Re[kpc])$, respectively. The black lines show the best linear fit, and the α symbol indicates the slope of the fit.

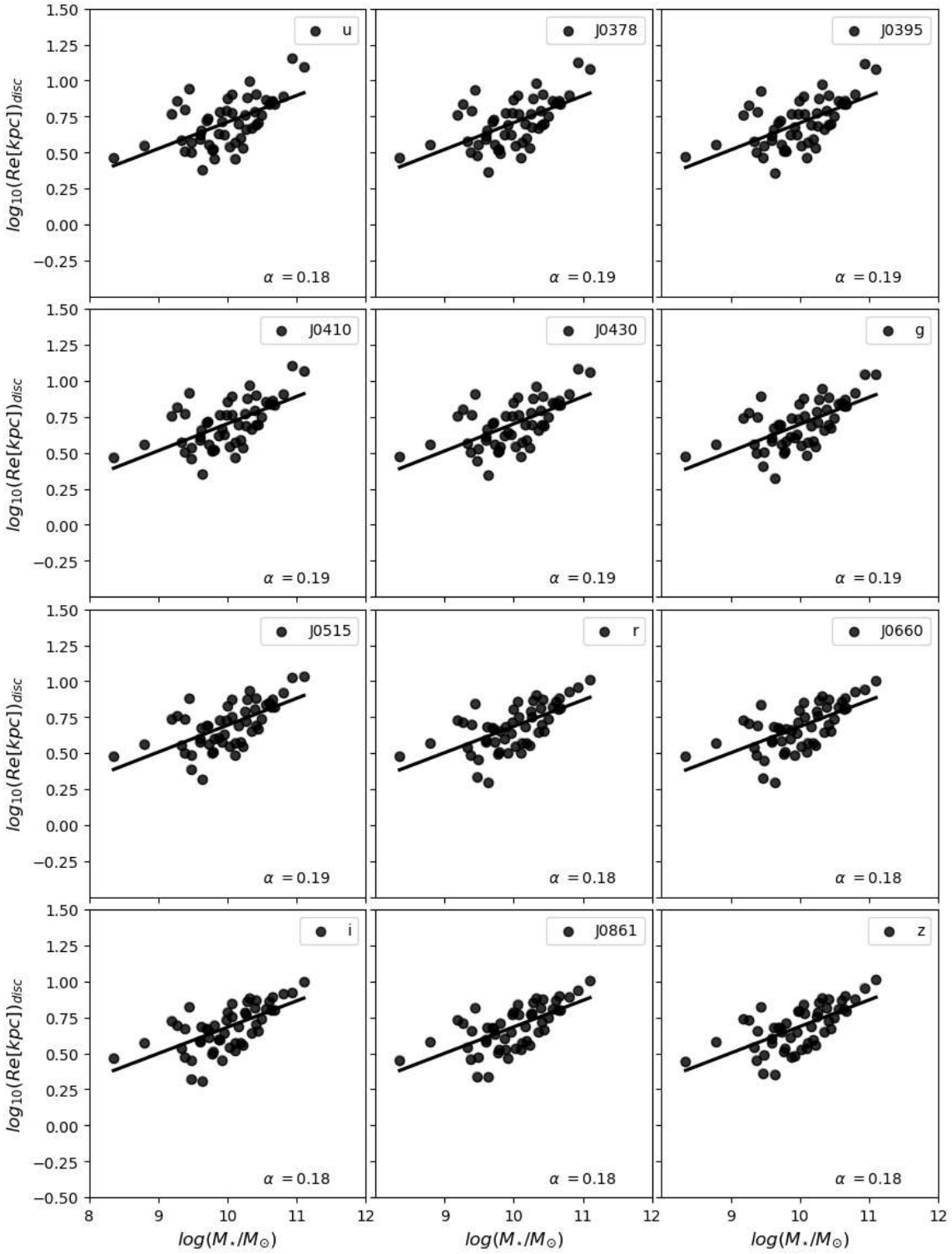

Figure D.3: Disc mass-size relation in the 12 S-PLUS bands. x-axis and y-axis show the galaxy's stellar mass and the disc's $log_{10}(Re[kpc])$, respectively. The black lines show the best linear fit, and the α symbol indicates the slope of the fit.

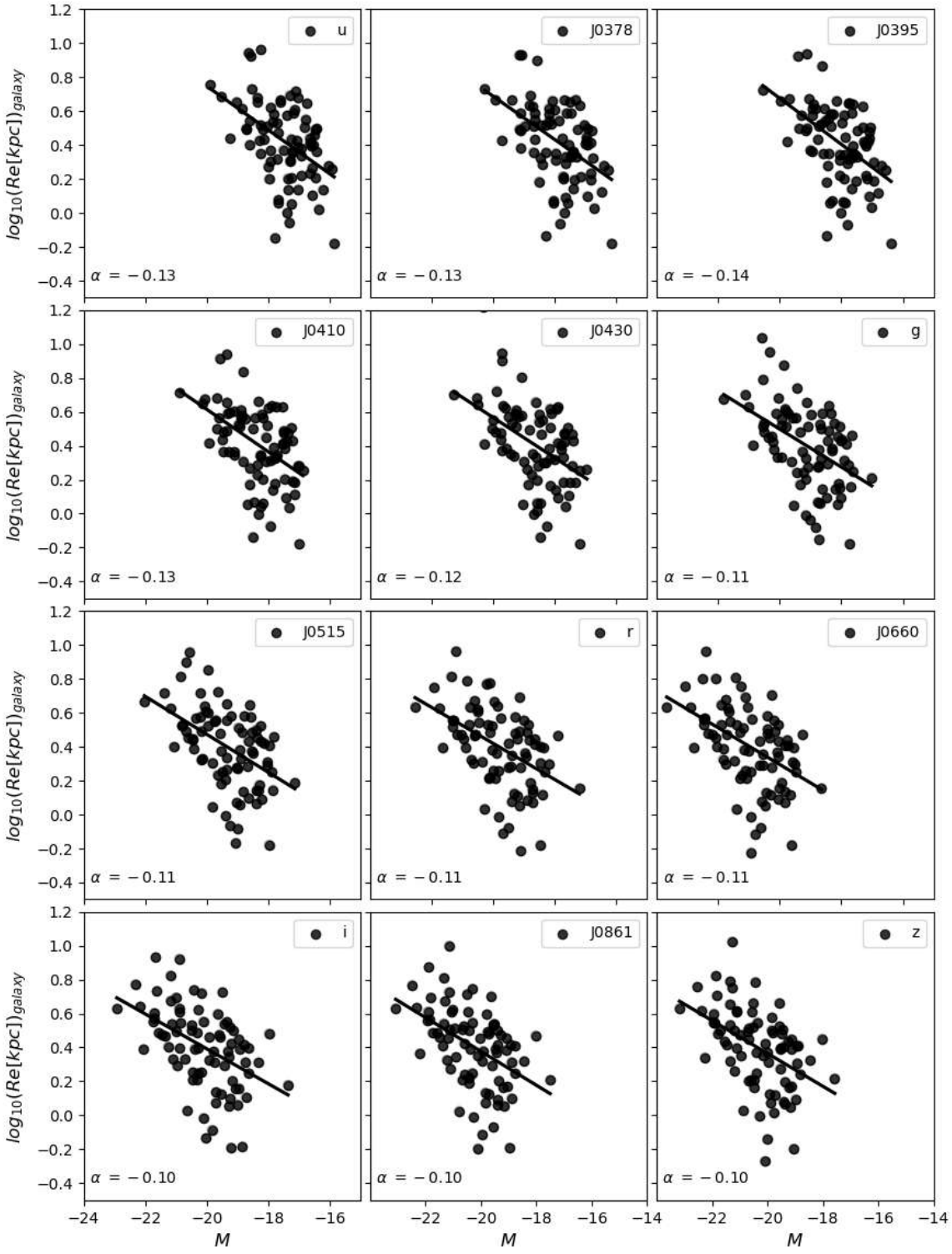

Figure D.4: Galaxy magnitude-size relation in the 12 S-PLUS bands. x-axis and y-axis show the absolute magnitude of the galaxy and the galaxy's $log_{10}(Re[kpc])$, respectively. The black lines show the best linear fit, and the α symbol indicates the slope of the fit.

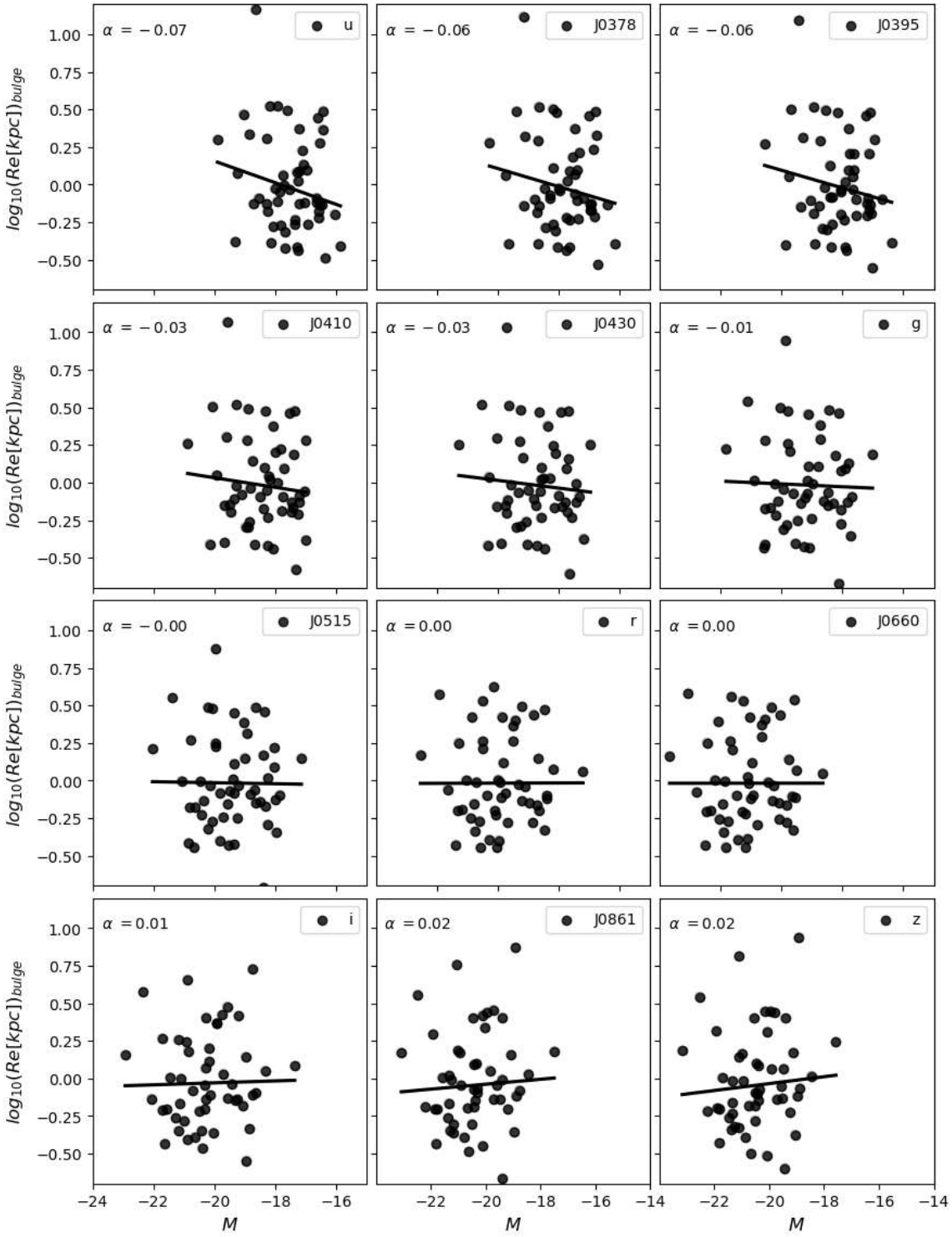

Figure D.5: Bulge magnitude-size relation in the 12 S-PLUS bands. x-axis and y-axis show the absolute magnitude of the galaxy and the bulge's $log_{10}(Re[kpc])$, respectively. The black lines show the best linear fit, and the α symbol indicates the slope of the fit.

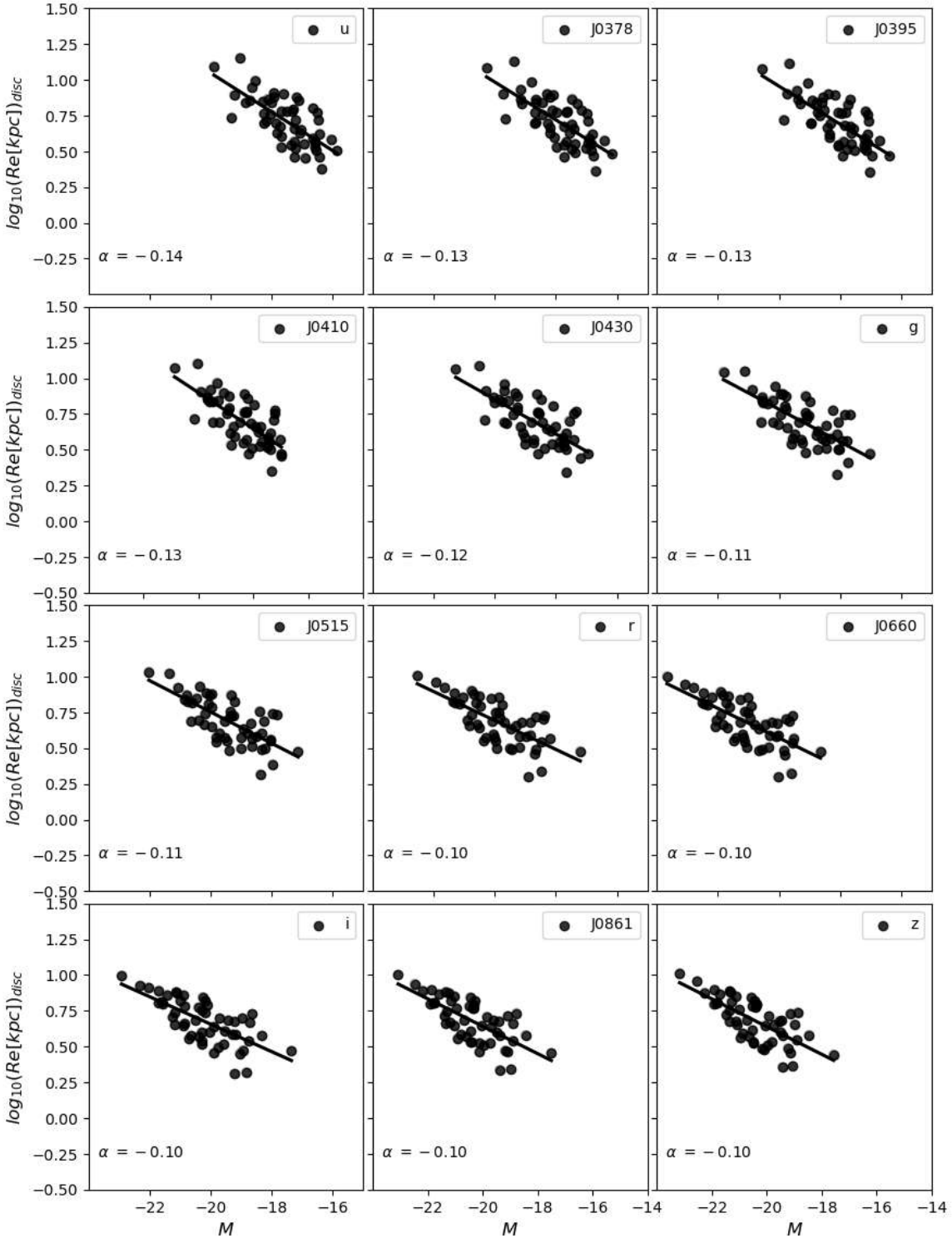

Figure D.6: Disc magnitude-size relation in the 12 S-PLUS bands. x-axis and y-axis show the absolute magnitude of the galaxy and the disc's $log_{10}(Re[kpc])$, respectively. The black lines show the best linear fit, and the α symbol indicates the slope of the fit.

Glossary

AGN Active Galactic Nucleus. 10

BCG Brightest Cluster Galaxy. 17

cD Central Dominant. 9

CDM Cold Dark Matter. 7, 15

CMD Colour Magnitude Diagram. 11

DBSCAN Density-Based Spatial Clustering. 53

DES Dark Energy Survey. 23

DST Dressler-Schectman test. 51

EGs Elliptical Galaxies. 9

ETGs Early-Type Galaxies. 42

EW Equivalent Width. 38

FWHM Full Width at Half-maximum. 21

GAMA Galaxy And Mass Assembly. 36

GS Galactic Survey. 23

ICM Intracluster Medium. 75

IMF Initial Mass Function. 35

LTGs Late-Type Galaxies. 42

MFS Marble Field Survey. 23

MS Main Survey. 22

MSG Main Sequence Galaxies. 42

NED NASA/IPAC Extragalactic Database. 25

NSFGs Non-Star Forming Galaxies. 41

PNe Planetary Nebulae. 21

Q Quiescent. 30

QG Quenched Galaxies. 42

S-PLUS Southern Photometric Local Universe Survey. 18

S0s Lenticular Galaxies. 10

SDSS Sloan Digital Sky Survey. 11

SED Spectral Energy Distribution. 30

SF Star-Forming. 30

SFGs Star-Forming Galaxies. 41

SFR Star Formation Rate. 38

SGs Spiral Galaxies. 10

SMC Small Magellanic Cloud. 23

SMF Stellar Mass Function. 38

sSFR Specific Star Formation Rate. 38

USS Ultra-Short Survey. 23

VFS Variability Field Survey. 23